Very high cycle fatigue characterization of additive manufactured Ti-6Al-4V alloys

Md Mehide Hasan Tusher

A Thesis
in
The Department
of
Mechanical, Industrial and Aerospace Engineering

Presented in Partial Fulfillment of the Requirements
for the Degree of
Master of Applied Science (Mechanical Engineering) at
Concordia University
Montreal, Quebec, Canada

April 2023

CONCORDIA UNIVERSITY

School of Graduate Studies

This is to certify that the thesis prepared

By: **Md Mehide Hasan Tusher**

Entitled: **Very high cycle fatigue characterization of additive manufactured Ti-6Al-4V alloys**

and submitted in partial fulfillment of the requirements for the degree of

Master of Applied Science (Mechanical Engineering)

complies with the regulations of the University and meets the accepted standards with respect to originality and quality.

Signed by the final Examining Committee:

______________________________ Chair
Dr. Mamoun Medraj

______________________________ Examiner
Dr. Mamoun Medraj

______________________________ Examiner
Dr. Biao Li

______________________________ Supervisor
Dr. Ayhan Ince

Approved by ______________________________

Dr. M. Pugh or Dr. S. Narayanswamy

__________2023 ______________________________

Dr. M. Debbabi

Abstract

Very high cycle fatigue characterization of additive manufactured Ti-6Al-4V alloys

Md Mehide Hasan Tusher

A wide range of industries rely on the laser powder bed fusion (L-PBF) technique to produce intricate structures. The Ti-6Al-4V alloy has recently gained a lot of popularity due to its excellent properties in the manufacture of components by L-PBF technology. It is necessary to consider the fatigue performance of L-PBF-Ti-6Al-4V alloy in very high cycle fatigue regime (VHCF) so that the alloy can achieve a wide range of success in various different fields in the future. A study is conducted to examine the effects of stress-relieved (SR) heat treatment on the very high cycle fatigue (VHCF) performance of L-PBF -Ti-6Al-4V alloy in this investigation. There are many factors that can affect the response of the VHCF of L-PBF-Ti-6Al-4V alloy, and this study aims to identify key factors that have a significant influence on the VHCF response of this alloy by combining controlled platform temperatures with stress-relieved heat treatment. To accomplish this, experiments were conducted on Ti-6Al-4V alloy samples manufactured on a substrate with a temperature of 80°C. These samples were subjected to Ultrasonic fatigue testing machine, applying a fully tension-compression load (R= -1). To examine the fractured surfaces of the specimens, a Hitachi Regulus 8230 Scanning Electron Microscopy (SEM) was employed, enabling the analysis of crack-initiating features such as their nature, size, and location. Additionally, in order to identify any defect resulting from the manufacturing process, printed samples were inspected using an XT H225 X-ray μ-CT system (Nikon, MI, USA), allowing computed tomography (CT) observations on the gage sections of the samples.

Acknowledgement

It is my deepest desire to express my deep appreciation to Allah, the Almighty and the Most Merciful, for the blessings, grace, and mercy He showed throughout my research, and for the success I have achieved in completing my M.A.Sc. thesis research.

In order for me to be able to accomplish this work, I would like to extend my sincere thanks to my great supervisor, Professor Dr. Ayhan Ince, who has been a great help throughout the journey. It would be difficult for me to adequately express my gratitude for his support in technical and financial terms, patience, advice, as well as motivation to me.

Having the opportunity to work with my supervisor, Professor Dr. Ayhan Ince, who is the director of the Ultrasonic Fatigue Testing Laboratory at Concordia University has been a fantastic experience. When I first enrolled in my M.A.Sc. program back in 2021, I had very little experience when it came to conducting research. Throughout my studies, Professor Ince has been a great mentor for me, giving me the enthusiasm and guidance that I needed to begin investigating the effects of stress relieved heat treatment on the very high cycle fatigue (VHCF) performance of additively manufactured Ti-6Al-4V alloy. I have been continuously motivated and given proper direction by him throughout my thesis process, which helped me achieve the seemingly impossible task of completing my thesis. As a result of his constant support and helpfulness, I have never had to go through any difficult time alone. There are no words to describe how grateful I am to him for the love and affection he has shown me over the years.

Natural Sciences and Engineering Research Council of Canada (NSERC) and research support from the faculty (FRS) have provided me with partial funding for this research, and I would like to acknowledge their support for this work.

There is no way I can express my gratitude enough for the constructive comments and suggestions from my thesis committee members, Dr. Mamoun Medraj, Dr. Biao Li, and Dr. Ayhan Ince, regarding the development of this thesis and its continuous extension.

I am grateful to my teachers from my home country Dr. Md. Rafiqul Islam, Dr. Md Rabiul Islam Sarker, Dr. Mohammad Uzzal Hossain Joardder, Monjur Mourshed, Mahadi Hasan Masud, Dr. Md Sazan Rahman, Md Saiful Islam who were always an inspiration for me to complete this research works.

Last but not least, I would like to acknowledge with gratitude my parents Md Delwar Hossain and Hamida Khanam for their love, prayers, constant moral support, inspiration, and sacrifices they have made for me during my life. I have no hesitation at all in stating that all of my accomplishments have been made possible by the sacrifices and efforts they have put in throughout their lives. The following is a memory of my father that I would like to share with you. I was told by my father back in 2021 that if I participated in an interview for the position of an assistant researcher in the lab of Professor Dr. Ayhan Ince, I would be selected to work there. At that time, he advised me to keep my commitment given to my supervisor. The illness of my father was taking place at that time. He told me, "If you were to visit Canada and earn some money, then you should send me some money so that I can buy some medicine". But unfortunately, my father died on October 15th,2020 before coming to Canada. So, I would say my father's death before I started my M.A.Sc. was one of the most important losses in my life. I do feel, however, that the prayers of my father are always with me anywhere I go. I would like to express my gratitude to my wonderful wife, Monira Mahfuza Moni, for her love, sacrifice, and constant encouragement throughout this journey. There is not a day that goes by when I do not think of her in my life. She keeps my mind at peace. In regard to her, I am unable to express my feelings in any way. I would also like to thank my brothers Md Arif Hossain, Md Rakibul Hassan Shoikot and sister Mohima Afrin Monica for taking good care of my mother over there in Bangladesh. Furthermore, I would like to express my appreciation to my parents-in-law Abul Kasem and Nasrin Kasem for their continuous prayers and good wishes. Afra Jahan Maymuna and Shazfa binte Shoikot, two of the sweetest and most precious members of my extended family, have always brought me a great deal of joy in my life, and I am very fortunate to have them in my life.

The last thing I would like to do is to dedicate my thesis book in memory of my late father, Md Delwar Hossain. There are so many things I miss about him and may my Almighty rest his soul in peace.

Table of Contents

List of Figures

List of Tables

List of Equations

List of Symbols

R	Load Ratio
A_s	Surface area
L	Location Parameter
S	Shape Factor
β	Material dependent constant
T	Return Period
Ra	Arithmetic mean surface roughness
Rp	Maximum height of the profile
Rz	Point height irregularities
Rv	Maximum depth of the valley
RSm	Mean width of the profile elements
Rmr	Average support ratio of a unit
Kt	Stress concentration factor
N	Number of cycles
σ	Stress amplitude
$\frac{da}{dN}$	Fatigue crack growth rate

List of Abbreviations

LCF	Low Cycle Fatigue
HCF	High Cycle Fatigue
VHCF	Very High Cycle Fatigue
RS	Residual Stress
LoF	Lack of Fusion
HIP	Hot Isostatic Pressing
SLM	Selective Laser Melting
AM	Additive Manufacturing
MAM	Metal Additive Manufacturing
LSP	Laser Shock Peening
AB	As built
HT	Heat treated
RT	Room Temperature
UNSM	Ultrasonic Nanocrystal Surface Modification
RBF	Rotating Bending Fatigue
UTS	Ultimate Tensile Strength
CGD	Constant Gage Diameter
CGV	Constant Gage Volume
CAT	Constant Amplitude Test
RA	Rough Area
HV	Vickers Hardness
L-PBF	Laser Powder Bed Fusion
UFTM	Ultrasonic Fatigue Testing Machine
NSERC	The Natural Sciences and Engineering Research Council of Canada
SEM	Scanning Electron Microscopy
FE	Finite Element
CT	Computed Tomography

EDS	Energy Dispersive Xray Spectroscopy
SR	Stress Relieved
FiE	Fisheye
FGA	Fine granular area
LEV	Largest Extreme Value
CDF	Cumulative Distribution Function
SMAT	Surface Mechanical Attrition
QFM	Quantized Fracture Mechanics
SIF	Stress Intensity Factor

Chapter 1

Introduction and Overview

1.1 Background

Metal Additive Manufacturing (MAM) is a process where fine metal powders are used to produce strong, complex components that are not possible with traditional methods [1-4]. In recent decades, MAM especially L-PBF has been one of the emerging fields that has gained a great deal of interest in industries around the world [1,4-13]. In order to create the 3D metal object using L-PBF, the computer program slices the design into many layers that serve as a framework for all the components of the object. In order for the final product to be created, the metal powders are then layered together and fused with a laser. In the industry, L-PBF is one of the most versatile systems available today and offers an unmatched level of design freedom. A number of benefits are associated with L-PBF, including improved efficiency, reduced waste, lower emissions, and a faster time-to-market for stronger and lighter parts. In the field of additive manufacturing (AM), L-PBF plays a significant role in the increase of the manufacturing industry and keeps it growing. Recently, some lightweight metal especially, Ti-6Al-4V alloy has gained much popularity in designing many structural components in the aerospace, automotive, defense, transportation, and bio-medical industries [2-4,11,13-17]. Ti-6Al-4V compressors and turbines used in aircraft or automobile engines are subjected to high-frequency cyclic loadings that induce fatigue failure [18-20]. It is found that L-PBF results in some features such as defects (porosity, inclusions, balling, laser spatter, etc.), residual stresses, surface roughness, etc. that significantly affect the fatigue behavior of Ti-6Al-4V parts [1,2,15,16,21-30]. Some other factors such as specimen geometry, load ratio, build orientation, size, shape, and location of the defects also affect the fatigue behavior of Ti-6Al-4V parts [31]. So, it is very important to consider the critical factors affecting Fatigue performance while designing L-PBF- Ti-6Al-4V parts. Recently, researchers have given attention to investigating the impact of post-treatment to get optimized fatigue performance of L-PBF-Ti-6Al-4V alloy. Among various post heat treatments, stress relief heat treatment is very common for Ti-6Al-4V alloy to reduce residual stress which is one of the detrimental factors to fatigue response. Though the main focus of stress relief heat treatment is to reduce residual stress, it is also very imperative to investigate whether this post heat treatment has an influence on defects statistics and microstructure ultimately on VHCF performance.

1.2 Ultrasonic Fatigue Testing Machine (UFTM) for VHCF

For performing the fatigue tests, an in-house built Ultrasonic Fatigue Testing Machine (UFTM) as shown in **Fig. 1** was used.

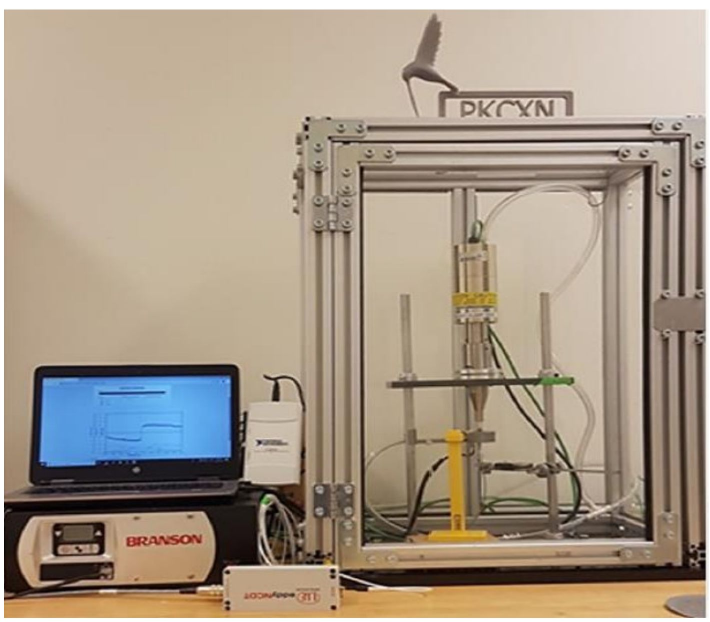

Fig. 1. *Ultrasonic Fatigue Testing Machine (UFTM) developed under the supervision of Dr. Ayhan Ince at Concordia University*

It is shown in **Fig. 1** that the testing machine used in the test is equipped with a piezoelectric converter model CH-20C supplied by Branson with a maximum displacement of 20 μm. The mechanical vibration was generated by driving the converter at a frequency of 20 kHz via a Branson DCX S-Series 120V power supply with a maximum power of 1250 W. The machine consists of a half wavelength horn with an amplification factor of 3.4 machined from Ti-6Al-4V alloy. In order to measure the displacement of the specimen during the fatigue test, the machine uses an eddy current sensor from Micro Epsilon eddyNCDT 3010 with static and dynamic resolutions of 0.025 and 0.04 microns, respectively. It is possible to use this sensor to calculate an accurate displacement of the specimen under the operating frequency of 20 kHz. The power supply and displacement sensor are controlled and monitored by a National Instruments USB-6210 DAC. To perform the tests, a steel stud is used at one end of the specimen to attach it to the horn, while the other end is left free. It is used to determine strain amplitudes of the specimen by positioning the eddyNCDT 3010 beneath the specimen.

1.3 Objectives

As discussed in **1.1**, post heat treatment has been demonstrated as a critical parameter to study fatigue performance in designing components. The thesis work is trying to consider stress relief heat treatment that influence the very high cycle fatigue (VHCF) performances of additively manufactured Ti-6Al-4V specimens and encompasses the following objectives:

I. Impact of defects on very high cycle fatigue (VHCF) performances of additively manufactured Ti-6Al-4V specimens.

II. Investigation on the most critical type of defects initiating fatigue crack.

III. Impact of microstructure on very high cycle fatigue (VHCF) performances of additively manufactured Ti-6Al-4V specimens.

IV. Investigation on the fracture morphologies of fatigue test specimens in VHCF regime.

This thesis is a part of a large research project, "***Very high cycle fatigue characterization of additive manufactured alloy***" funded by The Natural Sciences and Engineering Research Council of Canada (NSERC). The primary objective of this project is to investigate the effect of post heat treatment on the fatigue performances of additively manufactured alloy in very high cycle fatigue regime tested using Ultrasonic fatigue testing machine. The work presented in this thesis is fundamental to provide guidelines for experimental tests of investigating the effect of post heat treatment on very high cycle fatigue performance. The outcomes of these experimental tests will be used to validate numerical models and help the development of the designed components.

1.4 Thesis Organization

There are four chapters in this thesis book which are structured according to the paper-based format suggested by Concordia University and are grouped according to the order in which they are presented. The outcomes of this thesis in partial fulfillment of the requirements for the degree of Master of Applied Science (M.A.Sc.) in Mechanical, Industrial & Aerospace Engineering (MIAE) have led to two journal articles one of which is already published in a peer-reviewed in the ASTM International journal of Materials performance and characterization at the time of this submission. **Chapter 1** gives an overview of Metal Additive manufacturing (MAM), UFTM and objectives of the research. **Chapter 2** describes a systematic review of the critical factors affecting fatigue performance of L-PBF-Ti-6Al-4V alloy both in high cycle and very high cycle fatigue regimes. **Chapter 3** describes the impact of stress relieved heat treatment on very high cycle fatigue performance (VHCF) of additively manufactured Ti-6Al-4V alloy. It includes test setup, experiment matrix, fatigue lives measurement and analysis procedures. Finally, **Chapter 4** provides a summary of the findings and a number of recommendations for further investigation.

Chapter 2

High Cycle Fatigue and Very High Cycle Fatigue Performance of Selective Laser Melting Ti-6Al-4V Titanium alloy – A Review

Md Mehide Hasan Tusher[1], Ayhan Ince[1, *]

* Corresponding author: E-mail: ayhan.ince@concordia.ca

Article published in << Materials performance and Characterization>>

DOI: 10.1520/MPC20220088

2.1 Abstract

Additive Manufacturing (AM) of metallic alloys, especially Titanium (Ti), has recently received considerable attention due to its significant role in designing and developing many structural components with complex geometries in aerospace, defense, and biomechanical industries. AM technology based on selective laser melting (SLM) allows the production of lightweight structures with geometric flexibility, which has not been otherwise possible by the conventional manufacturing process. SLM-fabricated Ti-6Al-4V components often experience long loading histories in high cycle fatigue (HCF) and even very high cycle fatigue (VHCF) regimes. As a result, it is paramount to systematically investigate those components' fatigue behavior under both HCF and VHCF conditions. However, HCF and VHCF performances of SLM-Ti-6Al-4V alloy are still

[1] Department of Mechanical, Industrial & Aerospace Engineering, Concordia University, Montreal, Quebec, H3G 1M8, Canada

not fully understood due to the complex nature of fatigue responses in those regimes resulting from the defects/porosity and number of process parameters. In this context, the successful application of load-bearing components in both HCF and VHCF regimes necessitates optimizing process parameters and post-treatments for the optimal fatigue performance point of view. Several recent studies dealing with Ti-6Al-4V parts manufactured by SLM have explored parameters affecting fatigue performance in HCF and VHCF regimes. This paper presents a systematic and critical review analysis of recent findings related to critical parameters, particularly residual stress, surface roughness, build parameters, build orientation microstructural features, post-process treatment, manufacturing deficiencies, specimen geometries, load ratio affecting mechanical and fatigue properties, especially in HCF and VHCF regimes. The current study also aims to identify several crucial topics that need to be addressed for SLM Ti-6Al-4V alloy to effectively utilize its full potential in designing of advanced structural components.

Keywords: Additive manufacturing, selective laser melting, high cycle fatigue, very high cycle fatigue, Ti-6Al-4V

2.2 Introduction

It has been observed that additive manufacturing (AM) has gained much attention over the last several decades due to its unprecedented design freedom when combined with modern technology [1,4-13]. The powder-based AM technology, especially Selective Laser Melting (SLM), allows the production of lightweight structures with complex geometric features, which has not been otherwise possible by conventional manufacturing processes [1-4]. The SLM offers many advantages over traditional manufacturing processes such as casting, machining, and forming in the cost-effective and time-efficient manufacturing of complex parts/components [32-34]. The SLM is based on the layer-by-layer deposition of a near-net shape component using a laser beam as the thermal source [14,25]. In the SLM, a metallic powder is melted selectively by the laser based on layer-to-layer deposition. Moreover, smaller particles, thinner build layers, and slower scan strategies utilized in the SLM technique result in finer features, better surface finish, and tighter build tolerances compared to other layer-based AM techniques [35]. In recent years, SLM-processed alloys, especially Ti-6Al-4V, have recently received considerable attention due to their high strength, low density, and corrosion resistance [4]. Thus, Ti-6Al-4V plays a significant role in designing and developing many structural components with complex geometries in aerospace, automotive, defense, transportation, and biomechanical industries [2-4,11,13-17]. As for aircraft or automobile engines, Ti-6Al-4V compressors and turbine blades are subjected to high-frequency cyclic loadings, which induce fatigue failure [18-20]. In order to ensure the long-term reliability of cyclically loaded components, good fatigue performance is considered as one of the most important mechanical factors [21,36]. It has been a traditional practice in fatigue design to determine the fatigue limit of a component by analyzing its fatigue strength [37]. In terms of fatigue life, there are three different life regimes based on the number of fatigue cycles experienced by a component. The first one is low cycle fatigue (LCF) which lasts up to 10^5 cycles until failure. The second one is high cycle fatigue (HCF) which lasts between 10^5 and 10^8 cycles until failure, and very high cycle fatigue (VHCF), which lasts above 10^8 cycles till failure [38]. However, there are some studies to suggest that the HCF lasts between 10^4 and 10^7 cycles until failure and the VHCF, which lasts above 10^7 cycles until failure [4,39-41]. This paper discusses fatigue performance with the assumption of the HCF lasting between 10^4 and 10^7 cycles and the VHCF lasting beyond 10^7 cycles. A wide range of factors induced by the SLM process significantly influence fatigue behavior in both the HCF and VHCF regimes, along with the structural performance of components made of SLM materials. A number of variables are involved in the fabrication of the

SLM metallic part, such as rate of deposition, laser power, scanning speed, build layer thickness, processing temperature, build direction, and build environment. These variables directly affect resulting features such as surface roughness, residual stress (RS), microstructural morphology, and defects (e.g., surface and subsurface), including gas and shrinkage porosity, voids, inclusions, micro-cracking, balling, etc [1,2,15,16,21-30]. These SLM-resulting features significantly affect the fatigue behavior of SLM-Ti-6Al-4V parts in the HCF and VHCF regimes [1,2,14,21]. Some other factors also appeared to affect fatigue resistance and data dispersion, including the size, shape, and location of the pores on the specimen surface [14]. SLM processes often make use of inert gases or vacuum atmospheres in order to reduce the adverse effects of atmospheric gas absorption on material properties [42,43]. However, the use of a high vacuum environment may, however, results in melt vaporization and the escape of impurities, leading to the formation of the SLM with heterogeneous chemical properties [44,45]. Furthermore, flow rates and paths taken by inert gas during the production process significantly affect the porosity level in SLM fabricated parts [46]. Thus, the final SLM-Ti-6Al-4V part can contain gas porosity which is detrimental to HCF and VHCF performance. SLM parts also exhibit reduced microstructural heterogeneity and uneven RS due to low substrate temperatures [47,48]. Microstructural modifications of SLM metallic materials have been demonstrated either by roller mechanisms that apply a load to each layer after deposition or by incorporating a heat sink into the printed part [49]. An AM part commonly exhibits columnar grains with epitaxial properties, causing anisotropy in mechanical properties [50-57] . There is a direct relationship between anisotropy and the alignment of grain grids parallel to the build direction. As a result of longer grain boundary lengths, there is more accumulation of slip dislocations along the prior grain boundaries in the build direction compared to the orientation perpendicular to the build direction [58,59]. Thus, vertically oriented Ti-6Al-4V samples generally exhibit more plastic deformation before failure [60]. SLM-Ti-6Al-4V parts also exhibit lack-of-fusion defects that act as stress concentration sites causing cracks to propagate along the defect tip and ultimately fail, resulting from unoptimized process parameters [14,61,62]. There is a strong relationship between the fracture toughness anisotropy and the crack propagation path in the SLM parts [63]. According to previous works, cracks propagate through columnar grains in horizontally oriented samples, whereas cracks propagate along the columnar grain boundary in vertically oriented samples [28]. The ductility of Ti-6Al-4V parts is additionally anisotropic based on the build orientation [54] . It is also found that the tensile strength of the lower half of the sample blocks is stronger than the upper half because of oxygen strengthening and a finer microstructure [52,54,64]. Ductility and the fatigue performance of SLM-Ti-6Al-4V parts in the HCF and VHCF regimes also show a significant relationship. Vertically oriented Ti-6Al-4V parts have better ductility than horizontally oriented ones, and different post-heat treatments can increase their ductility [47,52,65-67]. The hardness of the SLM parts is also affected by the microstructure of the built materials. Ultimately, this property affects the HCF and VHCF performances of SLM-Ti-6Al-4V parts [49,68]. It has been demonstrated that the fracture toughness of SLM-Ti-6Al-4V parts is affected by the RS, which can be reduced by thermal treatment processes such as stress relief heat treatment. There is evidence that after post-heat treatment, the fracture toughness of SLM-fabricated parts of Ti-6Al-4V alloy increases with the loss of anisotropy [28,69]. Therefore, it is imperative to fully comprehend the as-built (AB) microstructure of metal SLM systems before selecting an appropriate post-heat treatment scheme to achieve the required fracture toughness. SLM-Ti-6Al-4V parts have low fatigue strength compared to wrought metal, mainly caused by the roughness of the build surface and the minimal levels of internal defects that can act as crack-initiating sites [60]. Though the opposite conclusion is available, the fatigue strength of SLM-Ti-6Al-4V parts is more optimized in a horizontal configuration than in a vertical direction [3,14,70-72]. Most usually, SLM parts have a higher Paris slope than their equivalents manufactured using EBM, which indicates a faster growth rate of fatigue cracks due to RS, grain orientation, and the number of grain boundaries at the crack tip, along with the degree of surface roughness and internal defects [60,73,74]. However, post-surface treatment and post-heat treatment processes can improve fatigue strength [75-82]. As per previous discussions, there are a number of critical factors that affect the fatigue performance of SLM-Ti-6Al-4V parts in the HCF and VHCF regimes that need to be taken into consideration. This paper provides a comprehensive overview of the critical factors such as microstructure, build orientation, fabrication parameters, RS, load ratio, test frequency, surface polish, specimen geometries, ductility, and heat treatment that have a significant impact on HCF and VHCF characteristics, and fracture mechanisms of the Ti-6Al-4V parts manufactured by the SLM technique. This paper also aims to describe recent advances in this field and highlights some key points that need to be addressed to continue progress in the field of the SLM technique. To support utilizing the benefits of this rapidly developing technology and fully employ the potential applications of the SLM Ti-6Al-4V parts, this paper attempts to provide a broad understanding of interconnections between the various aspects of the subject. The authors hope that the information from this paper will lead future studies for further improvements of the fatigue performance of Ti-6Al-4V parts in the HCF and VHCF regimes, as well as widening applications of SLM fabricated Ti alloys in different industry applications.

2.3 SLMed Titanium alloys

2.3.1 SLM technique

SLM is based on a layer-by-layer AM method for fabricating metallic parts from powder [16,83]. In addition to its ability to produce high-quality features and internal passages, the advantages of this system include its ability to maintain dimensional control while maintaining a high level of resolution [84,85]. Its ability to conserve raw materials and reduce energy consumption, part costs, and fabrication time has made the process attractive to industries such as aeronautics, automotive, and biotech [42,86-88]. **Fig. 2** illustrates a schematic representation of the SLM process.

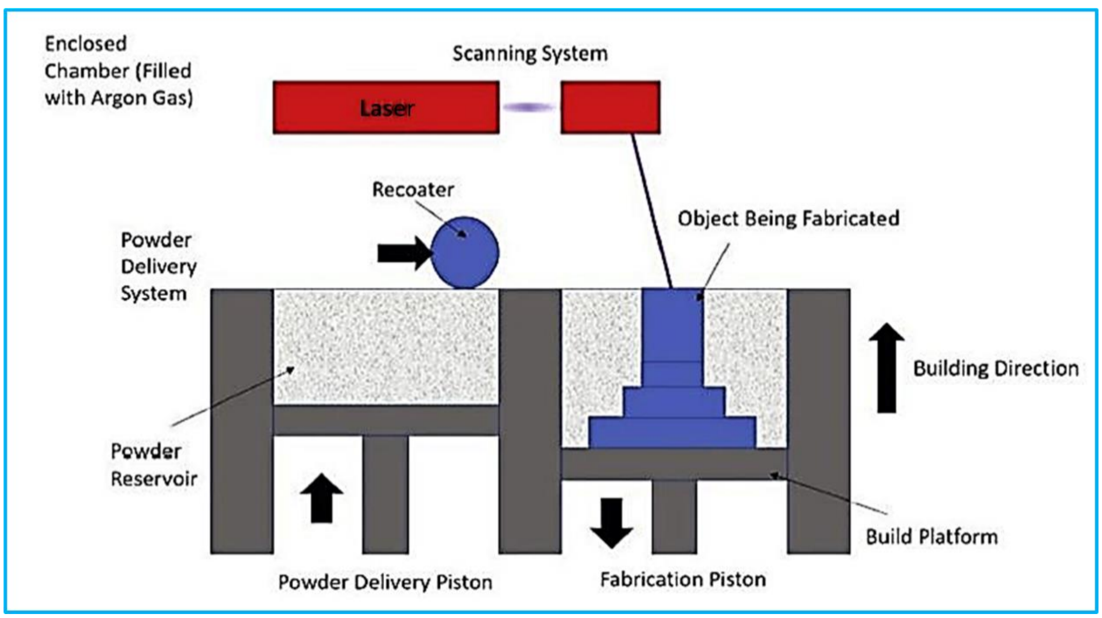

Fig. 2. *Schematic set up of SLM of method [89].*

SLM process involves several steps, including powder deposition and laser scanning, that take place in order to create a part [90]. It is necessary to conduct the melting and solidification procedure in an inert chamber in order to prevent the oxidation of the compound during melting and solidification [91].

In terms of operational sequence, it is possible to breakdown the SLM process into the following steps:

a. An STL file is typically used to export a 3D CAD model.
b. It is oriented in the optimal orientation for the build, depending on the Z-axis height, the surface finish, and the minimization of the support structure.
c. All the minimal support design iterations are incorporated into the support structure to generate.
d. Layers of equal thickness are sliced from the file and transferred to the machine.
e. Build plates are heated to reduce thermal gradients [92], preventing curling of the parts from thermal expansion [93].
f. Metal powder is dispersed on a mobile platform.
g. An intense laser beam (energy source) is used to deliver energy to the bed surface for melting the powder at particular locations/paths.
h. The build plate is then lowered by the thickness of the layer for the deposition of another layer.

A layer-by-layer process is carried out by repeating the sequence from f to h to create a solid three-dimensional component. There are two types of time assigned to build a product: primary and auxiliary. The former allows the powder to be scanned, which is process parameter-based, while the latter enables the build plate lowering and powder deposition, commonly referred to as "recoating" [94,95].

2.3.2 Ti-6Al-4V alloy

Ti-6Al-4V is an α+ β titanium alloy where Al stabilizes α and V acts as a β stabilizer. The nominal chemical composition of Ti-6Al-4V alloy is given in **Table *1***. This alloy solutes 6 wt% Al and 4 wt% V to pure Ti. Ti is an allotropic material that is found in two different crystal structures, namely α and β Ti. α-Ti exists below the β transus temperature, while β-Ti is found above the β transus temperature [96]. On the contrary, it is possible to maintain the dual phase α+ β Ti-6Al-4V alloy at room temperature. Although phases can transition in Ti-6Al-4V, the transition temperature and cooling rate associated with the fabrication process strongly affect the degree to which the phase transformation occurs [97]. It is predicted that when fast cooling is applied from above the ß transus temperature, the β phase is decomposed by a non-equilibrium martensite reaction instead of α + β transformation [96]. It is beneficial to undergo diffusional transformations in order to produce α + β phase, while alpha prime (α') martensite transformation is a diffusionless process that can be produced by rapid cooling [96]. Due to its chemical and mechanical properties, Ti-6Al-4V has become widely used in aerospace, defense, maritime, power generation, automotive, and biomedical industries [98-102]. These properties include a high strength-to-weight ratio, good stability at high temperatures, excellent corrosion resistance, excellent fatigue resistance, and a high level of biocompatibility [98-102]. This alloy shows poor thermal conductivity, low modulus of elasticity, and high chemical reactivity, with most of the materials used to form cutting tools that tend to weld to the cutting tool [102-107]. The poor thermal conductivity of this alloy makes it challenging to dissipate the heat generated during machining, and the low modulus of elasticity causes elastic recovery and chatter [102-107]. Thus, it is complicated to machine this alloy by traditional processes compared to other competitive metal alloys. Another downside of this alloy is that it is costly compared to other competitive metal alloys. The AM technology, particularly the

SLM, can produce complex components of Ti-6Al-4V with few machining steps to their net or near-net shapes [102,108]. Despite all the benefits of the SLM method, it also has many challenges due to its intrinsic properties like RS(es) that develop during solidification due to high cooling rates and temperature gradients that affect fatigue and fatigue crack propagation in SLM parts of Ti-6Al-4V alloy [102,109]. AB parts have an anisotropic microstructure due to the rapid cooling rates that occur during the part density maximization process, which is entirely composed of acicular α' martensite distributed within columnar prior β grains of the material [68,102,110-112]. Consequently, AB -Ti-6Al-4V parts manufactured by SLM feature higher hardness, yield strength, and tensile strength but have a lower ductility than their wrought counterparts. As a result, for most practical applications, the use of such AB parts in the service is very limited. As a potential solution, Metastable martensite can be transformed into a biphasic α-β structure via post-processing heat treatment to get a good balance between ductility and strength [67,102,113].

Table 1. wt% range of chemical composition of the Ti-6Al-4V alloy [114,115].

Fe	V	C	H	N	O	Al	Y	Other elements	Ti
≤ 0.3	3.5-4.5	≤0.08	≤0.015	≤ 0.05	≤ 0.2	5.5-6.75	≤ 0.005	≤ 0.40	Bal.

2.4 Effects of critical factors on HCF and VHCF performances of SLM -Ti-6Al-4V parts

Fatigue failure is one of the most common failure modes that occurs due to cyclic loadings. For aircraft or automobile engines, Ti-6Al-4V compressors and turbine blades are subjected to high-frequency cyclic loadings. The following information may help the readers to better understand loading scenarios of each component in each of their applications: When aircraft engines are in operation, their compressors and turbine blades are subjected to high-frequency cyclic loads in the form of cyclic vibrations at frequencies above 1 kHz throughout their service lives [18,19]. Turbine blades are supposed to operate for more than 1.5×10^4 hours before they can be rejected due to failure [19]. Thus, it can be observed that a turbine blade undergoes approximately 5.4×10^9 loading cycles during its service life. In general, HCF and VHCF fatigue performances are usually estimated using stress-life (S-N) or strain-life (ε-N) methods, where N indicates the cycles to failure. Several recent studies have involved Ti-6Al-4V parts manufactured through the SLM technique concerning HCF and VHCF performances. There are many critical factors that significantly affect the HCF and VHCF performances of SLM-Ti-6Al-4V parts. The significant factors revealed in the literature affecting the fatigue life of SLM-Ti-6Al-4V parts are regarded as microstructure, RS, defects (lack of fusion (LOF), pores, etcetera), fabrication parameters, post-processing treatment, load ratio (R-ratio), specimen geometry, etc.[2,3,14,21,70-72,76,80,89,96,102,110,116-149]. In this review paper, significant factors affecting the HCF and VHCF performances of SLM-Ti-6Al-4V parts are discussed in a systematic way to provide a better understanding of the effects of those factors.

2.4.1 Influences of microstructure on fatigue performance

There is a strong correlation between microstructure and fatigue behavior of SLM-Ti-6Al-4V specimens [150]. The appropriate conditioning, reduction, or removal of pores may not improve fatigue performance if the microstructure necessary to satisfy the optimal combination of strength and ductility is sacrificed simultaneously [151]. A sample with fine microstructure generally exhibits a higher fatigue strength than one with a coarse microstructure [152]. The microstructure of SLM-Ti-6Al-4V parts is mainly governed by the cooling rate [153]. In the SLM method, cooling rates of about 10^4~10^6 k/s are found that produce martensitic structures in AB samples which contains ultrafine acicular α phases among β grains (**Fig. 3**A) [1,29,96,110,151,154]. Zhang et al.[151] investigated the effect of microstructure on the fatigue performance of SLM-Ti-6Al-4V parts.

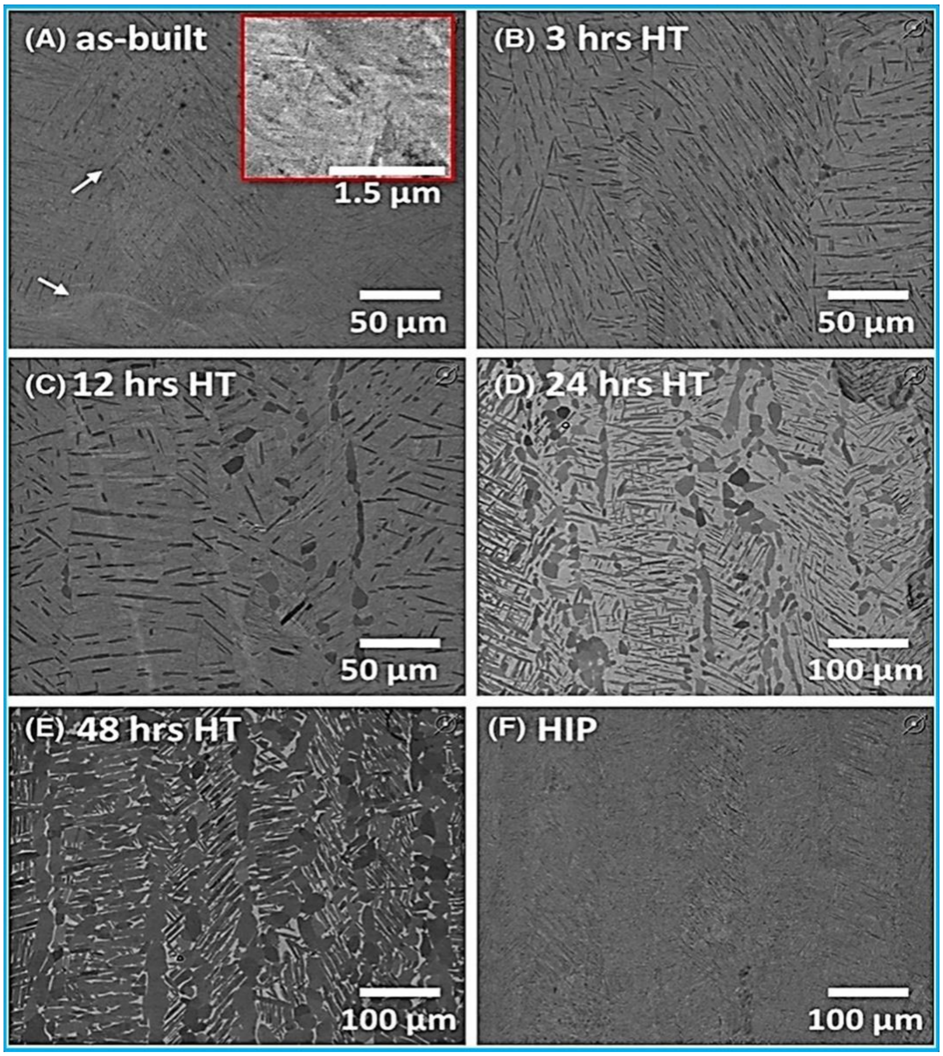

Fig. 3. *Microstructure evolution depending on different heat treatment temperatures and hot isostatic pressing. A higher magnification image of the martensitic structure is shown in the inset in (A). (A) As-built, (B) 3-h HT, (C) 12-h HT, (D) 24-h HT, (E) 48-h HT, and (F) HIP. Adapted from Zhang et al. [151] with permission from John Wiley and Sons.*

According to the authors, the thickness of the acicular martensites of AB Ti-6Al-4V samples is as tiny as a few hundred nanometers [151]. It is possible to discern the trace of the melting pools as well as the β-grains on the surface, as shown in figure 2*A* by the white arrows [151]. An initial HT of 3 hours decomposes the metastable martensitic structure into the regular α+β lamellar structure, with the thickness of most α laths below 1 μm [151]. It was demonstrated that the HT application over three hours decomposes the metastable martensitic structure into a regular lamellar structure with most of the laths having thickness below 1μm, which continued to grow after HT was continued **(Fig. 3*B*)** [151]. A bimodal type of microstructure shows that both strength and fatigue performance have reached good equilibrium after 12 hours of the HT treatment based on the Hall-Petch relation of Ti-6Al-4V **(Fig. 3*C*)** [151]. The reason for the improvement in the fatigue performance is the thickness of major α laths of about 5 to 10 μm whereas finer α laths are around 1 μm in the bimodal microstructure [151]. In addition, if the HT time used exceeds 24 hours, larger globules are more likely to be formed, which may result in a degraded strength; however, ductility may be increased in a moderate way **(Fig. 3*D*** and **Fig. 3*E*)** [151]. The HIP process produces a uniform structure with a well-defined Widmanstatten pattern, which will give a better fatigue performance than the AB samples due to the thickness of the lath of about 1-2 μm **(Fig. 3*F*)** [151]. Hasib et al.[155] also mentioned that α/ α' lath thickness is the most critical factor controlling the fatigue crack growth (FCG) resistance, ultimately, the fatigue performance of SLM-Ti-6Al-4V parts. It has been shown that greater lath thicknesses lead to a higher fatigue threshold and better FCG resistance [155]. Li et al.[156] also found refined microstructure of HIPed Ti6Al4V parts near defects that helps to improve HCF performance. Yu et al.[78,157] also discovered mostly needle-shaped α′ martensites in AB-Ti-6Al-4V parts. However, HIP, HT-920 ^{0}C, and HT 850- 550

^{0}C treatments coarsen the α laths and form β grains [78,157]. Zhang et al.[158] showed that subsequent heat treatment with furnace cooling helps to increase α lath thickness (**Fig. 4**).

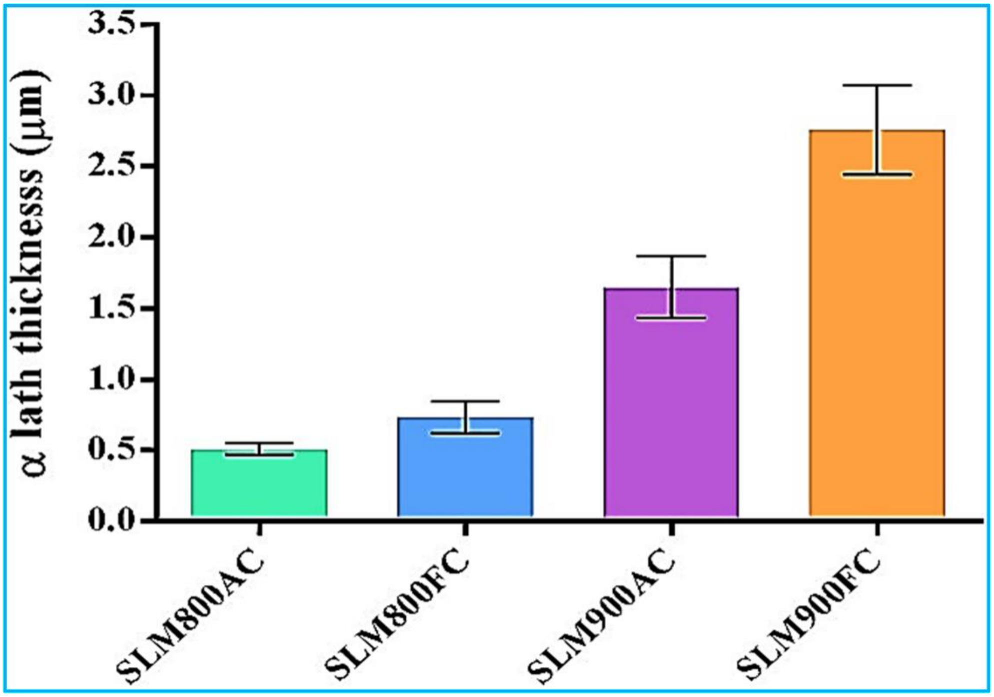

Fig. 4. *Heat treatment* effects on *the α lath thickness of SLM-Ti-6Al-4V parts. Here, AC and FC stand for air cooling and furnace cooling, respectively. Adapted from Zhang et al.[158] with permission from Elsevier.*

Following post-processing treatment, martensites decompose further into fine, dispersive lamellar α + β grains (**Fig. 5**) [78,157]. The width of the lamellar α phase gradually increased from 0.3 to 3.1 μm as the heat treatment temperature increased from room temperature to 950 ^{0}C [157].

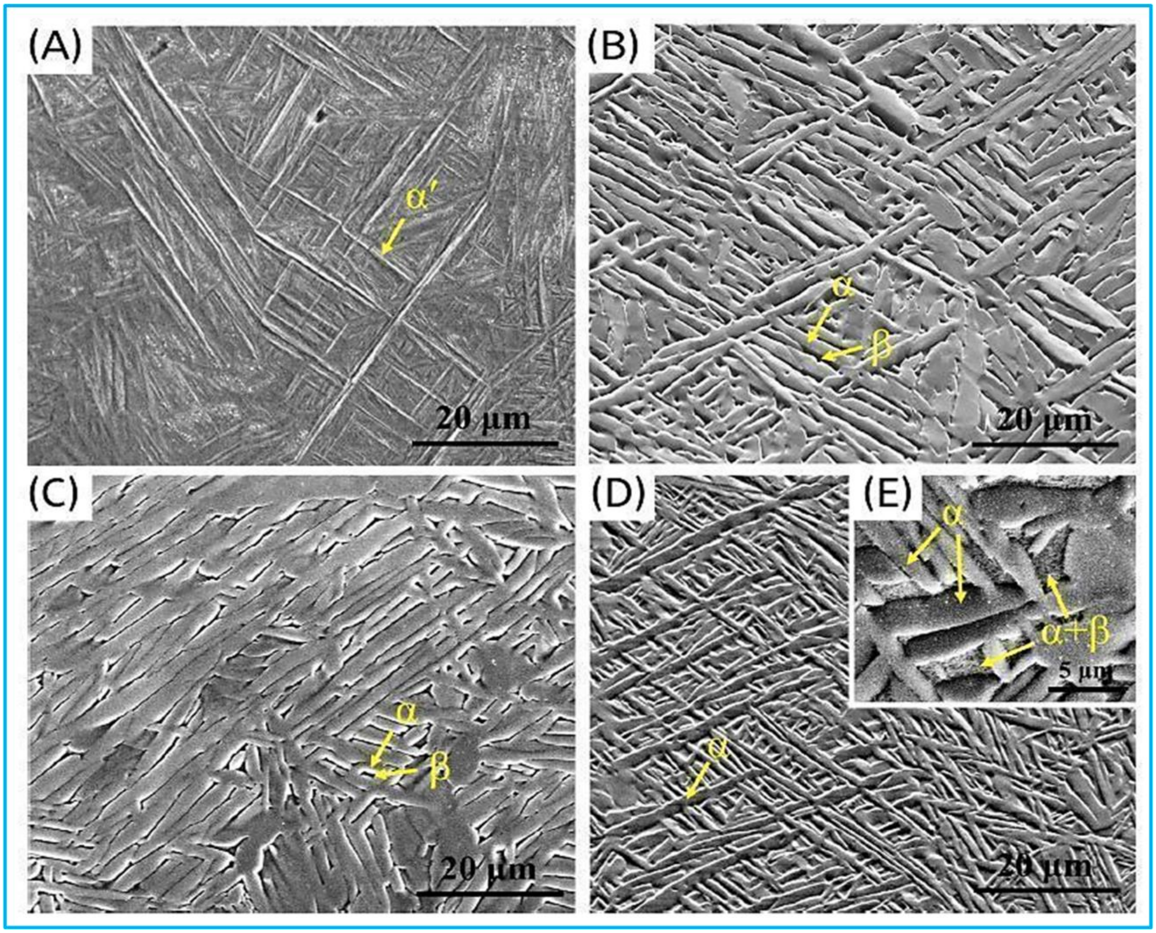

Fig. 5. *shows SEM micrographs of the microstructures of (A) SLMed, (B) HIPed, (C) HT-920^{0}C, (D), and (E) HT-850-550^{0}C Ti-6Al-4V specimens. Adapted from Yu et al.[78] with permission from Elsevier.*

According to Leuders et al.[159] heat treatment and HIP treatment enhance fatigue strength by changing the microstructure of the martensite material into a dominated α -Ti microstructure (**Fig. 6*A*** and **Fig. 6*B***). If the part temperature is raised above the martensite decomposition temperature by repeated reheating, ultrafine Widmanstatten structures will be found [101]. There is a possibility of getting pure α' or α" or a combination of α' or α" due to total martensitic transformation if a high cooling rate in the molten pool is used [110]. Sufficient reheating can decompose the martensitic phases and the massive phases as they are meta-stable. Reheating decomposes the α' phase at a temperature as low as 400 ^{0}C suggesting, that stress-relieving heat treatment above 400 ^{0}C can easily decompose the α' martensite [154].

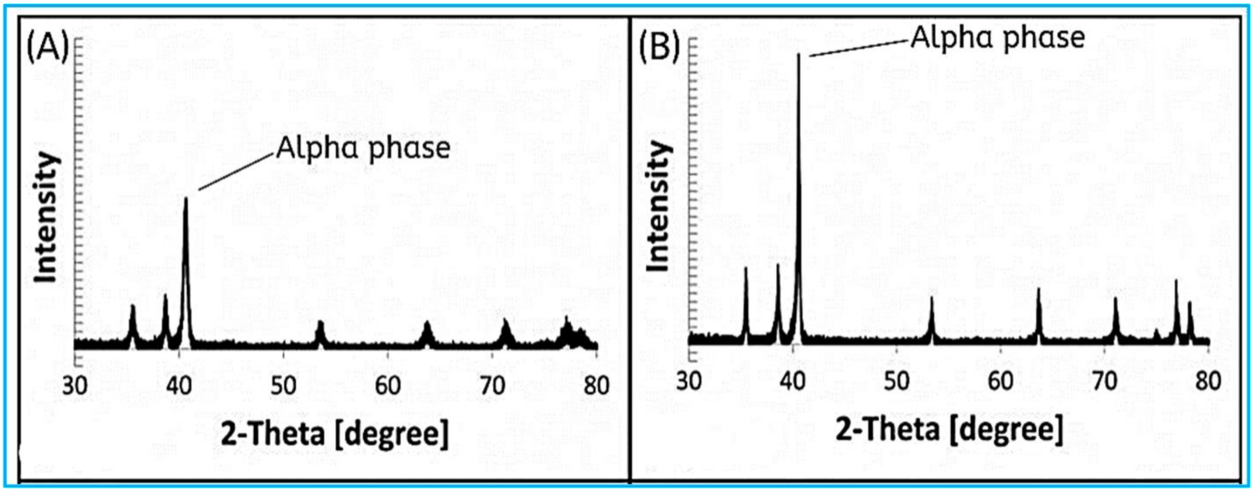

Fig. 6. *shows (A) XRD spectra for Ti-6Al-4V specimens in AB condition and (B) XRD spectra for Ti-6Al-4V specimens heat treated (HT) for 2 h at 800^{0}C. Adapted from Leuders et al.[159] with permission from Elsevier.*

Furthermore, increased power density can also decompose the α' martensite. For α+β microstructures, if the cooling rate is increased, the size of the α colonies and the thickness of individual α plates will decrease. According to Yang et al.[68] four different martensites (primary, secondary, tertiary and quartic α′ martensites) are found in the microstructure of SLM-Ti-6Al-4V parts that can be controlled by adjusting the fabrication parameters. SLM-Ti-6Al-4V parts show improved fatigue-resistant but poorer ductility than the EBM-Ti-6Al-4V parts. This is because of the high density of dislocations and twins inside the needle-shaped α' martensite, generally with a lath width between 0.2-1μm [68,96,159-161]. By sacrificing plastic strain and the fine structure, the dislocation strengthening effect is enhanced at the expense of dislocation motion being further restricted [159,160]. When the microstructure of an SLM sample is annealed in a range between 400^0C to 800^0C, RS are removed, and α' martensite is decomposed, resulting in an improved stress intensity factor [96]. It is found that α' martensite will completely decompose at a temperature higher than 700^0C but the temperature below 600^0C results in an incomplete decomposition [96]. As for the α+β microstructure, fatigue performance is improved with a decrease in α phases [96]. However, Kasperovich and Hausmann[32] postulated that due to the irregular martensitic microstructure, unexpanded particles, pores, and microcracks exist in SLM-Ti-6Al-4V parts, the fatigue strength of SLM parts appears to be lower than that of wrought Ti-6Al-4V components. Ivanova, Biederman, and Sisson Jr. [162] reported that the crack begins in the alpha phase of the HCF regime and propagates through the alpha phase as a cleavage fracture of T-textured alpha grains. It is most likely due to this process that this alloy exhibits abnormal mean stress behavior under HCF. In addition, Rafi [160] asserted that alpha-phase embrittlement could occur when oxygen content increases on the surface. Leyens and Peters [98] stated that interstitial elements (oxygen, hydrogen, nitrogen, and carbon) play a critical role in the ductility and, ultimately, the fatigue strength of the Ti-6Al-4V parts.

2.4.2 Influences of defects on fatigue properties

Process inherent defects play an important role in the fatigue behavior of SLM-Ti-6Al-4V parts both in HCF and VHCF regimes, as these defects act as a stress raiser [14,21,76,120,159,163-165]. There are different types of defects that can be found in SLM-Ti-6Al-4V parts, e.g., porosity, LOF, rough surface, balling, hot tears, fish scales etcetera [47,67,121,163,166-168]. **Fig. 7-Fig. 9** show different types of defects present in SLM samples.

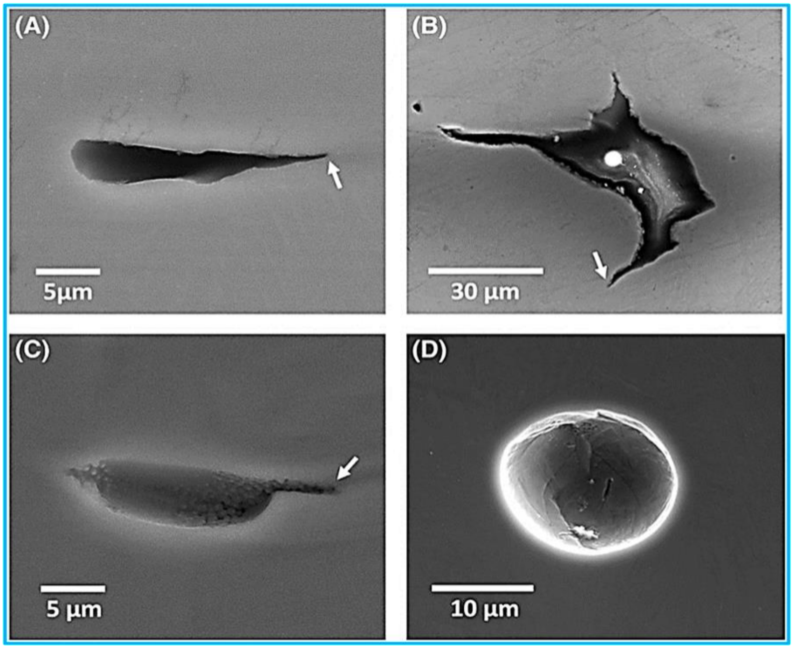

Fig. 7. *SEM images showing the cross section of pores on the longitudinal sections of the AB sample; (A)-(C) lack of fusion pores with sharp edges of different curvature marked by white arrows; (D) spherical pores. Adapted from Zhang et al. [151] with permission from John Wiley and Sons.*

Kasperovich and Hausmann [32], Du et al.[120], Li et al.[127] , Liu et al.[2], Liu et al.[169], Gong et al.[153,163] , Xu et al.[71], Liu and Wang [70], Pessard et al. [170], and Hu et al. [164] investigated the effect of porosity/defects and found a detrimental impact of porosity/defects both on HCF and VHCF performances. Du et al.[120] used 10 groups of specimens with different porosity levels (Group_1:2.85 %, Group_2:5.18 %, Group_3:8.03 %, Group_4:1.20 %, Group_5:0.83 %, Group_6:2.40 %, Group_7:53 %, Group_8: 4.73 %, Group_9:1.28 %, Group_10:0.20 %) to investigate the effect of porosity on the fatigue strength of SLM-Ti-6Al-4V parts.

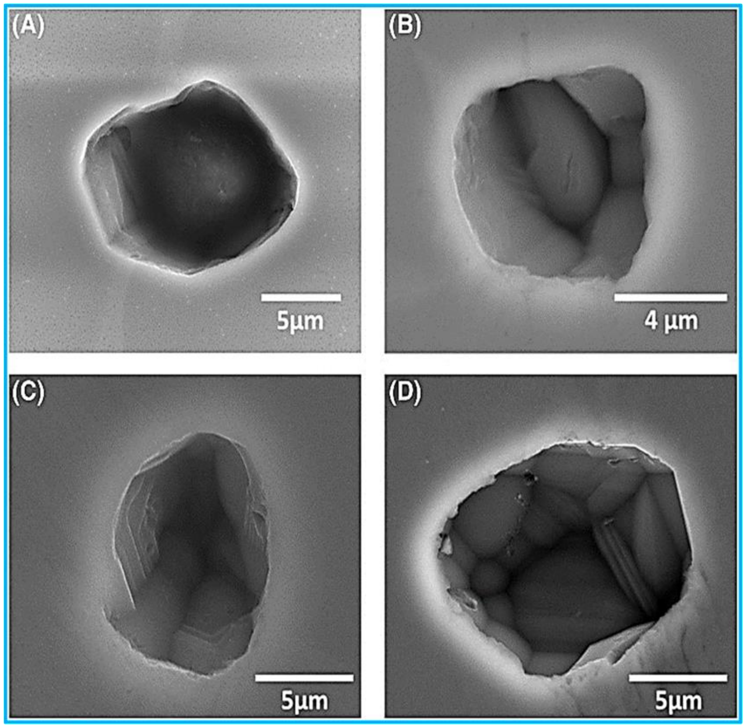

Fig. 8. *(A) -(D) Faceting of spherical pores under HT for 48 hours. Adapted from Zhang et al.[151] with permission from John Wiley and Sons.*

The authors found the highest fatigue strength (300 MPa at 10^7 and 280 MPa at 10^8 failure cycles) for the specimen group 10, which showed the lowest porosity (0.20%). In contrast, the lowest fatigue strength (90 MPa at both 10^7 and 10^8 failure cycles) was found for the specimen group 3 containing the largest porosity (8.03%) at 10^7 failure cycles (**Fig. 10**) [120].

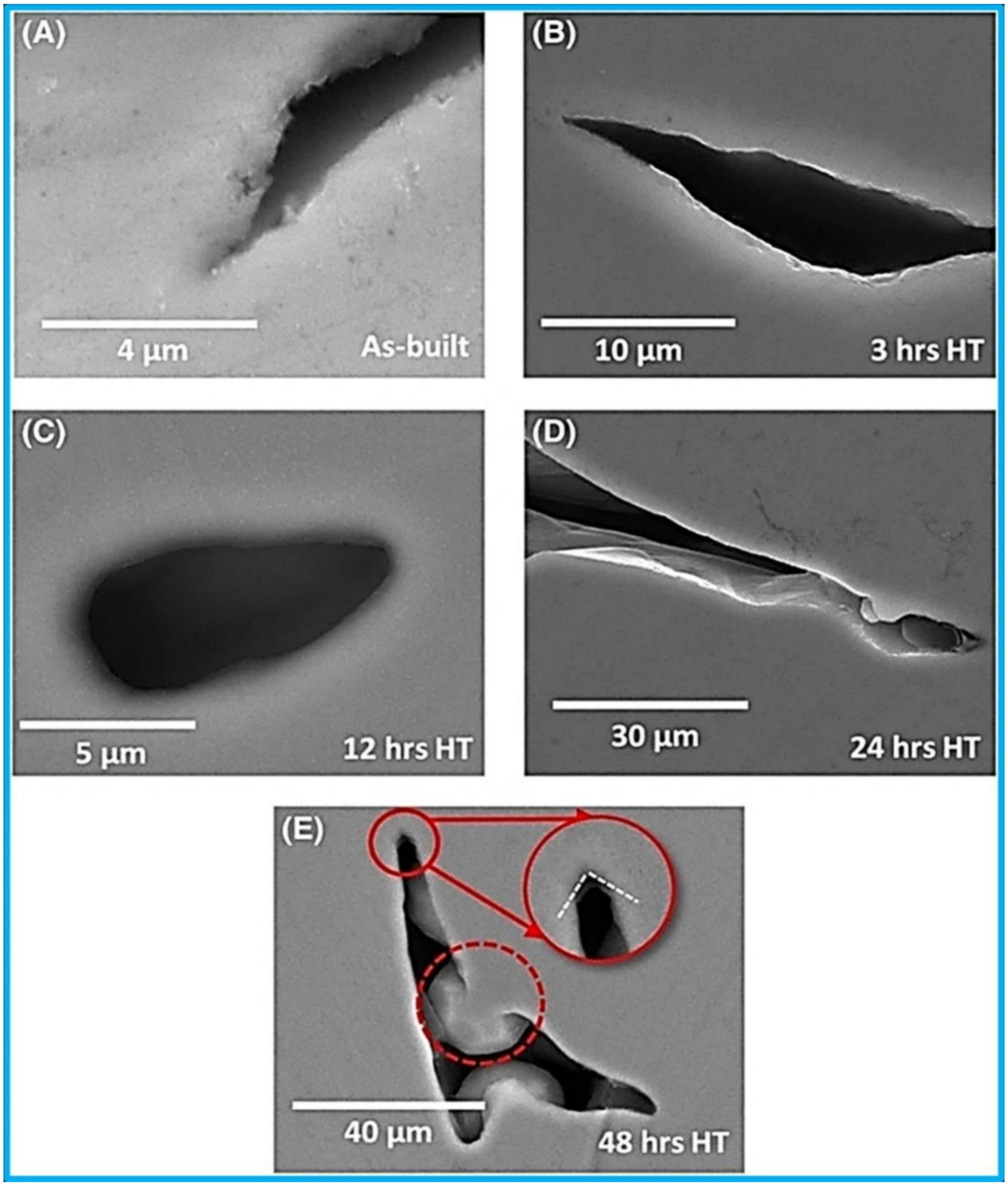

Fig. 9. *shows SEM images showing the sharp edges on the cross sections of LOF pores in the (A) as-built sample, as well as HT samples for (B) 3, (C) 12, (D) 24, and (E) 48 hours. Adapted from Zhang et al.[151] with permission from John Wiley and Sons.*

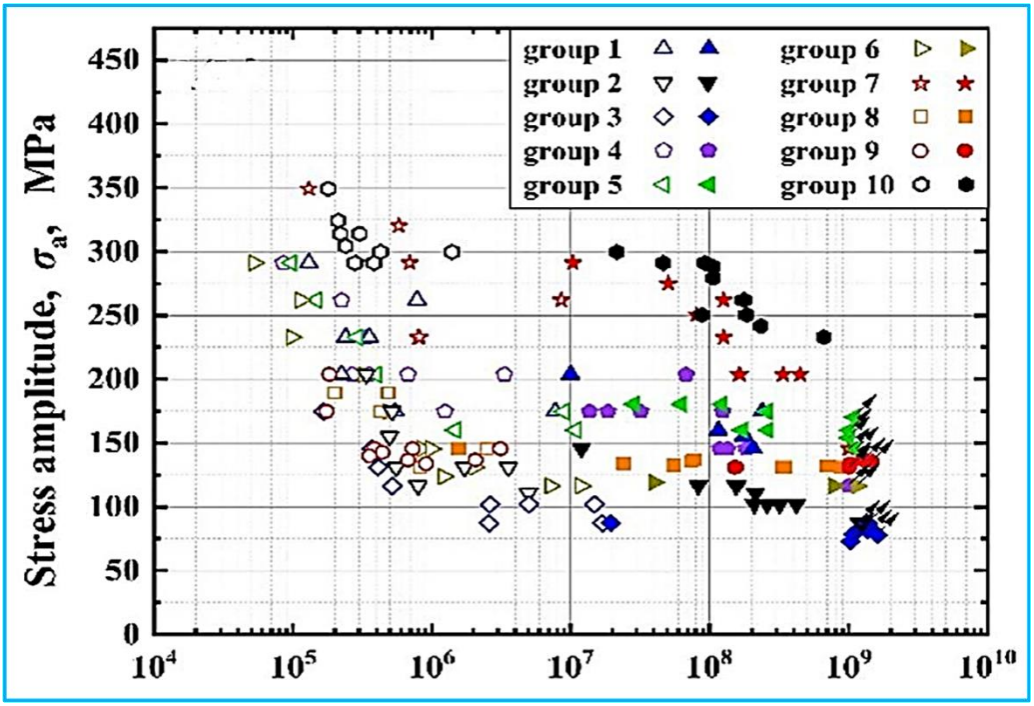

Fig. 10. *S-N curves for different specimen groups. Adapted from Du et al.[120] with permission from John Wiley and Sons.*

To understand the effect of defects/porosity on the fatigue strength of SLM-Ti-6Al-4V parts, figure 10 is reproduced from the data mentioned in the literature. As illustrated in **Fig. 11**, if the porosity/defects level increases, the fatigue performance will decrease sharply. When the porosity is about 0.20%, the fatigue strength is 300 MPa, but when the porosity level increases to 8.03%, the fatigue strength decreases sharply to 90 MPa. It can also be found that there is a relationship between the porosity level and the fatigue strength trend, as shown by the S-N curves. As for specimen groups with a high porosity level, the S-N curve shows a single-wise trend, whereas for specimen groups with a low porosity level, the S-N curve shows a stepwise trend, as illustrated by Du et al. [120] (**Fig. 12**).

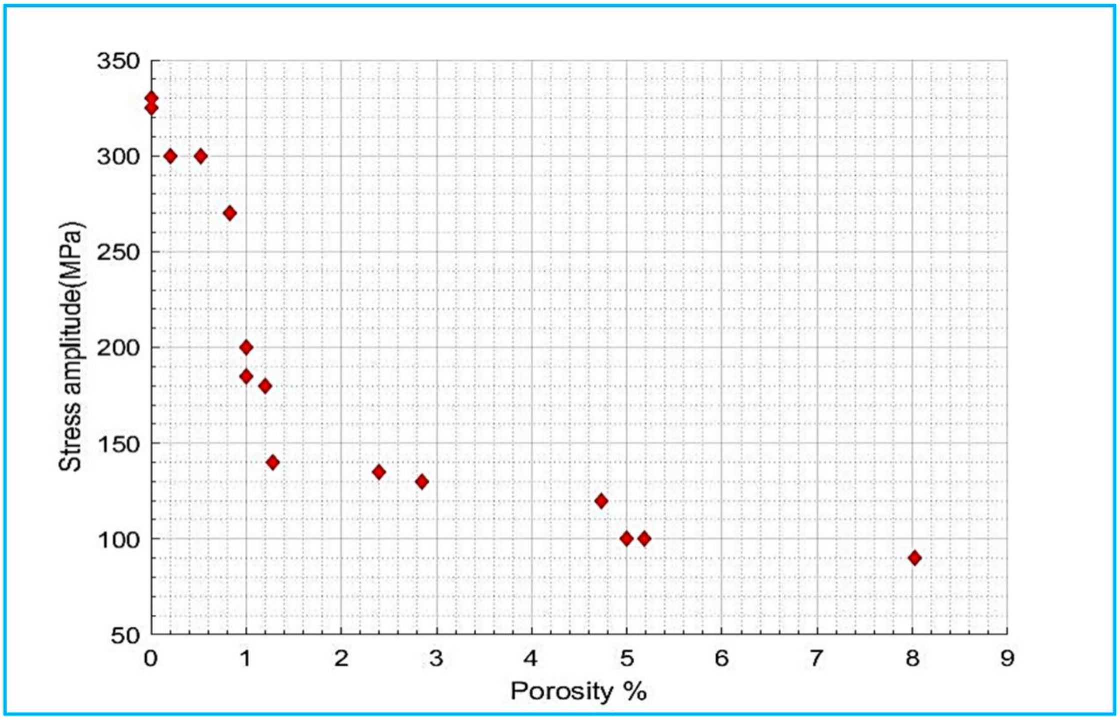

Fig. 11*. Reproduced graph showing the effect of porosity on fatigue strength based on data reported in the literature. The data points are collected from Du et al.[120], Gong et al.[153] ,and Hu et al. [164].*

Liu et al.[2] ,Gong et al.[153], Zhang et al. [171], Liu et al.[169] and Hu et al.[164] asserted that slit-shaped and LOF defects have the most detrimental impact on fatigue life as fatigue cracks initiate from LOF defects regardless of the build directions. Choi et al.[168] mentioned that oxygen and nitrogen-related inclusions are more detrimental to the fatigue performance of SLM-Ti-6Al-4V parts than LOF defects or gas pores. Moreover, Hu et al. [164] stated that the low fatigue resistance and a large scatter in fatigue lives are due to the random distribution of defect sizes and positions. Gong et al.[153] reported that if the volume fraction of small pores or voids in the material exceeds 5%, the fatigue properties of the material will be significantly reduced.

Additionally, the authors pointed out that defects caused by insufficient energy significantly impact fatigue properties more than those caused by excessive energy input [153].

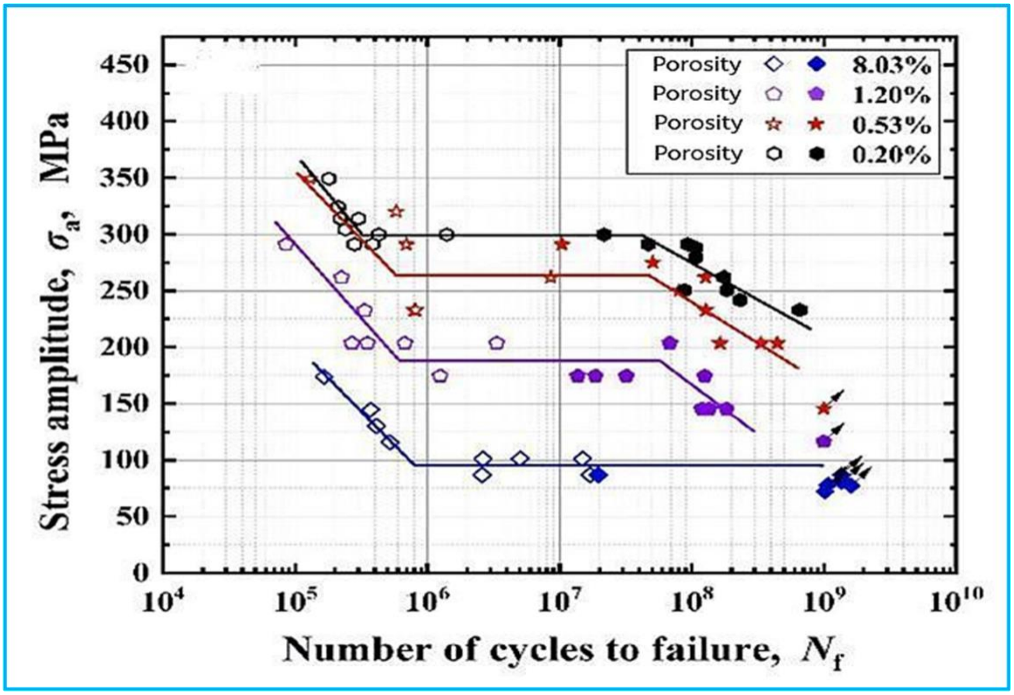

Fig. 12. *Impact of porosity on the trend line of the S-N curve based on the data mentioned by Du et al.[120] with permission from John Wiley and Sons.*

There is also a significant impact of microstructural defects, such as balling, on the fatigue performance of the SLM part [172]. Liu et al.[128] extensively investigated the effect of defect size and depth of defects on the VHCF performance, which is illustrated in **Fig. 13**. It appears that the smaller effective size of the defect accounts for the fatigue failure of the specimens in higher fatigue cycles. A relationship appears between fatigue lives and the size of the defect. There is evidence in figure 12*A* to suggest that in all the specimens tested, the effective defect size, which causes microcracks to initiate, varies from 50 to 100 µm. The authors found the critical defect size to be approximately 46 µm for SLM-Ti-6Al-4V specimens for fatigue failure with push-pull loads.[128] However, Pessard et al.[170] mentioned that the critical defect size is approximately 30 µm for SLM-Ti-6Al-4V specimens for fatigue failure with push-pull loads. Based on **Fig. 13*B***, it can be seen that the depth of the defect causing the crack increases with the number of cycles until failure. The study demonstrated that fatigue cracks would likely initiate at a depth between 100 and 500 µm below the surface of the sample. da Costa et al.[4] and Jiao et al.[14]also mentioned that a defect size and location play a significant role in crack initiation and fatigue life. There may be more significance to the irregular shape than the size of the pores when it comes to fatigue life, while for pores of the same size, the location may have greater significance than the shape.

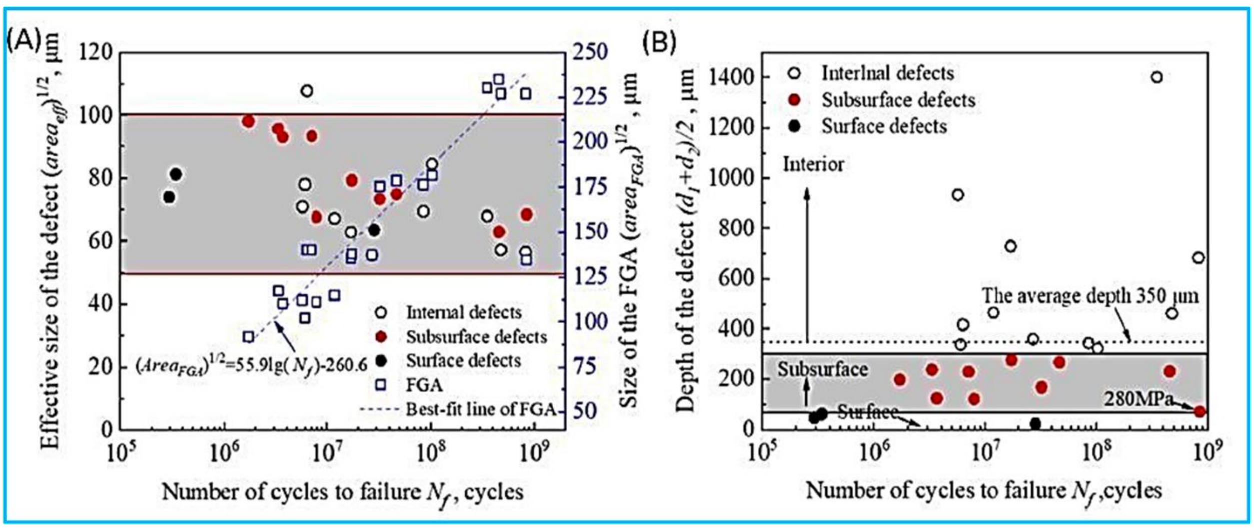

Fig. 13. *shows the relationship between (A) The effective defect size and the number of cycles to failure of the SLM Ti-6Al-4V in the VHCF regime, (B) The depth of defects and the number of cycles of the SLM Ti-6Al-4V in the VHCF regime. Adapted from Liu et al.[128] with permission from Elsevier.*

2.4.2.1 Influences of fabrication parameters on the defect/porosity formation

As discussed in section **2.4.2** that porosity/defects levels play an essential role in HCF and/or VHCF performances. It has been reported that fabrication parameters have a significant impact on porosity/defect levels, ultimately, on the fatigue performance of the SLM-Ti-6Al-4V parts. Du et al.[120] investigated the effect of fabrication parameters on HCF and VHCF behavior. The authors concluded that the order of influence on the formation of porosity by individual parameters is laser power > hatch spacing > layer thickness > scan speed [120]. The authors recommended that the optimal fabrication parameters are 160W laser power, 70µm hatch spacing, 30µm layer thickness, and 1000mm/s scan speed, resulting in 76.2 J/mm^3 laser energy density (**Fig. 14**) [120]. But, after analyzing the data mentioned by Hasib et al.[155], it can be concluded that laser power and scan speed are the most influential factors affecting the relative density of the SLM parts. The authors found a relative density of more than 99% using 300 W laser power and 1200 mm/s scan speed, while for laser power 100 W and scan speed 400 mm/s, the relative density was 90% [155]. For both cases layer thickness and hatch distance were the same (0.03mm and 0.12 mm respectively), which gave the same energy density of about 69.45 j/mm^3 [155].

Hasib et al.[155] also found the maximum relative density (>99%) using laser power 300W and scan velocity 1200 mm/s. This supports the statements of Du et al. [120] as the laser power is greater than the recommended value of 160W and the scan speed is more than recommended value of 1000 mm/s.

Kasperovich and Hausmann [20,32] discussed the effect of fabrication parameters on the porosity levels and found that the porosity reduces significantly with the increasing scanning velocity up to 1.25 m/s. However, the authors did not find decreased porosity levels further after increasing the scanning velocity. A spot size also plays a vital role in the porosity level. The lowest porosity level was found by using a scanning speed of 1.25 m/s and 200 W laser power alongside with large spot size (**Fig. 15**) [20,32].

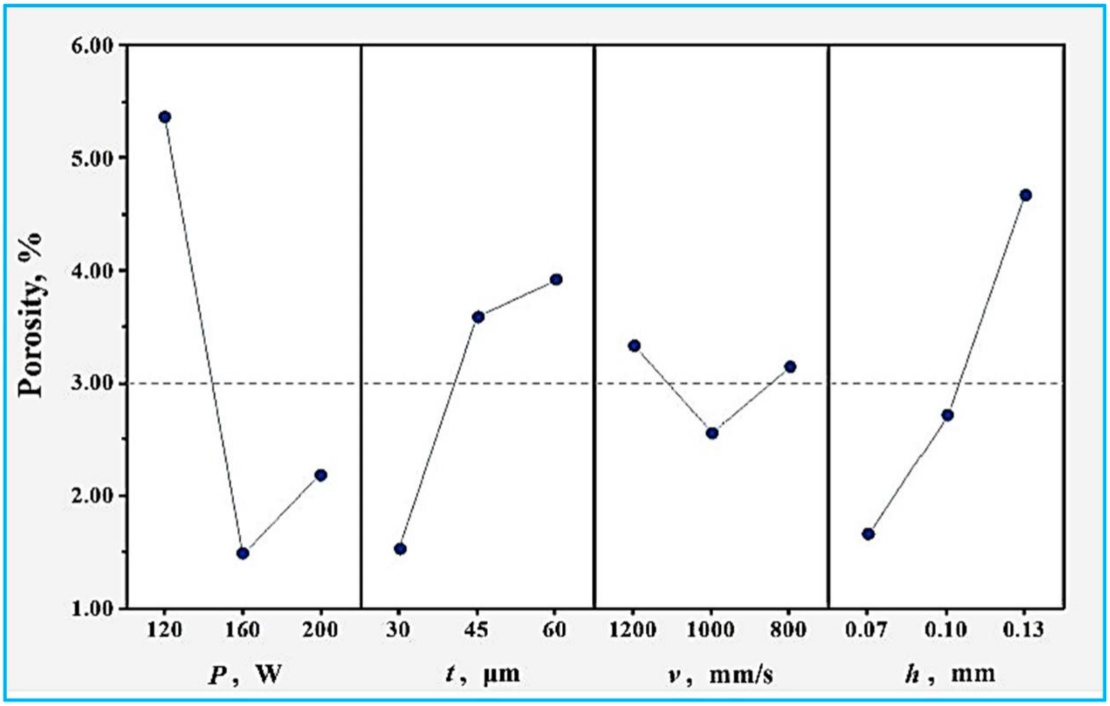

Fig. 14*. Effect of fabrication parameters on porosity. Adapted from Du et al.[120] with permission from John Wiley and Sons.*

A study conducted by Qiu, Adkins, and Attallah [173], revealed that with increasing laser power and scanning speed, the porosity level decreases (**Fig. 16**). The authors stated that an increase in scanning speed without keeping the laser power constant could lead to an increase in porosity. This is due to reduced energy input and LOF defects [173].

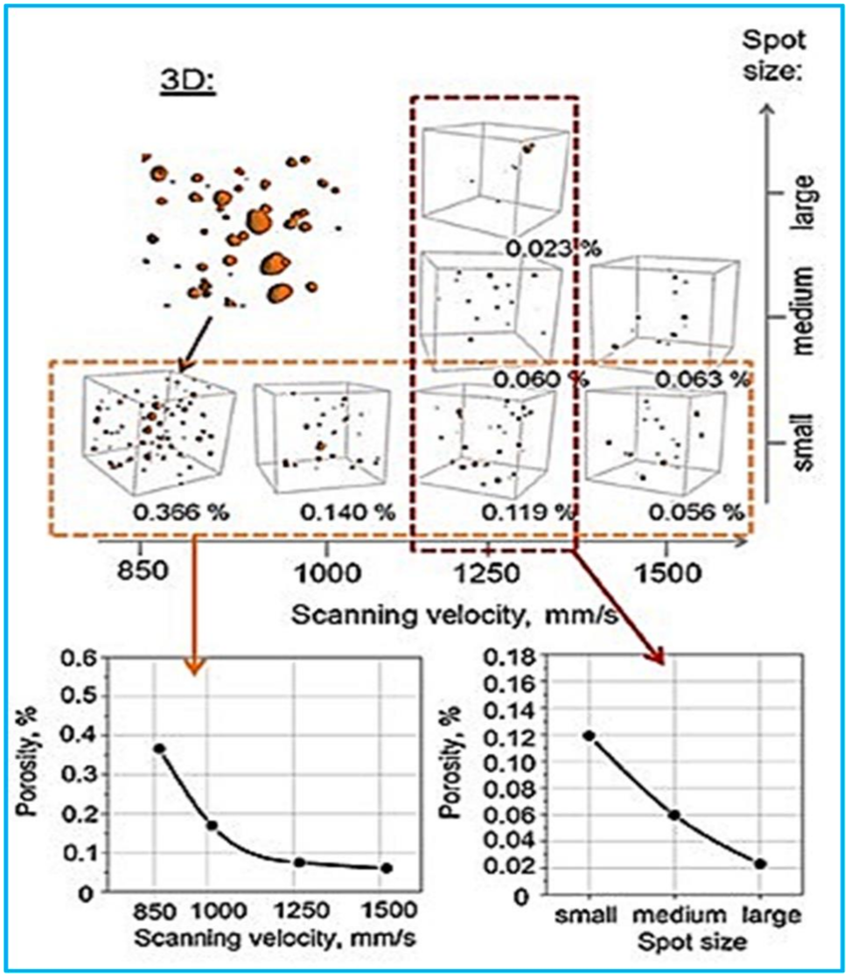

Fig. 15. *Effect of scanning speed and spot size on porosity level. Adapted from Kasperovich and Hausmann [32] with permission from Elsevier.*

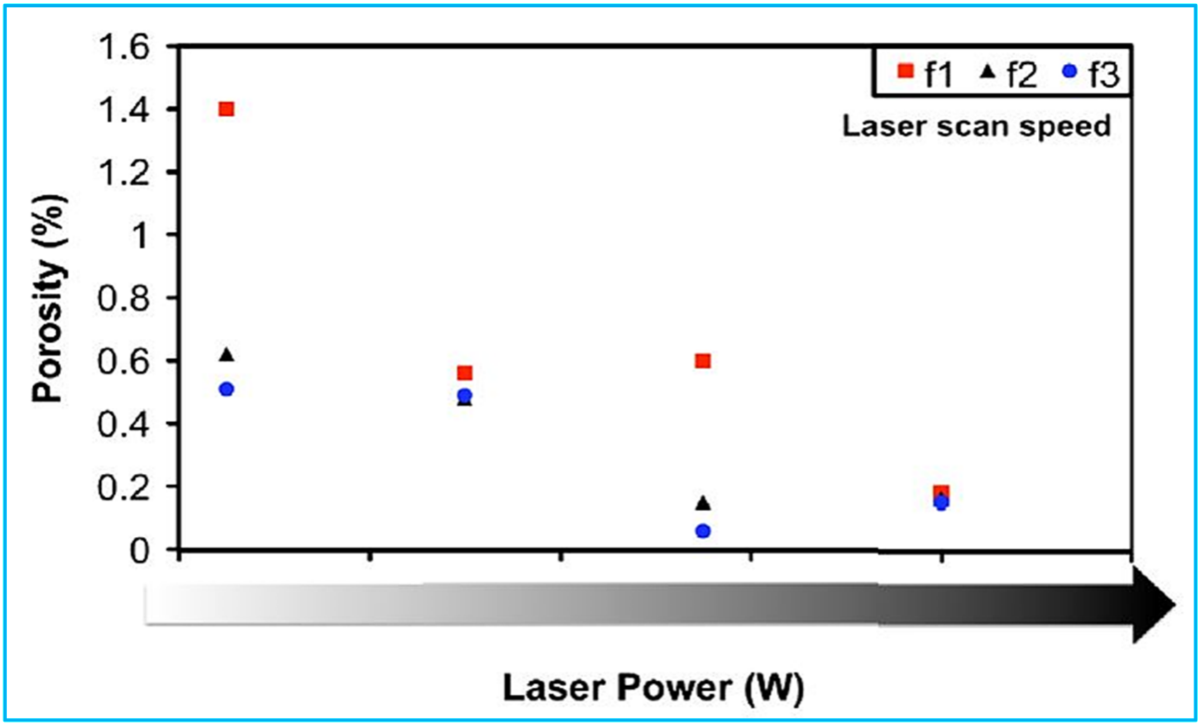

Fig. 16. Dependency of porosity level on laser power and scanning speed (f1<f2<f3). Adapted from Qiu et al.[173] with permission from Elsevier.

Based on the extensive study of Elsayed et al.[174] on the effect of fabrication parameters on porosity content, it has been established that the porosity content decreases with an increase in the laser power and/or a decrease in scanning speed and hatch spacing (**Fig. 17*A-B***). The amount of energy applied to the powder increases with a reduction in scanning speed or high laser power. Increased energy enhances the diffusion process and seals the pores due to surface tension and capillary forces. It is also possible to obtain continuous tracks due to the low scanning speed. Furthermore, a small hatch spacing between adjacent scanning lines would cause the powder to melt entirely between scanning lines by increasing the overlapping area [174].

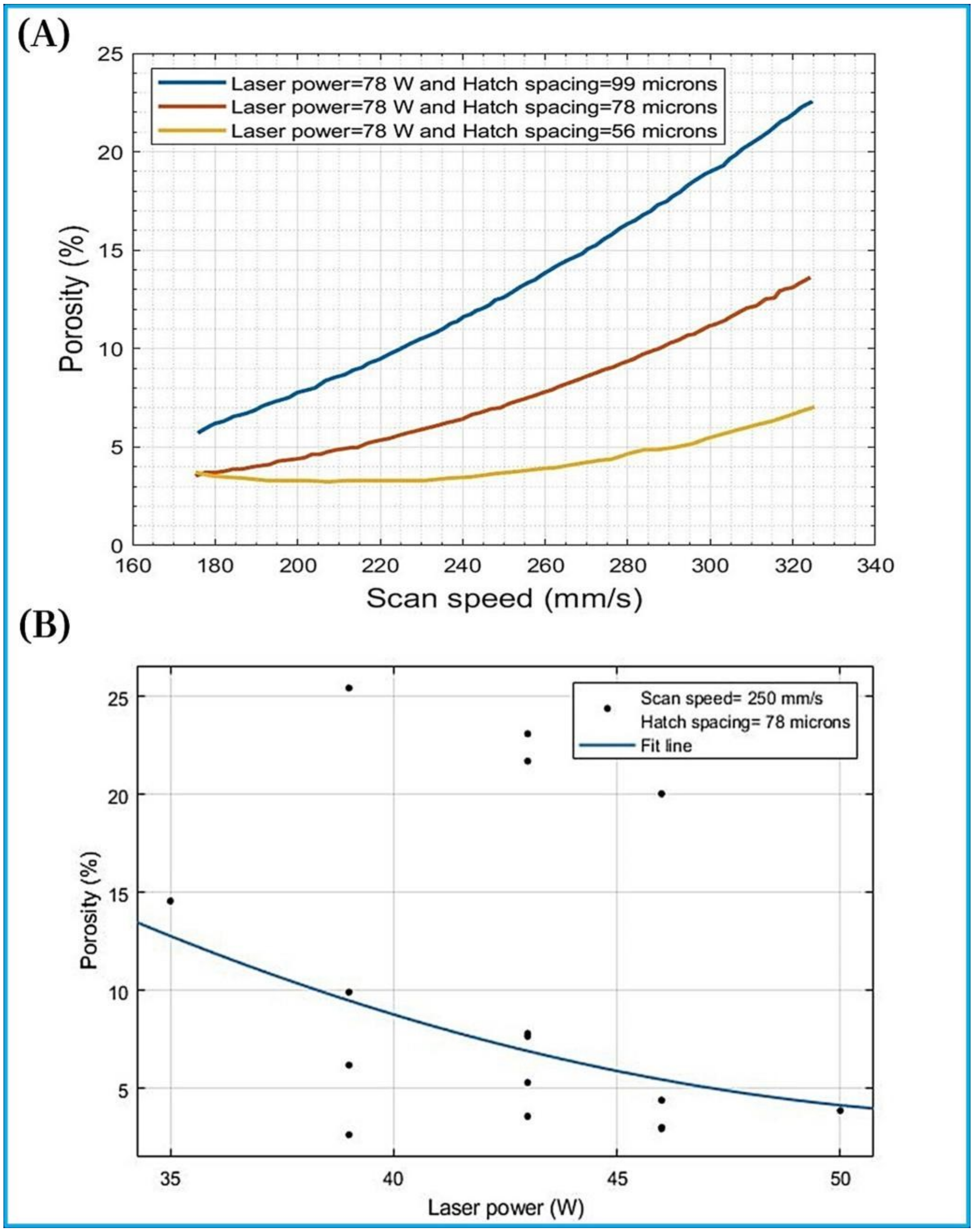

Fig. 17. *shows (A) the interaction between scan speed and hatch distance on porosity, (B) the effect of laser power on porosity the effect of scan speed on porosity. Reproduced from Elsayed et al. [174] .*

To understand the effect of the scan speed on the defect formation, **Fig. 18** is reproduced from the data sets in the literature. As illustrated in the figure, that defect level exhibits the most in the 200 to 400 mm/s scan speed range. After a scan speed of 400 mm/s, the defect level reduces gradually. On the other hand, a scan speed of 900 mm/s results in a substantial reduction of the defect level as well, resulting in virtually no defects.

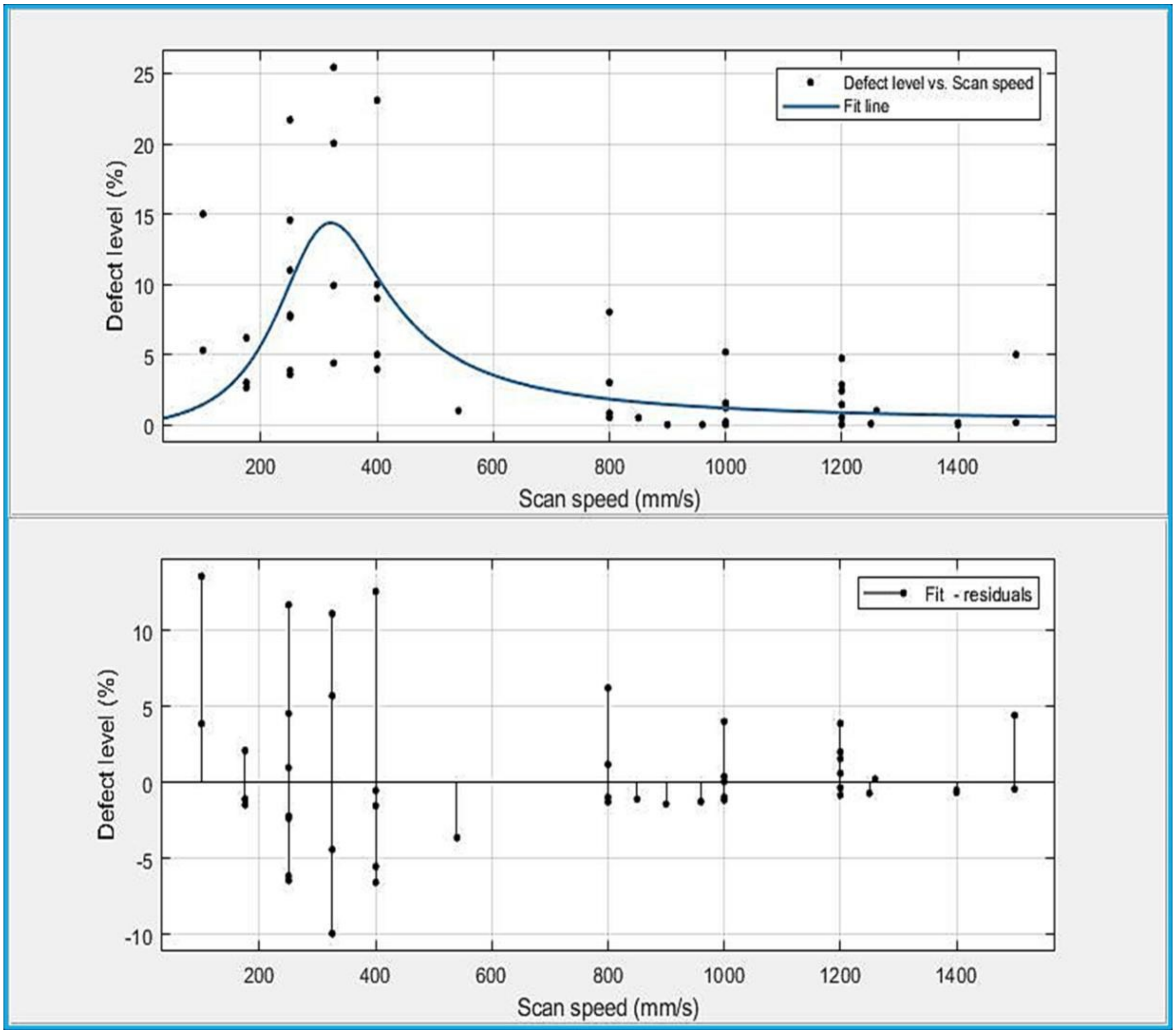

Fig. 18. *Effect of scan speed on the defect formation based on the data sets mentioned in the literature. The data points are collected from Gong et al.[153],Hu et al.[164],Du et al.[120],Kasperovich and Hausmann[20,32],Elsayed et al.[174],Song et al.[175], Xiao et al.[148],Palmeri et al.[134],Meng et al.[176],Jin et al.[124], and Hasib et al.[155] .*

Thus, a scan speed greater than 900 mm/s can be recommended to minimize the defect level. However, Jin et al.[124] mentioned that the defect level is not too sensitive to the scan speed. In order to gain a better understanding of how the layer thickness affects defect formation, **Fig. 19** has been reproduced from the datasets in the literature.

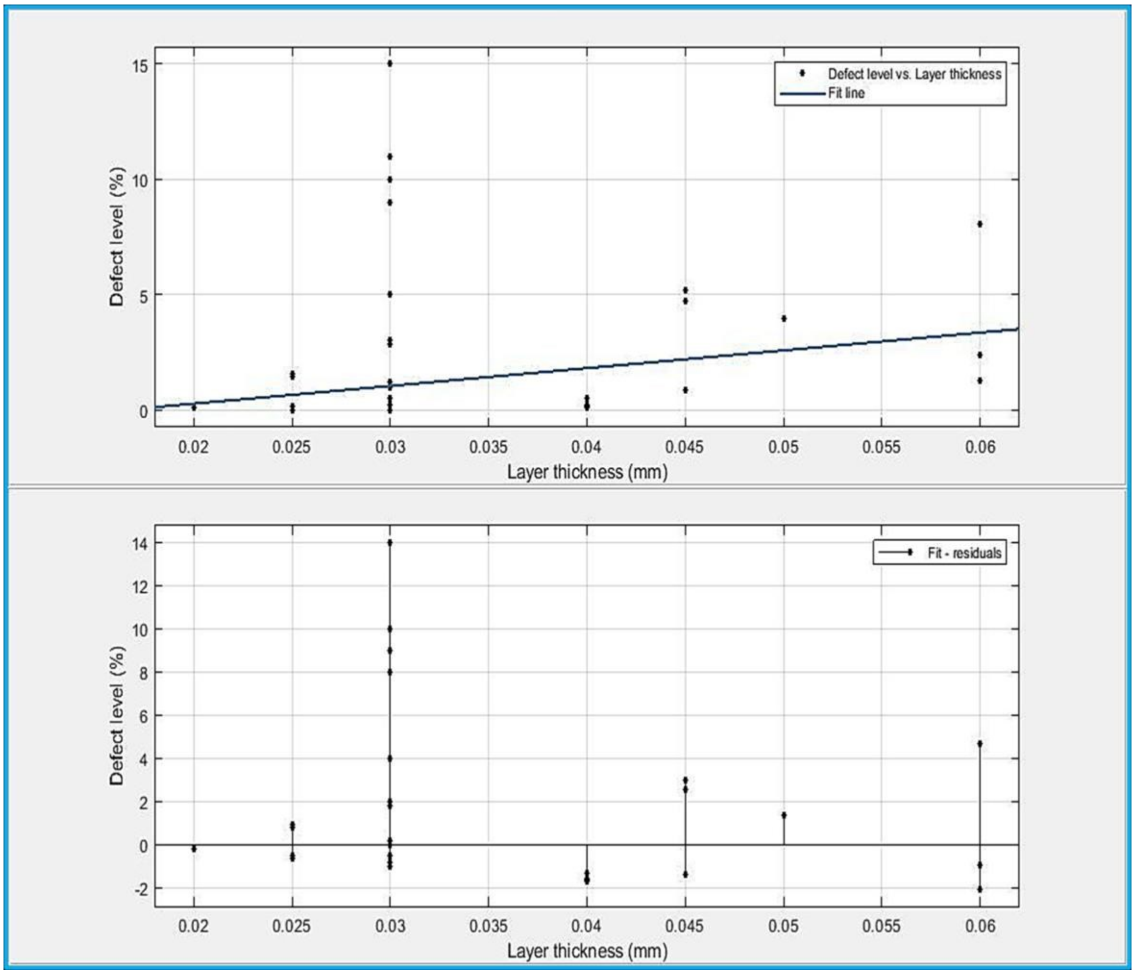

Fig. 19. *Effect of layer thickness on the defect formation based on the data sets mentioned in the literature. The data points are collected from Gong et al.[153],Hu et al.[164],Du et al.[120],Kasperovich and Hausmann[20,32],Elsayed et al.[174],Song et al.[175], Xiao et al.[148],Palmeri et al.[134],Meng et al.[176],Jin et al.[124] and Hasib et al.[155].*

As illustrated in the figure, the defect level increases with layer thickness. So, it can be recommended to use the layer thickness as low as possible. The data in **Fig. 20** were reproduced from the literature in order to understand the effect of hatch distance on defect formation. The effect of hatch distance on defect formation is unclear, as illustrated in **Fig. 20**, despite Elsayed et al. [174] mentioned that increased hatch distance contributes to a broader range of defect levels. So, further extensive research is required to conclude the effect of hatch distance on defect formation.

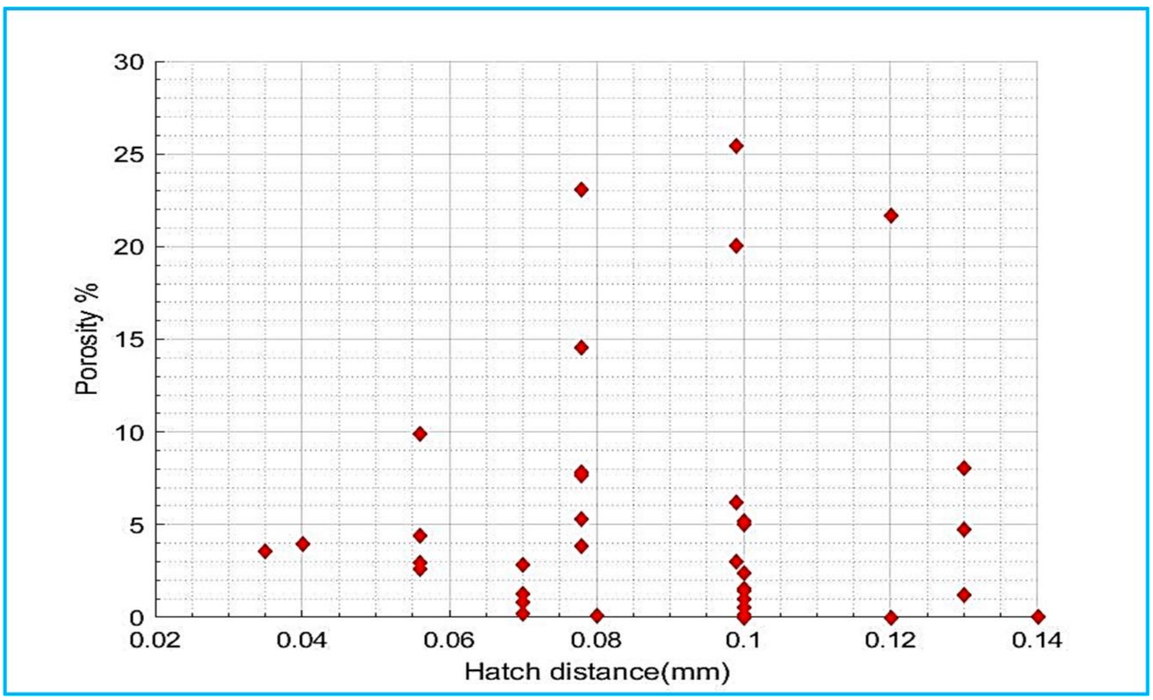

Fig. 20*. Effect of hatch distance on the defect formation based on the data sets mentioned in the literature. The data points are collected from Gong et al.[153],Hu et al.[164],Du et al.[120],Kasperovich and Hausmann[20,32],Elsayed et al.[174],Song et al.[175], Xiao et al.[148],Palmeri et al.[134],Meng et al.[176],Jin et al.[124] and Hasib et al.[155].*

To understand the effect of the laser power on the defect formation, **Fig. 21** is reproduced from the data sets in the literature. As illustrated in the **Fig. 21** that the defect level increases with a decrease in the laser power.

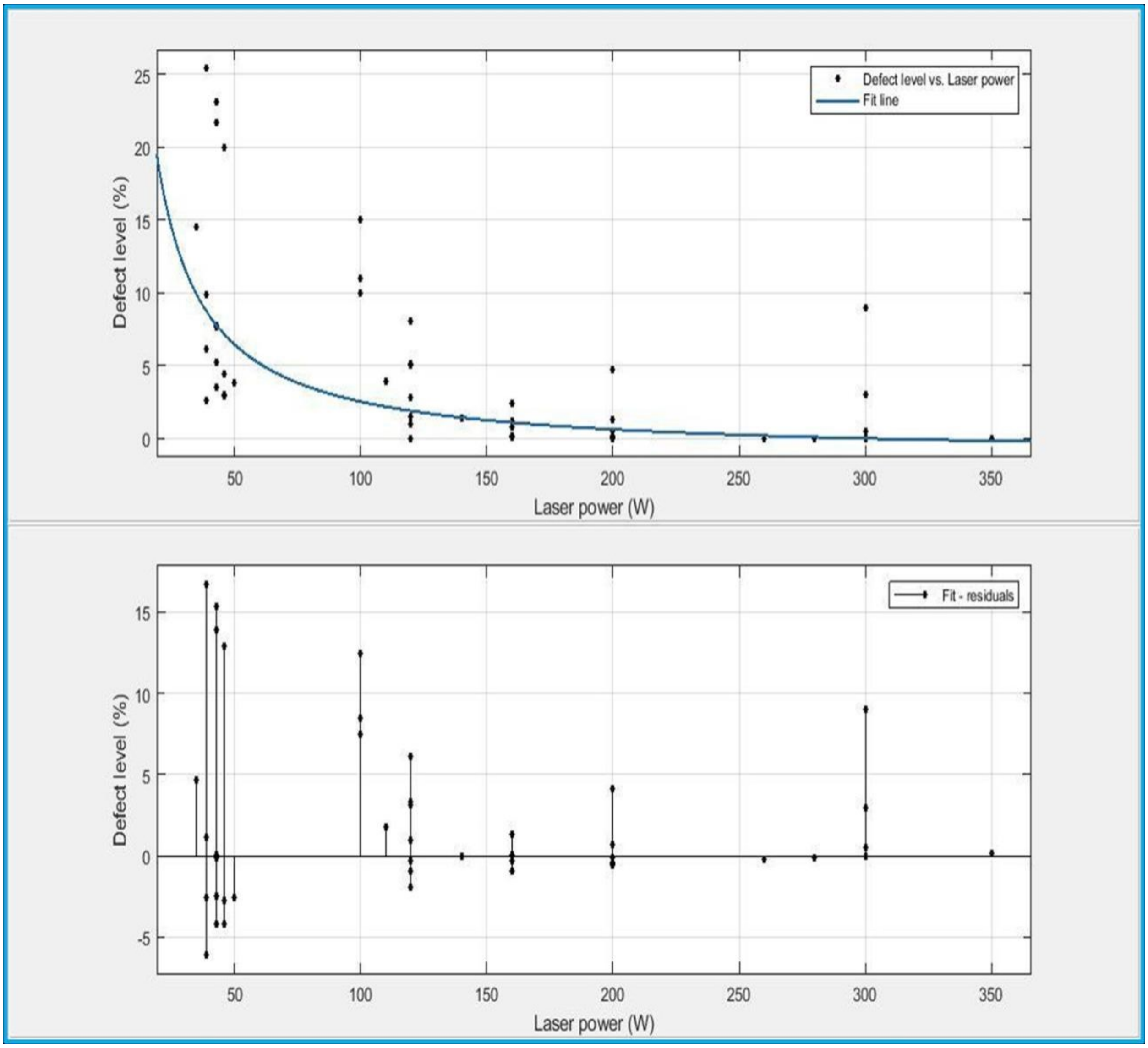

***Fig. 21**. Effect of laser power on the defect formation based on the data sets mentioned in the literature. The data points are collected from Gong et al.[153],Hu et al.[164],Du et al.[120],Kasperovich and Hausmann[20,32],Elsayed et al.[174],Song et al.[175], Xiao et al.[148],Palmeri et al.[134],Meng et al.[176],Jin et al.[124] and Hasib et al.[155].*

It is also seen that the defect level goes down to almost zero when the laser power exceeds 160 W. So, it can be recommended to use laser power of more than 160 W. In order to provide a complete understanding of the effect of energy density on defect formation, **Fig. 22** is reproduced from the data sets presented in the literature. As illustrated in the figure, the defect level increases with a decrease in energy density.

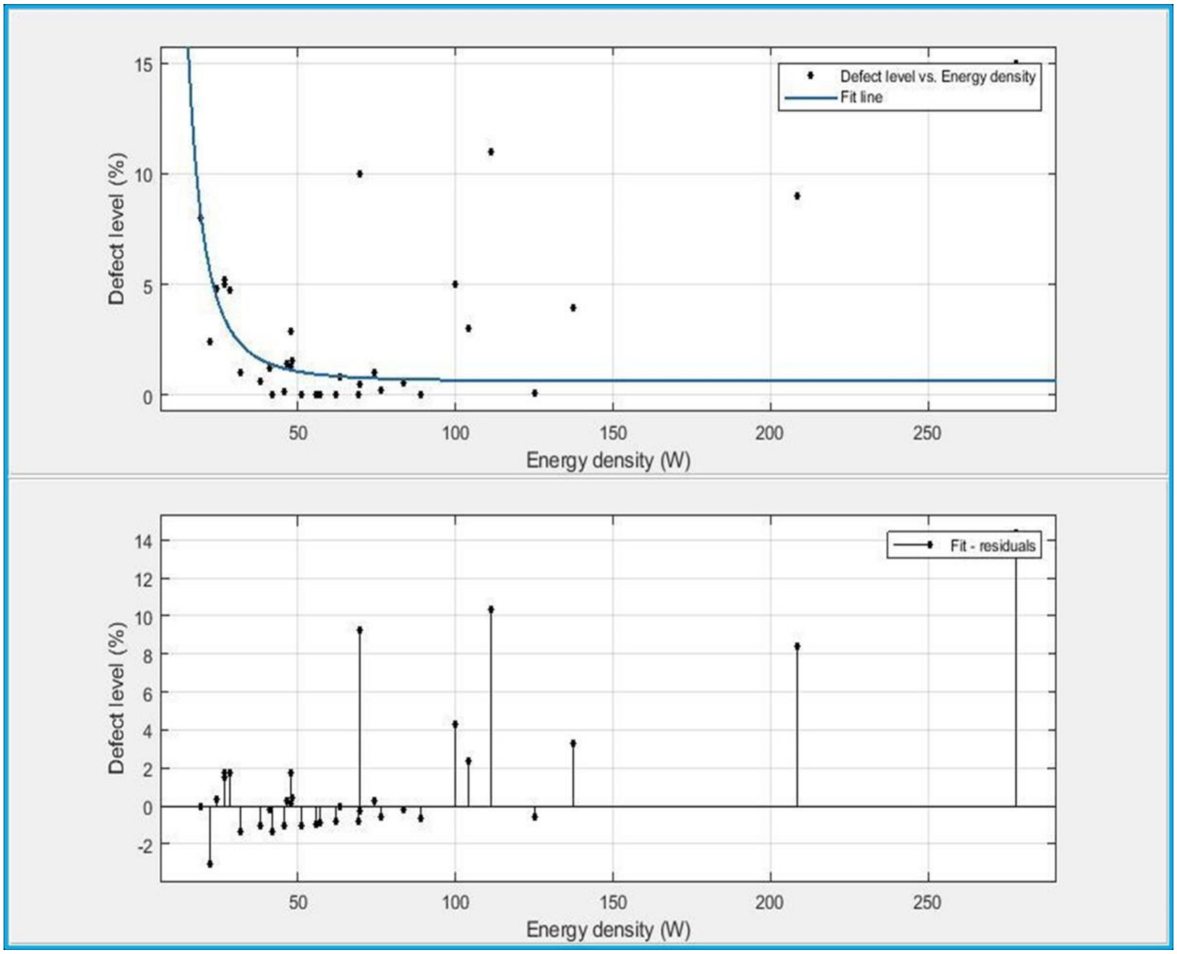

Fig. 22. *Effect of energy density on the defect formation based on the data sets mentioned in the literature. The data points are collected from Gong et al.[153],Hu et al.[164],Du et al.[120],Kasperovich and Hausmann[20,32],Elsayed et al.[174],Song et al.[175], Xiao et al.[148],Palmeri et al.[134],Meng et al.[176],Jin et al.[124] and Hasib et al.[155].*

It is also seen that the defect level goes down to almost zero when the energy density is more than 40 j/mm^3. So, it can be recommended to use an energy density of more than 40 j/mm^3. To achieve the highest relative density of the part, it is thus helpful to use the recommended laser power and energy density along with other fabrication parameters as illustrated in **Fig. 18**-**Fig. 22**. Karimi et al.[177] investigated the effects of remelting on the development of porosity in SLM-Ti-6Al-4V parts. The authors indicated that with the increase in melting sequence from single to triple melting, the number of internal defects increases. Fusion pores are visible in a single melted sample. Still, as the melting process progresses, these pores disappear, leaving only spherical pores [177]. It is evident that both the number and the size of pores decrease with increasing the number of melting steps. Miao et al.[178] mentioned that rescanning improves the relative density of SLM-Ti-6Al-4V parts by reducing the number and size of the pores. Palmeri et al.[134] investigated the effect of building orientation on porosity formation. The authors found almost 100% relative density for the samples with building orientations of 0^0 ,15^0, and 30^0 , while for 45^0 ,60^0, 75^0 ,and 90^0 building orientations, the relative density decreased to 99.83%,99.81%,99.79% , and 99.77%, respectively [134].

2.4.3 Influences of residual stress (RS) on fatigue properties

RS has a significant impact on HCF and VHCF performances. For the fatigue performance assessment of the SLM fabricated parts, it is necessary to take into account any RS that may still remain within the material prior to any fatigue analysis assessment. It is imperative to note that there can be RS in SLM parts due to a variety of factors, including high-temperature gradients, process parameters (process gas, laser power, hatch spacing, scan speed, scan orientation, scan strategy, layer thickness, platform temperature), part geometry and most importantly, rapid melting and solidification with subsequent thermal cycles during SLM processes [5,6,32,149,179-181]. RS strongly affects the initiation and growth of cracks arising from the rapid localized temperature fluctuations during the SLM process [69]. Leuders et al.[159,161],Edwards et al.[182] ,Cain et al.[183], Shamsaei and Simsiriwong[184] and da Costa et al.[4] asserted that compressive RS has a positive impact on fatigue behavior while tensile RS has a detrimental effect on the fatigue performance of SLM-Ti-6Al-4V parts. **Fig. 23** schematically shows the detrimental effect of tensile RS on fatigue performance in terms of inducing higher crack growth rates.

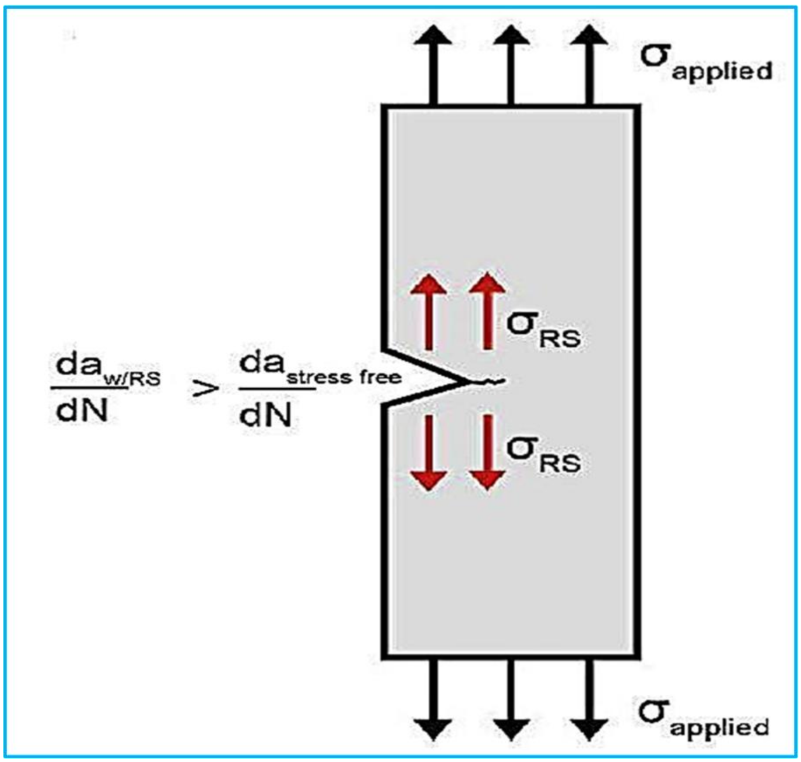

Fig. 23. *Reduced fatigue properties due to additional internal tensile RS. Adapted from Bartlett and Li[179] with permission from Elsevier.*

It is necessary to appropriately select the fabrication process parameters and utilize post-fabrication heat treatment processes to reduce or eliminate detrimental RS (es).

There are a variety of techniques that can be used to reduce or eliminate detrimental residual stresses, including the use of appropriate fabrication process parameters (process gas, laser power, hatch spacing, scan speed, scan orientation, scan strategy, layer thickness, platform temperature) and the utilization of post-fabrication heat treatment processes.

2.4.3.1 Influences of critical parameters affecting residual stresses

Marques et al.[5], Pauzon et al.[6], Xiao et al.[149], Bartlett and Li[179],Luo et al.[180], and Ali et al.[181] studied the critical parameters that have a significant impact on the RS in metal powder bed fusion. **Fig. 24** shows the primary process parameters that significantly affect the RS formation.

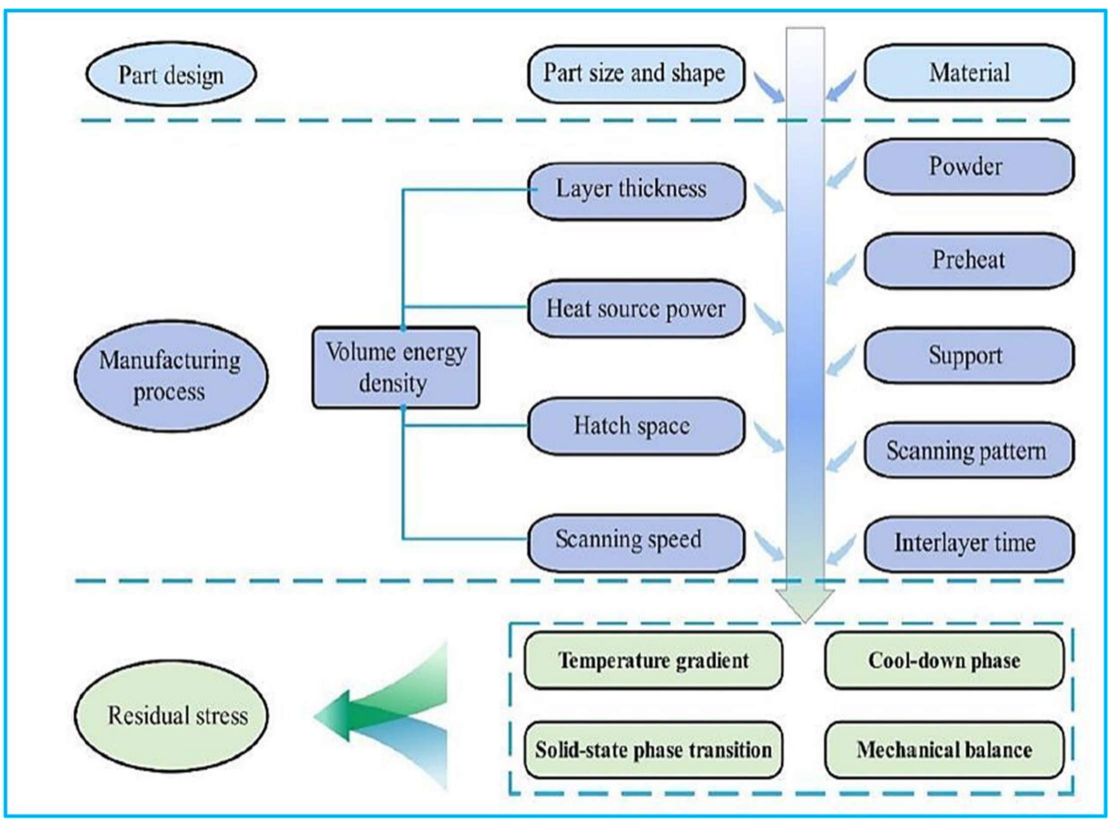

Fig. 24. *An analysis of the principal process parameters influencing RS formation in the AM process [185].*

Table *2* provides a summary of known parameters that are related to the development of RS.

Table 2. Summary of known processing parameters that are related to the development of RS [5,6,149,178-181,185].

Parameters	General effect on RS
Laser power	As laser power increases, RS increases as well
Scan speed	As laser power decreases, RS increases as well
Scan orientation	Provides control over the distribution of the RS. The magnitude of RS is also affected by scan orientation.
Scan vector length	RS increases with longer vectors
Scan strategy	No obvious impact
Layer thickness	Layer thickness lower RS
Platform temperature	Higher base plate temperature lowers RS
Interlayer dwell time	Material dependent. Affect RS magnitude
Re-scan	Implementation of re-scan reduces the magnitude of RS
Sample size	RS increases with increasing part size
Sample thickness	RS decreases with increasing sheet thickness

The effect of scan speed, laser density, scanning patterns, and platform temperature are shown graphically in **Fig. 25**.

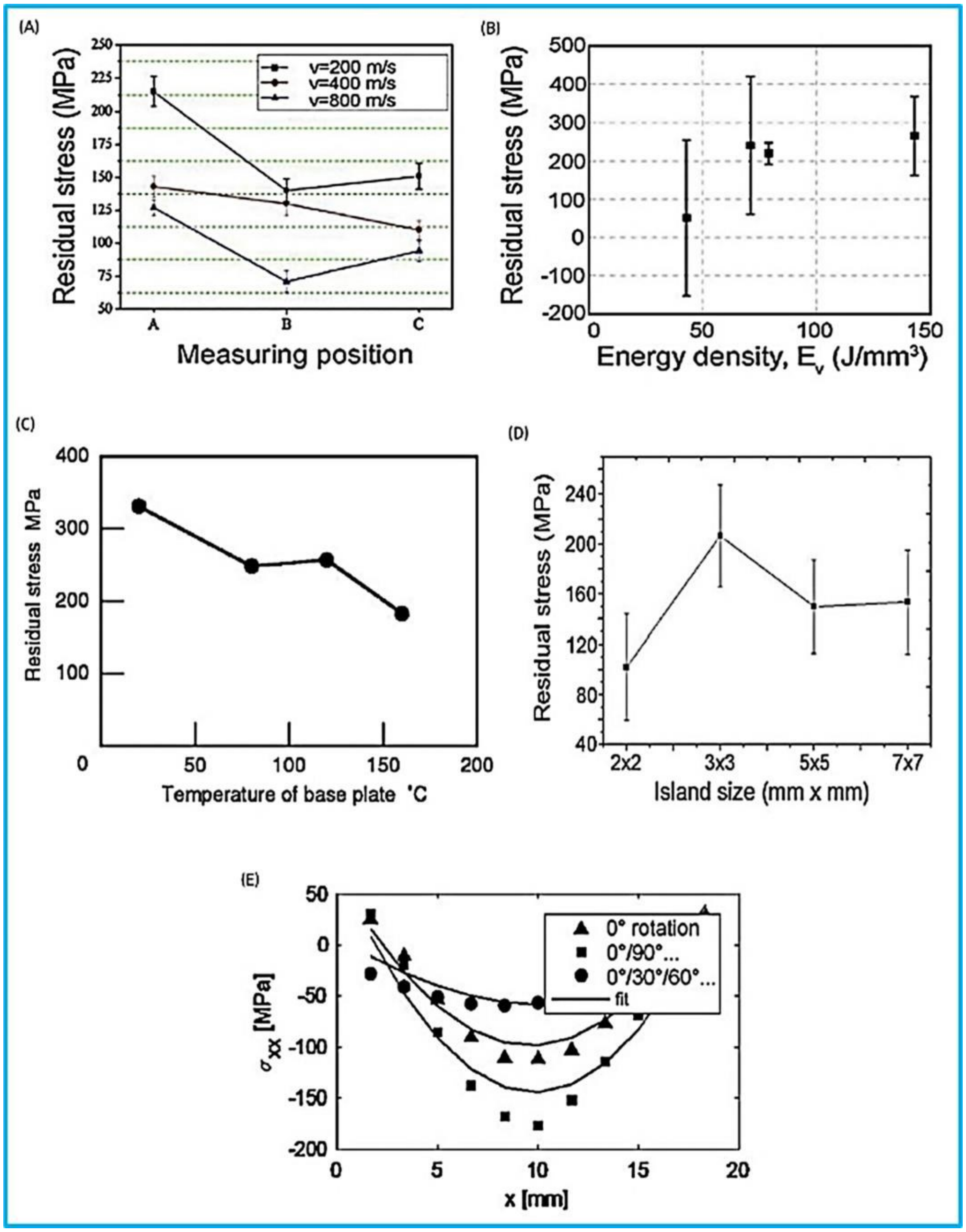

Fig. 25. *shows (A) The magnitude of RS as a function of scan speed, (B) Trends of RS magnitude versus energy density, (C) Preheating temperature and RS magnitude at the top surface, (D) Trends of RS magnitude versus island size, and (E) The magnitude of RS versus three different rotation angles layer-to-layer. Adapted from Bartlett and Li [179] with permission from Elsevier.*

However, Xiao et al.[149] mentioned that the RS does not monotonously increase or decrease as the laser power, scanning speed, or hatch spacing is increased. In terms of the RS, the effect of scanning speed is greater than the effect of laser power, which is, in turn, more significant than that of hatch spacing [149].

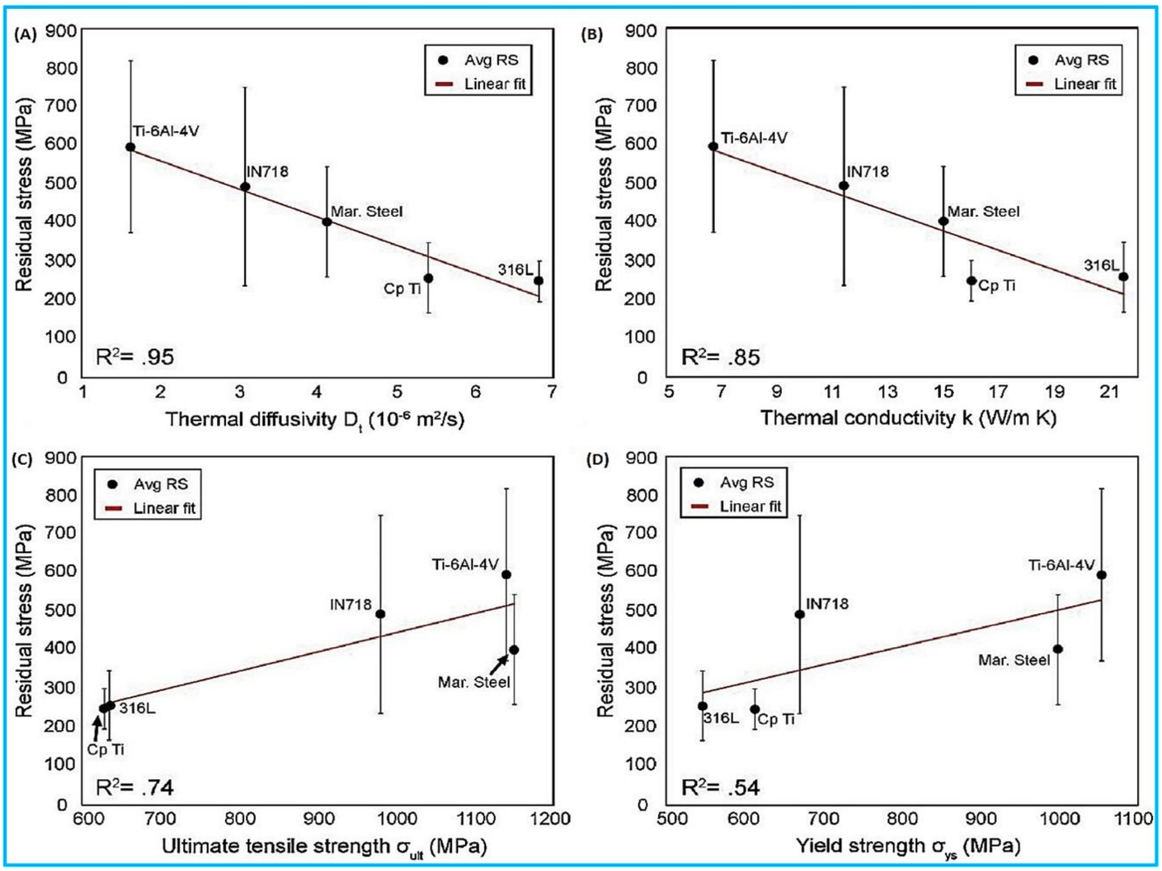

Fig. 26. *shows (A) The average value of maximum RS reported for various materials versus thermal diffusivity, (B) The average value of maximum RS reported for various materials versus thermal conductivity, (C) The average value of maximum RS reported for various materials versus ultimate tensile strength, and (D) The average value of maximum RS reported for various materials versus yield strength. Adapted from Bartlett and Li [179] with permission from Elsevier.*

In another study, Xiao et al.[148] investigated the effect of rescanning cycles on the RS. The authors found 39% excess RS for the samples with one-time rescanning than the samples without rescanning. However, as the number of rescanning cycles increases, RS decreases due to decreased cooling rate. Luo et al.[180] mentioned that rescanning with an energy density of 75% resulted in 33.5%–38.0% reductions in RS for the porous Ti-6Al-4V parts. According to Bartlett and Li [179], RS is also susceptible to changes in thermal diffusivity, thermal conductivity, ultimate tensile strength, and yield strength, as represented in **Fig. 26**. Lueders et al.[159] analyze the influences of RS both on the AB and heat-treated samples (800^0 C) to confirm the effects of the heat treatment on residual stress. For AB samples, RS was measured on the sample surface and at a depth of 100 µm from the surface. The authors found that the heat treatment reduces almost all the tensile RS, while AB samples, especially vertically built samples, keep high internal stresses [159,186]. It is also important to note that the AB specimens have a very high RS gradient inside the specimens as well as the highest stresses being encountered in the interior areas of the specimens [159]. Thus, it is found that the heat treatment helps to reduce the RS. In another study, Leuders et al.[161] also studied the effect of the HIP on the RS. The authors measured the RS for the SLM-Ti-6Al-4V parts both in AB condition and after HIP + shot peening at different distances from the initial surface (at a depth of about 120 µm and 180 µm). The authors found tensile RS of about 800 MPa at a depth of 0.115mm from the surface in AB condition. **Fig. 27** shows the Results of the XRD measurements depending on the build orientation. After HIP + shot peening, tensile RS was relieved, and compressive RS was introduced [159,161]. After shot peening, the samples showed an RS of about -910 MPa at the surface and -475 MPa at a depth of 180 µm from the surface [159,161].

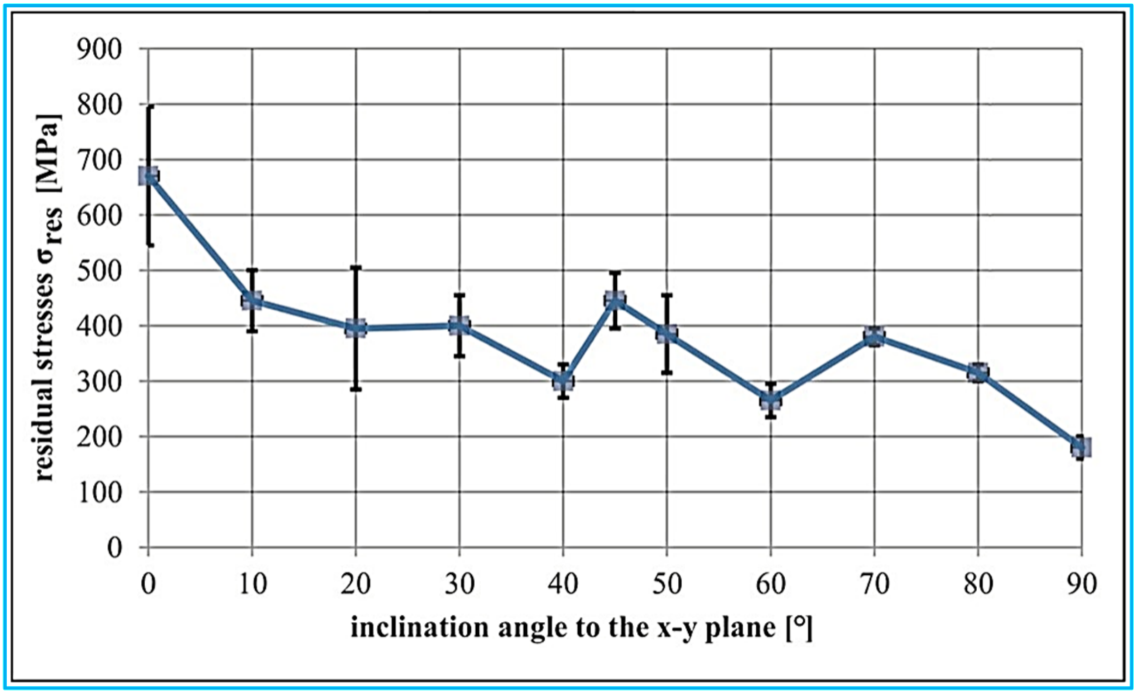

Fig. 27. *Surface RS analyses for SLM-Ti-6Al-4V parts in the AB condition depending on the build orientation. Adapted from Leuders et al.[161] with permission from Elsevier.*

Thus, it is evident that HIP treatment helps to reduce the tensile RS; instead, it helps to increase compressive RS, which helps to improve fatigue performance. The values of RS mentioned by Leuders et al.[159,161] are tabulated in **Table *3***.

Table 3. RS for SLM-Ti-6Al-4V samples in different material conditions [159,161].

Material condition/measuring point	Sample depth, mm	RS σ_{rs} (MPa)	
		X- direction	Y- direction
AB/point 1	Surface	+90	+235
AB/point 2	Surface	+120	+215
AB/point 3	0.1	+265	+775
AB/point 4	0.115	N/A	800 ± 35

HIP+ Shot peened	Surface	N/A	−910 ± 125
HIP+ Shot peened	0.177	N/A	−475 ± 35
800^0C/point 1	Surface	−5	+10
800^0C/point 2	Surface	+5	−5

From the table above, it is clearly visible that RS exists not only in the build direction but also in other directions i.e., crack propagation direction. Ali et al.[181] investigated the effect of pre-heating on RS of SLM-Ti-6Al-4V parts. When the pre-heating temperature was 100^0C, the measured RS was 214 MPa, but after increasing the temperature to 370^0C, RS was reduced by almost 71% (61 MPa). At 470^0C preheating temperature, RS becomes 25 MPa (almost 88.3% reduction), and finally, at 570^0C, RS becomes almost zero. Miao et al.[178] found rescanning as a potential method to reduce the RS in SLM-Ti-6A-4V parts. The authors measured RS of about 254 MPa after rescanning, which was 322 MPa before rescanning [178]. Choi et al.[168] investigated the effect of deposition/scan strategy on RS in SLM-Ti-6Al-4V parts. The authors found that the raster pattern with a continuous scan/deposit (RP-1) reduces RS compared to the raster pattern with an inter-track pause scan/deposit (RP-2). RP-1 gave tensile RS of about 150 MPa in the deposited layer, which was 50% lower than that in RP-2 [168]. Acevedo et al.[187] mentioned that LSP (Laser shock Peening) also helps to reduce RS.

2.4.4 Influences of post-processing heat treatment/HIP on fatigue properties

Leuders et al.[159,186] performed fatigue tests on SLM-Ti-6Al-4V parts in order to evaluate the effects of heat treatment on fatigue strength in the HCF regime. The authors found that the post-heat treatment significantly affects fatigue behavior. The authors showed that the post-heat treatment increases the fatigue life of SLM-Ti-6Al-4V parts compared to the AB specimens [159].

The authors reported almost 3.5 times (93000 cycles at a stress amplitude 600MPa) and 10 times (290000 cycles at a stress amplitude 600MPa) higher fatigue life than AB specimens (27000 cycles at a stress amplitude 600MPa) when the post heat treatment temperature was 800^0 C and 1050^0 C respectively. The results from Frkan et al.[75] suggest that the higher the heat treatment temperature, the longer the life expectancy in the HCF (**Fig. 28**).

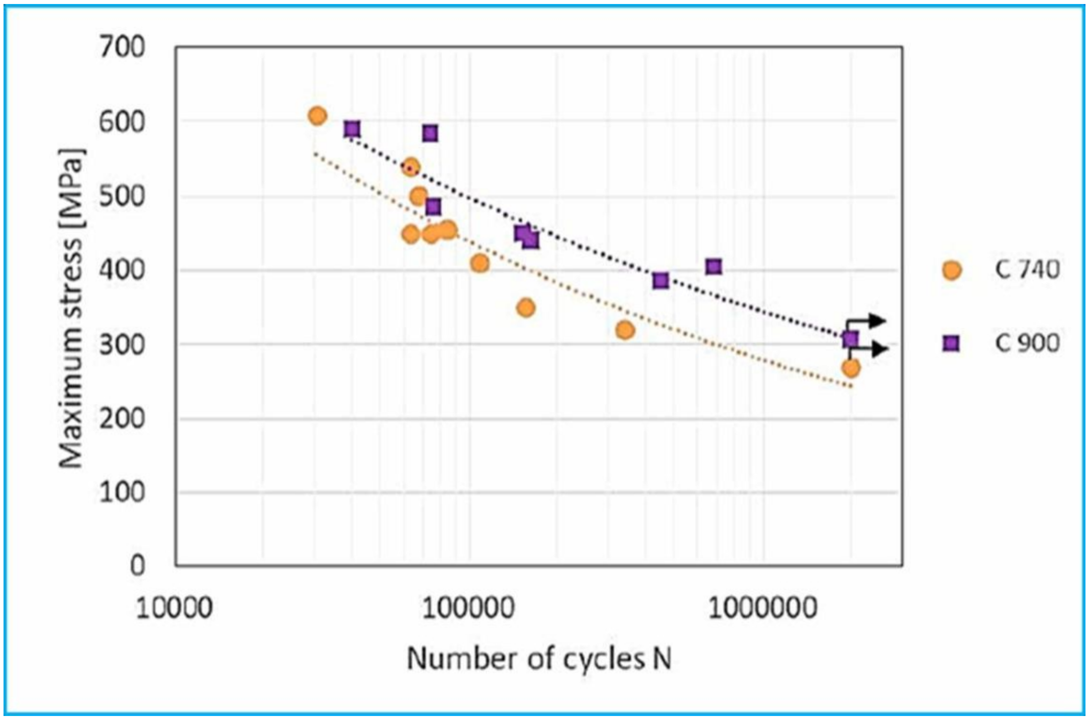

Fig. 28. *Heat treatment temperature effects the fatigue behavior of SLM-Ti-6Al-4V parts. C 700 and C 900 correspond to heat treatment temperature 700^0 C and 900^0 C for the vertically built samples. Adapted from Frkan et al.[75] with permission from Elsevier.*

As for HIP (Hot isostatic pressing) treatment, the authors reported improved fatigue strength (630MPa with a standard deviation of 5.3 MPa) compared to both AB and heat-treated samples [159]. The authors also asserted that stress-relieving heat treatment, even at a lower temperature, improves the fatigue crack growth behavior similar to wrought Ti-6Al-4V parts [159]. Despite improved fatigue crack growth behavior, heat-treated samples show significant fatigue scatter compared to AB samples [159]. Thone et al.[188] also independently confirmed the conclusions above. Bhandari and Gaur[76] and Cutolo et al.[152] also suggested that heat treatment improves fatigue life by reducing the RS (**Fig. 29**).

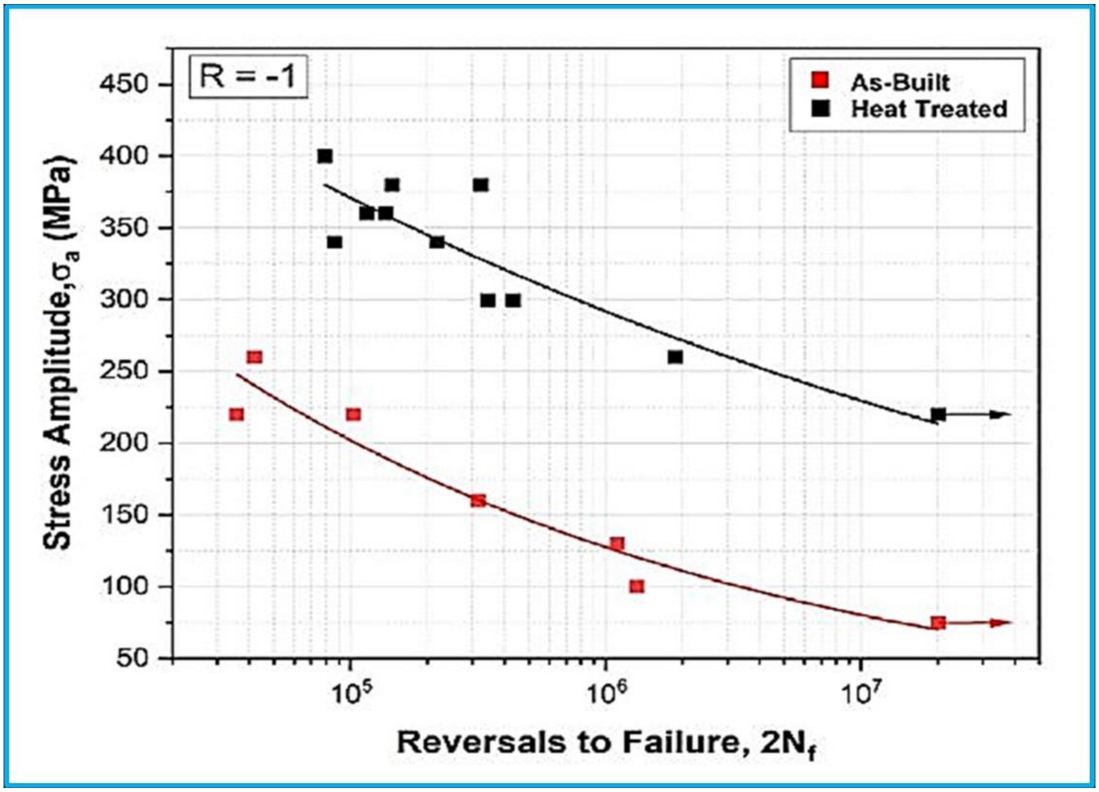

Fig. 29. *S–N curves for Ti-6Al-4V parts for AB and heat-treated condition. Adapted from Bhandari and Gaur[76] with permission from Elsevier.*

In their study, Li et al.[156] proffered that improved HCF performance can be achieved with HIP treatment through the reduction in the defect size and the change in the microstructure surrounding the defects, even though HIPed parts may show significant amounts of defects (~40 m-~200 m). The authors also confirmed that HIP treatment does not eliminate sub-surface defects. Yu et al.[78] also mentioned that both Heat treatment and HIP treatment improve the HCF life. As a further result, the authors concluded that the modification of microstructure in HIPed samples and the reduction or elimination of pores in the samples are associated with an increase in the period of fatigue crack initiation, resulting in an increased fatigue life compared to AB samples. Karami et al.[189] recommended HIP treatment, along with sandblasting and chemical etching, for improving the fatigue performance of SLM-Ti-6Al-4V lattice structures. Benedetti et al.[190] claimed that HIP treatment helps to reduce the porosity throughout to a value of below 0.05 % compared to 0.35 % in AB conditions. It might be the reason of having higher fatigue resistance for the HIPed samples.

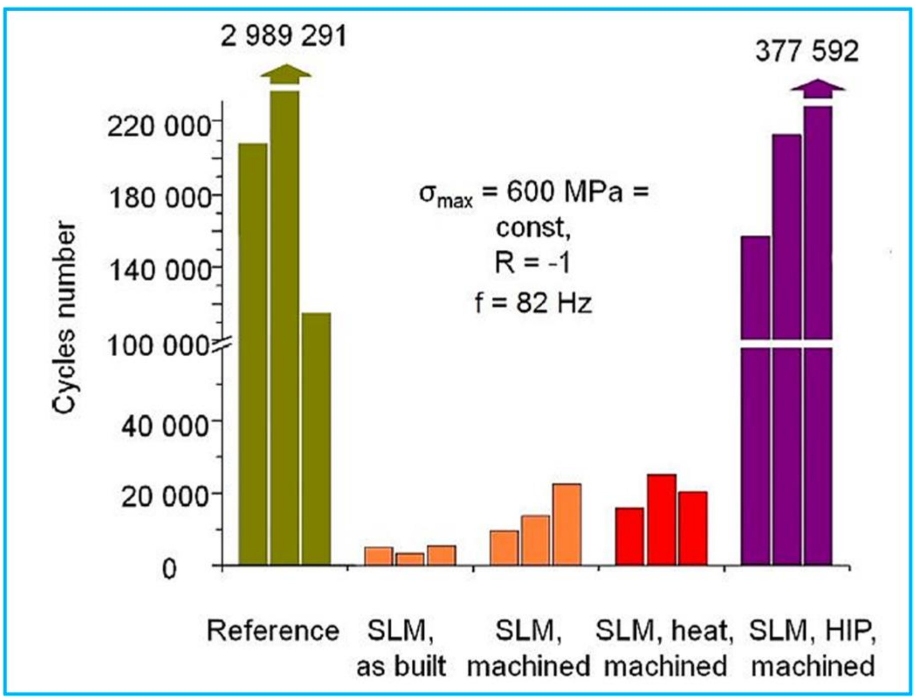

Fig. 30. *Fatigue behavior of SLM-Ti-6Al-4V components in HCF regime compared to reference material (wrought Ti-6Al-4V) at the constant stress of 600 MPa. Adapted from Kasperovich and Hausmann [32] with permission from Elsevier.*

Kasperovich and Hausmann [20,32] investigated the effect of post-treatment on HCF lives at a constant stress 600MPa under load ratio -1 and reported that the HIP treatment provides ductile fracture behavior and increases fatigue strength in the HCF region. **Fig. 30** shows that although heat treatment does not significantly improve HCF strength due to the inherent defects that still exist, the HIP improves the fatigue life significantly for SLM-Ti-6Al-4V parts close to that conventionally processed Ti-6Al-4V parts [20,32]. According to Chastand et al.[39] the HIP treatment strongly affects the fatigue life in the HCF region of SLM-Ti-6Al-4V parts, and the HIP treatment can improve the fatigue life by almost 90% compared to stress-relieved (SR) parts. HIPed specimens, at a higher number of cycles and a very high number of cycles, show fatigue life at the level of wrought processes, whereas stress-relieved parts are at the casting level (**Fig. 31**) [39,40]. Gunther et al.[40] investigated the effect of HIP treatment on fatigue life in the VHCF region and found superior fatigue performance of HIPed Ti-6Al-4V parts compared to AB parts in the VHCF region. Wycisk et al.[165] investigated the effect of SR heat treatment and HIP treatment of SLM-Ti-6Al-4V specimens both in HCF and VHCF regimes. The authors found that HIPed specimens show superior fatigue life compared to heat-treated samples in both regimes as the HIP process cures inherent process defects (**Fig. 32**).

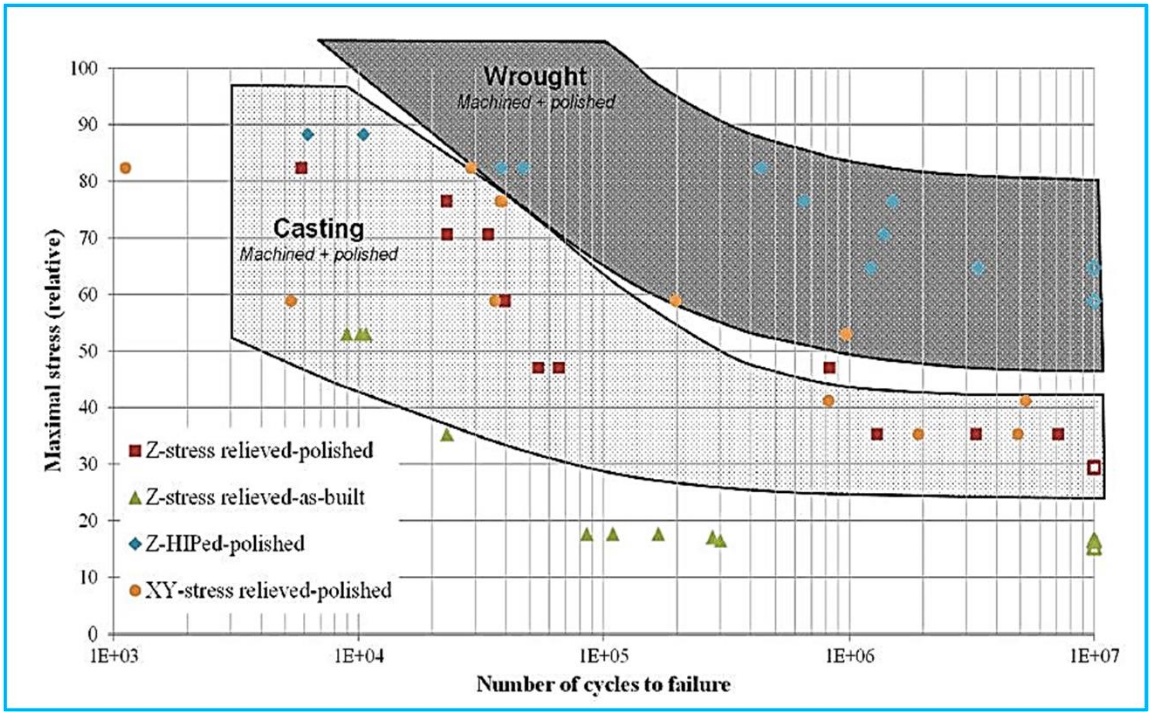

Fig. 31. *Fatigue life of SLM-Ti-6Al-4V specimens. Adapted from Chastand et al.[39] with permission from Elsevier.*

Tridello et al.[146] showed that the heat treatment improves the VHCF performance as heat treatment shifts the crack origin to internal defects, and Wycisk et al.[165] confirmed the same for the HIPed specimens. Edwards and Ramulu [182] also recommended post-treatment, such as SR or HIP, for SLM-Ti-6Al-4V parts to reduce RS, which significantly improves fatigue performance (see section 3.3). The reasons for the increased fatigue strength are attributed to the relief of internal RS (es) and the change of α' martensite microstructure into an α-Ti dominated microstructure after heat treatment and HIP treatment [20,126,152,159,161].

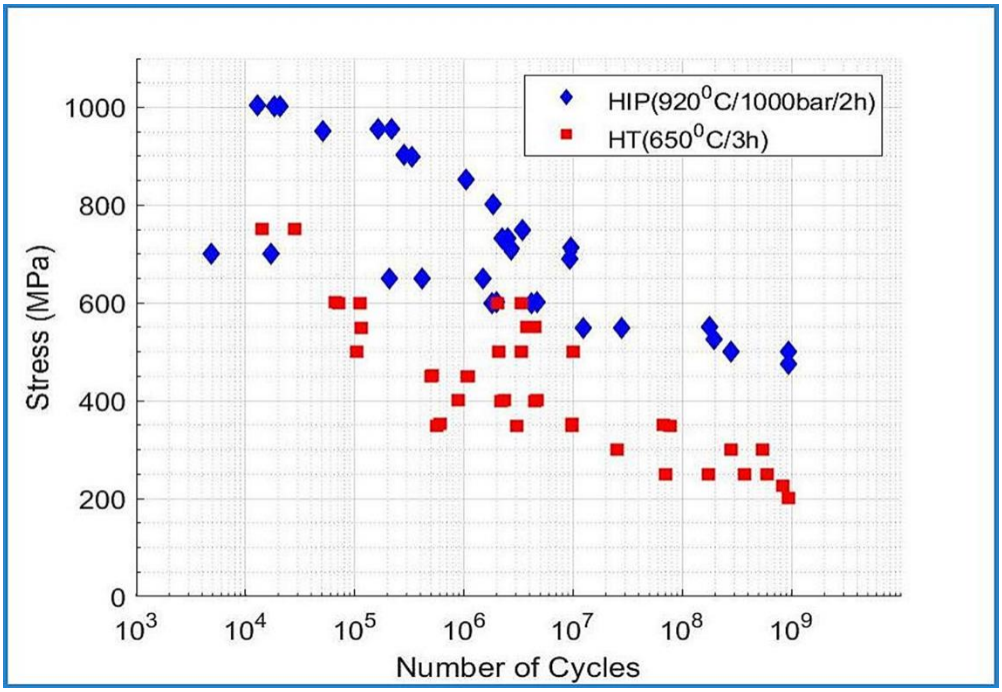

Fig. 32. *Reproduced S-N curve of SLM-Ti-6Al-4V parts under SR and HIP treatment based on data reported in Fig.(2)-(6) by Wycisk et al. [165].*

Thus, heat treatment and HIP increase the fatigue strength of SLM-Ti-6Al-4V parts [20,126,152,159,161]. Mertova, Dzugan, and Roudnicka [191] also investigated the effect of HIP treatment in the HCF region and found significant improvement in fatigue life after the HIP treatment as the HIP treatment reduces the porosity significantly (from 0.67± 0.30% to 0.01± 0.01%). du Plessis and Rossouw [192] suggested that Ti-6Al-4V specimens show reduced porosity after the HIP treatment, especially nearly zero at the core region of the specimen leading to higher fatigue life, while, Chastand et al.[39], Kasperovich and Hausmann [20] indicated that the HIP modifies the microstructure and removes unmolten particles and cold joints, but the heat treatment does not change the porosity; the heat treatment does not improve durability. In contrast, it was reported by Dallago et al. [193,194] that even though HIP treatments reduce internal porosity considerably, substantial change in fatigue resistance is not be found (**Fig. 33**) because the internal porosity does not impact the fatigue resistance in the same way as surface defects (i.e., sharp notches), that have a large impact on the fatigue resistance and it cannot be reduced by the HIP treatment. Qiu, Adkins, and Attallah [173] showed that the HIP treatment closes almost all the porosity; ultimately, it increases the fatigue life of SLM-Ti-6Al-4V parts, as discussed in section **2.4.2** .

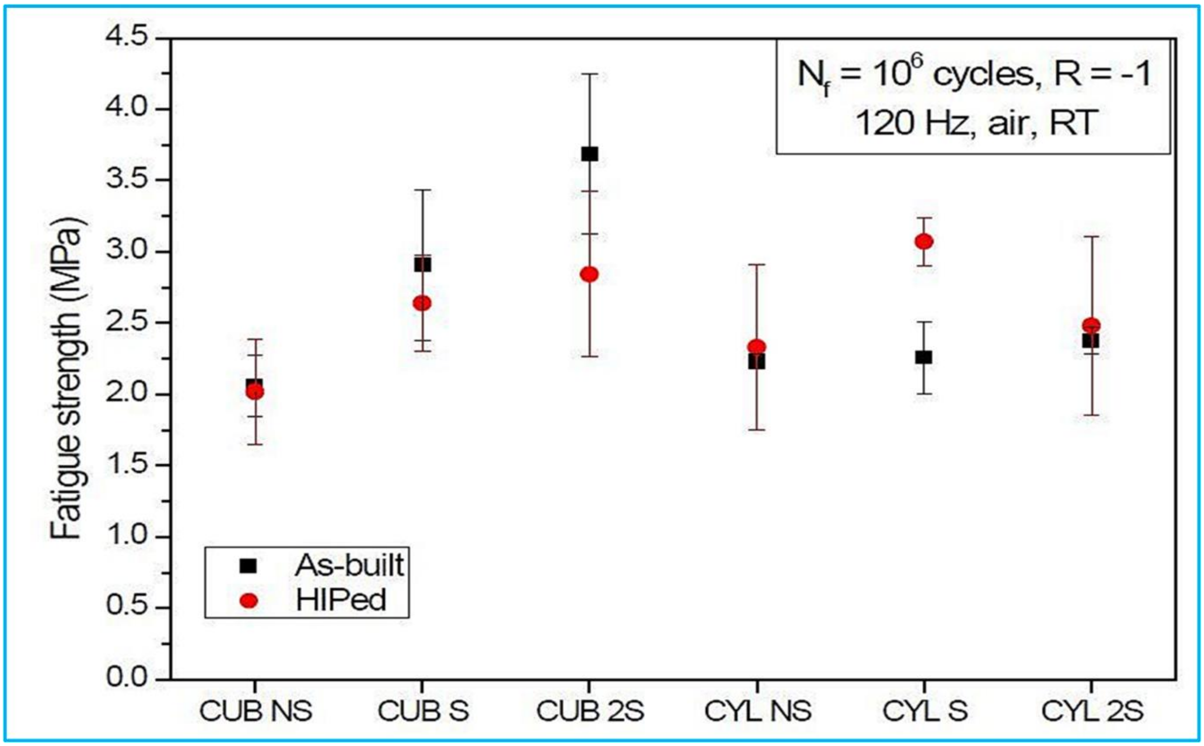

Fig. 33. *Fatigue resistance for each structure type. Here, (CUB-NS), (CUB-S), (CUB-2S), (CYL-NS), (CYL-S), and (CYL-2S) denote regular cubic cells, single staggered cubic cells, double staggered cubic cells, regular cylindrical cells, single staggered cylindrical cells, and double staggered cylindrical cells respectively. Adapted from Dallago et al. [194] with permission from Elsevier.*

Interestingly, Cutolo et al.[152] claimed that compared to SR heat treatments, the HIP treatment seems to reduce the fatigue performance of SLM-Ti-6Al-4V parts (**Fig. 34**), mainly due to the coarsening of the microstructures, which can result in a lower crack propagation resistance. Qiu, Adkins, and Attallah [173] also claimed that HIP treatment significantly improves ductility but reduces the strength of SLM-Ti-6Al-4V parts. Section **2.4.8** shows that ductility plays an essential role in the fatigue performance of the SLM-Ti-6Al-4V parts.

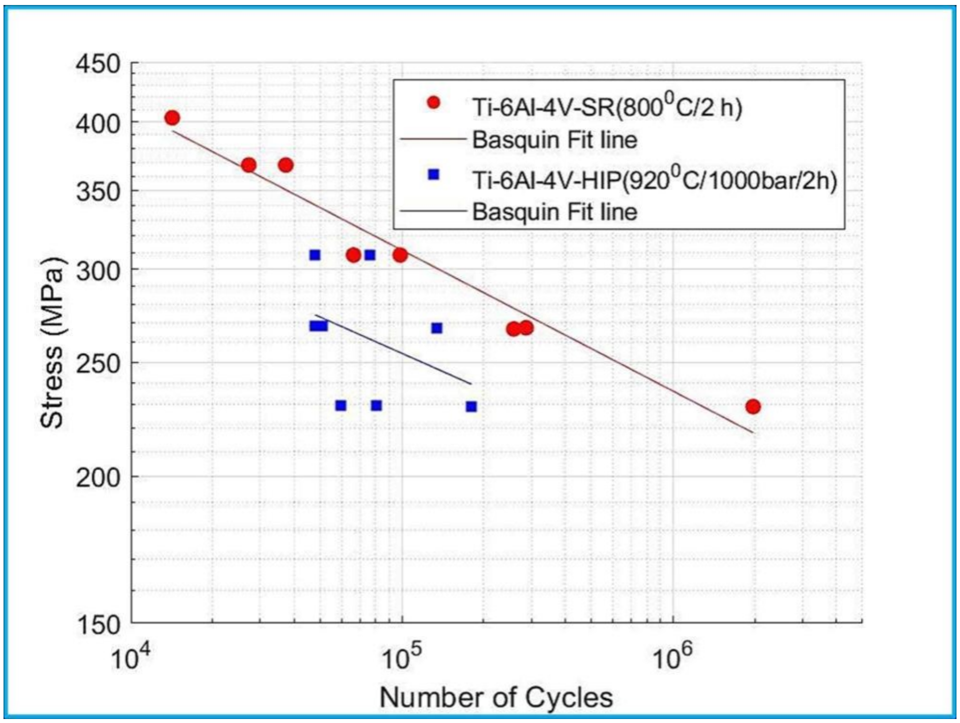

Fig. 34. *Reproduced S-N curve showing the influence of post-treatments on fatigue performance of SLM-Ti-6Al-4V parts based on the data reported by Cutolo et al.[152].*

Qian et al.[79] investigated the effect of different temperatures on the HCF performance. As indicated by the author, the sample was heated up to 600^0C in the SEM chamber using thermal radiation controlled by an electro-hydraulic servo system. This study was conducted to investigate the effect of different temperatures both on vertically and horizontally built samples. Based on the findings, the authors concluded that the increased temperature reduces the fatigue life of SLM-Ti-6Al-4V parts for both batches (**Fig. 35**).

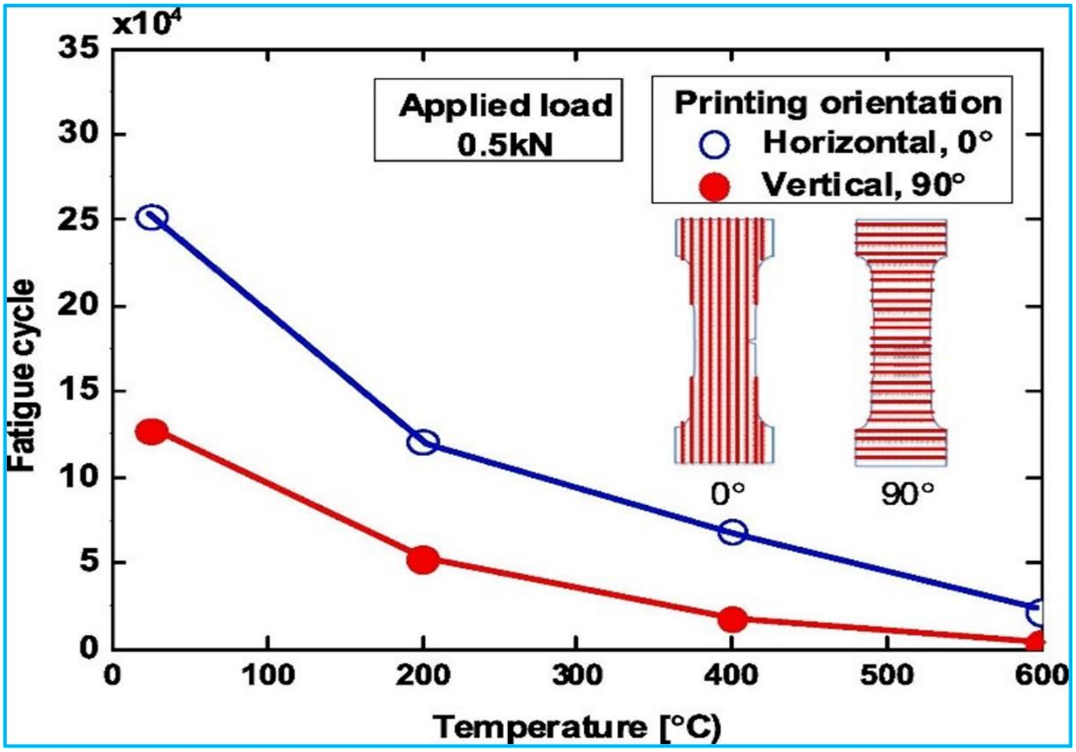

Fig. 35. *The correlation between fatigue life and the temperature for specimens with different building orientations. Adapted from Qian et al. [79] with permission from Elsevier.*

The crack growth rate of Ti-6Al-4V parts also increases with temperature, whereas the slope of the crack length curve gives an idea of the crack growth rate. The steeper the slope, the faster the crack will grow. **Fig. 36** shows the relationship between crack length and fatigue life at different temperatures.

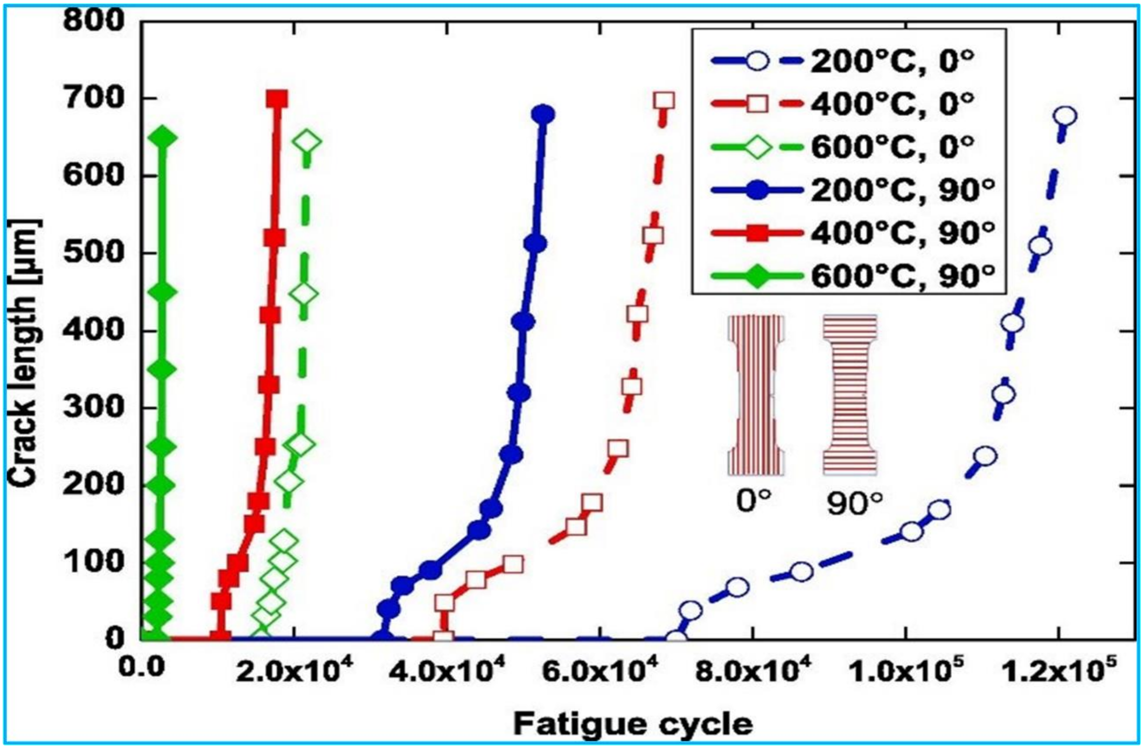

Fig. 36. *The correlation between crack length and fatigue cycle number at different temperatures. Adapted from Qian et al.[79] with permission from Elsevier.*

Fig. 37-**Fig. 39** are reproduced based on the data reported in the literature that will help the readers to understand how the HCF and VHCF performances are affected by the post-treatment. **Fig. 37** illustrates that AB components show a maximum fatigue limit in the range of 290 MPa to less than 100 MPa. In contrast, **Fig. 38** illustrates that heat-treated components show a maximum fatigue limit in the range of 200-300 MPa, which is higher than the fatigue limit for AB components. In the case of parts going through HIP treatment, as illustrated in **Fig. 39**, it will be found that the fatigue limit for the HIPed parts shows the highest fatigue limit of about from 400 MPa to 500 MPa. Thus, after discussing the matter, it can be suggested that HIP treatment may be the best post-treatment to achieve maximum fatigue strength.

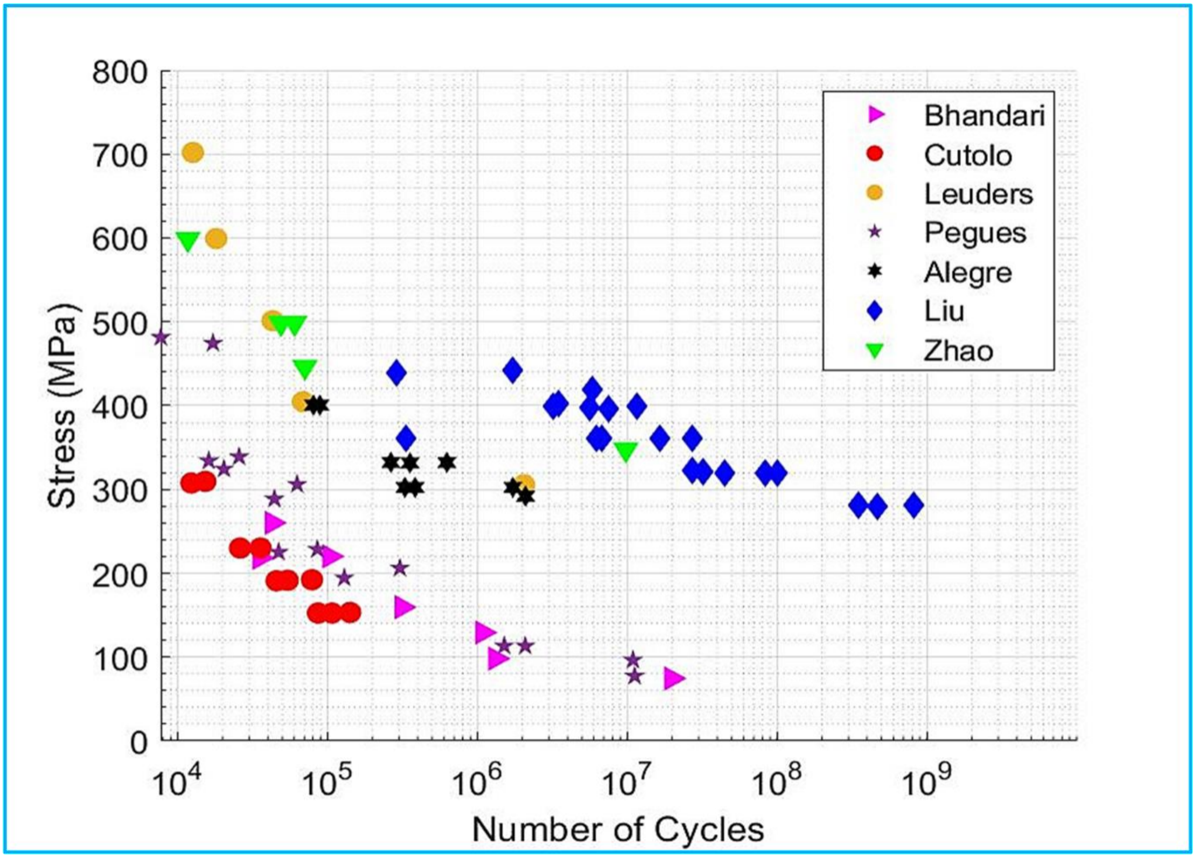

Fig. 37. *S-N curves of AB-Ti-6Al-4V parts based on the data reported in the literature. The data points are collected from Bhandari and Gaur[76], Cutolo et al.[77],Leuders et al.[186],Pegues et al.[80],Alegre et al.[116],Liu et al.[128], and Zhao et al.[47].*

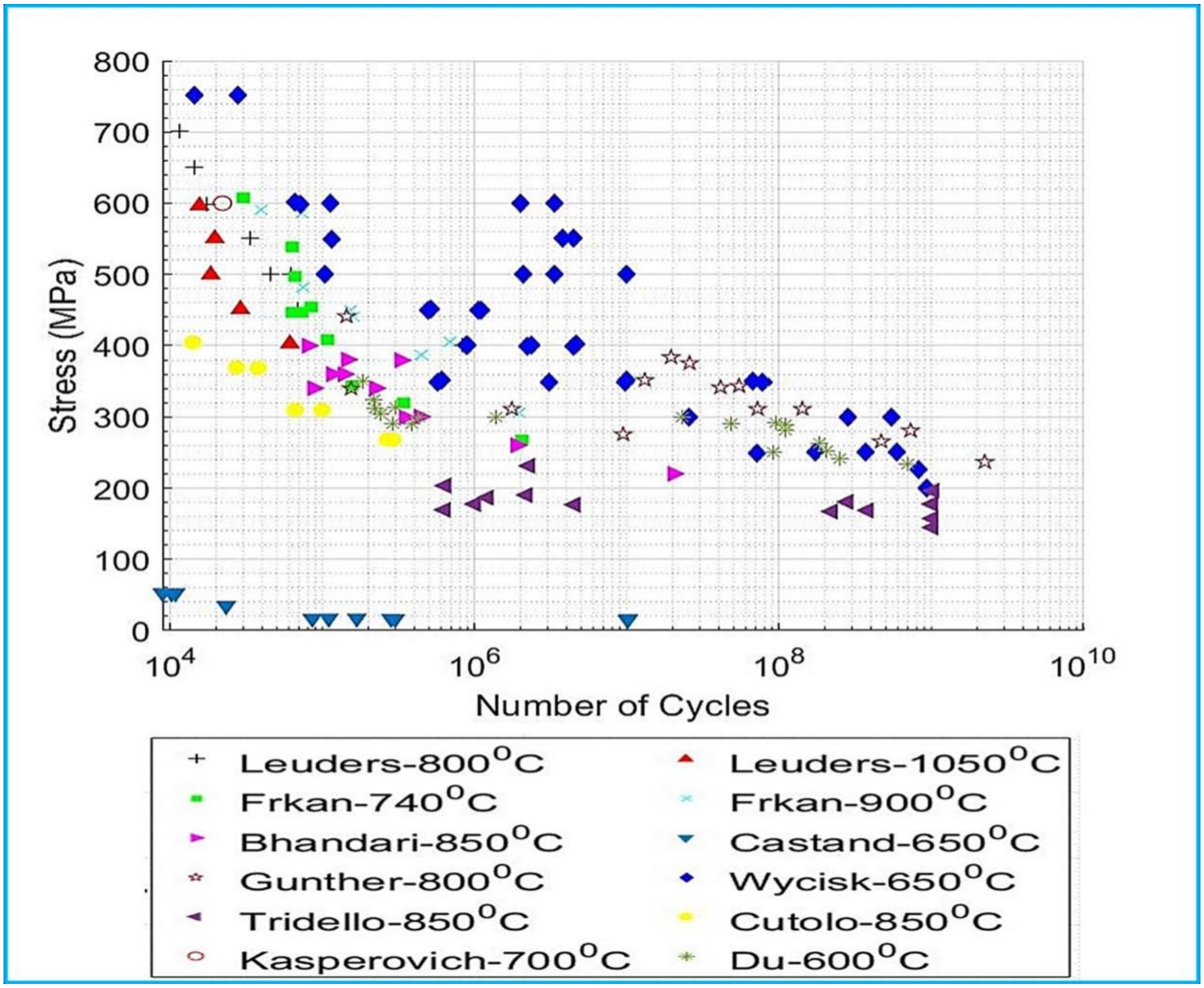

Fig. 38. *S-N curves of HT-Ti-6Al-4V parts based on the data reported in the literature. The data points are collected from Leuders et al.[159,186],Frkan et al.[75] Bhandari and Gaur[76],Chastand et al.[39],Gunther et al.[40],Wycisk et al.[165],Tridelloet al.[146] Cutolo et al.[77], Kasperovich and Hausmann[32], and Du et al.[119].*

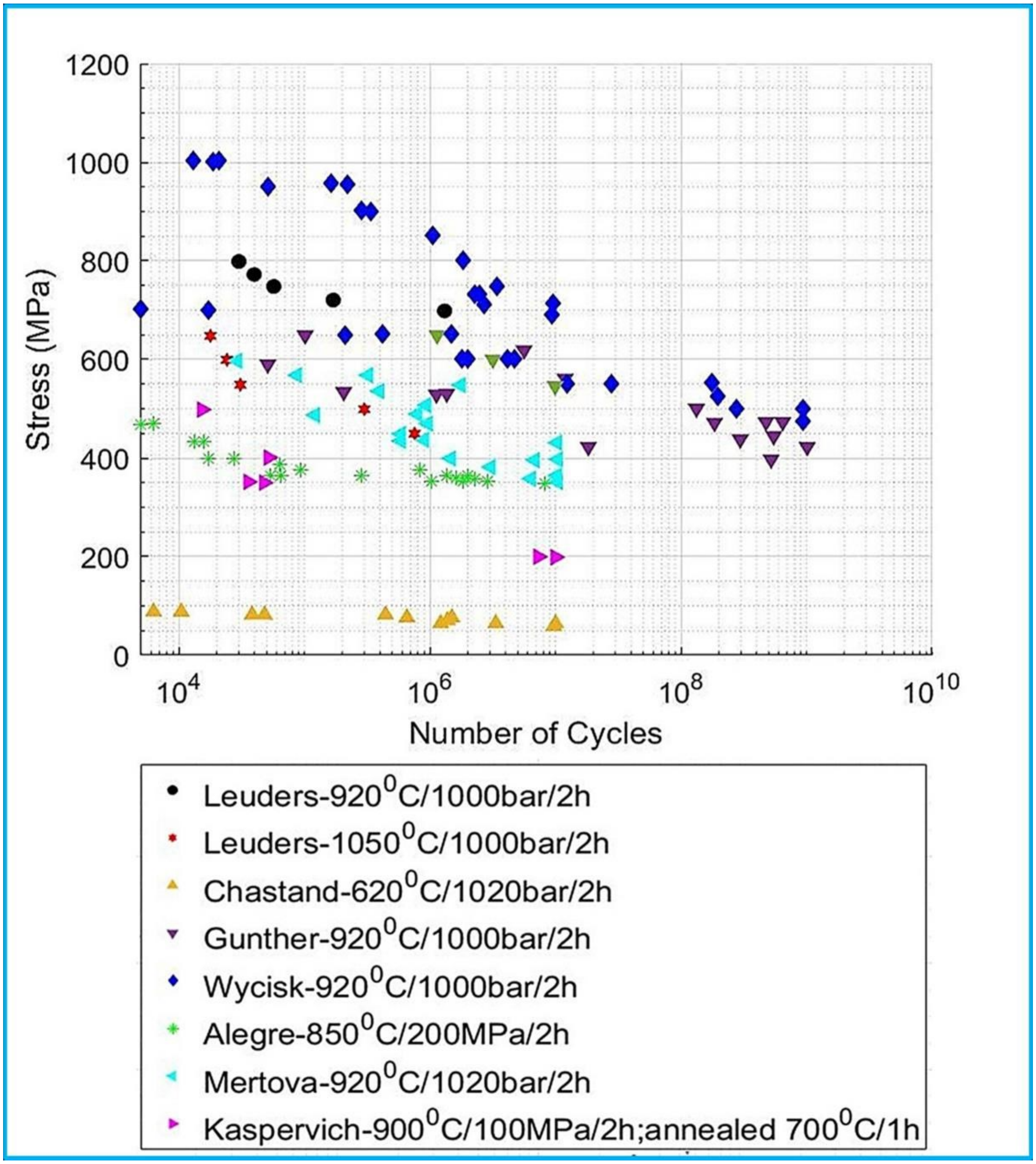

Fig. 39. *S-N curves of HIPed-Ti-6Al-4V parts based on the data reported in the literature. The data points are collected from Leuders et al.[186], Chastand et al.[39], Gunther et al.[40]Frkan et al.[75] Bhandari and Gaur[76],Chastand et al.[39],Gunther et al.[40],Wycisk et al.[165],Alegre et al.[116],Mertova et al.[191], and Kasperovich and Hausmann[32].*

2.4.5 Influences of Surface roughness and post-surface treatment on fatigue properties

The SLM technique offers some of the most promising advantages when fabricating complex geometries close to net shapes compared to conventional manufacturing techniques. Despite this, sometimes it may be challenging to fabricate complex and near-net-shape geometries of Ti-6Al-4V alloy due to the need for post-build surface treatment after the build was completed. The surface roughness usually acts as a crack initiator in a way similar to inner pores. Therefore, increased surface roughness is one of the potential reasons for degrading fatigue life [20,32,163,195,196]. As a result, for the design of SLM-Ti-6Al-4V parts, it is crucial to consider the effects of the surface finish on the fatigue behavior of built parts [197]. Pegues et al.[80] investigated the effect of the surface roughness on the HCF performance of SLM-Ti-6Al-4V parts. The authors used two types of specimens: machined with polish sample and AB sample, where two batches of AB samples with different surface roughness were considered. According to the authors, samples with a lower surface roughness showed a higher fatigue strength than samples with a greater surface roughness. The sample with the surface roughness of 31.41µm had a fatigue strength of about 75 MPa. On the contrary, the sample with the surface roughness of 0.45 µm displayed almost 1.5 times the fatigue strength (~115 MPa) of the previous sample. According to Wycisk et al. [41], the surface roughness exerts a significant influence on fatigue performance. The authors found that if the surface finish is improved from Ra=13µm to Ra=0.5µm ,the fatigue strength can improve almost 2.5 times (~205 MPa to 510 MPa) [41]. Chastand et al.[39] reported that the surface roughness significantly affects the fatigue life of the components at 10^7 cycles and that the post-machining and polishing treatment doubled the fatigue life compared to the AB specimens. da Costa et al.[4], Kahlin et al.[196], and Nakatani et al.[81] also asserted that the surface roughness has a detrimental impact on fatigue strength as increased surface roughness reduces both the HCF and VHCF strength (**Fig. 40**).

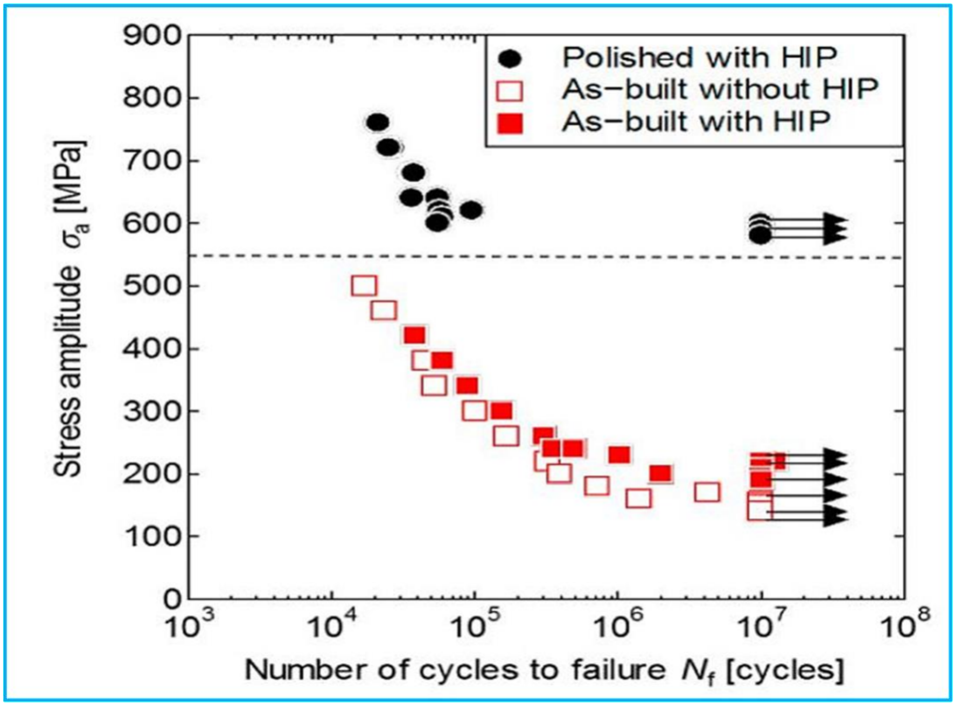

Fig. 40. *S-N curve showing the impact of surface roughness on the fatigue performance of SLM-Ti-6Al-4V parts. Adapted from Nakatani et al.[81] with permission from Elsevier.*

Mertova, Dzugan, and Roudnicka [191] and Kasperovich and Hausmann [20,32] also confirmed that machining with a good surface finish gives superior fatigue life compared to AB samples (**Fig. 41**).

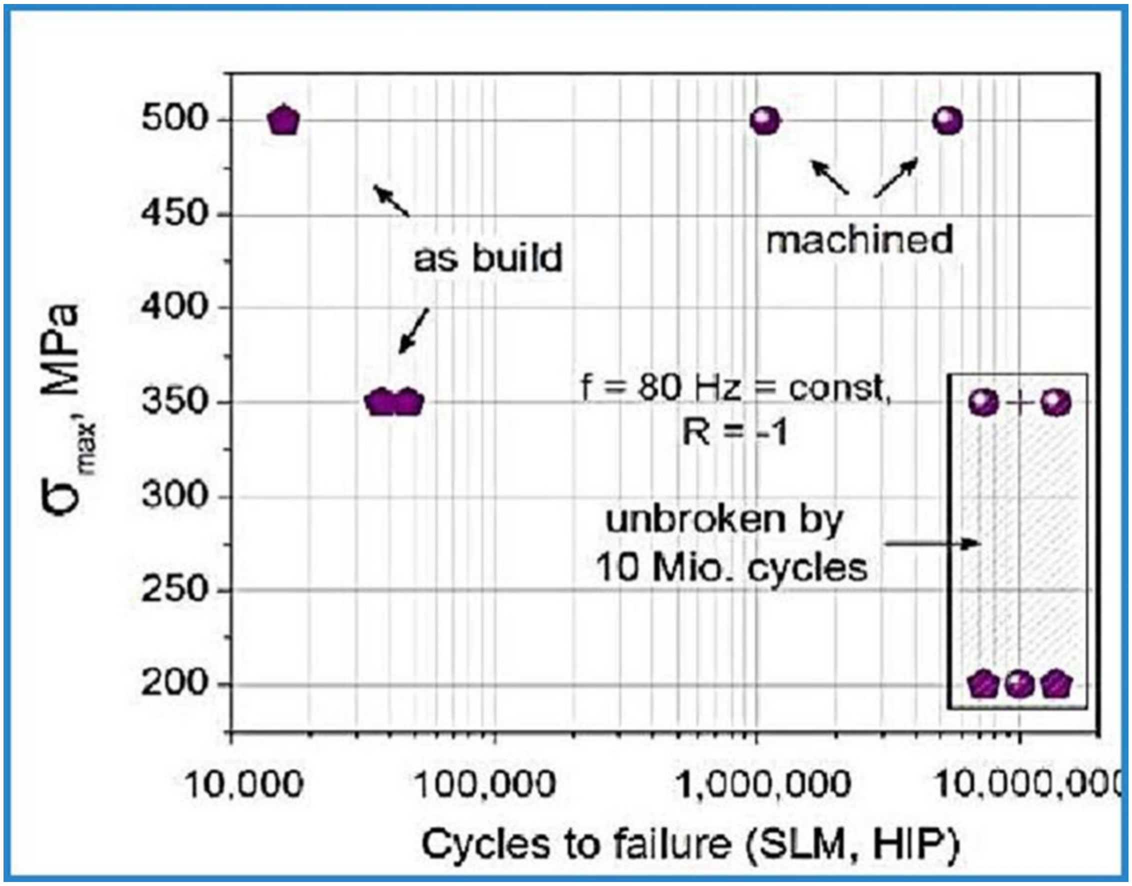

Fig. 41. *Effect of machining/surface roughness on the fatigue performance in the HCF region. Adapted from Kasperovich and Hausmann [32] with permission from Elsevier.*

However, Edwards and Ramulu [182] reported no significant influence of machined surface conditions over AB surface conditions. Benedetti et al.[198] reported that electropolishing does not significantly influence the increment in fatigue resistance. As for shot peening, Wycisk et al.[41] found a higher fatigue strength (435 MPa) compared to AB samples but a lower fatigue strength (about 15% lower) than the polished samples (**Fig. 42**). This finding is counterproductive to the theory that shot peening affects the outer surface with compressive RS, which improves fatigue performance higher than polished samples [41,199]. Despite higher fatigue strength, polished and shot-peened samples show significant fatigue scatter compared to AB samples due to the surface and sub-surface crack initiation [41] .

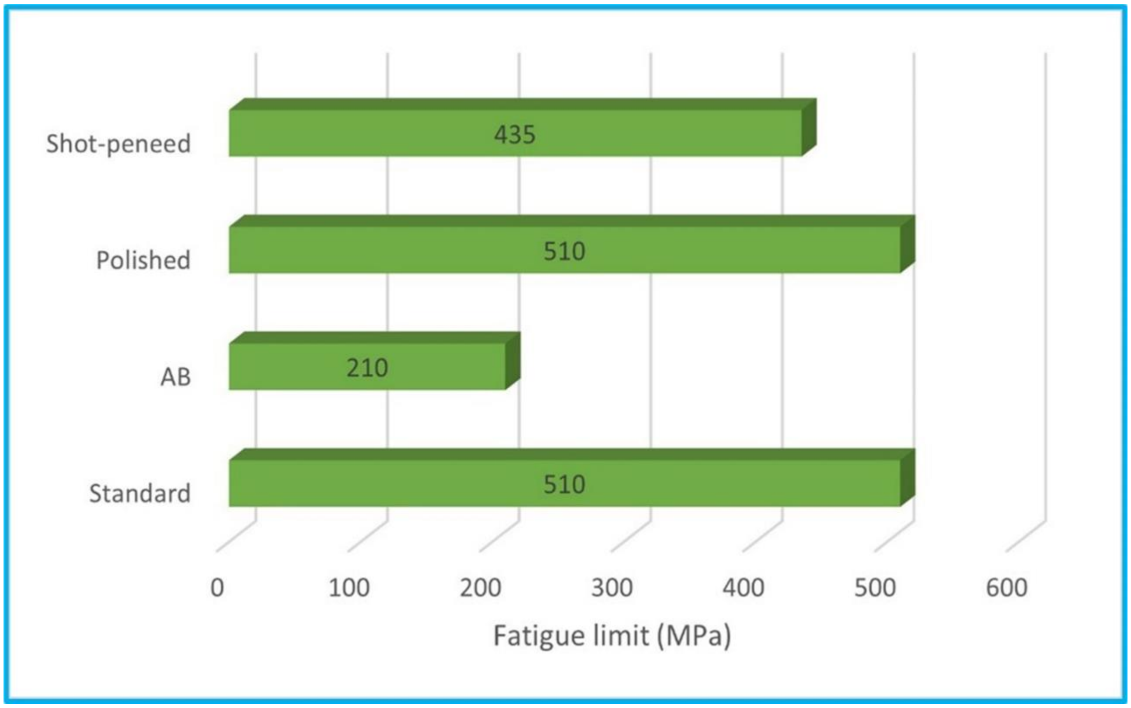

Fig. 42. *Comparison of the fatigue limit of SLM-Ti-6Al-4V parts. Reproduced from the data reported by Wycisk et al. [41] .*

A study conducted by Yan et al.[82] demonstrated that ultrasonic surface mechanical attrition (SMAT) can produce a nanostructured layer on the surface of the Ti-6Al-4V parts. The nanostructured layer comprises a nanocrystalline grain layer, a sub-grain layer, and a layer that coexists with fine and coarse grains. It was found that the fatigue resistance of the SMAT specimens was 580 MPa, which was twice as high as the fatigue resistance of the AB specimens (290 MPa) and 57% higher than the fatigue resistance of the HIP specimens (370 MPa) (**Fig. 43**).

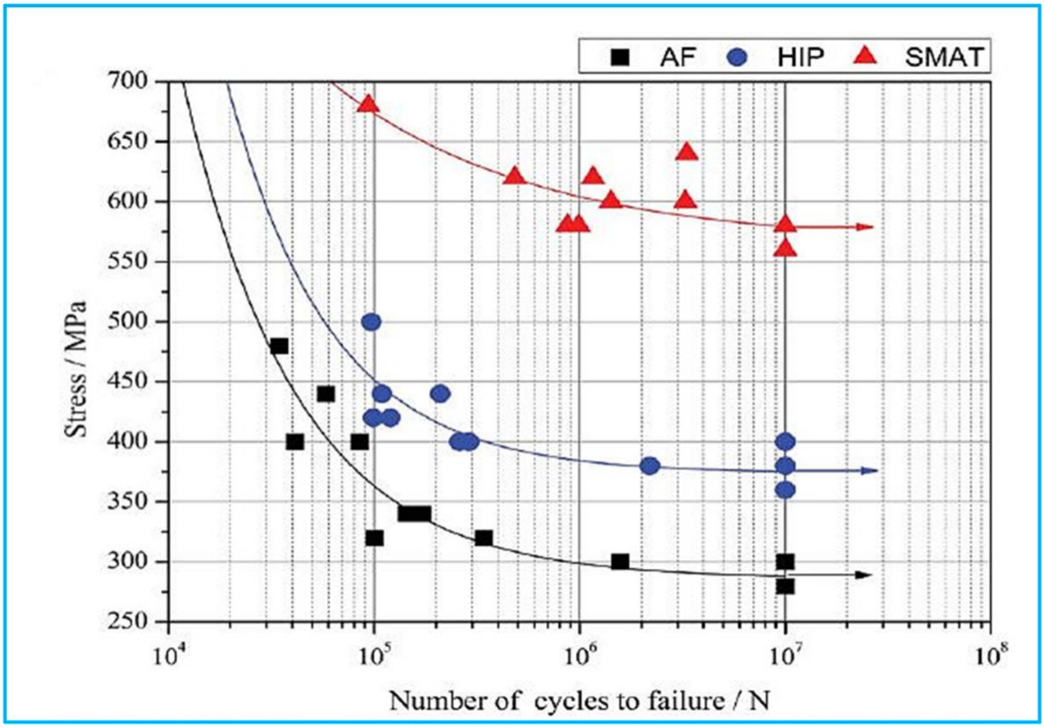

Fig. 43. S-N curves of SLM-Ti-6Al-4V specimens under AF, HIP, and SMAT conditions.[82]

Zhang et al.[200] investigated the effect of ultrasonic nanocrystal surface modification (UNSM) on the HCF performance of SLM-Ti-6Al-4V parts. The authors used both low and high ultrasonic vibration amplitudes while investigating the effect of UNSM on the fatigue performance of SLM-Ti-6Al-4V parts. It was found that UNSM gives a better surface finish than the samples without UNSM, which helps to improve the fatigue performance of the samples with UNSM (**Fig. 44**).

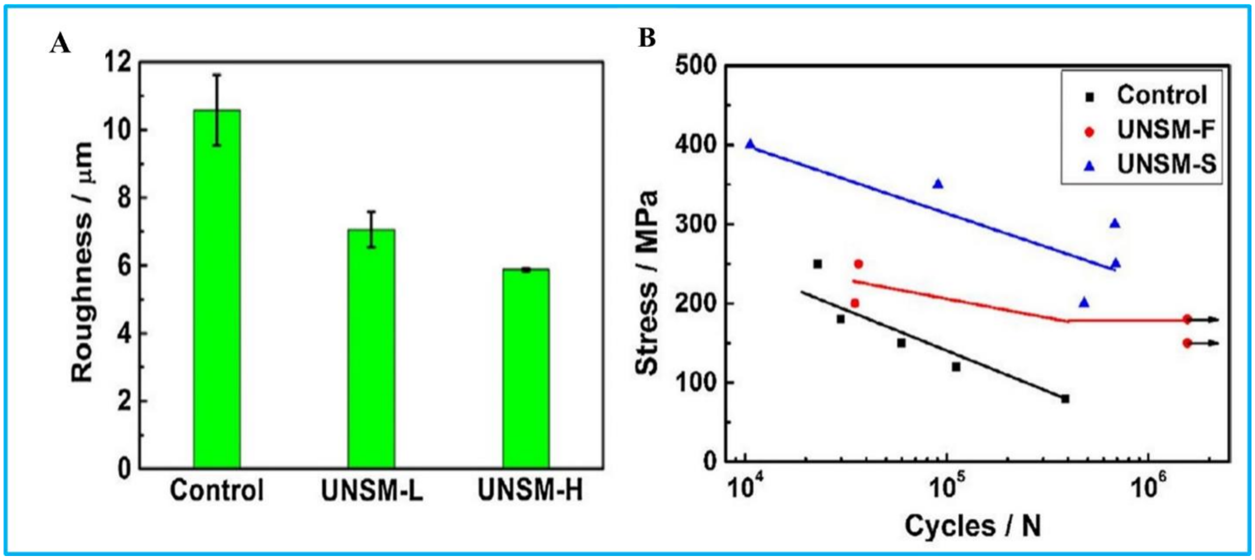

Fig. 44. *shows (A) Roughness profiles. Here, control denotes the samples without UNSM, whereas L and H denote low and high ultrasonic vibration amplitudes used in UNSM. (B) S-N curve of Ti-6Al-4V parts with and without UNSM. Here, F and S denote the fast and slow rotation speeds of the RBF samples during processing, respectively. Adapted from Zhang et al. [200] with permission from Elsevier.*

Kahlin et al.[196] extensively investigated the effect of different post-surface processing methods (shot peening, laser shock peening, centrifugal finishing, laser polishing, and linishing) on the fatigue performance of SLM-Ti-6Al-4V parts. The authors found increased fatigue strength of about 125% ,70%, 25%, and 17% after centrifugal finishing, shot peening, linishing, and laser shock peening, respectively, compared to AB samples (**Fig. 45**) [196]. But, for laser polishing, it is found 50% reduced fatigue strength compared to AB samples [196]. The authors recommend centrifugal finishing or shot peening to get the fatigue strength of AB samples same levels as wrought and machined Ti-6Al-4V parts [196].

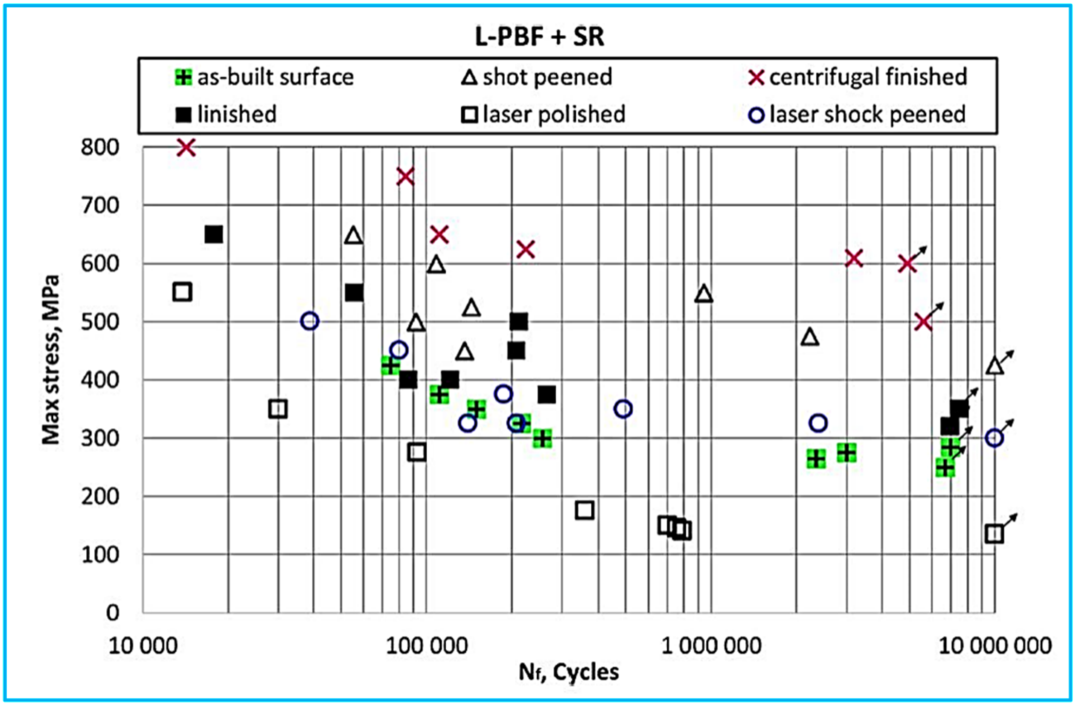

Fig. 45. *Fatigue life for L-PBF/SLM Ti-6Al-4V parts subjected to various post-surface treatments. Arrows indicate run-out tests. Adapted from Kahlin et al.[196] with permission from Elsevier.*

To understand the impact of surface roughness on fatigue performance properly, **Fig. 46** is reproduced from the data mentioned in the literature. It is seen from the **Fig. 46** that the effect of surface roughness on the fatigue performance of SLM-Ti-6Al-4V parts is not consistent. As seen in the **Fig. 46**, the fatigue strength is approximately 540 MPa for a surface roughness value of 0.45 µm, but for a surface roughness value of 31.42 µm, the fatigue strength is approximately 80 MPa, which is about 6 times lower than that of the previous value. Interestingly, when the surface roughness value is 10.5 µm, the fatigue strength is approximately 80 MPa, which is the same as the surface roughness value of 31.42 µm. Furthermore, when the surface roughness value is 5.13 µm, the fatigue strength is approximately 110 MPa, which is almost same for the surface roughness value 15 µm. Hence, it is evident from the results presented above that the effect of surface roughness on the fatigue performance of SLM-Ti-6Al-4V parts is inconsistent. Thus, despite the wide range of fatigue properties associated with surface post-processed materials, surface roughness alone cannot provide a sufficiently strong indicator of fatigue properties due to the fact that prior surface defects can be hidden under a smooth surface. The reason is that removing surface roughness does not eliminate internal defects, and eliminating porosity with retaining AB surface roughness does not produce the expected fatigue performance [191]. In order to achieve optimal fatigue performance, it is recommended to eliminate both the high surface roughness and inner defects. In conclusion, it is pertinent to remember that fatigue strength after post-processing is determined by a combination of surface roughness, surface RS, microstructure, and the remaining defects left in close proximity of the surface.

2.4.5.1 Effect of fabrication parameters on surface roughness

Fabrication parameters significantly affect the surface roughness value .The linear model proposed by Elsayed et al.[174] for the SLM of Ti 6Al-4V parts has shown that the surface roughness is related to laser power levels. The authors concluded that increasing the laser power could result in a reduction in surface roughness of SLM-Ti-6Al-4V parts for both top and side surfaces (**Fig. 47**). The reasons the authors mentioned are the flattening of the melt pool during injection and the elimination of balling phenomenon resulting from the increased energy density [174].

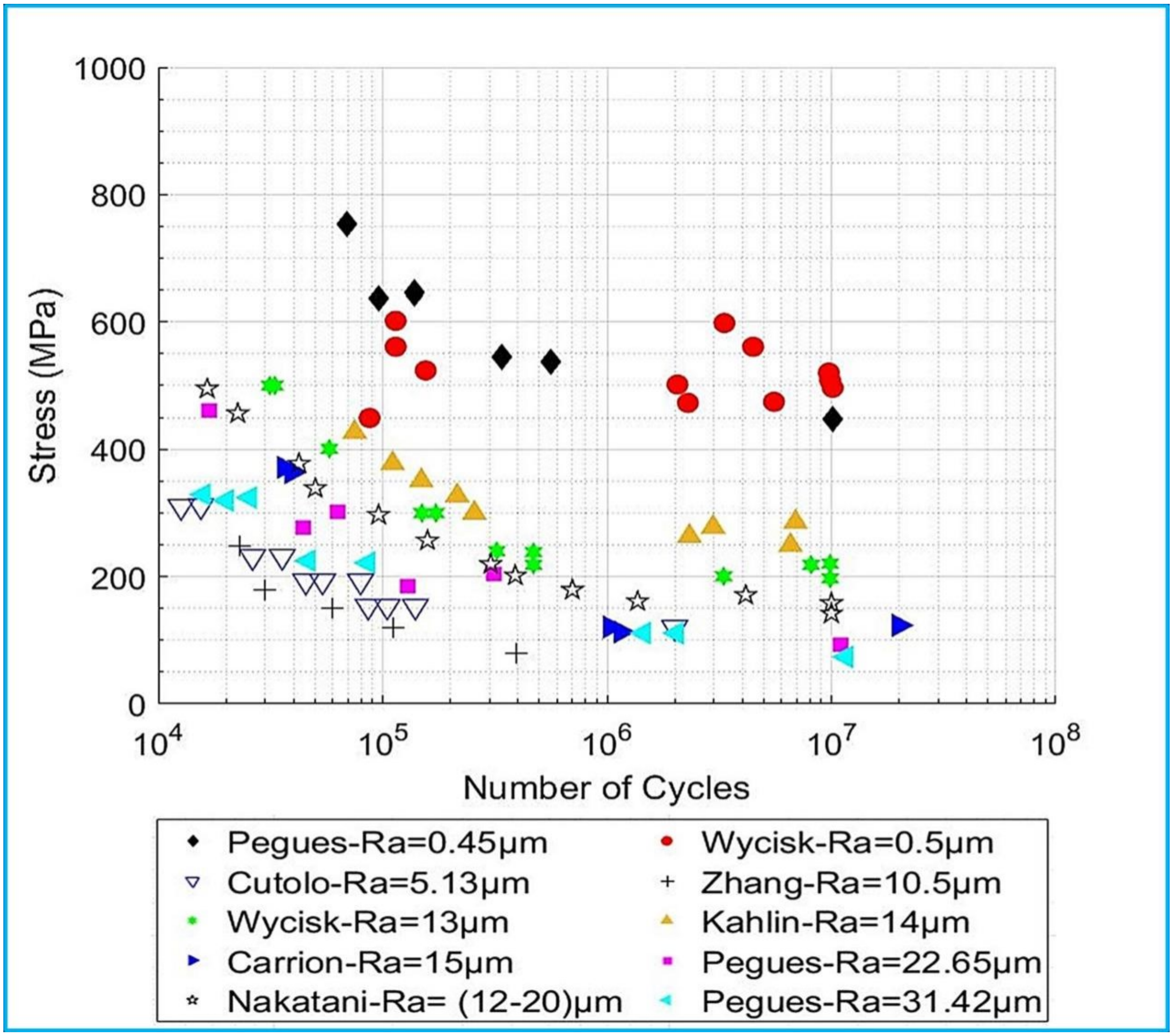

Fig. 46. *S-N curves showing the impact of surface roughness on the fatigue performance of SLM-Ti-6Al-4V parts based on the data in the literature. The data points are collected from Wycisk et al. [201],Carrion et al.[118],Nakatani et al.[81],Kahlin et al.[196], Zhang et al.[200],Pegues et al.[80],and Cutolo et al.[77] .*

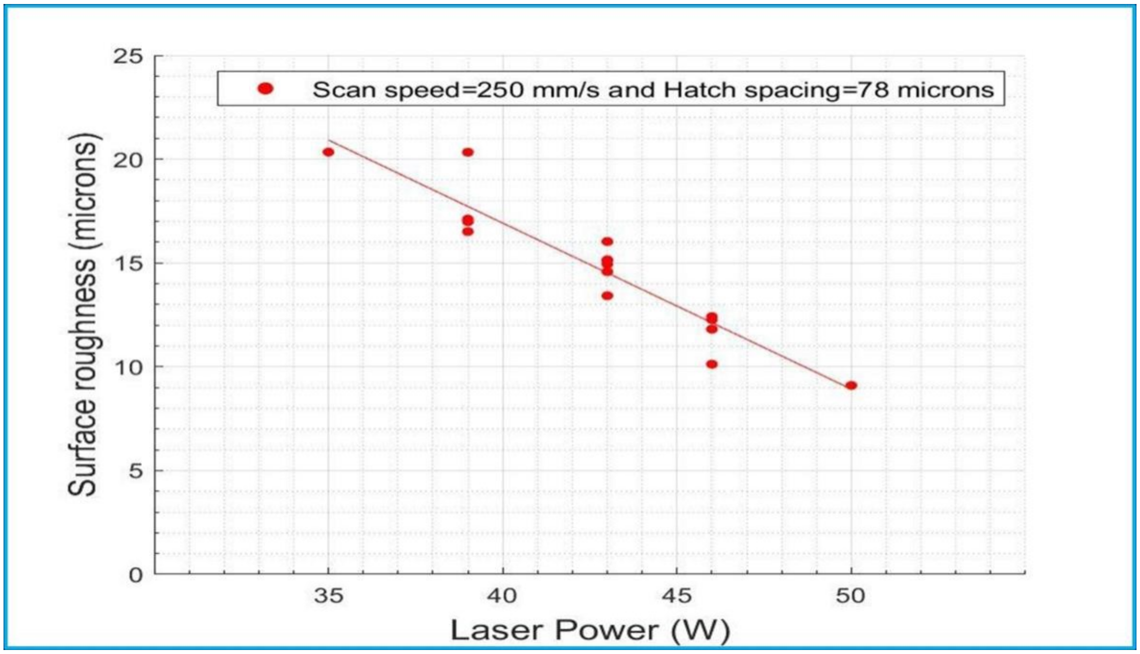

Fig. 47*. Effect of laser power on the surface roughness of SLM-Ti-6Al-4V parts. Reproduced from the data points reported by Elsayed et al.[174].*

Nakatani et al.[81] asserted that particle size and layer thickness used in the SLM technique significantly influence the surface roughness of AB parts. The authors have also noted that unfused particles on the surface of the material produce more scatter in the roughness value.

Table 4 will help the readers to understand the effect of fabrication process parameters on the surface roughness.

Table 4. Effect of process parameters on surface roughness, Ra of AB- Ti-6Al-4V specimens fabricated by SLM.

Build orientation	Powder size (μm)	Laser power (W)	Scan speed (mm/s)	Layer thickness (mm)	Hatch distance (mm)	Energy density (J/mm^3)	Surface roughness, Ra (μm)	Refs.

Vertical	15–45	280	1200	0.03	0.14	55.56	15	Carrion et al.[118]
Inclined (45^0)	15–45	280	1200		0.14		13.24-23.07	Pegues et al.[202]
Vertical	9						6.83	Benedetti et al.[190]
Vertical	40						10-13	Masuo et al.[203]
Vertical				0.06			5.13±0.61	Cutolo et al.[77]
Vertical							2.04	da Costa et al.[4]
Vertical	40						12-20	Nakatani et al.[81]
Vertical	15-45	280	1200	0.06	0.14		14	Kahlin et al.[196]
Vertical		370		0.06			13	Gretemeier et al.[204]
Vertical	15-45	400	1000	0.05	0.16	50	15.45	Fatemi et al.[35]
Vertical	50			0.03			17	Kahlin, Ansell, and Moverare [205]

Vertical	50			0.03			17	Kahlin,Ansell, and Moverare[206]

So, optimized fabrication parameters should be used to control the surface roughness.

2.4.6 Influences of building orientation on fatigue properties

The build orientation is considered one of the significant factors playing an important role in the HCF and VHCF performance of SLM-Ti-6Al-4V parts. There has been a general tendency for the researchers when investigating the effect of the build orientation to construct the samples along three directions; that is, horizontally (0^0), inclinedly (45^0), and vertically (90^0) (**Fig. 48**). Edwards and Ramulu [182] extensively investigated the effect of the build orientation and found significant dependence on the fatigue performance of SLM-Ti-6Al-4Vconcerning the specimen build orientation. The authors tested the samples built in three different orientations. The fatigue strength of samples built in the X-direction was 60% greater than that of samples built in the Z-direction (Vertical) and 30% greater than that of samples built in the Y-direction (Horizontal) at a lifetime of about 2×10^5 cycles (**Fig. 49**) [182].

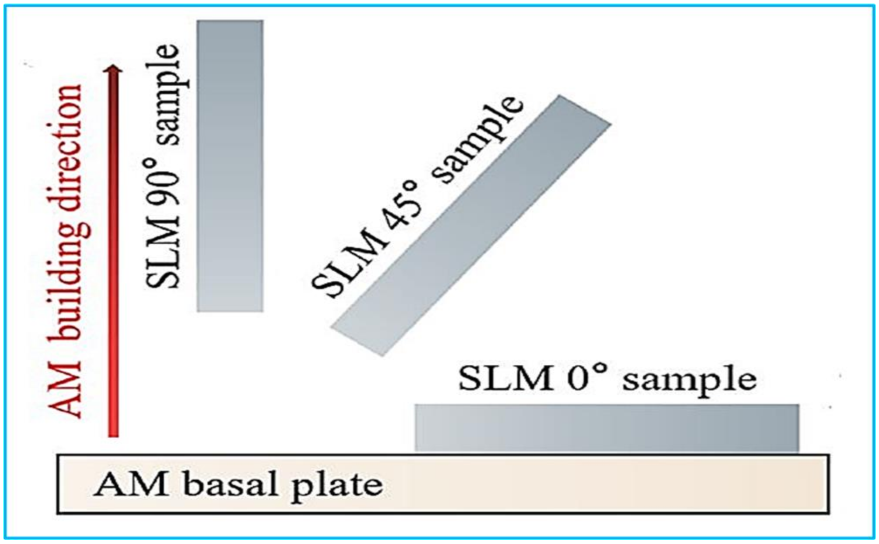

Fig. 48. *Schematic of the specimen orientations while building. Adapted from Xu , Liu and Wang[70] with permission from Elsevier.*

Qian et al.[72] investigated the effect of build orientation on both HCF and VHCF behavior of SLM-Ti-6Al-4V parts. The authors observed a correlation between the angle of the build orientation and fatigue performance in HCF and VHCF regimes, as the higher the angle is, the worse the performance (**Fig. 50***A*) [72]. The authors reported maximum fatigue performance for the horizontal samples, while vertical samples showed the lowest. The reduction of fatigue performance was 7% from 0^0 to 45^0 , but it was larger (about 23%) from 45^0 to 90^0 [72]. Moreover, the authors postulated evident differences for the specimens built in different directions in the HCF region, but in the VHCF region, the difference was negligible (**Fig. 50***B*) [72]. Chastand et al.[39] also reported higher fatigue performance for the horizontally built samples compared to vertically built samples.

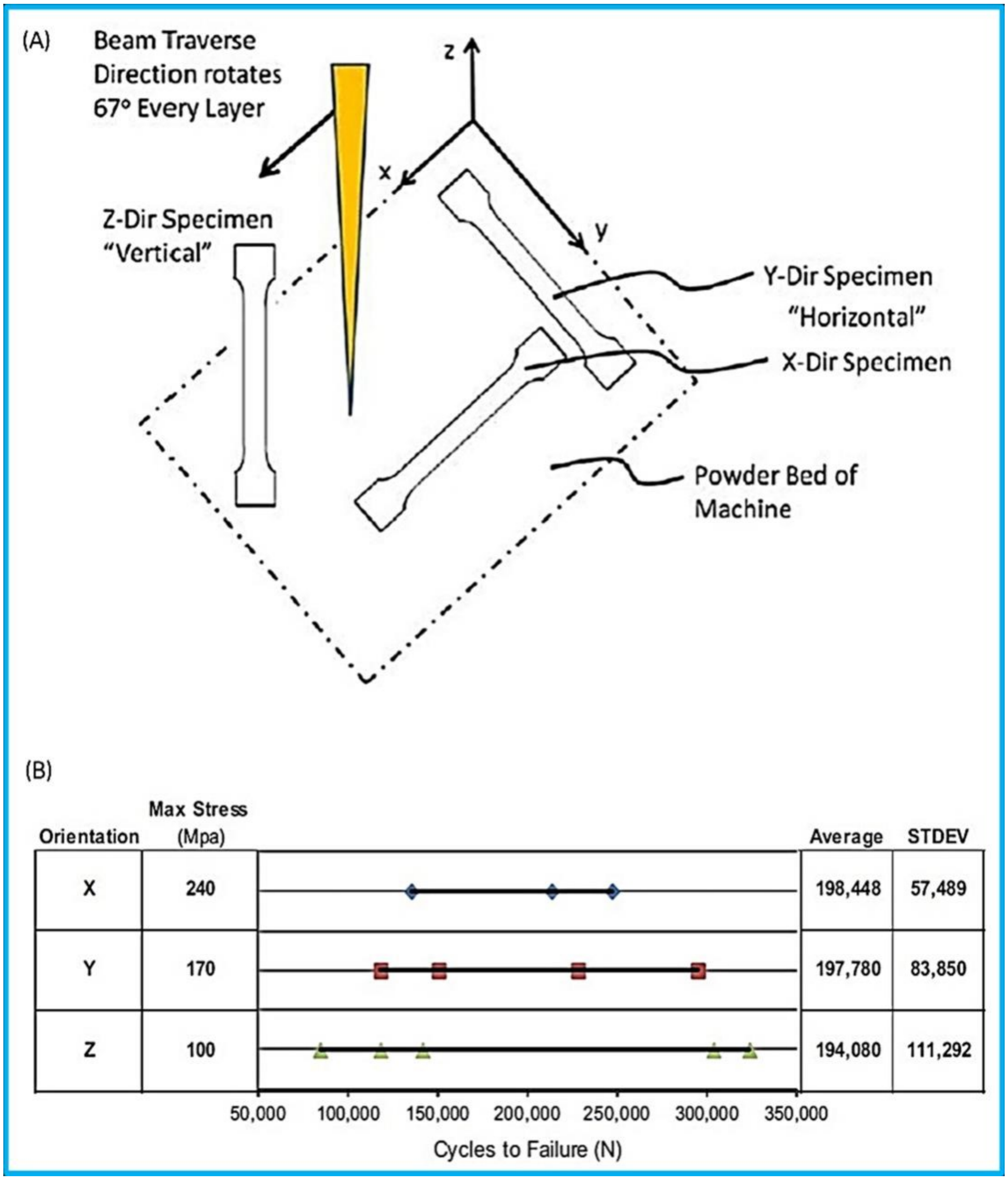

Fig. 49. *shows (A) a Schematic of specimen build orientations [182] (B)The fatigue strengths of samples built with different orientations targeting a lifetime of about* $2{\times}10^5$ *cycles. Adapted from Edwards and Ramulu [182] with permission from Elsevier.*

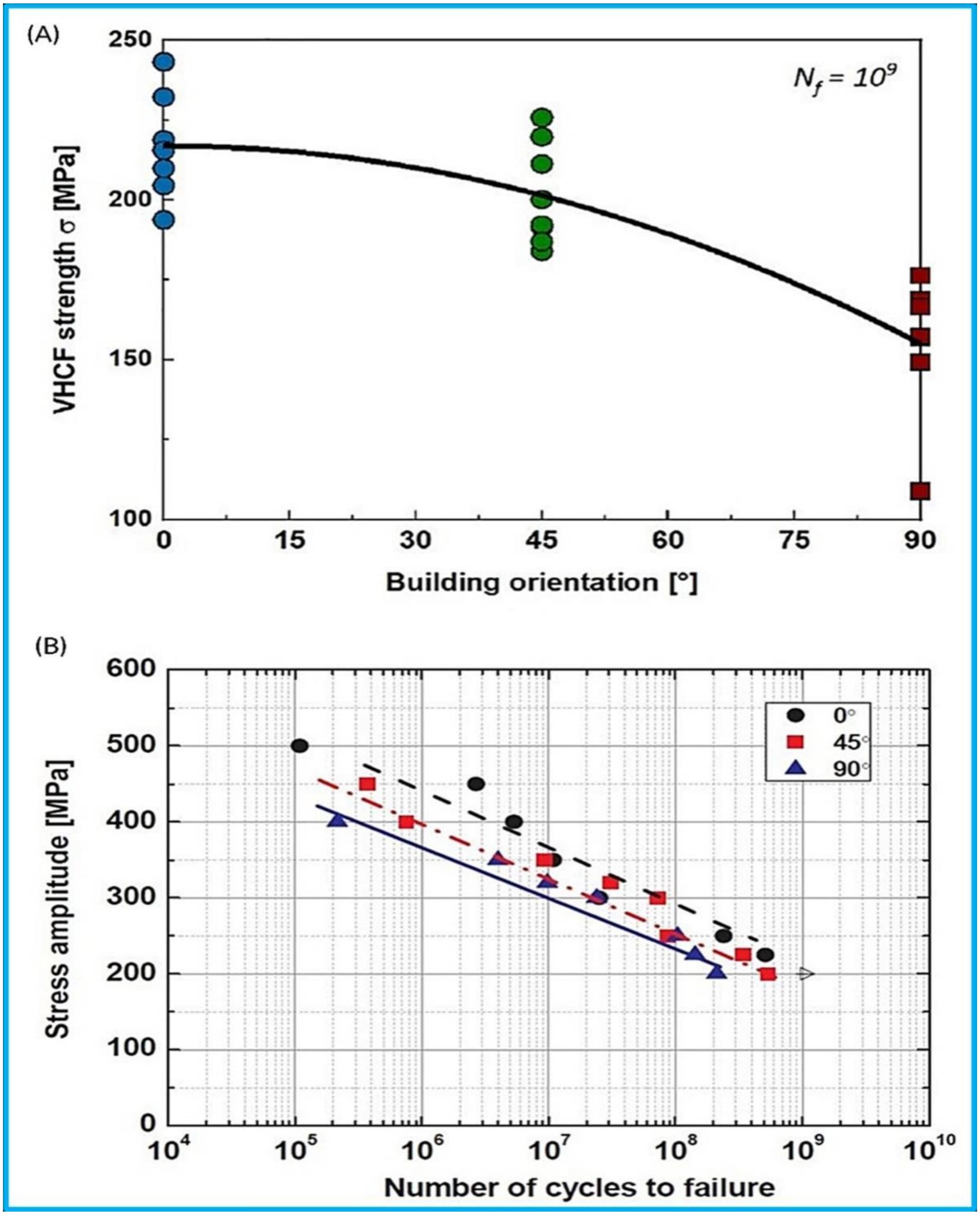

Fig. 50. *shows (A) The correlation between the angle of building orientation and fatigue performance at the VHCF region and (B) The fatigue performance difference in HCF and VHCF regimes. Adapted from Qian et al.[72] with permission from Elsevier.*

The reduced fatigue performance of the vertically constructed samples attributes to more significant and numerous defects, along with unmelted particles in the vertically constructed samples [79]. Xu et al.[70,71] also investigated the effect of the build orientation on both HCF and VHCF performance and reported maximum fatigue performance for the horizontal samples, while vertical samples showed the lowest. Chang et al.[3] investigated the effect of the build orientation after annealing treatment at 800^{0} C for 2 h. Interestingly, the authors found higher fatigue strength for the vertically built samples with larger fatigue scatters than the horizontally built samples. The fatigue strength of the vertically constructed samples showed about 546 MPa, while that of the horizontal samples showed about 530 MPa (**Fig. 51**). Jiao et al.[14] investigated the effect of the build orientation on HCF performance more extensively. The authors used three different load ratios (R=-1,0.1,0.5) while investigating the effect of the build orientation on the fatigue performance of SLM-Ti-6Al-4V parts. Like Chang et al. [3],it was found higher fatigue strength for the vertically built samples compared to the horizontally built samples for all the load ratios. The higher fatigue performance of the vertically built samples can be explained by the presence of smaller elliptical crack source pores farther away from the surface with a lower density than the horizontal samples [14]. Leuders et al.[159] and Edwards and Ramulu [182] pointed out that for a given applied stress range, there is a considerable scatter in the number of cycles until failure and found the minimum scatter for the samples built in the X-direction while vertically built samples show the maximum scatter. Horizontally built samples showed the lowest surface roughness (30 µm), while vertically built samples showed the highest surface roughness (39 µm) [182]. This result verifies the discussion of section **2.4.5** .

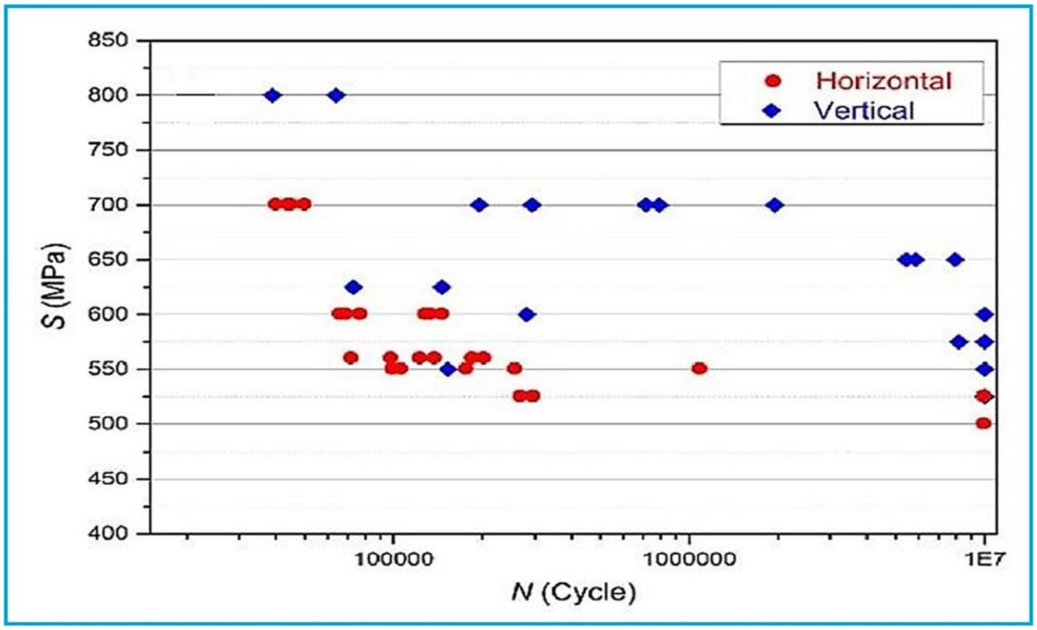

Fig. 51. *S-N curve showing the fatigue results in different building directions of SLM-Ti-6Al-4V parts after annealing treatment. Adapted from Chang et al.[3] with permission from Elsevier.*

It has also been demonstrated that cracks that are parallel to the build layers show lower fracture toughness than cracks that are transversal to the build layers [73,159]. Qiu, Adkins, and Attallah [173] found poor ductility for the horizontally built samples compared to vertical samples. There is a shred of evidence in section 3.8 that ductility influences HCF and VHCF performance. Horizontal specimens may result in the production of uniform material. So, there is a recommendation to investigate the horizontal samples further [73]. A sharp thermal gradient runs along the thickness of the specimens laid on the base of the build chamber, resulting in non-uniform microstructures [73].

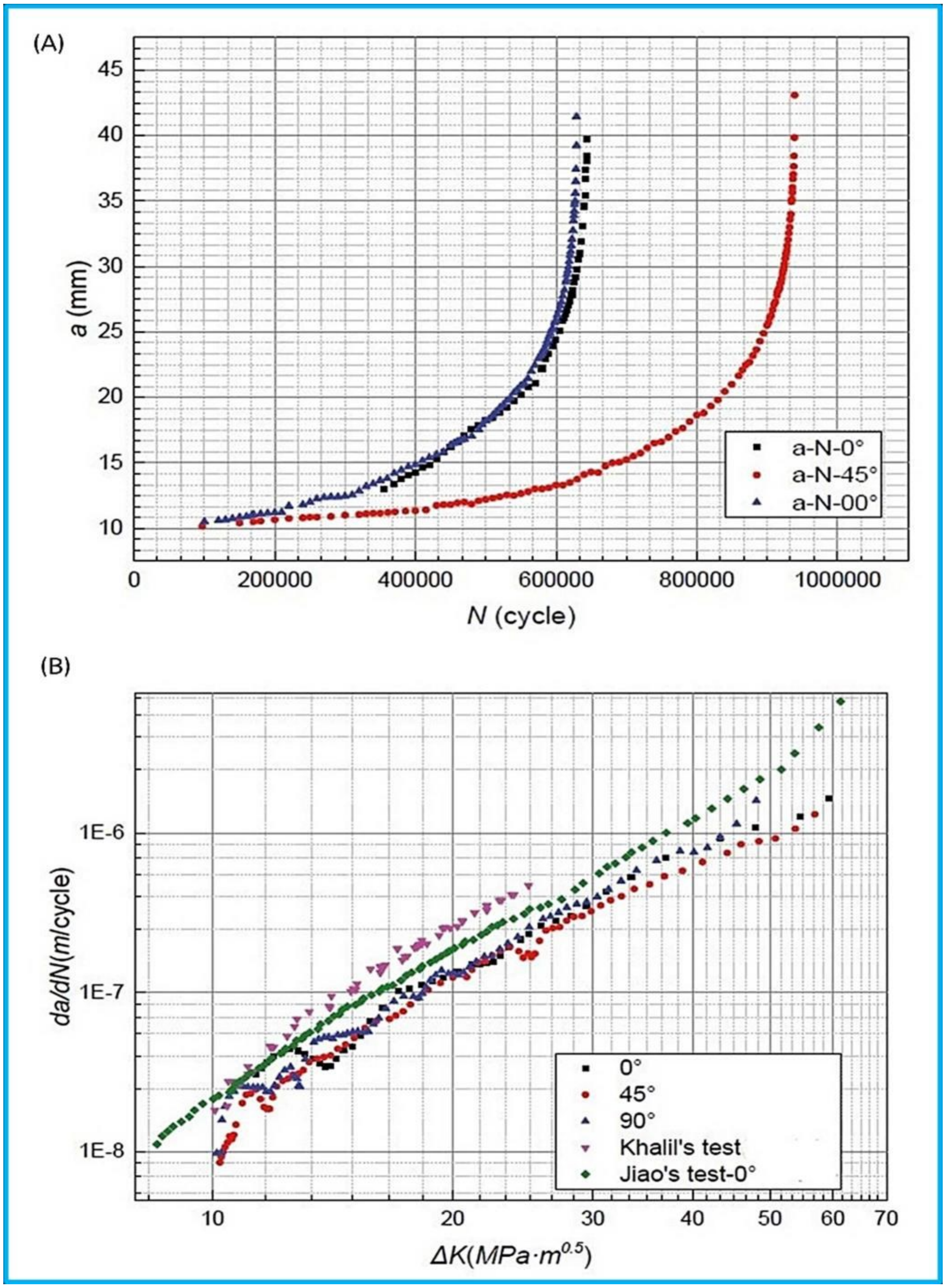

Fig. 52. *shows (A) a-N curves of SLM-Ti-6Al-4V parts built in different directions (B) da/dN- ΔK curve. Adapted from Sun et al.[207] with permission from Elsevier. The data for Khalil's and Jiao's tests will be found in Khalil[208] and Jiao et al.[209].*

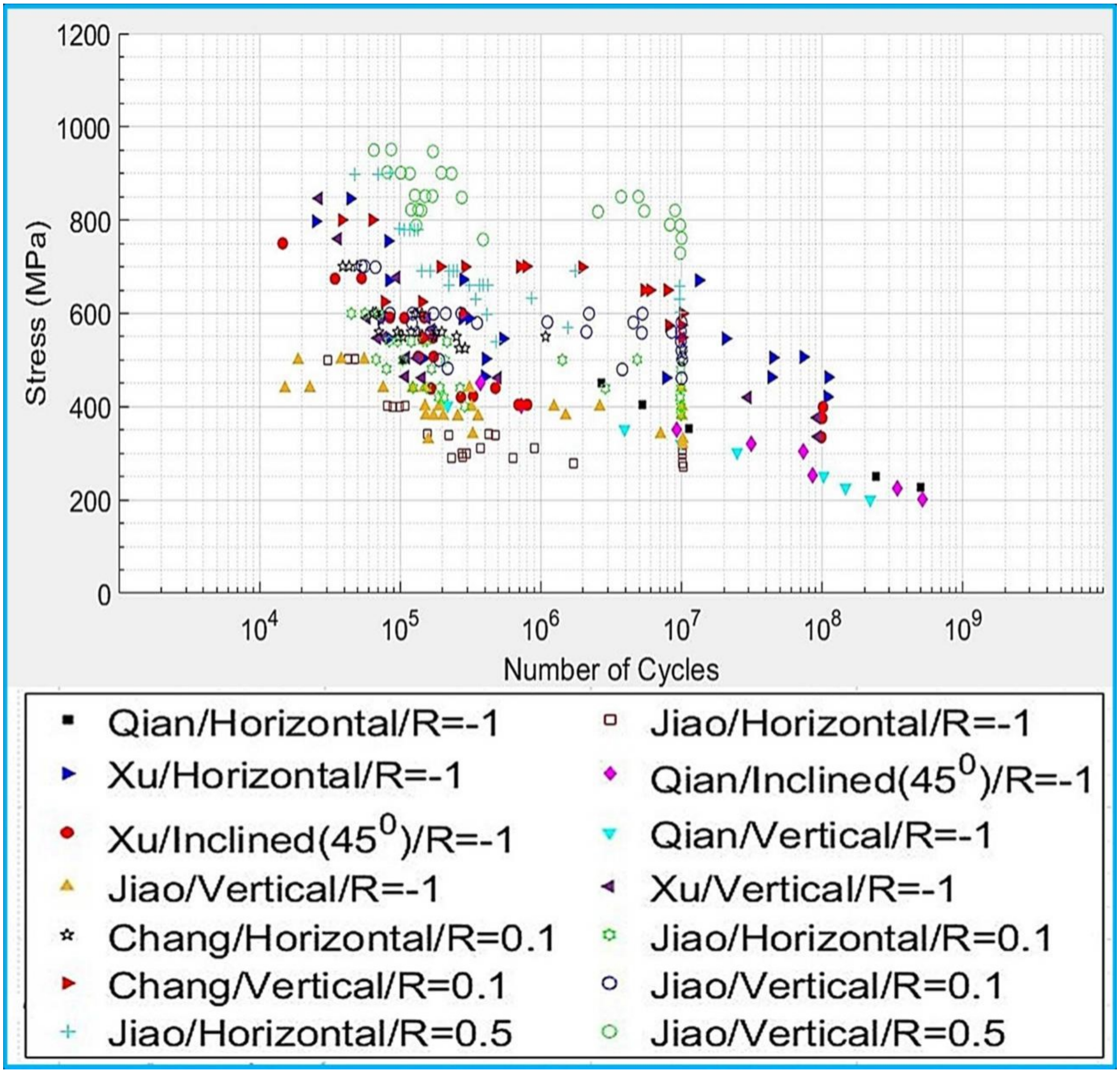

Fig. 53*. S-N curve showing the effect of the build orientation on the fatigue performance of SLM-Ti-6Al4V parts based on the data in the literature. The data points are collected from Chang et al.[3],Qian et al.[72],Jiao et al.[14], and Xu et al.[70,71].*

Sun et al.[207] investigated the fatigue crack growth life of the specimens built in different directions. The authors found almost similar fatigue crack growth life and crack growth rate for both horizontal (643600 cycles) and vertical samples (629068 cycles), but the samples built in 45^0 showed 1.49 times and 1.46 times longer fatigue crack growth life with slower crack growth rates than vertically and horizontally built samples respectively (**Fig. 52*A-B***) [207].

In order to properly understand the effect of the built orientation on the fatigue performance of SLM-Ti-6Al-4V parts, **Fig. 53** is reproduced based on the data found in the literature for different load ratios. **Fig. 53** shows that there is no certainty as to how the orientation of the built parts has an impact on the fatigue performance of the SLM-Ti-6Al-4V parts. Therefore, in order to make the figure more comprehensible, **Fig. 53** is separated into three different figures, each of which represents one of three different load ratios.

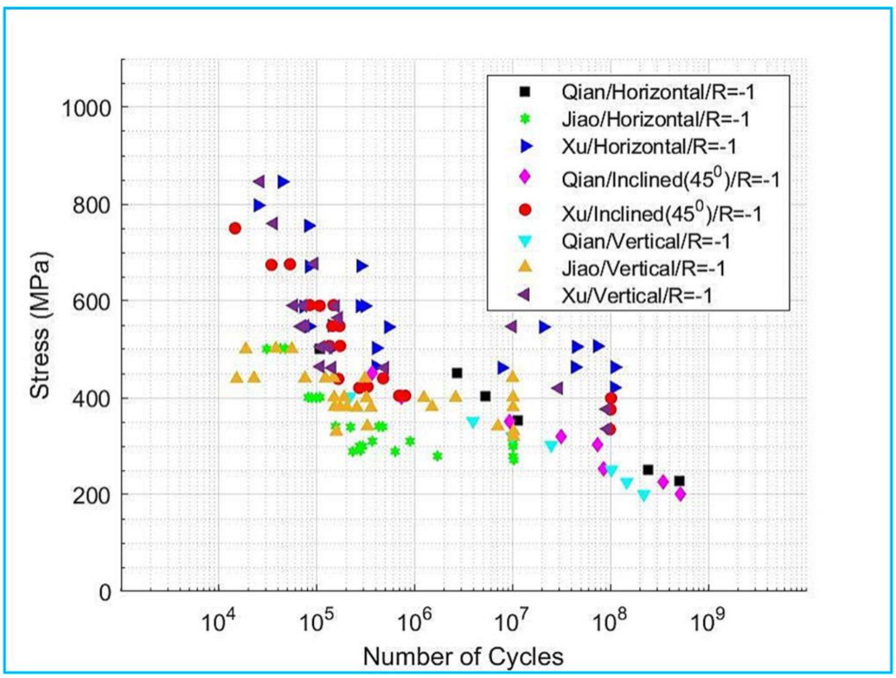

Fig. 54. *S-N curve showing the effect of building orientation on the fatigue performance of SLM-Ti-6Al4V parts at R=-1 based on the data in the literature. The data points are collected from Qian et al.[72],Jiao et al.[14], and Xu et al.[70,71].*

In **Fig. 54**, data points for the load ratio=-1 are plotted, and there is no doubt that horizontal samples show superior fatigue performance than vertical samples at a load ratio of -1 if the data sets of Jiao et al.[14] are not taken into consideration. **Fig. 55** illustrates the data points for the load ratio=0.1, and it can be seen that vertical samples exhibit superior fatigue performance than horizontal samples when a load ratio of 0.1 is used.

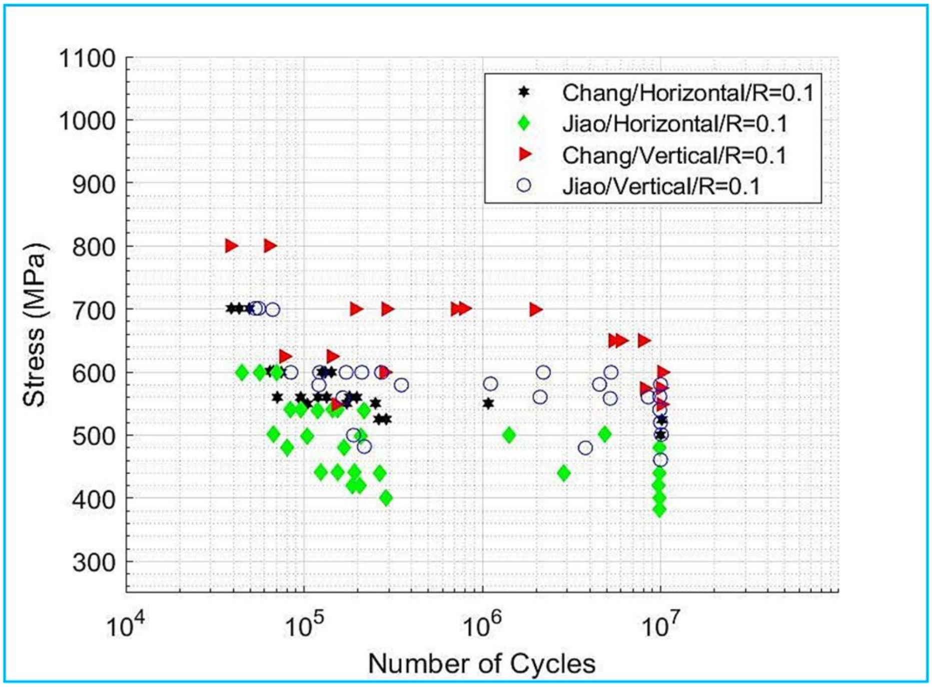

Fig. 55. *S-N curve showing the effect of building orientation on the fatigue performance of SLM-Ti-6Al4V parts at R=0.1 based on the data in the literature. The data points are collected from Chang et al.[3], and Jiao et al.[14].*

In **Fig. 56**, data points for the load ratio=0.5 are plotted, and it is clear that for load ratio=0.5, vertical samples show higher fatigue performance compared to horizontal samples.

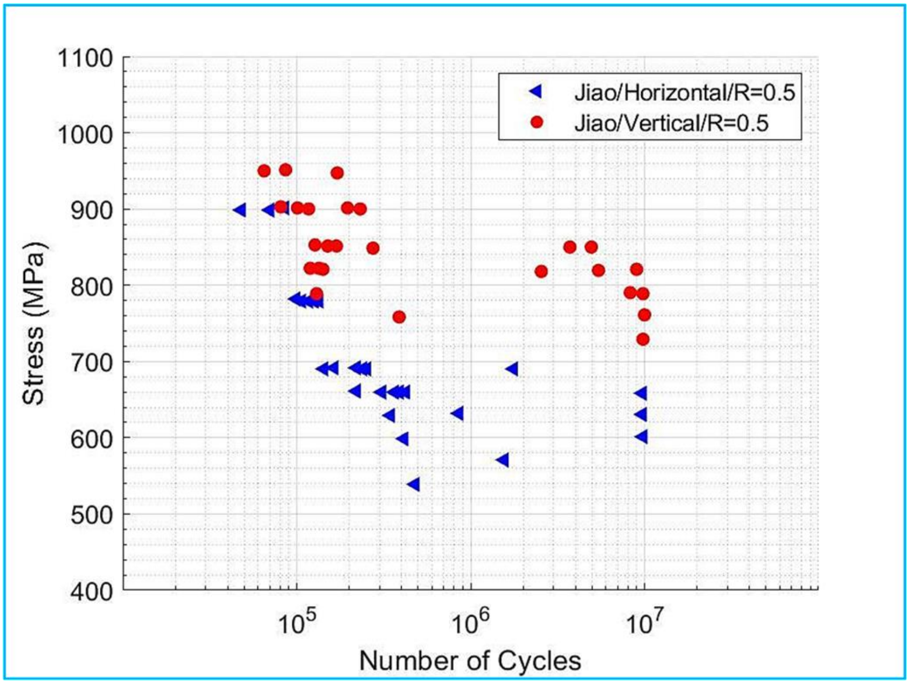

Fig. 56. *S-N curve showing the effect of building orientation on the fatigue performance of SLM-Ti-6Al4V parts at R=0.5 based on the data reported by Jiao et al.[14].*

Based on the fatigue data, it can be cautiously stated that the effect of building orientation on fatigue performance depends on the load ratio. The following recommendation is, therefore, to take into account the load ratio when considering the impact of the built orientation on fatigue performance. However, further research works should be carried out for a proper understanding of the impact of build orientation on the fatigue performance of SLM-Ti-6Al-4V parts.

2.4.7 Influences of specimen geometry on fatigue properties

There has been limited research works to study the effect of specimen geometries on the HCF and VHCF performance of SLM-T-6Al-4V parts. However, specimen geometries are considered to have a significant effect on the performance of HCF and VHCF performance. Pegues et al.[210] investigated the impact of the surface area size of the gage section on the HCF performance. The authors used three different types of specimens with different surface areas keeping the control volume constant (**Fig. 57**). The results of this study demonstrate that for a given volume of SLM-Ti-6Al-4V parts, increasing the surface area at the gage section results in a reduction in the fatigue life of those parts due to multiple cracks that are induced within close proximity to one another (**Fig. 58**) [210]. Li et al.[127] also suggested that increasing the surface area at the gage section of parts made of SLM-Ti-6Al-4V for a given volume will result in a reduction in their fatigue life as a result of larger defects (**Fig. 59**). In another study, Pegues et al.[211] investigated the effect of control volume on the HCF performance. For this study, the authors kept the surface area constant while the control volume was changed (**Fig. 60**). It was found that the samples with lower gage volumes showed improved fatigue life than the samples with higher gage volumes due to the crack initiation shifts from the surface crack initiation to the internal crack initiation at sub-surface defects (**Fig. 61**) [211].

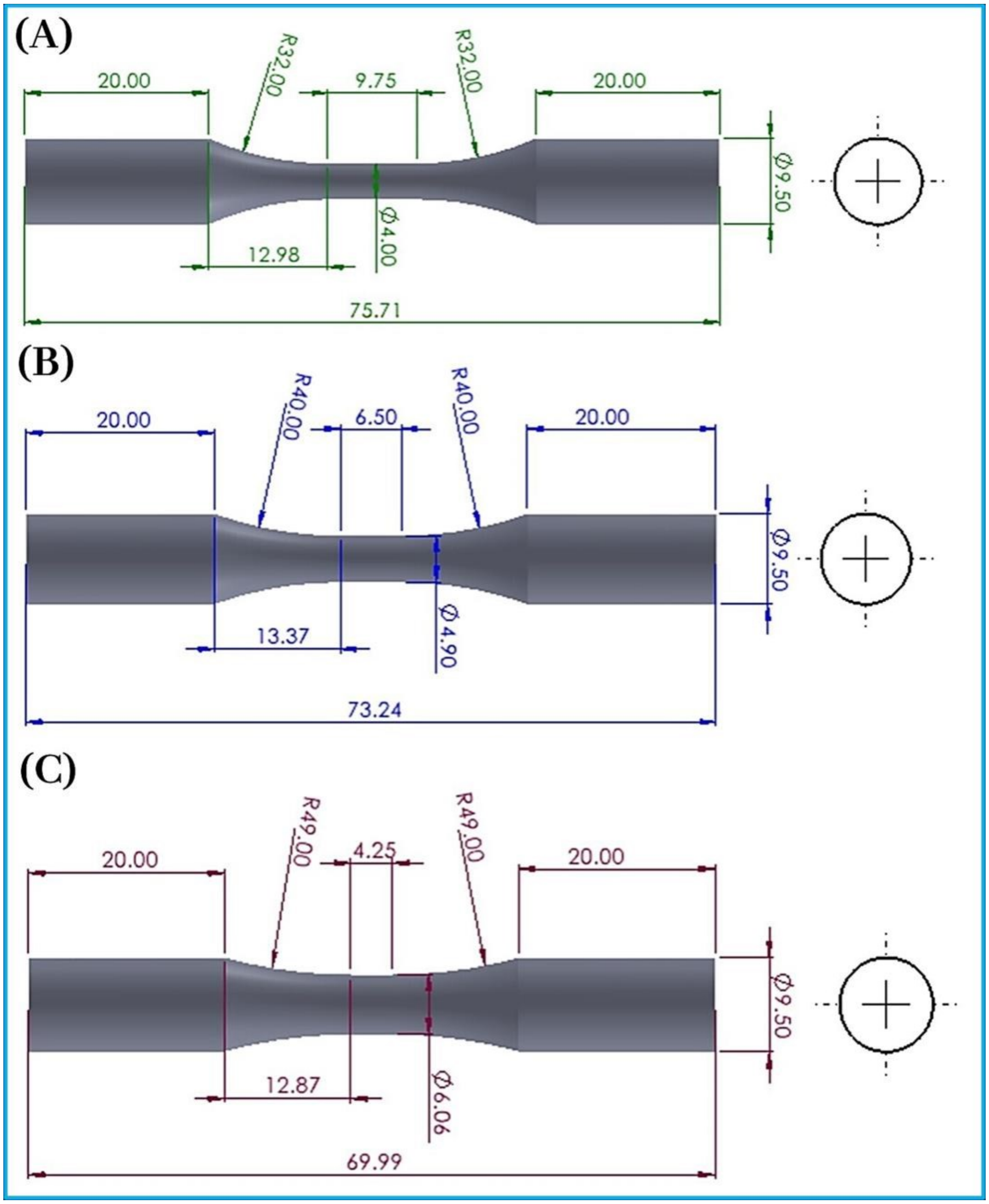

Fig. 57. *shows (A) Specimen geometries showing the control volume and surface area of 123 mm^3 and 126mm^2 (B) Specimen geometries showing the control volume and surface area of 123 mm^3 and 100mm^2 (C) Specimen geometries showing the control volume and surface area of 123 mm^3 and 81mm^2. Redrawn from the data reported by Pegues et al. [210].*

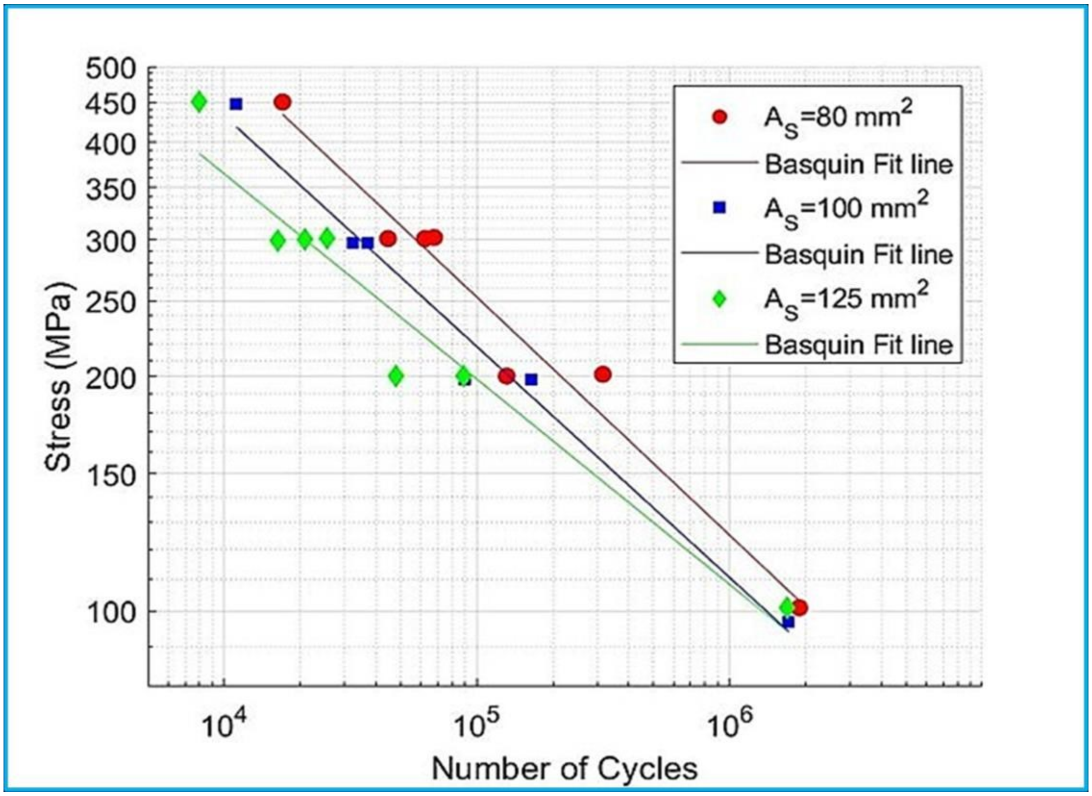

Fig. 58. *Reproduced S-N curve of SLM-Ti-6Al-4V parts showing the effect of surface area on fatigue performance based on the data points reported by Pegues et al.[210].*

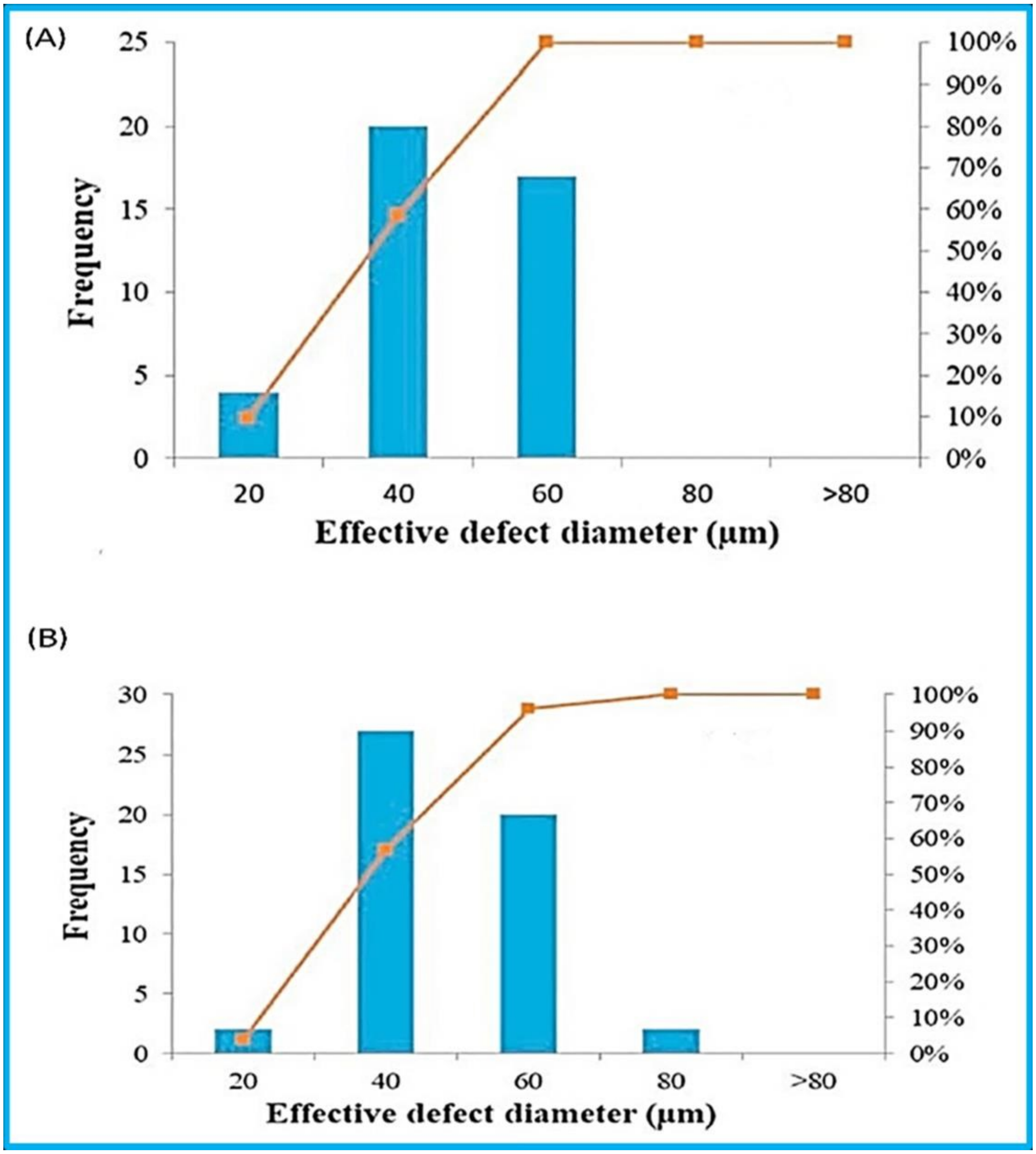

Fig. 59. *shows (A) The histogram for the effective defect diameter for the sample with a gage area of 81 mm^2 (B) The histogram for the effective defect diameter of the sample with a gage area of 123 mm^2. Adapted from Li et al.*[127] *with permission from Elsevier.*

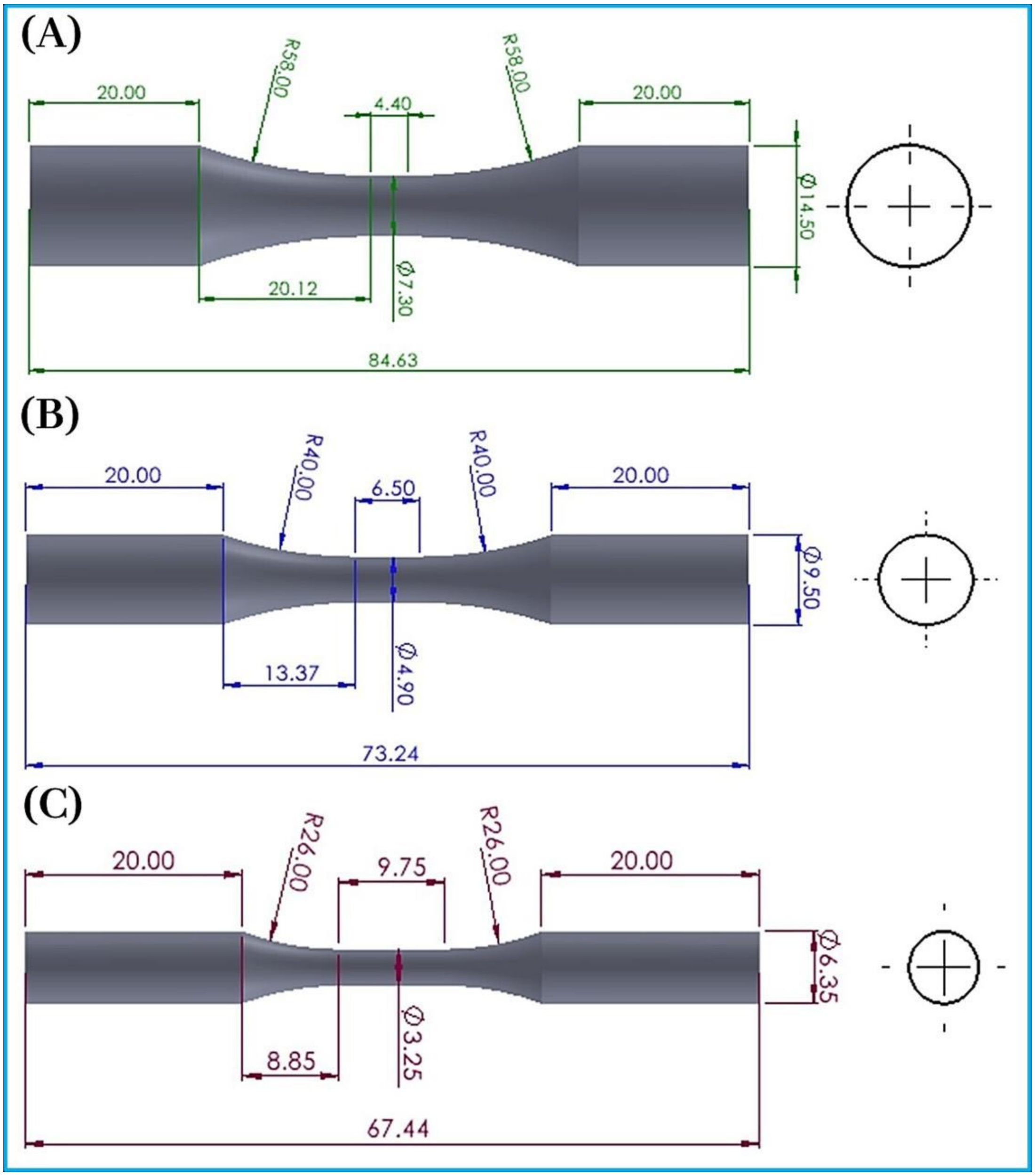

Fig. 60. *shows (A) Specimen geometries with a control volume of 184 mm^3, (B) Specimen geometries with a control volume of 123 mm^3, and (C) Specimen geometries with a control volume of 81 mm^3. Redrawn from the data reported by Pegues et al. [211].*

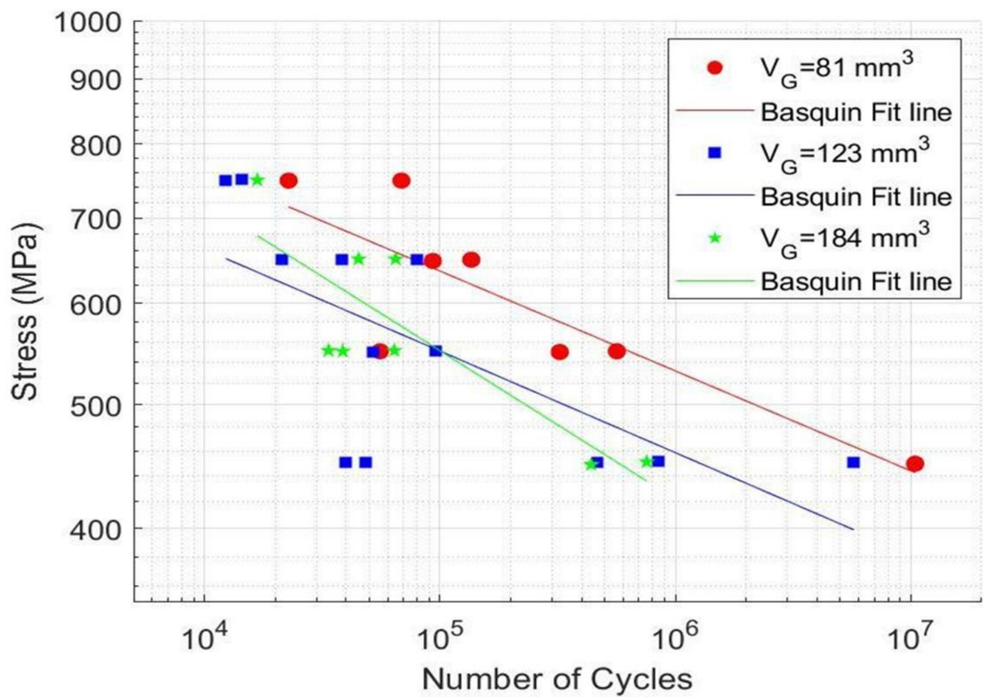

Fig. 61. *Reproduced S-N curve showing the effect of control volume on fatigue performance of SLM-Ti-6Al-4V parts based on the data points reported by Pegues et al. [211].*

In a more extensive research completed by Pegues et al.[202] demonstrated the relationship between the gage diameter and the HCF behavior. The authors used five sets of specimens to complete the assessments where three sets were designed with decreasing gage diameter, and the remaining two sets were designed keeping the gage diameter constant. However, for all the sets of specimens, the surface area at the gage section was increased by 25% (**Fig. 62**). The authors came to the conclusion that fatigue behavior is more sensitive to the part gage diameter than the surface area. It was found that the samples with smaller gage diameters show decreased fatigue life than the samples with higher gage diameters due to the crack initiation shifts from the surface crack initiation to the internal crack initiation at sub-surface defects (**Fig. 63**) [202].

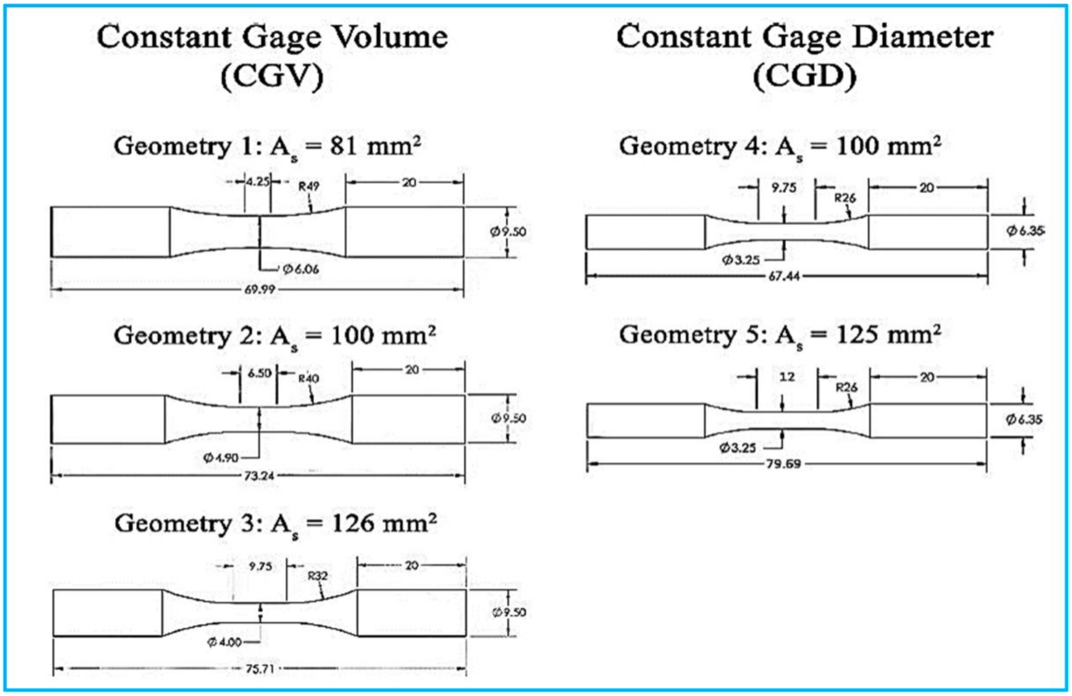

Fig. 62. *Dimensions of geometry with constant volume and constant gage diameter. Adapted from Pegues et al.[202] with permission from Elsevier.*

The results of this study demonstrate that decreasing the gage diameter results in a reduction in the fatigue life of those parts. It can be explained by the fact that there are multiple cracks in close proximity to each other, which allows early crack coalescence to occur, ultimately leading to the deterioration of crack growth stability [202]. In addition, a specimen with the gage diameter of 4.90 mm or less shows higher surface roughness on the down-skin surface resulting in shorter fatigue life, whereas the gage diameter larger than 4.90 mm lowers the down-skin surface roughness which gives improved fatigue life [202]. Moreover, the difference between the load bearing and nominal stress amplitudes increases as the part diameter is decreased, which gives significant scatter in the HCF data [202].

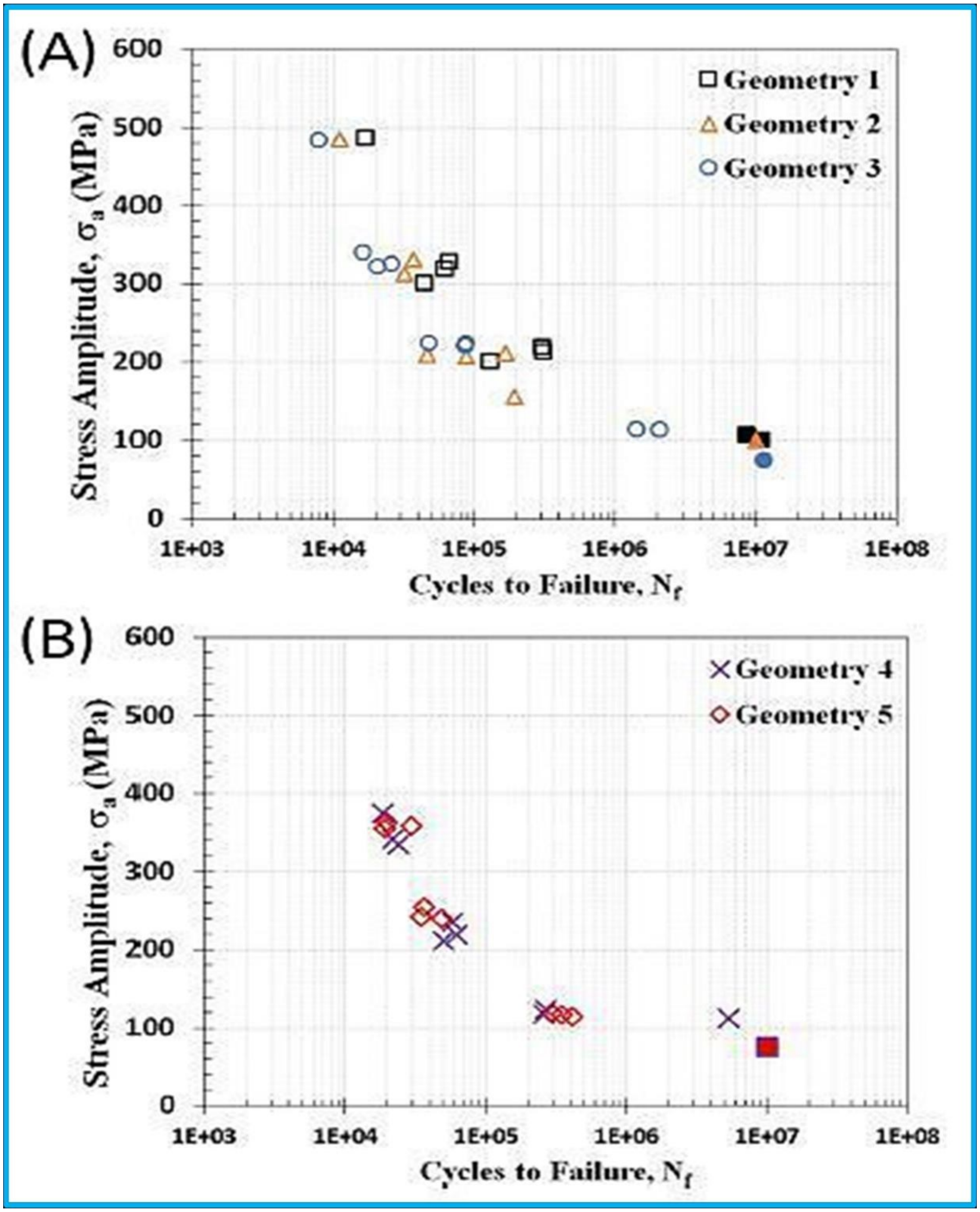

Fig. 63. *shows (A) S-N data points for different specimen sizes with constant gage volume and (B) S-N data points for different specimen sizes with constant gage diameter. Adapted from Pegues et al.[202] with permission from Elsevier.*

Additionally, the larger gage diameter increases the solidified part volume beneath the layer edge resulting in efficient heat dissipation, which is one of the significant factors contributing to the improvement of the fatigue life of specimens with the gage diameter larger than 4.90mm [202].

2.4.8 Influences of parts mechanical strength and ductility on fatigue properties

Ductility does not have a significant role in fatigue performance in the HCF region [159]. However, the combination of improved ductility and a reduction in RS can slightly increase a number of cycles [159,186]. Leuders et al.[159,186] extensively investigated the role of ductility on the fatigue life of SLM-Ti-6Al-4V parts. The authors used different post-processing treatments to confirm the effect of ductility on fatigue performance. According to the authors, HIPed specimens treated at 920^0 C gives fine structure and high monotonic strength, whereas HIPed specimens treated at 1050^0C give coarse microstructure with reduced UTS, ductility, and ductile β-phase that plays a significant role in the crack initiation. Ti-6Al-4V parts treated at 1050^0 C shows lower ductility and lower strength, which promotes local plastic deformation that accumulates the fatigue damage under cycling loading and increases the notch sensitivity significantly, resulting in lower fatigue life (***Fig. 64***) [159,186]. Therefore, it can be concluded that if the critical factors like RS, microstructure, and porosity are taken into consideration, then it can be regarded that improved ductility plays a role in fatigue life improvements of SLM-Ti-6Al-4V parts [159,186].

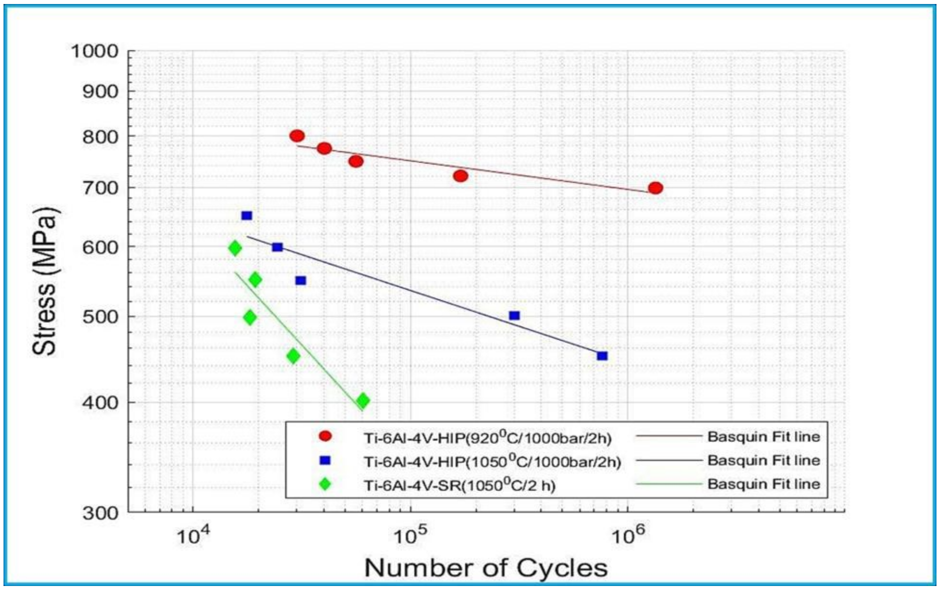

Fig. 64. *Reproduced S-N curve of SLM-Ti-6Al-4V parts under different post-treatments based on the data points reported by Leuders et al.[186].*

Frkan et al.[75] also suspected that improved ductility helps to increase the fatigue performance of SLM-Ti-6Al-4V parts. It is also believed that a higher degree of ductility can lead to a decrease in fatigue crack growth [212]. Zhang et al.[151] reported that an increase in yield strength contributes to the fatigue performance increase of SLM-Ti-6Al-4V parts.

2.4.9 Influences of load ratio/mean stress and frequency along with loading type on fatigue properties

Pan and Hong [135] extensively investigated the effect of mean stresses and load ratios on the HCF and VHCF performances of Ti-6Al-4V parts. When the mean stress, $\sigma_m = 0$, i.e., R= -1, was used, the authors found the alternating stress, σ_a, in the range between 400 and 550 MPa both in HCF and VHCF regimes [135]. In the VHCF regime, after increasing the σ_m between 166 and 312 MPa, it was found that the fatigue resistance exhibited a high scattering in the range between 203 and 375 MPa [135]. Additionally, it was shown that when the value of σ_m increases to 468 MPa (R=0.5), 728 MPa (R=0.7), and 832 MPa (R=0.8), the fatigue resistance decreased to about 176, 140, and 111 MPa respectively [135]. In light of the above discussion, it seems that the fatigue resistance of SLM-Ti-6Al-4V parts decreases with increasing load ratios and mean stresses (

Fig. 65).

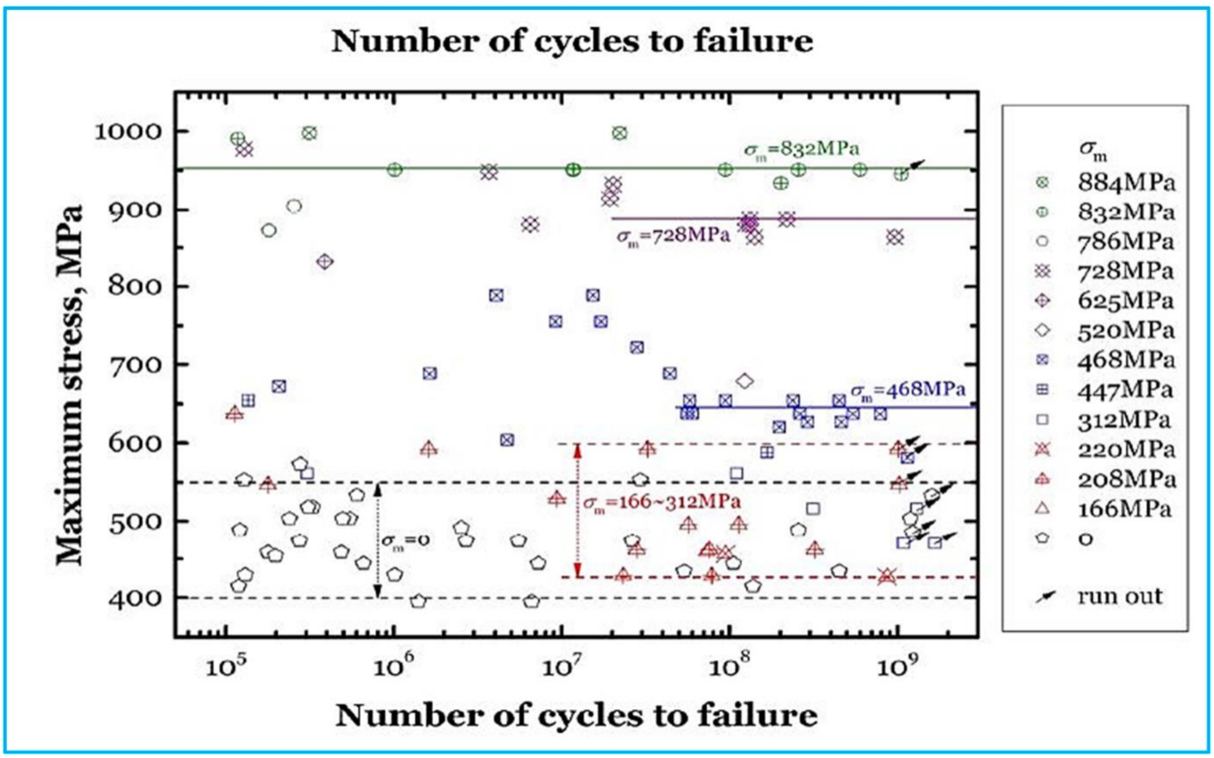

Fig. 65. *S-N data of Ti-6Al-4V parts under different values of mean stresses, σ_m. Adapted from Hong and Pan[135] with permission from John Wiley and Sons.*

Wycisk et al.[165] investigated the effect of the load ratio and test frequency on the HCF and VHCF performances. The authors found a higher fatigue strength (σ_{max}=680±35 MPa) for the specimens tested under the tension-tension loading (load ratio=0.1) whereas the specimens tested under the tension-compression loading (load ratio=-1) showed the maximum fatigue life of 575 MPa at a number of cycles 10^7(**Fig. 66**) [165]. As compared to the tension–tension loading, crack initiation under the tension–compression has less influence on fatigue life [165]. In addition, the authors demonstrated that the crack initiation point shifts from the surface crack initiation to internal crack initiation after 10^7 cycles for R=-1 and 10^6 cycles for R=0.1. However, the authors did not find any significant impact of test frequency on the fatigue life of SLM-Ti-6al-4V parts (**Fig. 67***A-B*) [165].

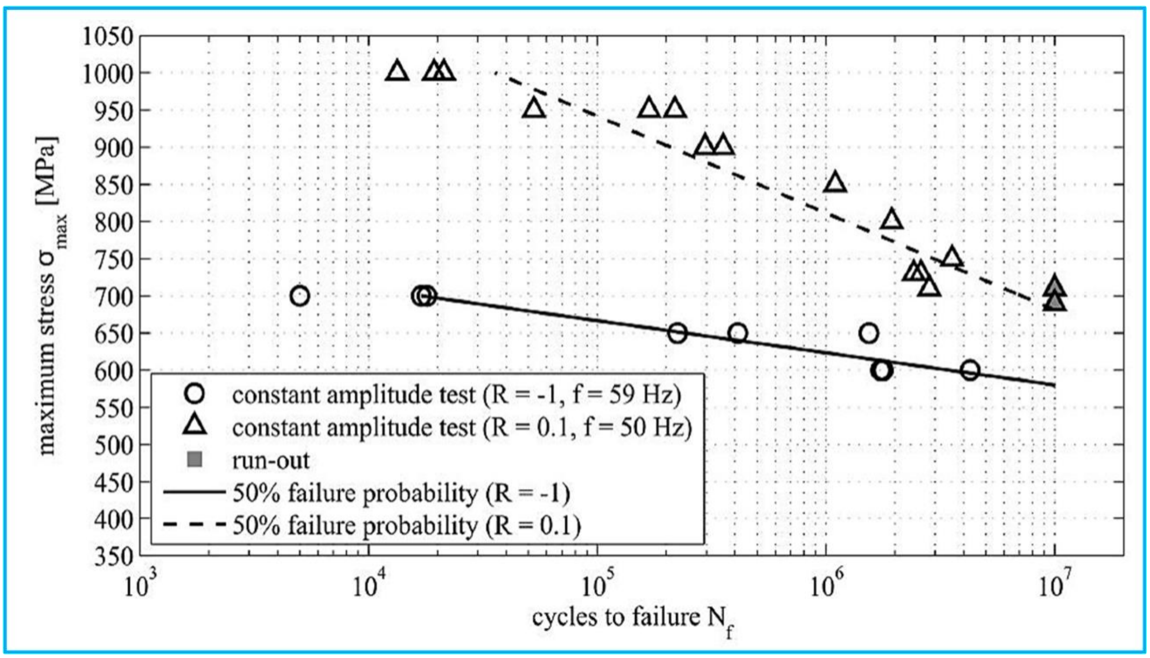

Fig. 66. *S-N curve of HIPed Ti-6Al-4V specimens showing the effect of load ratio [165].*

Du et al.[119], Bhandari and Gaur[76] also confirmed that fatigue lives of SLM-Ti-6Al-4V parts decrease with increasing load ratios or the mean stresses (**Fig. 68** and **Fig. 69**).

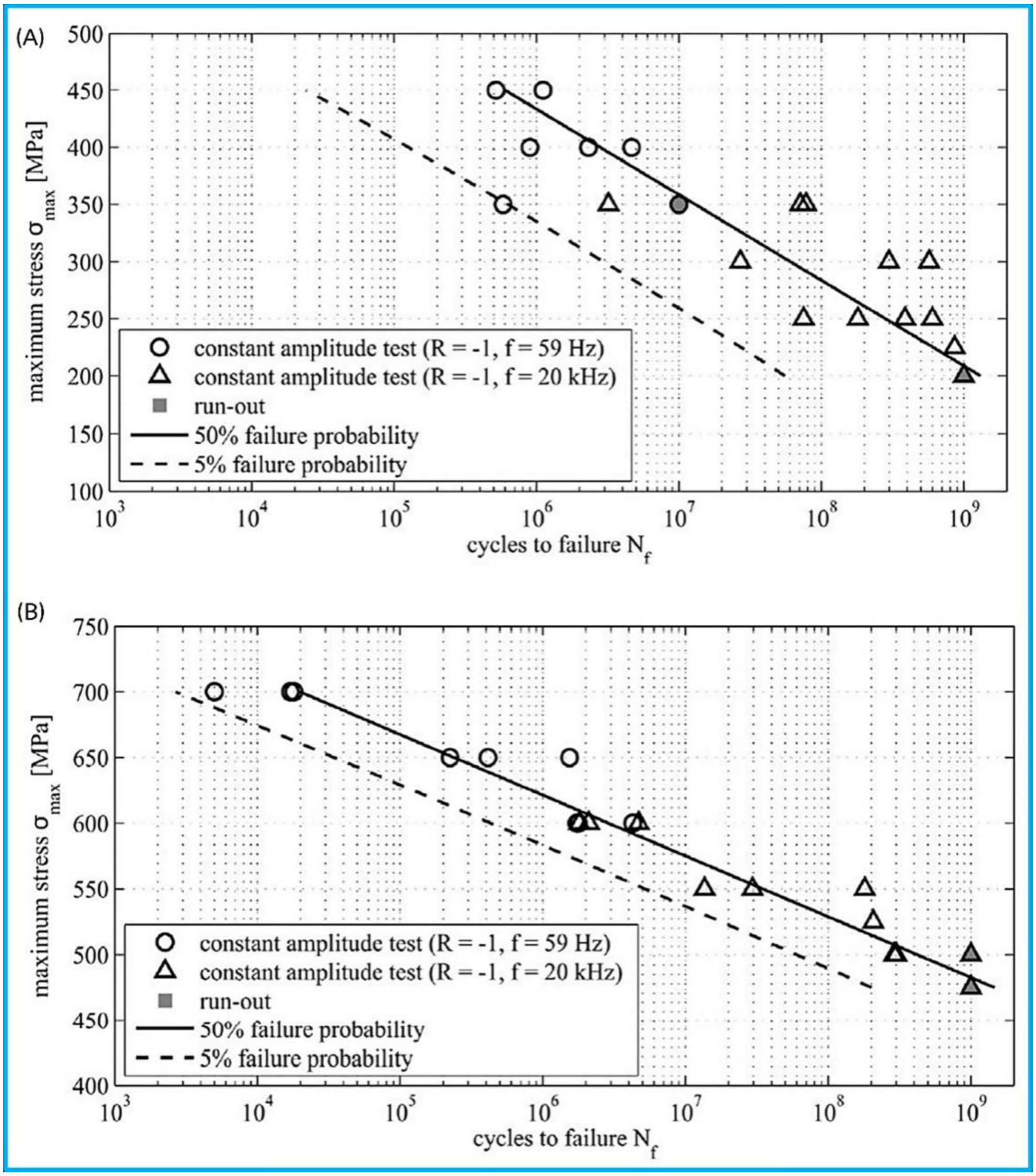

Fig. 67. *shows (A) The effect of test frequency on the VHCF performance under tension-tension loading at Stress-relieved condition and (B) The effect of test frequency on the VHCF performance under tension-tension loading at HIPed condition [165].*

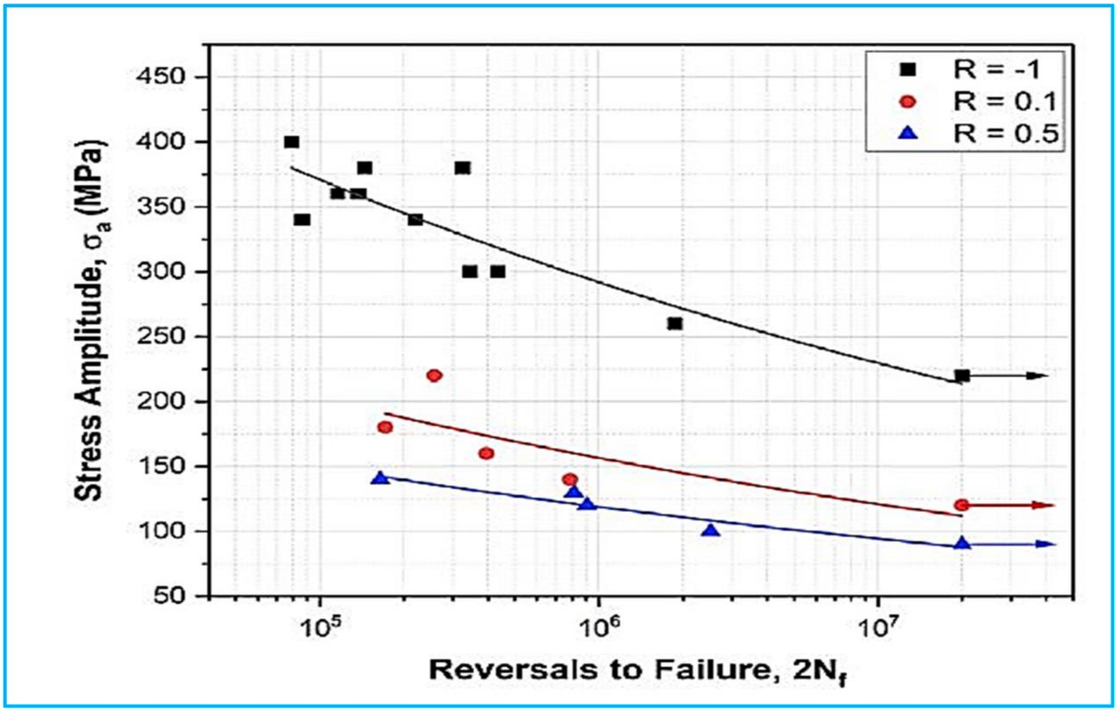

Fig. 68. *Effect of load ratios on fatigue performance in heat-treated material condition. Adapted from Bhandari and Gaur[76] with permission from Elsevier.*

Chengqi Sun et al.[144] demonstrated the effect of loading types on the VHCF behavior of SLM-Ti-6Al-4V parts. The authors found the surface crack initiation under the rotating bending test, while ultrasonic fatigue tests gave the interior crack initiation in the VHCF region. In addition, ultrasonic fatigue tests show higher fatigue performance compared to rotating bending fatigue tests, which is also important to note (**Fig. 70**) [144].

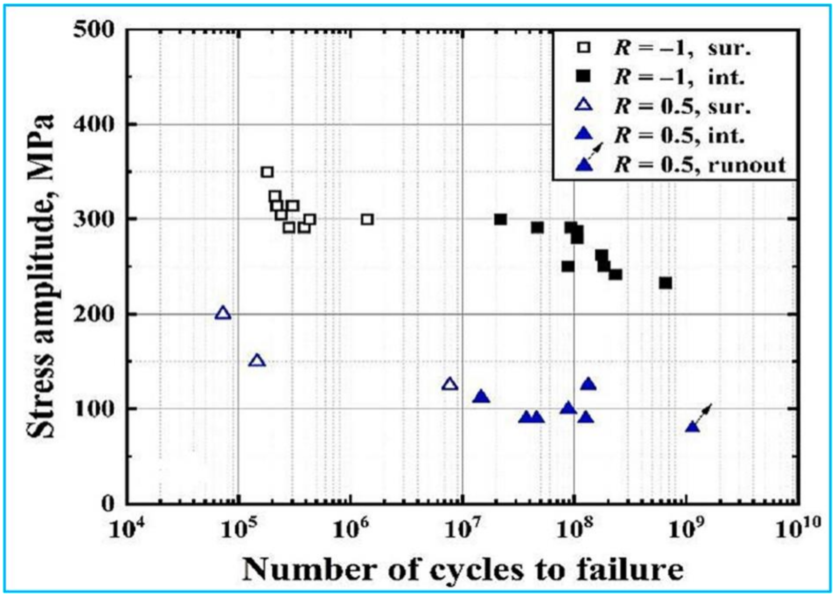

Fig. 69. *Effect of load ratio on fatigue performance of SLM-Ti-6Al-4V parts. Adapted from Du et al.[119] with permission from Elsevier.*

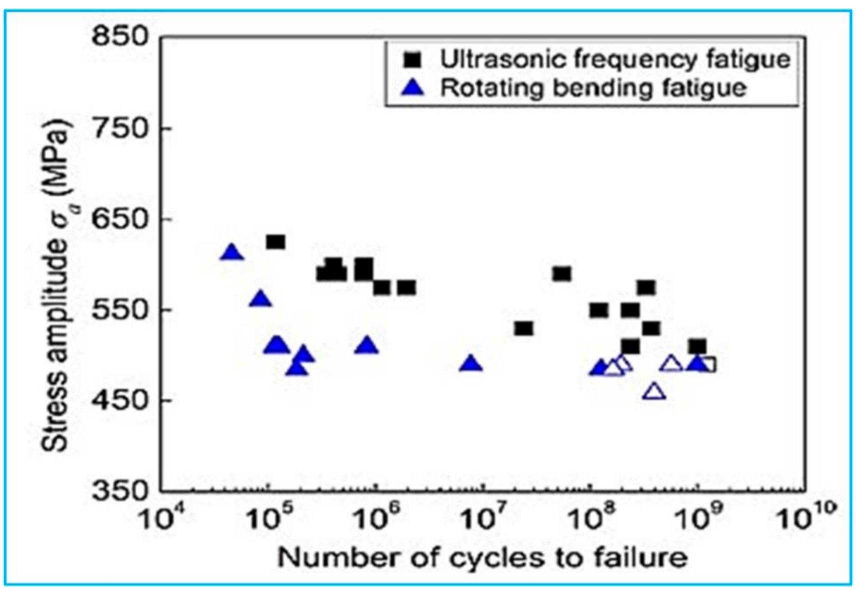

Fig. 70. *Comparison of S-N data under different loading types. Adapted from Sun et al.[144] with permission from Elsevier.*

The stress ratio does not have a significant impact on the crack initiation pattern in the HCF region, while for VHCF, the stress ratio significantly impacts the defect types [119].

It has been reported that the size of the irregularly shaped fusion defects with facets found in the VHCF regime is significantly larger than that of the regularly shaped LOF defects at R=0.5, but the irregularly shaped fusion defects without facets are smaller than the size of the regular shaped ones [119]. The size of defects with regular shapes on the fracture surface that do not contribute to crack initiation at R = 0.5 has been suggested to be very similar to that of defects that will be found at R = -1 contributing to crack initiation [119]. So, from the above discussion, it can be confirmed that the crack initiation mechanism may be altered by different stress ratios (mean stress), which will ultimately affect the HCF and/or VHCF performances.

2.4.10 Influences of fabrication process on fatigue properties

Du et al.[120] and Carrion et al.[118] investigated the impact of the fabrication process on the fatigue performance of SLM-Ti-6Al-4V parts. Du et al.[120] mentioned that fatigue strength is very sensitive to the variation of energy density. In **Fig. 71**, the correlation between energy density and stress amplitude is presented for two different fatigue strengths that are marked σ_{w_7} and σ_{w_8} in the figure where σ_{w_7} and σ_{w_8} corresponds to fatigue strength at 10^7 and 10^8 cycles. It has been observed that fatigue strength increases with increasing energy density though the fatigue strength decreases significantly when the energy density goes up further from 76.2 j/mm^3 to 83.3 j/mm^3 [120].

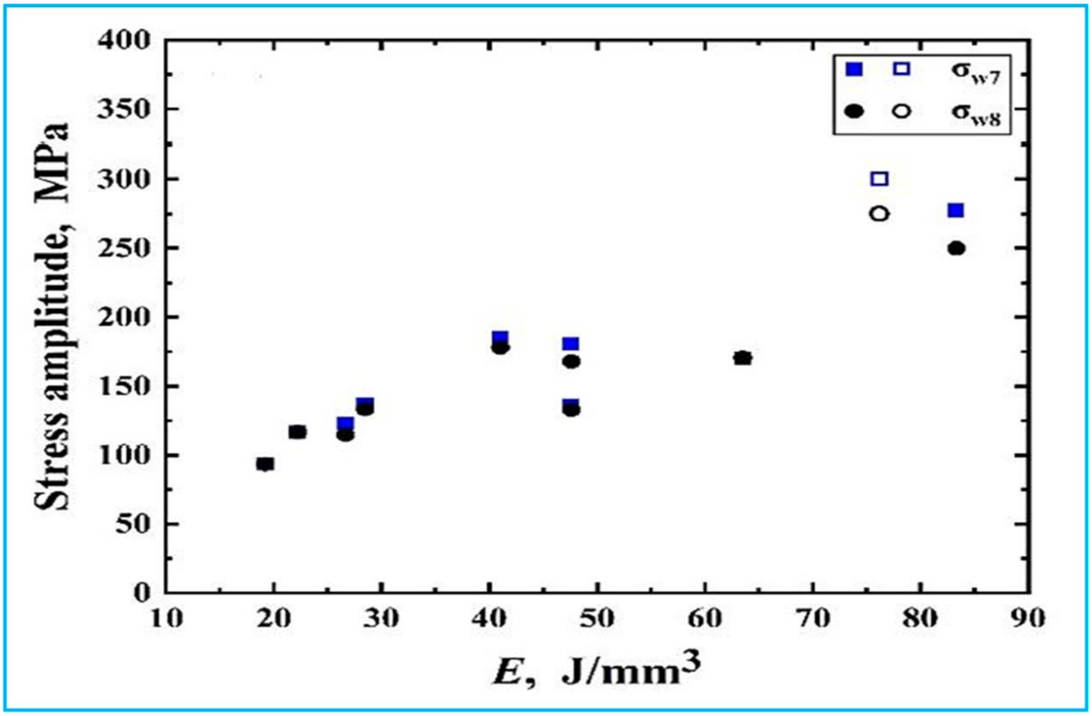

Fig. 71. *Effect of Energy density on stress amplitude.* σ_{w7} *and* σ_{w8} *correspond to the fatigue strength at cycles* 10^7 *and* 10^8*, respectively. Adapted from Du et al.[120] with permission from John Wiley and Sons.*

Carrion et al.[118] investigated the effects of powder recycling on the HCF performance of SLM-Ti-6Al-4V parts. There is evidence from the study that the used powder may yield smaller internal pores because it is more flowable and less compressible than the new powder. The recycling powder had a minimal impact on the microstructure and fatigue performance of the AB Ti-6Al-4V specimens. This is attributed to the fact that both specimen sets manufactured from new and used powder had similar grain sizes and shapes. However, the samples fabricated from the used powder, when presented in the machined surface condition, exhibited longer HCF lives when compared with the samples fabricated from the new powder (**Fig. 72***A-B)*. This is because the samples fabricated from used powder had smaller effective defect sizes.

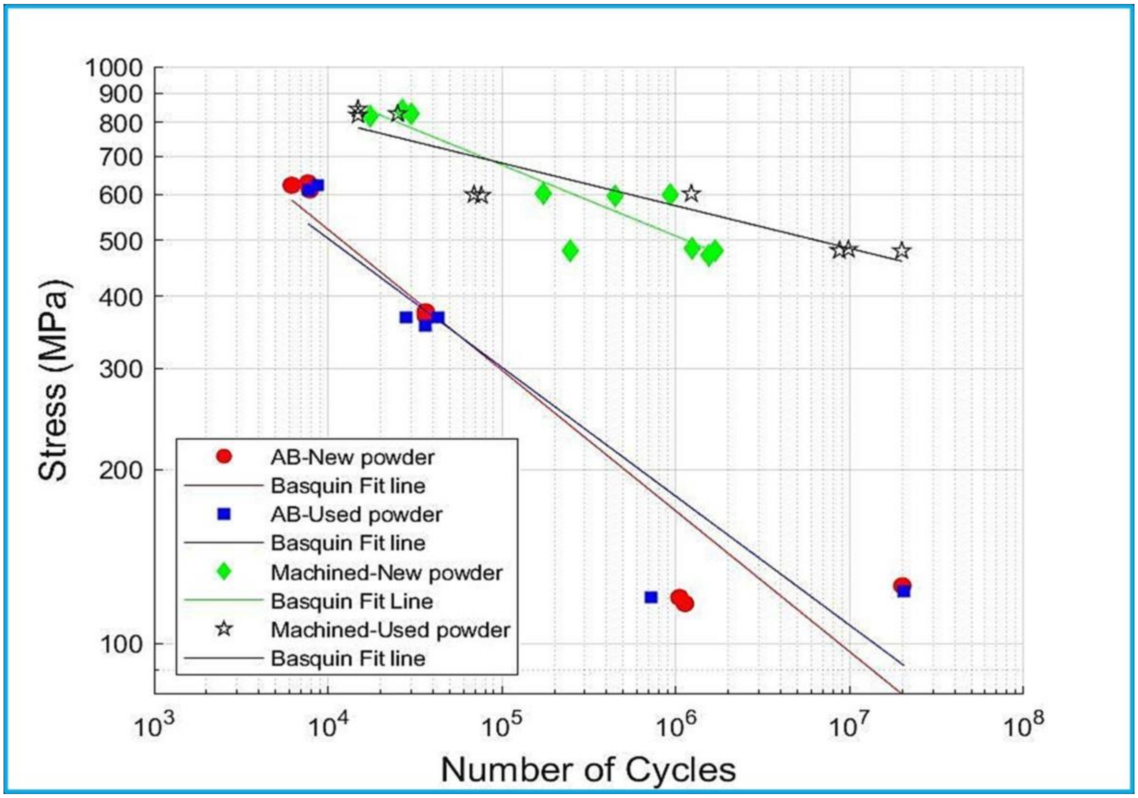

Fig. 72. *Reproduced S-N curve showing the effect of powder recycling on the fatigue performance of AB and machined samples based on the data reported by Carrion et al. [118].*

2.4.11 Influences of corrosion properties on fatigue performance

There have been limited research studies conducted on the effect of corrosion properties on the fatigue performance of SLM-Ti-6Al-4V parts. Wegner et al.[7] investigated the impact of corrosion on fatigue properties of SLM-Ti-6A-4V parts by using the corrosion fatigue test. For the constant amplitude test (CAT), the samples were prepared by a special procedure schematically illustrated in **Fig. 73**.

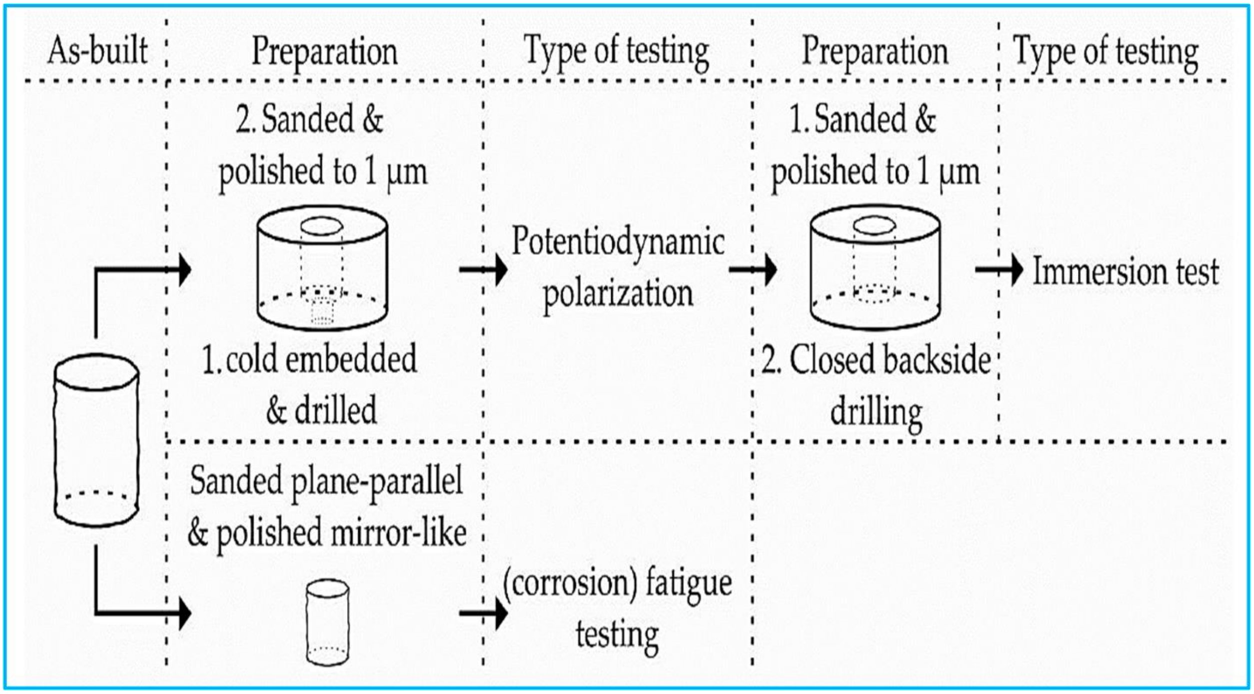

Fig. *73. Overview of the corrosion fatigue sample preparation [7].*

After preparing the samples, an in vitro corrosion cell was developed to enable a medial superposition by simulated body fluid (SBF) at 37^{0}C to perform the CAT (**Fig. 74**) [7]. It is seen that corrosion properties have a significant impact on fatigue properties. There is a drastic decrease in fatigue strength so that the trend S-N curve is bent as a result of locally intensified corrosion caused by process-induced surface roughness, which acts as multiple crack initiation sites due to corrosion (**Fig. 75**) [7].

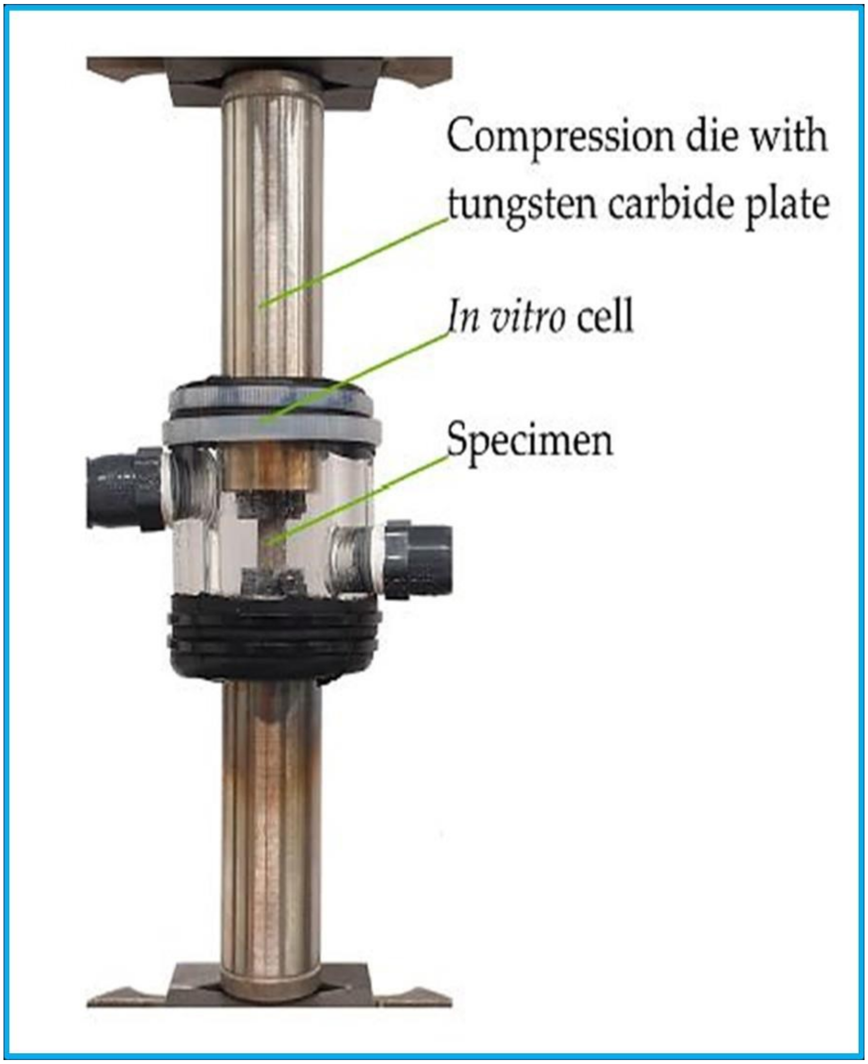

Fig. 74. *Experimental setup for corrosion fatigue test [7].*

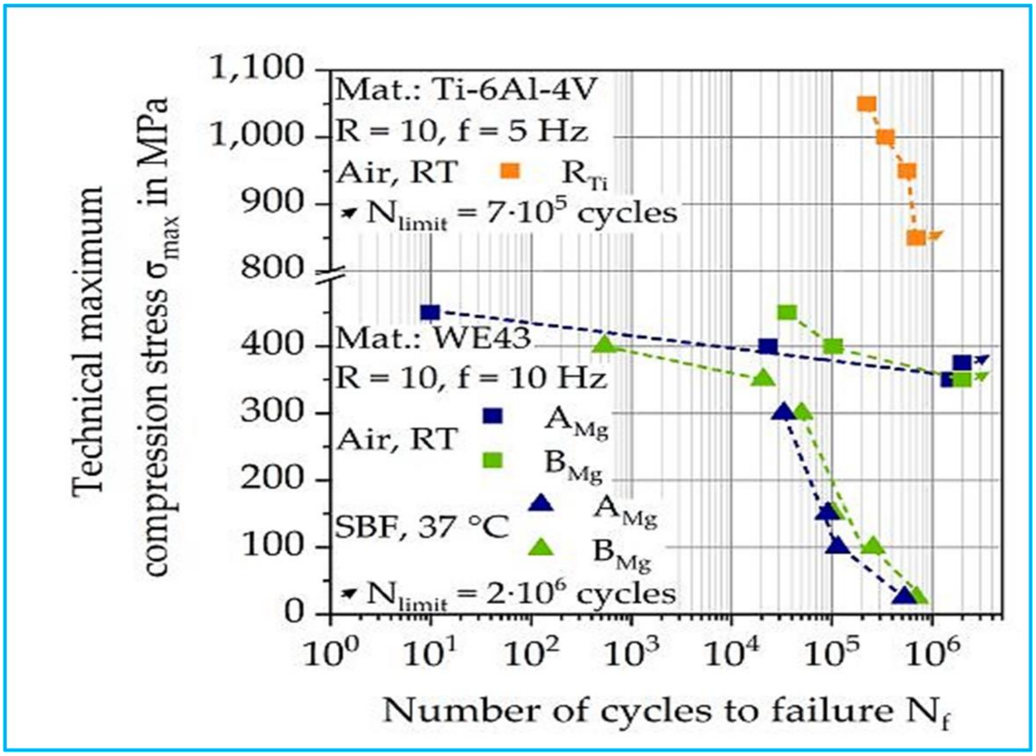

Fig. 75. *Trend S-N curves for two batches of Mg alloy WE43 in comparison to the batch of Ti-6Al-4V at RT and in SBF at 37 °C [7].*

In order to further understand how the fatigue performance of the Ti-6Al-4V parts are affected by a number of critical factors, it would be helpful to tabulate some fatigue data depending on a number of primary parameters. **Table *5*** presents the results of some studies that have been carried out on the fatigue and fracture toughness of parts manufactured by SLM based on some critical parameters. There is an opportunity for readers to better understand the impact of those factors on the fatigue performance of Ti-6Al-4V alloy.

Table 5. Fatigue and fracture toughness of Ti-6Al-4V parts manufactured by SLM based on some critical parameters.

Alloy	Machine	Type of tests	Process Parameters								Post Treatment		Fatigue strength/ no. of cycles	Fracture toughness, MPa$\sqrt{m}$	Load Ratio	Frequency (Hz)	Specimen geometry	Risk volume[a] (mm^3)	Refs.
			Laser Power (W)	Scan speed (mm/s)	Layer thickness (mm)	Hatch distance (mm)	Build orientation	Energy density, j/mm^3	Shielding gas	Platform temperature	Post Heat/HIP Treatment	Post Surface Treatment							
SLM-Ti-6Al-4V	SLM 250 HL	Axial Fatigue, Fracture toughness	400		0.03		Horizontal		Argon, Vacuum	100^0C	Annealed at 800^0C, 1050^0C, HIP at 920^0C and 1000 bar	AB+ Machined	2.7×10^4 cycles at 600 MPa	1.4	0.1	40	Flat		Leuders et al.[159]
												AB+ Machined+ HT-1050	2.9×10^5 cycles at 600 MPa	3.9 ± 0.4					
												AB+ Machined+ HIP	2×10^6 cycles at 600 MPa	4					
							Vertical					AB+ Machined	2.7×10^4 cycles at 600 MPa	1.7					
												AB+ Machined + HT-800	9.3×10^4 cycles at 600 MPa	3.7					
												AB+ Machined + HT-1050	2.9×10^5 cycles at 600 MPa	6.1					
SLM-Ti-6Al-4V	SLM 250 HL	Fracture toughness	400		0.03		Vertical		Argon	200^0C	HT-800^0C, HT-1050^0C and HIP-920^0C	AB+ Machined	---	1.42	0.1	100	Flat		Leuders et al.[213]
												AB+ Machined+ HT-800^0C		3.93					
												AB+ Machined + HT-1050^0C		3.62					
												AB+ Machined+ HIP-920^0C		4.20					
												AB, Machined	2×10^6 cycles at 325 MPa	3.06	-1				
												AB+ Machined+ HT-800^0C	2×10^6 cycles at 325 MPa	8.46					
												AB+ Machined + HT-1050^0C	2×10^6 cycles at 225 MPa	7.79					
												AB+ Machined+ HIP-920^0C		9.04					
SLM-Ti-6Al-4V	EOS M270	Axial Fatigue								200^0 C	---	AB	10^7 cycles at 550 MPa	---	0.1	50	Dog bone		Rafi et al.[214]
SLM- Ti-6Al-4V	SLM 250 HL	Axial Fatigue, Fracture toughness	200		0.03		Vertical	45.33	Argon	180^0 C	650^0C for 3h	AB	10^7 cycles at 210 MPa		0.1	50	Hourglass	13.93	

												AB + Machined + HT-650	10^{7} cycles at 500 MPa	3.48					Wycisk et al.[215]
SLM- Ti-6Al-4V	SLM 250 HL	Axial Fatigue, Ultrasonic fatigue testing	175	710	0.03		Vertical		Argon	200^{0}C	800^{0}C for 2hrs, HIP at 920^{0}C and 1000 bar	AB+ Polished+ HT	10^{6} cycles at 400 MPa	---	-1	10	Hourglass		Gunther et al.[40]
												AB+ Polished + HT	10^{9} cycles at 250 MPa			19000			
												AB+ Polished + HIP	10^{9} cycles at 400 MPa			19000			
SLM- Ti-6Al-4V	EOS M270xt	Ultrasonic fatigue testing	200		0.03		Vertical	45.33	Argon	180^{0}C	650^{0}C for 3hrs, HIP at 920^{0}C and 1000 bar	AB + Machined + HT	10^{9} cycles at 200 MPa		-1	20000	Hourglass		Wycisk et al.[165]
												AB + Machined + HIP	10^{9} cycles at 483 MPa						
SLM- Ti-6Al-4V	EOS M270xt	Axial fatigue	170	1250	0.03	0.1	Inclined (45^{0})	45.33	Argon	---	650 ^{0}C for 3 hrs	AB+HT	10^{7} cycles at 210 MPa	----	0.1	50	Hourglass	13.93	Wycisk et al.[201]
												AB + HT+ Polished	10^{7} cycles at 510 MPa						
												AB + HT+ Shot peened	10^{7} cycles at 435 MPa						
SLM- Ti-6Al-4V	Concept Laser M2	Axial Fatigue	110-200	850-1500	0.04				Argon	---	HT-700^{0}C for 1 hr and 900^{0}C for 2 hrs, HIP	AB	2.3×10^{3} to 5.6×10^{3} cycles at 600 MPa	---	-1	82	Dog bone	294.5	Kasperovich and Hausmann[32]
												AB + Machined	1.2×10^{4} to 2×10^{4} cycles at 600 MPa						
												AB + Machined+ HT	3×10^{4} cycles at 600 MPa						
												AB + Machined+ HIP	1.5×10^{5} to 3×10^{5} cycles at 600 MPa						
SLM- Ti-6Al-4V	Self-developed SLM system	Axial Fatigue	300	1000	0.04	0.12	Vertical	62.5	Argon	---	500 °C for 2 h, 920 °C for 2 h, 850 °C for 2 h, 550 °C for 4 h, HIP at 920^{0}C for 2 h and 100 MPa	AB	10^{6} cycles at 325 MPa	---	-1	20	Dog bone	712.75	Yu et al.[78]
												AB+HT-920	10^{7} cycles at 350 MPa						
												AB+HT-(850-550)	10^{7} cycles at 350 MPa						
												AB + HIP	10^{7} cycles at 460 MPa						
SLM- Ti-6Al-4V	EOS M290	Axial Fatigue	280	1200	0.03	0.05	Vertical	155.56		---	HIP at 900^{0}C and 120 MPa for 2hrs	AB	10^{7} cycles at 290 MPa	---	-1	130	Hourglass	12.1	Yan et al.[82]
												HIP	10^{7} cycles at 370 MPa						
												SMAT	10^{7} cycles at 580 MPa						
SLM- Ti-6Al-4V	ProX200	Rotating bending fatigue test		33.33	0.03		Vertical			---	---	AB+ UNSM-Fast rotation speed	$>10^{6}$ cycles at 150 MPa	---	-1	60	Hourglass		Zhang et al.[200]
												AB+ UNSM-Slow rotation speed	6.89×10^{5} cycles at 250 MPa						

SLM- Ti-6Al-4V	ProX DMP320	Axial fatigue			0.06		Vertical			---	Stress relieved at 850^0C, HIP at 9200 C and 1000 bar	AB	2×10^6 cycles at 120 MPa	---	-1	60	Hourglass		Cutolo et al.[77]
												AB+HT	2×10^6 cycles at 235 MPa						
												AB+HIP	2×10^5 cycles at 220 MPa						
SLM- Ti-6Al-4V	Renishaw AM400		400		0.06		Vertical			---	Stress relieved at 850^0C for 1hr	AB+ Polished+ HT	10^9 cycles at 180 ± 20MPa				Gaussian	~1749.13	Tridello et al.[146]

Note: [a] The risk volume is calculated manually from the dimensions of the samples mentioned in the literature where risk volumes were not found in the literature.

2.5 Fracture mechanism at HCF and VHCF regimes

Generally, surface-without-rough area (RA) crack initiation takes place in LCF and is not the predominant type of crack initiation in HCF and VHCF cracks [135]. Ti-6Al-4V samples manufactured by SLM and tested in HCF and VHCF regions show a definite difference in fracture mechanism. It is common to find surface cracks with RA in both HCF and VHCF regimes and interior cracks with RA in VHCF regimes [135]. It is important to note that if the failure occurs on the surface with RA or without RA, it is a surface crack-induced failure, and if it occurs on the interior with RA, it is an internal crack-induced failure [135]. There is evidence to indicate that the RA region is the distinct region for the crack initiation and early growth in titanium alloys with Bimodal microstructure (BM) that are prone to internal crack-induced VHCF [135]. RA region is also a typical fractographic feature for internal crack and surface crack-indued VHCF in titanium alloys with Equiaxed microstructure (EM) [135]. Du et al.[119] investigated the fracture mechanism of SLM-Ti-6Al-4V parts subjected to different load ratios (R=-1 and R=0.5). The authors found surface crack initiation in the HCF region (**Fig. 76**) whereas internal crack initiation was observed in the VHCF regime (**Fig. 77**) for both the stress ratios.

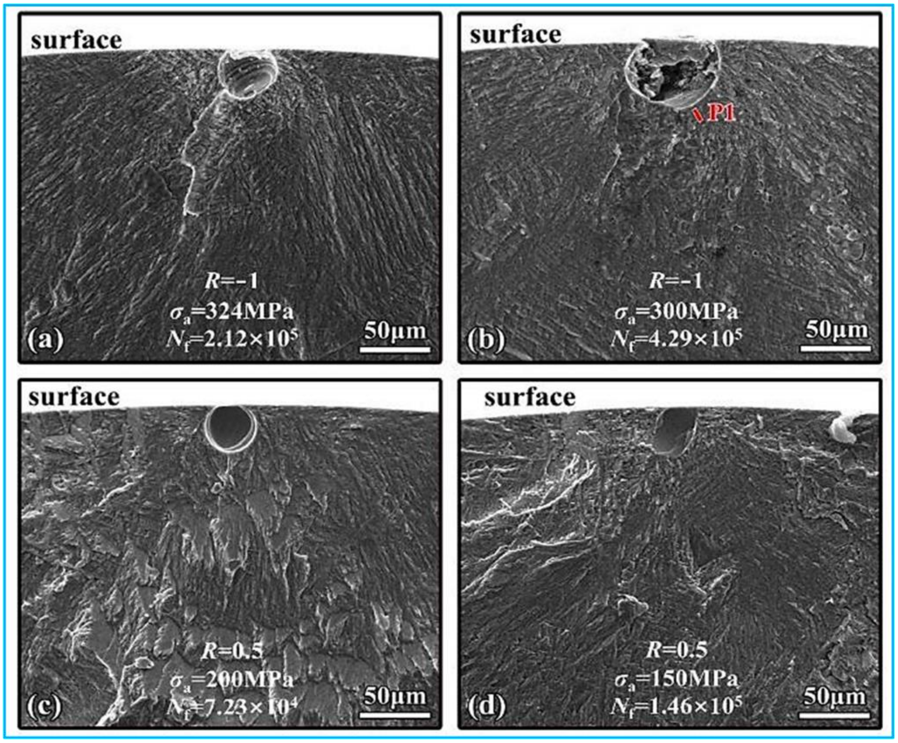

Fig. 76. *Fracture surface morphologies showing the surface crack initiation failed in LCF and HCF regimes, (A)R=-1,* σ_a *= 324 MPa and* N_f *= 2.12* $\times 10^5$*;(B) R=-1,* σ_a *= 300 MPa and* N_f *= 4.29* $\times 10^5$*;(C) R=0.5,* σ_a *= 200 MPa and* N_f *= 7.23* $\times 10^4$ *; (D) R=0.5,* σ_a *= 150 MPa and* N_f *= 1.46* $\times 10^5$*; P1 in (B) being the location of transmission electron microscopy (TEM) sample cut by focused ion beam (FIB). Adapted from Du et al. [119] with permission from Elsevier.*

There are two types of defects categorized as regular (type I) and irregular defect (type II) while testing the SLM-Ti-6Al-4V parts under HCF and VHCF regimes where regular defects are the LOF defects with a regular shape (almost equiaxed) but without nonmetallic inclusions and irregular defects are the LOF defects with an irregular shape (large aspect ratio) [72,119].

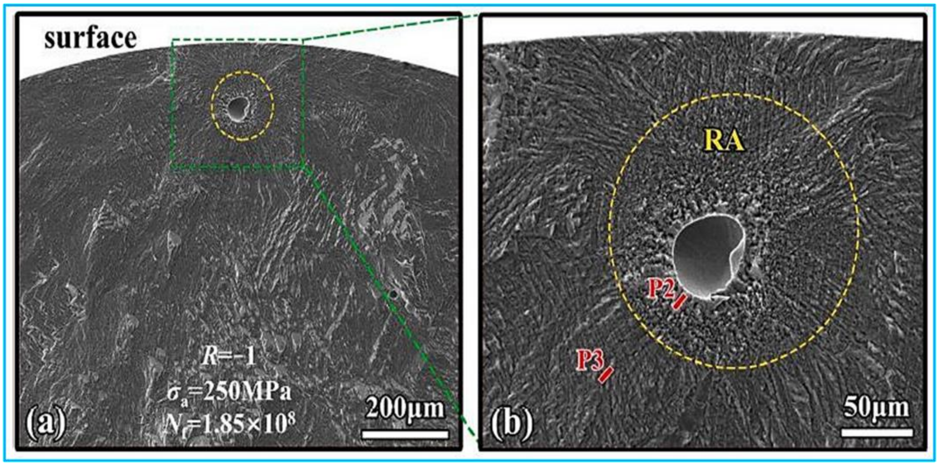

Fig. 77. Fracture surface morphologies showing the internal crack initiation with rough area (RA) in VHCF regime, (A) R=-1, σ_a = 250 MPa and N_f = 1.85 ×10^8; (B) Enlarged view of RA marked by green box in (A); P2 and P3 in (B) being the location of transmission electron microscopy (TEM) sample cut by focused ion beam (FIB). Adapted from Du et al. [119] with permission from Elsevier.

In the HCF regime, type I defects dominate the crack initiation regardless of the stress ratios used.[119] On the contrary, in the VHCF regime, both type I and type II defects can be found [119]. There is a tendency for type I defects to play a dominant role in crack initiation when specimens are subject to VHCF under R=-1; however, at R=0.5, type II defects will play a prominent role in initiating the crack in VHCF regimes [119]. In the VHCF regime at R=-1, RA surrounding the crack origin is found, while at R=0.5, the RA feature is not seen [119]. Qian et al.[72] also investigated the fracture mechanism of SLM-Ti-6Al-4V parts subjected to load ratio =-1 both in HCF and VHCF regimes. It is interesting to note that the authors found similar crack initiations both in the HCF and VHCF regimes which contradict the statement of Du et al. [119] about the surface crack initiation in the HCF regime. In both HCF and VHCF regimes, it is evident that cracks originate from the internal surface of the components both in HCF and VHCF regime and exhibit the same type of subsurface-induced failure (**Fig. 78**) [72].

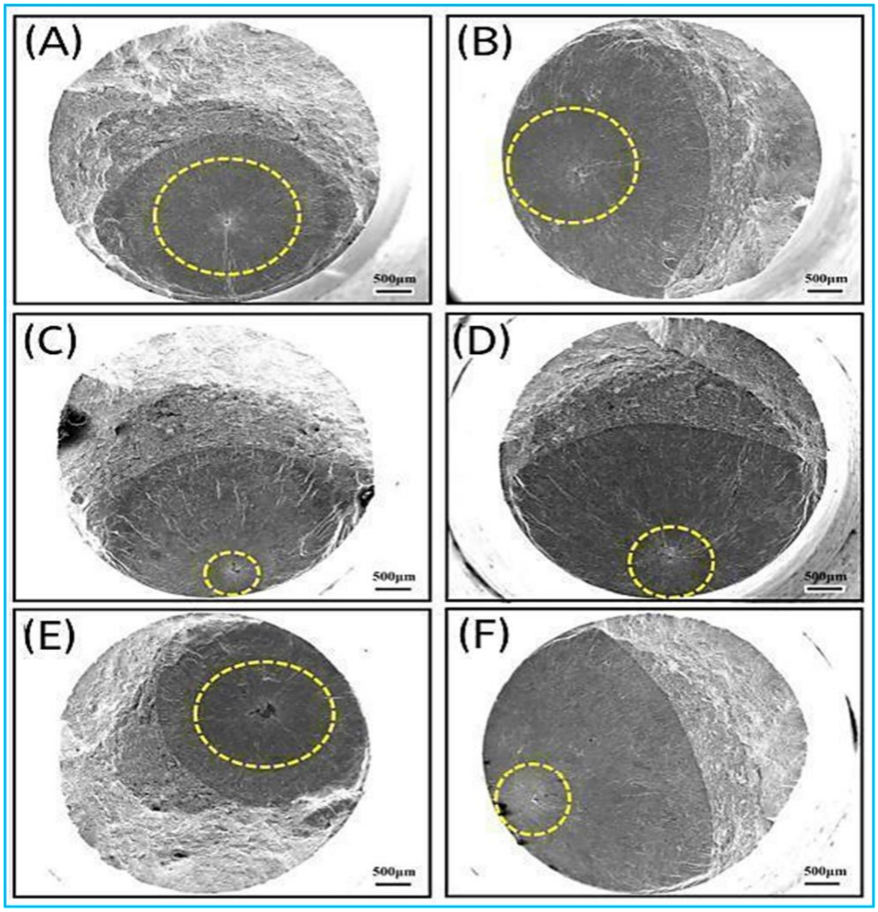

Fig. 78. *Shows fracture surface morphologies of the the internal crack initiation with RA both in HCF and VHCF regime (A) 0°, σ_a = 450 MPa and $N_f = 2.68 \times 10^6$; (B) 0°, σ_a = 300 MPa and $N_f = 2.51 \times 10^7$; (C) 45°, σ_a = 450 MPa and $N_f = 3.7 \times 10^5$; (D) 45°, σ_a = 320 MPa and $N_f = 3.1 \times 10^7$; (E) 90°, σ_a = 400 MPa and $N_f = 2.15 \times 10^5$; (F) 90°, σ_a = 250 MPa and $N_f = 1.03 \times 10^8$. Adapted from Qian et al.[72] with permission from Elsevier.*

However, the RA encompassing the internal defect is confirmed in the VHCF regime, and as a matter of fact, this is the characteristic region in which cracks usually begin to appear in the VHCF regime [72]. There is found a fish eye pattern (FiE) that is formed outside the RA both in HCF and VHCF regimes which contradicts the results of Du et al.[119] about the feature of the fracture surface of HCF [72]. Liu et al.[128] mentioned that for R=-1, fine granular area (FGA) represents the basic characteristic region of fatigue crack initiation in the VHCF region. Sun et al.[144] also confirmed that FGA is a basic characteristic region of fatigue crack initiation in the VHCF region. However, there is no clear relationship between the FGA size and fatigue life of SLM-Ti-6Al-4V parts (**Fig. 79**).

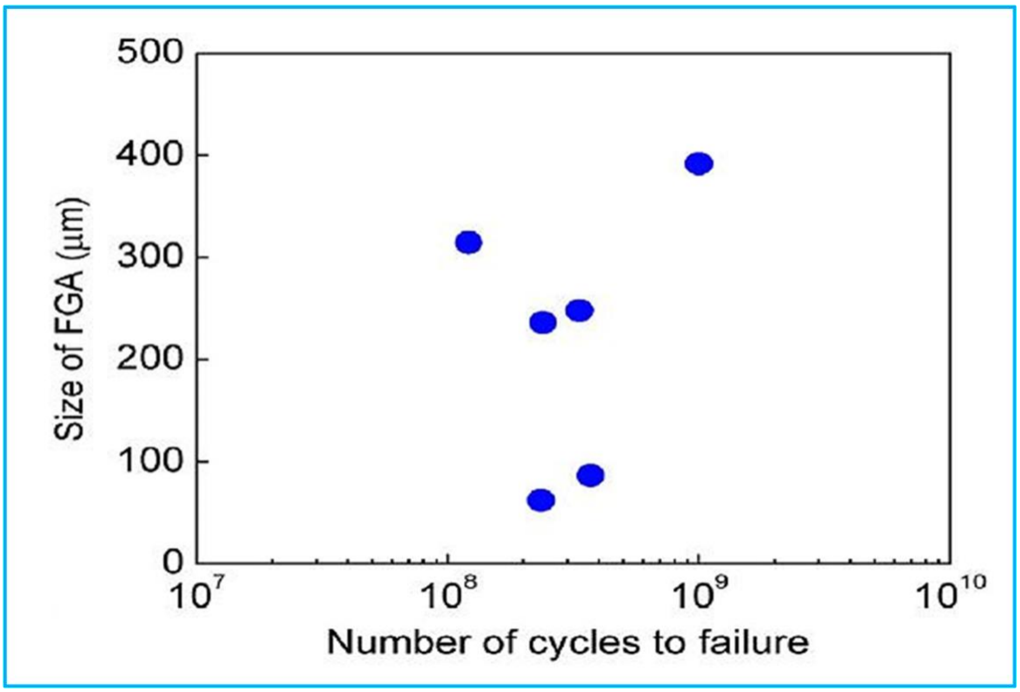

Fig. 79*. Variation of FGA size with fatigue life. Adapted from Sun et al.[144] with permission from Elsevier.*

Pan and Hong [135] investigated the fracture mechanism of Ti-6Al-4V parts both in HCF and VHCF regimes extensively subjected to different load ratios (-0.3, -1, 0.1, 0.5, 0.6,0.7, 0.8) both in HCF and VHCF regimes. The authors found surface crack initiations with RA both in HCF and

VHCF regions regardless of stress ratios (**Fig. 80**). However, both sub-surface and internal crack initiations with RA are found in the VHCF region (**Fig. 81** and **Fig. 82**).

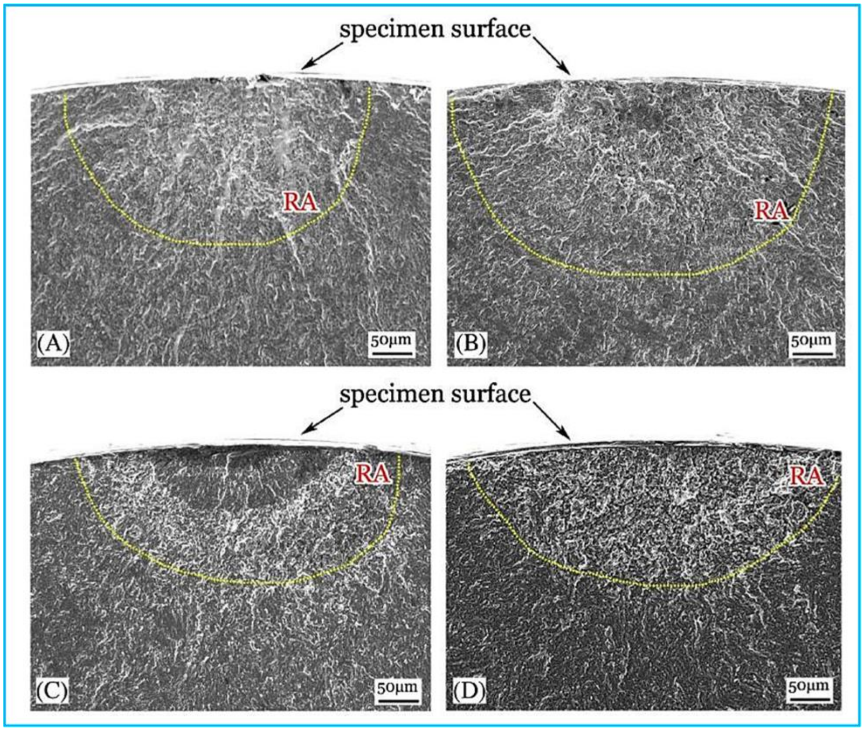

Fig. 80. *shows Surface crack initiation with RA morphologies depending on different loading conditions: (A) R = −1,* $\sigma_m = 0$*,* $\sigma_a = 533$ *MPa, and* $N_f = 6.04 \times 10^5$*; (B) R = −1,* $\sigma_m = 0$*,* $\sigma_a = 444$ *MPa, and* $N_f = 1.06 \times 10^8$*; (C) R = 0.8,* $\sigma_m = 784$ *MPa,* $\sigma_a = 89$ *MPa, and* $N_f = 1.8 \times 10^5$*; (D) R = 0.8,* $\sigma_m = 884$ *MPa,* $\sigma_a = 113$ *MPa, and* $N_f = 2.22 \times 10^7$*. Adapted from Hong and Pan [135] with permission from John Wiley and Sons.*

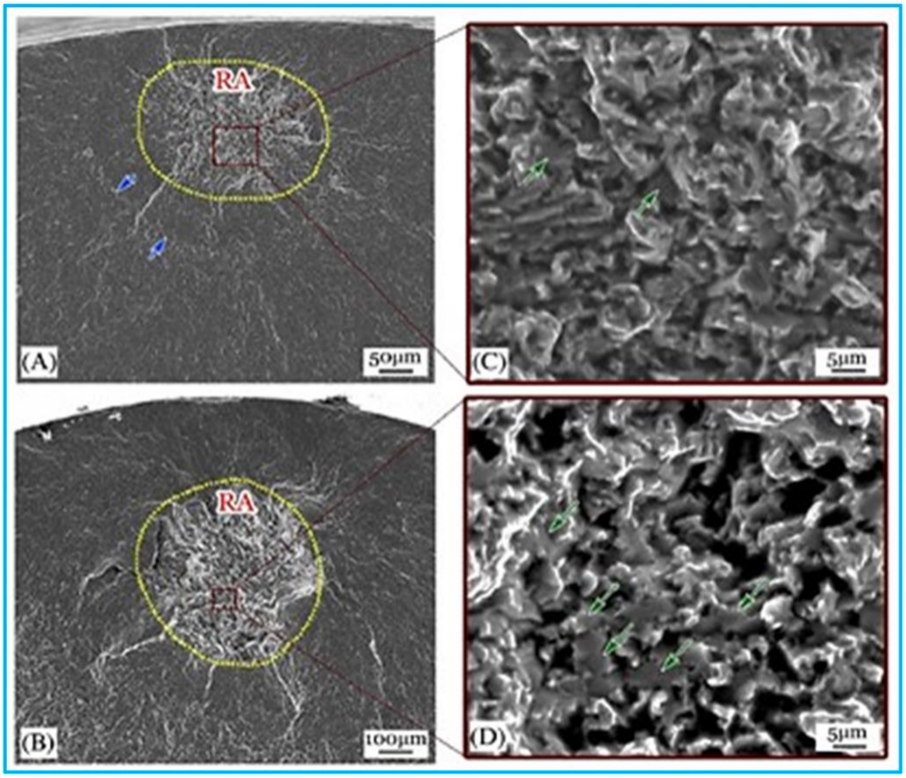

Fig. 81. *shows Internal crack initiation with RA morphologies failed in VHCF regimes depending on different loading conditions: (A) R = −0.3,* σ_m *= 166,* σ_a *= 293 MPa, and* $N_f = 7.33 \times 10^7$*; (B) R = 0.5,* σ_m *= 468,* σ_a *= 159 MPa, and* $N_f = 4.61 \times 10^8$*; (C, D) RA region detail, with arrows indicating the facets of the cleavage that is marked by the box in (A) and (B). Adapted from Hong and Pan [135] with permission from John Wiley and Sons.*

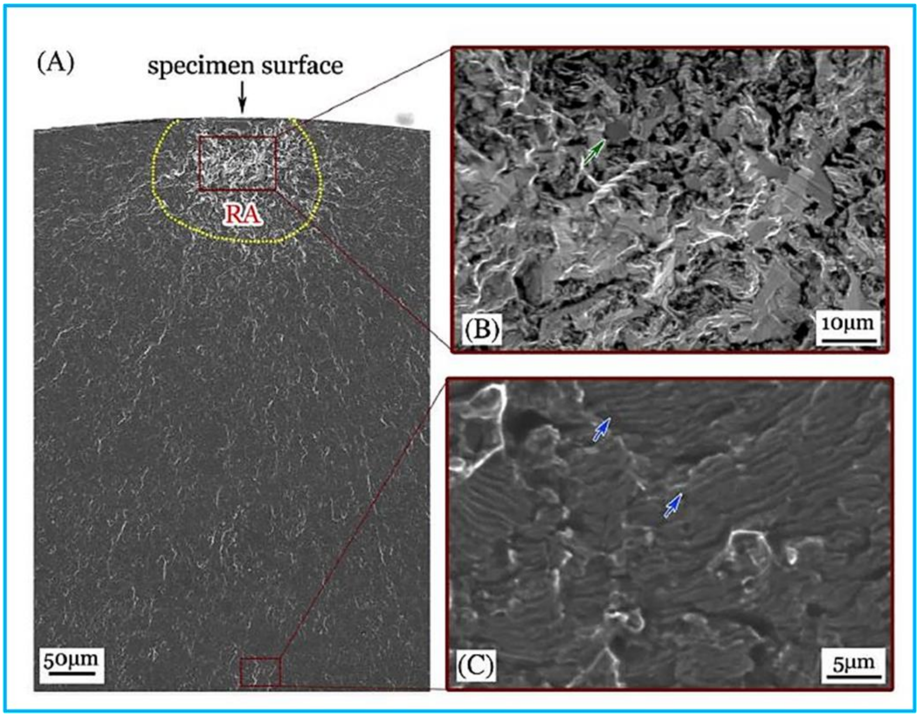

Fig. 82*. shows sub-surface crack initiation with RA morphologies failed in the VHCF regime. (A)R = 0.1, σ_m = 312 MPa, σ_a = 249 MPa, and $N_f = 1.10 \times 10^8$; (B) RA enlargement marked by the box in (A) where the arrow is indicating the cleavage facet; and (C) enlargement of a region outside RA region where fatigue striations will be found (Marked by arrows). Adapted from Hong and Pan [135] with permission from John Wiley and Sons.*

Liu et al.[128] illustrated the defect features as shown in **Fig. 83** where the red indicates internal defects, and green means subsurface defects.

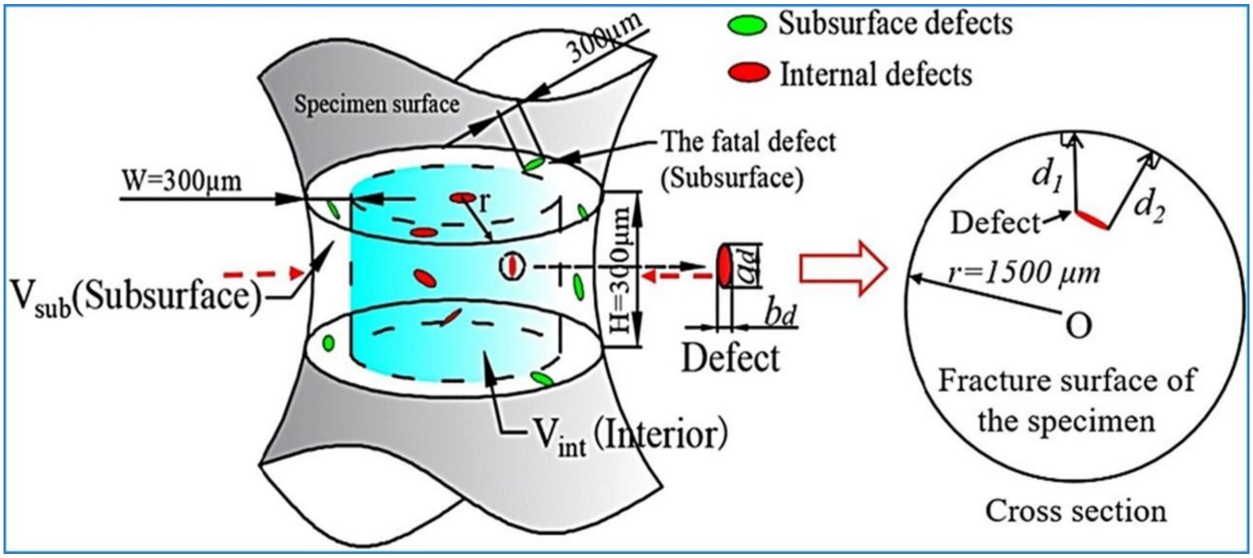

Fig. 83. *Schematic diagram of defect features. Adapted from Liu et al.[128] with permission from Elsevier.*

The authors proposed a new location parameter, L, for describing crack initiation mechanism properly considering the orientation of the defects as follows[128]:

$$L = 1 - \frac{d_1 + d_2}{2r}; 0 \leq L \leq 1 \qquad \text{Eq. 1}$$

Here,

r = Radius of the fatigue fracture surface in μm

$\frac{d_1+d_2}{2}$ = Average depth of the defect from the surface

Larger values of the parameter L indicate a higher probability of cracks initiating at surface defects.[128] A defect that has an L value ranging between 0.9 and 1 is classified as a surface defect; a defect that has an L value between 0.8 and 0.9 is classified as a subsurface defect, and a defect that has an L value between 0 and 0.8 is classified as an internal defect [128]. To correlate the fatigue strength with defect features, another parameter, D, is proposed as follows [128]:

$$D = S\sigma_a(\sqrt{area_{eff}})L^{\beta} \qquad \text{Eq. 2}$$

Here,

S = Shape factor of the irregular defect

β = Material dependent constant

$\sqrt{area_{eff}}$= Murakami's parameter (Briefly explained in Sec.5)

σ_a= Stress amplitude

Considering the value of D, it is possible to determine which defects are more destructive [216]. This can be done by considering the amount of contribution of the fatal defect to the internal crack driving force [216]. The consideration of the Index β is chiefly to identify how far a material contributes to the prolongation of fatigue life and how far it interacts with the matrix in the material [217]. Thus, fatigue crack initiation and propagation are directly related to the defects and their adjacent martensite laths. Based on the values of β=0, 0.25, and 0.1, **Fig. 84** illustrates the relationship between the D values and the number of cycles to failure in the VHCF regime [218,219].

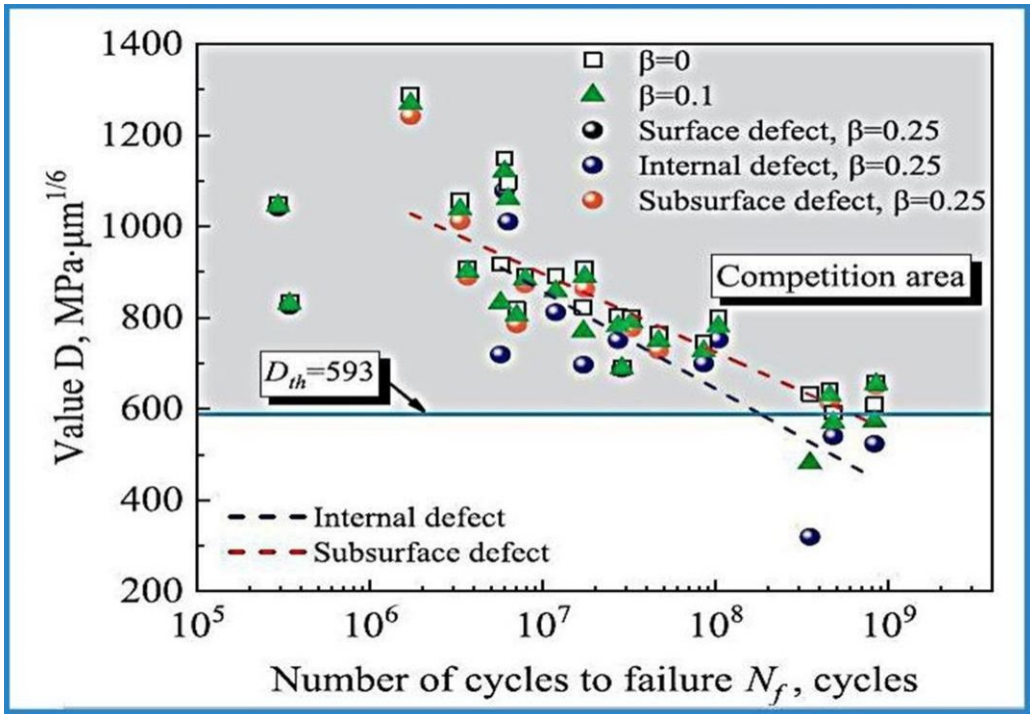

Fig. 84. *Correlation between the value D and the number of cycles to failure N_f in the VHCF regime. Adapted from Liu et al.[128] with permission from Elsevier.*

D values have a reasonably linear relationship with fatigue life, with the largest and lowest values of about 1298 and 593, respectively, for β = 0 [128]. There is, however, a certain degree of dispersion in the data when D is set to 0.25. This is accompanied by a clear trend in which the value of D gradually declines as fatigue life continues to increase [128]. A subsurface crack initiation (red dashed line) is shown in **Fig. 84** to have significantly larger D values than internal (blue dashed line) and surface crack initiations. The D values are similar to those for β = 0.1 and 0.25 [128]. Thus, the selection of the material-dependent constant β may not affect the values of D [128]. Zhu et al.[219] mentioned that subsurface defects and internal defect crack initiations coexist at a value of D greater than 593. As illustrated in figure 83, the value of D = 593 can be taken as the threshold value of D for crack initiation of subsurface defects, as internal defects will be found D less than 593. It is also clear from the data that it might be possible to find initiations of internal defect cracks at any value of D, but initiations of subsurface defect cracks will only be observed at values of D greater than the threshold value, D_{th} = 593 [128].

2.6 Prediction of Fatigue strength

2.6.1 Prediction of Fatigue strength considering defect size

The above discussions show that fatigue performance is sensitive to the defects (pores, LOF defects, etcetera) that are the dominant crack source of fatigue failure for the SLM Ti-6Al-4V parts. The low fatigue strength of the SLM-Ti has been attributed to the initial defects, which are invariably formed during the SLM process, and came to light from the fatigue test results and fracture surfaces that were observed. Several well-known existing formulas can predict the HCF of material concerning the √area parameter first proposed by Murakami et al.[220]. It has been proposed by Murakami et al.[220] that using a statistical analysis of the extreme value counts of the inclusion/defect size can be used as a method to determine the fatigue limit of steels. Though the model proposed by Murakami et al.[220] is based on steels, it can be used for Ti-6Al-4V material both at room and elevated temperatures as well.[1] The predicted fatigue limit, σ_w based on Murakami's model, is presented by ***Eq. 3 - Eq. 12***.

For surface inclusion [220]:

$$\sigma_w = \frac{1.43(120 + HV)}{(\sqrt{area_{max}})^{1/6}} \qquad \text{Eq. 3}$$

Here,

HV= Vickers hardness

$\sqrt{area_{max}}$ = Maximum defect size included in the risk volume of the sample.

For inclusion just below the surface [220]:

$$\sigma_w = \frac{1.41(120 + HV)}{(\sqrt{area_{max}})^{1/6}} \qquad \text{Eq. 4}$$

For internal inclusion [220]:

$$\sigma_w = \frac{1.56(120 + HV)}{(\sqrt{area_{max}})^{1/6}} \qquad \text{Eq. 5}$$

Liu et al.[221] modified the ***Eq. 3*** by considering the internal threshold value and proposed the following equation for the HCF regime:

$$\sigma_w = \frac{2(120 + HV)}{(\sqrt{area_{max}})^{1/6}} \qquad \text{Eq. 6}$$

Wang et al.[222] and Yang et al.[223] introduced fatigue life (N) into the Murakami model and modified the model for fatigue strength predictions as follows [224]:

$$\sigma_w = (3.09 - 0.120 logN)\frac{(120 + HV)}{(\sqrt{area_{max}})^{\frac{1}{6}}}[\frac{1 - R}{2}]^{\alpha} \qquad \text{Eq. 7}$$

For the lower bound of a scatter of fatigue strength, the author proposed the ***Eq. 8*** as follows [220]:

$$\sigma_w = \frac{1.41(120 + HV)}{(\sqrt{area_{max}})^{1/6}} \qquad \text{Eq. 8}$$

In another study, Liu et al. [221] modified the Murakami's equation for predicting the VHCF strength considering the effect of hydrogen during forming GBF and proposed the following equation:

$$\sigma_w = \frac{2.7(120 + HV)^{15/16}}{(\sqrt{area_{max}})^{3/16}} \qquad \text{Eq. 9}$$

S-N relationship within the HCF regime for a stress ratio R = 1 is generally described by the Basquin equation, as shown in ***Eq. 10***:

$$\sigma_a = c.(2N)^b \qquad \text{Eq. 10}$$

Here,

σ_a = Stress amplitude

c = Fatigue strength coefficient

b = Basquin exponent

It can be assumed that Basquin equation is also valid to predict the S-N curve in the VHCF region. Considering the ***Eq. 4*** **and** ***Eq. 6***, Liu et al. [221]proposed the Basquin's constant as follows:

$$c = 1.12\frac{(120+HV)^{9/8}}{(\sqrt{area_{in}})^{1/8}} \qquad \text{Eq. 11}$$

And

$$b = \frac{1}{3}\log\left(1.35(120+HV)^{-\frac{1}{16}}(\sqrt{area_{in}})^{-\frac{1}{48}}\right) \qquad \text{Eq. 12}$$

By rearranging the equations proposed by Tanaka and Akiniwa [225], Chapetti et al.[226], and Mayer et al.[227], Liu et al. [221] derived the Basquin's constant. The Basquin's constants are listed in **Table *6***.

Table 6. Basquin exponent (b) and fatigue strength coefficient (c) predicted by different authors.

b	c	Refs.
$\frac{1}{3}\log\left(1.35(120+HV)^{-\frac{1}{16}}(\sqrt{area_{in}})^{-\frac{1}{48}}\right)$	$1.12\frac{(120+HV)^{9/8}}{(\sqrt{area_{in}})^{1/8}}$	Liu et al. [221]
$-\frac{1}{48}$	$2.5\frac{(120+HV)}{(\sqrt{area_{in}})^{1/6}}$	Chapetti et al.[226]
$-\frac{1}{n}$ n= 28.82 for the bainitic bearing steel, 100Cr6 (similar to JIS SUJ2), with tensile strength 2387 MPa.	$(2C)^{\frac{1}{n}}(\sqrt{area_{in}})^{-\frac{1}{6}}$ C=6.47×10^{98} for the bainite steel, 100Cr6, (similar to JIS SUJ2), with tensile strength 2387 MPa	Mayer et al.[227]
$-\frac{1}{m_A}$	$\frac{2}{\sqrt{\pi}}\left(\frac{4}{C_A(m_A-2)}\right)^{\frac{1}{m_A}}(\sqrt{area_{in}})^{\frac{1}{m_A}-\frac{1}{2}}$	Tanaka and Akiniwa[225]

m_A =14.2 for the quenching and tempering bearing steel, JIS SUJ2, with tensile strength 2316 MPa	C_A=3.44×10^{-21} for the quenching and tempering bearing steel, JIS SUJ2, with tensile strength 2316 MPa	

2.6.1.1 Determination of initial crack size using extreme value statistics

The K_{Imax} of a subsurface defect, as demonstrated in **Fig. 85**, is located at the closest location to the free surface. In this area, cracks have the greatest chance of forming and penetrating quickly through it. It is likely that this will result in a semi-elliptical crack appearing on the surface.

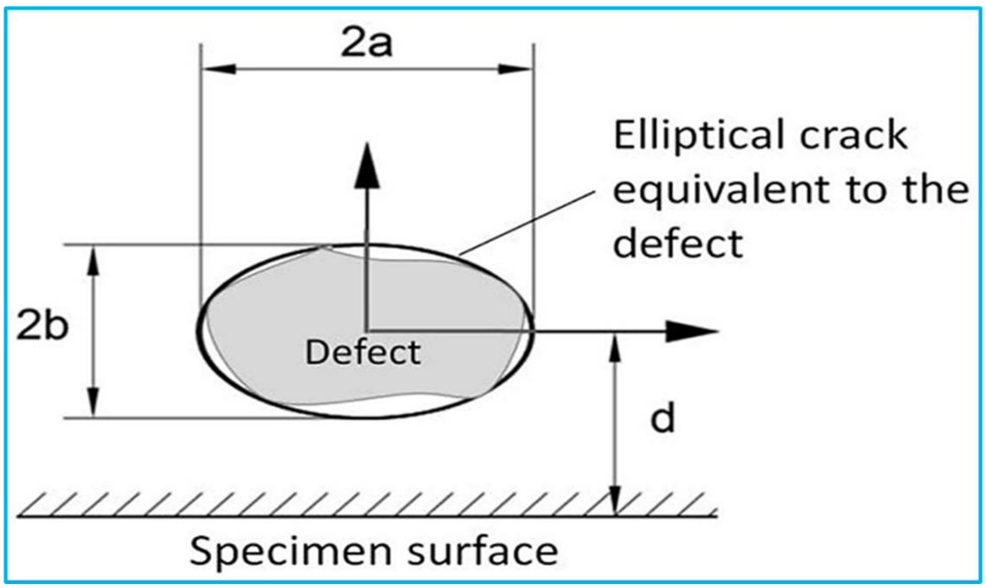

Fig. 85. *An illustration showing a semi-elliptical crack on the surface. Adapted from Jiao et al.[14] with permission from Elsevier.*

It can therefore be assumed that the subsurface defects are semi-elliptical surface cracks by neglecting the short life of penetration. An analysis of the semi-elliptical cracks was conducted by measuring their half-length a, and their depth b. Equation (4) requires two values: hardness, HV, and the maximum defect size in the risk volume of the sample, $\sqrt{area_{max}}$. Here is a quick overview of the proposed effective $\sqrt{area}$ method by Murakami to determine the size of the initial crack. As a first step, the standard inspection area, S_0, is fixed. After selecting random areas from the sample n times, the area with a defect size of S_0 is selected again and again until the maximum defect size is found among defects present in each of the selected areas. The j^{th} smallest size among the n values found in the above procedure is denoted as $\sqrt{area}_{max,\,j}$, for j=1, …, n. The cumulative probability function, F (%), and the reduced variates, y, are introduced and the following equations can be used to calculate the values for F_j and y_j for given j:

$$F_j = \frac{j}{n+1} \times 100\ (\%) \qquad \text{Eq. 13}$$

$$y_j = -\ln\left(-ln\frac{j}{n+1}\right) \qquad \text{Eq. 14}$$

The n data of ($\sqrt{area}_{max,\,j}$, F_j or y_j) are plotted in the semi-logarithmic graph of which the horizontal axis represents $\sqrt{area}_{max}$ and the vertical logarithmic axis represents F and y. It is then using the least squares method, a linear trend line equation that fits the data is formed in the form of ***Eq. 15*** with two coefficients, m and c.

$$\sqrt{area}_{max} = m \times y + c \qquad \text{Eq. 15}$$

Now, for finding the $\sqrt{area_{max}}$,the value of y corresponding to the risk volume should be determined by the following equation:

$$y = -\ln\left(-ln\frac{T-1}{T}\right) \qquad \text{Eq. 16}$$

Here,

T=Return period:

$$T = \frac{V}{V_0} \qquad \text{Eq. 17}$$

However, Kakiuchi et al.[1] used the following equation to find the return period:

$$T = \frac{V + V_0}{V_0} \qquad \text{Eq. 18}$$

Here,

V= Control Volume, mm^3

However, Kakiuchi et al.[1] mentioned that V is defined as the volume, which is 5% of the control volume (Volume at the gage section in the specimen for dog bone shaped specimen).

V_0= Standard volume, mm^3 = $S_0 \times h_0$

Here,

h_0= Virtual thickness, mm = Mean value of $\sqrt{area}_{max,\,j} = \frac{\Sigma\sqrt{area_{max,j}}}{n}$

S_0= Standard detection area, mm^2

Substituting the value of y in ***Eq. 15*** obtained from ***Eq. 16***, $\sqrt{area}_{max}$ is estimated using ***Eq. 17*** or ***Eq. 18.*** This procedure is schematically illustrated in **Fig. 86**.

2.6.2 Prediction of Fatigue strength considering surface roughness

Fatigue performance is also sensitive to the surface roughness, the dominant crack source of fatigue failure for the SLM Ti-6Al-4V parts. Murakami et al.[220] mentioned that surface roughness must be considered as a crack problem rather than a notch problem. Murakami et al.[220] proposed an equation for the fatigue limit considering the surface roughness. The predicted fatigue limit σ_w is presented by the following Eq. as follows:

$$\sigma_w = \frac{1.41(120 + HV)}{(\sqrt{area_r})^{1/6}} \left[\frac{1-R}{2}\right]^{\alpha} \qquad \text{Eq. 19}$$

Here,

$\sqrt{area_r}$ = Maximum equivalent surface defect size determined from the surface roughness profile.

R= Load ratio

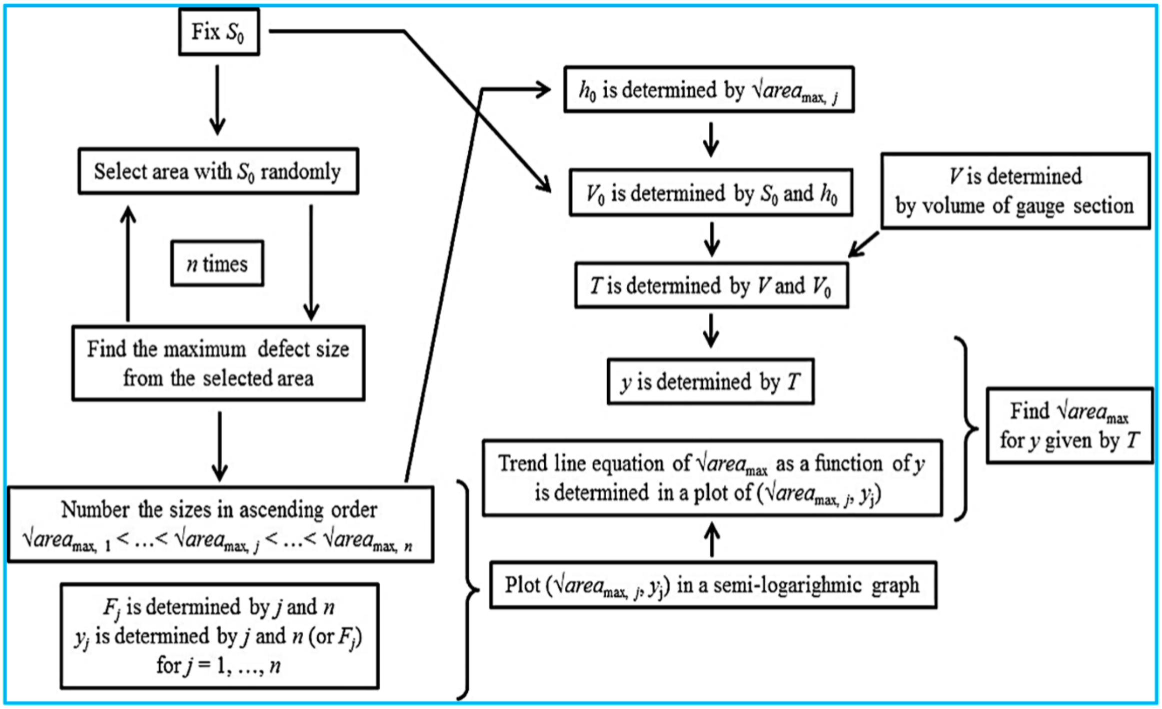

Fig. 86. *Block diagram of procedure to determine √area. Adapted from Kakiuchi et al.[1] with permission from Elsevier.*

2.6.2.1 Determination of maximum equivalent surface defect size using extreme value statistics

Murakami et al.[220] proposed the following equations to calculate the equivalent defect size for periodic surface notches as artificial surface roughness:

$$\frac{\sqrt{area_r}}{2b} \cong 2.97\left(\frac{a}{2b}\right) - 3.51\left(\frac{a}{2b}\right)^2 - 9.74\left(\frac{a}{2b}\right)^3;\ a/2b < 0.195 \qquad \text{Eq. 20}$$

$$\frac{\sqrt{area_r}}{2b} \cong 0.38; \mathrm{a}/2\mathrm{b} > 0.195 \qquad \text{Eq. 21}$$

Here,

a=Depth of the notch (Vertical distance of root to peak), µm

2b= Pitch of the periodic notches (horizontal distance of peak to peak), µm

Schematic representation of a and b from a surface roughness profile is shown in **Fig. 87**:

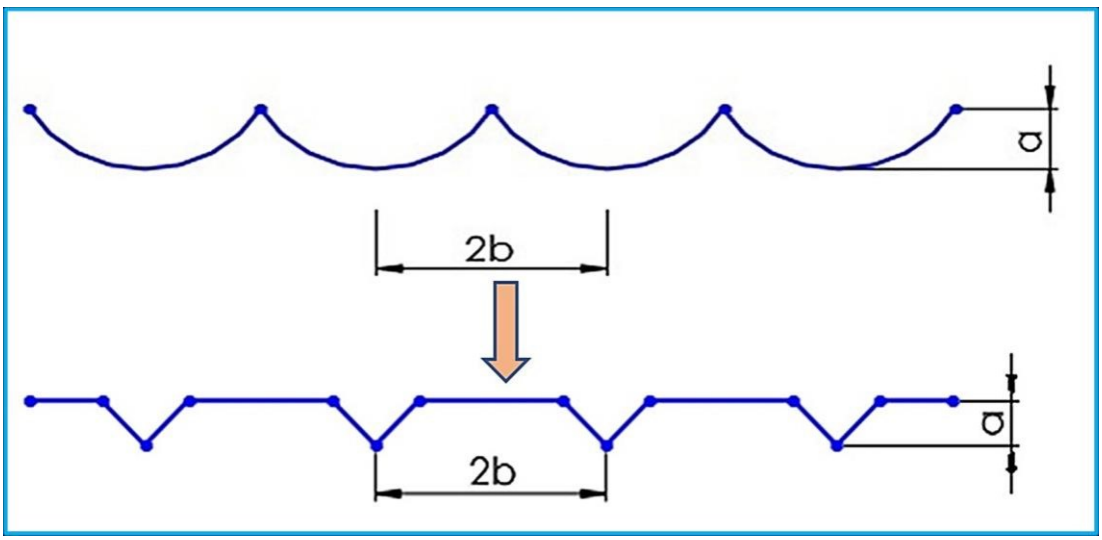

Fig. 87. *Notches and their equivalent cracks.*

2.7 Fatigue life prediction model

Pugno et al.[228] proposed a generalized Paris equation for the prediction of fatigue life. The Paris equation was generalized using Quantized Fracture Mechanics (QFM), which substituted SIF, K(a), with a mean value:

$$K^*(a, \Delta a) = \sigma\sqrt{(\pi\,(a + \frac{\Delta a}{2}))} \qquad \text{Eq. 22}$$

Here,

σ = Applied remote stress

a = Initial crack length

Δa = Fracture quantum, a material constant

By considering the additional crack size, Pugno et al.[228] proposed the following generalized Paris law:

$$\frac{da}{dN} = C(\Delta K^*(a, \Delta a, \Delta\sigma))^l \qquad \text{Eq. 23}$$

Here,

C and l are Paris equation constants.

By integrating ***Eq. 23***, the total number of cycles N_C^{P*} can be found for the fatigue collapse for the critical crack length a_c:

$$N_C^{P*} = \frac{1}{C}\int_a^{a_c} \frac{da}{\sqrt{(\Delta K^*(a, \Delta a, \Delta\sigma))^l}} \qquad \text{Eq. 24}$$

In order to address the effect of load ratio R on the VHCF responses of the SLMed Ti-6Al-4V parts, a unified statistical model was introduced by Paolino et al.[229,230] to describe the fatigue life based on the obtained S-N data and the distribution of defect sizes. **Fig. 88** shows a typical duplex S-N curve showing gigacycle fatigue data with two plateaux where the upper plateau represents a transition stress, and the lower plateau represents a fatigue limit.

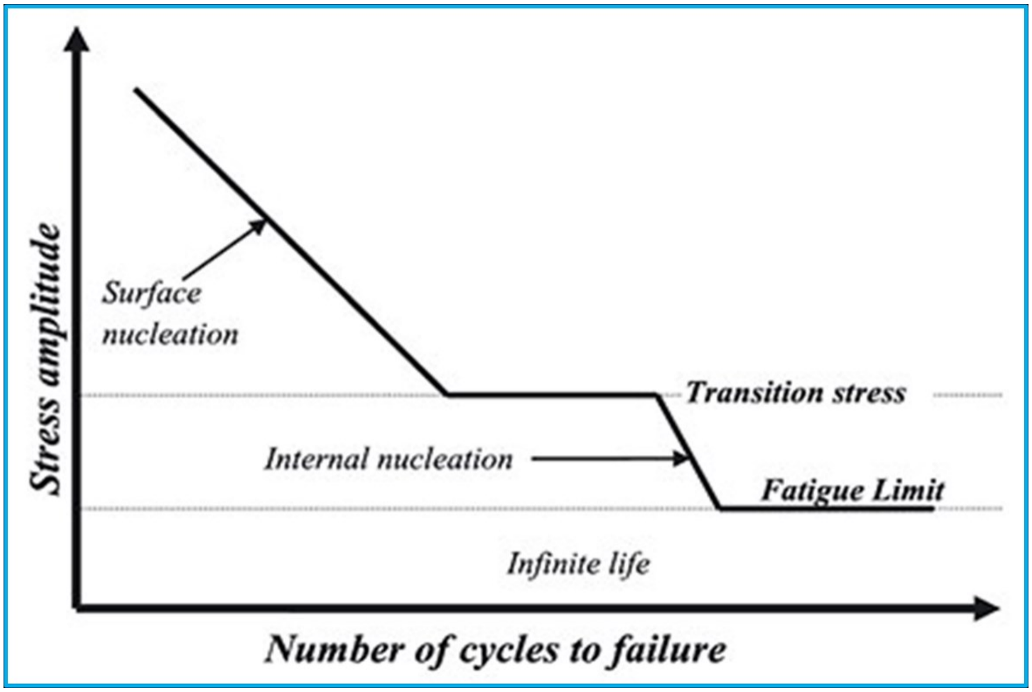

Fig. 88. *Typical duplex S-N curve. Adapted from Paolino et al. [229] with permission from John Wiley and Sons.*

The authors proposed the cumulative distribution function (cdf) of the fatigue life of a duplex S-N curve in the form of ***Eq. 25*** [229,230]:

$$F_y = F_{Y|surf} F_{x_t} + F_{Y|int} F_{x_l}(1 - F_{x_t}) \qquad \text{Eq. 25}$$

Here,

$$F_{x_l} = cdf\ of\ the\ logarithm\ of\ the\ fatigue\ limit = \Phi[\frac{x - \mu_{x_l}}{\sigma_{x_l}}] \qquad \text{Eq. 26}$$

$$F_{x_t} = cdf\ of\ the\ logarithm\ of\ the\ transition\ stress = \Phi[\frac{x - \mu_{x_t}}{\sigma_{x_t}}] \qquad \text{Eq. 27}$$

In ***Eq. 26*** and ***Eq. 27***, μ_{x_l} and $\mu_{x_t}$are the mean value of X_l and X_t, respectively, whereas σ_{x_l} and σ_{x_t} are the standard deviation of X_l and X_t.

$$F_{Y|int} = \text{cdf of the fatigue life if crack nucleates superficially}$$

$$= \Phi[\frac{y - (a_{Y|int} + x.b_{Y|int})}{\sigma_{Y|int}}] \qquad \text{Eq. 28}$$

$$F_{Y|surf} = \text{cdf of the fatigue life if crack nucleates superficially}$$

$$= \Phi[\frac{y - (a_{Y|surf} + x.b_{Y|suf})}{\sigma_{Y|surf}}] \qquad \text{Eq. 29}$$

In ***Eq. 28*** and ***Eq. 29***, $a_{Y|int}$, $b_{Y|int}$, $a_{Y|surf}$, $b_{Y|surf}$ are four constant coefficients related to the Basquin's law whereas $\sigma_{Y|int}$, $\sigma_{Y|surf}$ are the standard deviations of Y|int and Y|surf, respectively.

After considering the ***Eq. 26 - Eq. 29***, F_Y finally becomes:

$$F_Y = \Phi\,[\frac{y-(a_{Y|surf}+x.b_{Y|suf})}{\sigma^{Y|surf}}]\,\Phi\,[\frac{x-\mu_{x_t}}{\sigma^{x_t}}] + \Phi\,[\frac{y-(a_{Y|int}+x.b_{Y|int})}{\sigma^{Y|int}}]\,\Phi\,[\frac{x-\mu_{x_l}}{\sigma^{x_l}}](1\text{-}\,\Phi[\frac{x-\mu_{x_t}}{\sigma^{x_t}}]) \qquad \text{Eq. 30}$$

Considering both mean stress and stress amplitude effects on the VHCF performance, Du et al.[119] establish the P-S-N model using equivalent stress amplitude. "Smith-Watson-Topper" (SWT) model was used to compute equivalent stress, $\sigma_{a,eq}$ for different stress ratios as follows:

$$\sigma_{a,eq} = \sigma_{max}\sqrt{\frac{1-R}{2}} \qquad \text{Eq. 31}$$

Here, σ_{max} is the maximum stress.

Du et al.[119] established the P-S-N model taking into account the defect size distribution, and proposed the following equation:

$$F_Y(y;x) = F_{Y,HCF}(Y;X)F_{x_t}[\frac{x-\mu_{x_t}}{\sigma_{x_t}}] + F_{Y,VHCF}(Y;X)\,[[1 - F_{X_l}(\frac{x-\mu_{x_l}}{\sigma_{x_l}})] \qquad \text{Eq. 32}$$

Here,

$F_{Y,HCF}(y;x) = \int_0^{\infty} \Phi(\frac{y-\mu_{Y,HCF}(x,\sqrt{area_d})}{\sigma_{Y,HCF}}.\,f_{LEV}\,(\frac{\sqrt{area_d}-\mu_{\sqrt{area_d}}}{\sigma_{\sqrt{area_d}}})d\sqrt{area_d}$ is the cdf of the finite fatigue life y in the HCF region.

$F_{Y,HCF}(y;x) = \int_0^{\infty} \Phi(\frac{y-\mu_{Y,HCF}(x,\sqrt{area_d})}{\sigma_{Y,HCF}}.\,f_{LEV}\,(\frac{\sqrt{area_d}-\mu_{\sqrt{area_d}}}{\sigma_{\sqrt{area_d}}})\,d\sqrt{area_d}$ is the cdf of the finite fatigue life y in the VHCF region.

The fatigue life y is the logarithm of the number of cycles to failure ($y = \log_{10}N_f$), and x is the Logarithm of the equivalent stress amplitude $\sigma_{a,\,eq.}$

X_t is the transition stress of each specimen, which follows the normal distribution with mean value μ_{X_t} and standard deviation σ_{X_t}.

$\Phi(\frac{y-\mu_{Y,HCF}(x,\sqrt{area_d})}{\sigma_{Y,HCF}})$=The cdf of the normally distributed conditional finite fatigue life y.

Where, $\sqrt{area_d} = Initial\ defect\ size$;

$\mu_Y(x,\sqrt{area_d}) = c_Y + n_Y x + m_Y \log_{10}\sqrt{area_d}$ and σ_Y is the standard deviation.

The probability density function (pdf) of the initial crack size $\sqrt{area_d}$,which follows the largest extreme value (LEV) distribution with parameters $\mu_{\sqrt{area_d}}$ and $\sigma^{\sqrt{}}{}_{\overline{area_d}}$ is presented as follows:

$$f_{LEV}(\frac{\sqrt{area}_d - \mu_{\sqrt{area_d}}}{\sigma_{\sqrt{aea_d}}}) = \frac{1}{\sigma_{\sqrt{area_d}}} e^{\frac{\sqrt{\cancel{area_d}}-\mu_{\sqrt{\cancel{area_d}}}}{\sigma_{\sqrt{area_d}}}} .\, e^{-e^{\frac{\sqrt{\cancel{area_d}}-\mu_{\sqrt{\cancel{area_d}}}}{\sigma_{\sqrt{area_d}}}}} \qquad \text{Eq. 33}$$

To determine the coefficient of the mean fatigue life μ_Y and the standard deviation of the mean fatigue life under σ_Y in HCF and VHCF regimes, multiple linear regression was used. A maximum likelihood approach was applied to estimate the coefficients ($\mu_{\sqrt{area_d}}$,$\sigma_{\sqrt{area_d}}$) of the LEV distribution by taking into account the sizes of the defects. For both the HCF and VHCF regimes, the authors used two LEV distributions for defect size $\sqrt{area_d}$ for the case of R = -1, while for the case of R = 0.5, only one LEV distribution was considered. By applying the maximum likelihood principle, the authors could determine the mean value μ_{x_t} and the standard deviation σ_{X_t} of the stress by considering equation (30) and all the results of tested samples, including runout ones.

2.8 Conclusion

A comprehensive overview of the state of art on the fatigue behavior of Ti-6Al-4V alloy manufactured by SLM has been presented and discussed. The key conclusions drawn from the studies in the literature can be summarized as follows:

1. Microstructures play an important role in HCF and/or VHCF performances. Fine needle-shaped α' martensite, with a typical lath width of about 0.2-1μm, contains a high density of dislocations leading to higher fatigue strength with lower ductility of SLM-Ti-6Al-4V parts. As for the α+β microstructure, fatigue performance will be improved with a decrease in α phases. The crack begins in the alpha phase of the HCF regime and propagates through the alpha phase as a cleavage fracture of T-textured alpha grains. Alpha phase embrittlement can occur when oxygen content increases on the surface.
2. Porosity has a significant impact on the HCF and VHCF performance of the SLM-Ti-6Al-4V specimens. Porosity can be regarded as one of the most detrimental defects of fatigue

behavior. If the porosity level increases, the fatigue strength will decrease sharply. The porosity level also changes the trend/slope of the S-N curve.

3. In general, fatigue failure is primarily a consequence of surface defects and internal defects (i.e., porosity or oxide) occurring fatigue life regime from HCF to VHCF.
4. As a result of the detrimental orientation of the absence of fusion defects, vertical samples tend to have a lower fatigue strength than horizontal samples. However, the opposite statement is available. The load ratio influences the effect of building orientation on the fatigue performance of SLM-Ti-6Al-4V parts.
5. RS plays a significant role in the HCF and/or VHCF performances. It is suggested that reduced RS appeared to be one of the reasons for showing improved fatigue life, and thus different post-processing treatments should be performed to reduce the RS.
6. Optimized fabrication parameters also significantly influence the HCF and VHCF behavior of SLM-Ti-6Al-4V parts by reducing the porosity/defects level.
7. Post-processing treatment can improve the fatigue life of Ti-6Al-4V parts, but there is also conflicting conclusion regarding the detrimental effect of the post-processing treatment on fatigue life.
8. Optimized fabrication parameters, i.e., scanning strategy, scanning speed, energy density, layer thickness, hatch spacing, etc, can help get the optimal relative density of SLMed Ti-6Al-4V parts.
9. The effect of surface roughness on the fatigue performance of SLM-Ti-6Al-4V parts is inconsistent. Thus, despite the wide range of fatigue properties associated with surface post-processed materials, surface roughness alone cannot provide a sufficient indicator of fatigue properties due to the fact that prior surface defects can be hidden under a smooth

surface. The reason is that removing surface roughness does not eliminate internal defects, and eliminating porosity with retaining AB surface roughness does not produce the expected fatigue performance. In order to achieve optimal fatigue performance, it is recommended to eliminate both the high surface roughness and inner defects. In conclusion, it is pertinent to remember that fatigue strength after post-processing is determined by a combination of surface roughness, surface RS, microstructure, and the remaining defects left on the surface.

10. Specimen geometry, especially the gage diameter, plays a significant role in HCF behavior. The decreased gage diameter results in a reduction in the fatigue life of those parts due to multiple cracks that are induced within close proximity to one another.
11. Ductility and yield strength are also considered to have some influence on the fatigue behavior of SLM-Ti-6Al-4V parts if RS is taken into consideration.
12. Load ratio and loading type also affect the fatigue behavior of SLM-Ti-6Al-4V parts. Fatigue lives of SLM-Ti-6Al-4V parts decrease with increasing load ratios or the mean stresses. However, there is no significant impact of test frequency on fatigue life.
13. Corrosion properties have a significant impact on the fatigue properties of SLM-Ti-6Al-4V parts. There is a drastic decrease in fatigue strength due to locally intensified corrosion.
14. In the HCF region, surface crack initiation is found, whereas internal crack initiation dominates in the VHCF regime. However, opposite conclusions can easily be found that internal crack initiation dominates both in HCF and VHCF regimes.
15. RA encompassing the internal defect and Fie pattern can be found in the VHCF region, which is the characteristic region in which cracks usually begin to appear in VHCF.

16. Some traditional approaches, based on the Murakami model considering $\sqrt{area_{in}}$ parameter, can be used to predict fatigue performance.

2.9 Future prospects

SLM Ti-6Al-4V parts face several challenges that need to be addressed in order to utilize their full potential for wider engineering applications. Ishikawa diagram (**Fig. 89**) illustrates some critical scientific and technological challenges. The solidification science and the process metallurgy fields need to be brought together to provide integrated solutions for those challenges.

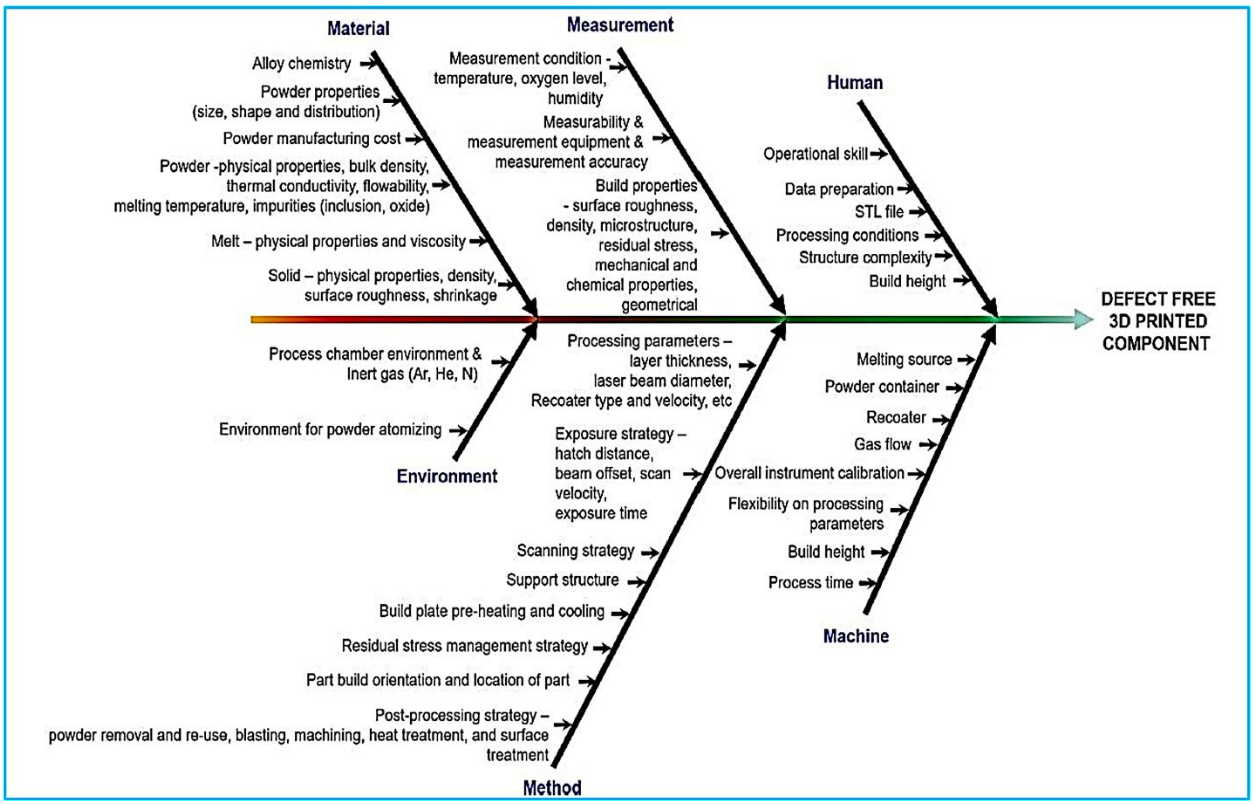

__Fig. 89.__ Metal AM challenges identified by an Ishikawa diagram. Adapted from Kotadia et al.[125] with permission from Elsevier.

As a result, future research should be focused on several areas that can further advance the process and SLM-Ti-6Al-4V alloy. To fully establish the relationship between the process and microstructure of SLM Ti-6Al-4V alloys, as well as to fully explore their great potential, future studies are required to examine the following aspects:

1. To overcome some of the challenges in SLM Ti-6Al-4V alloy, mathematical simulations, digital twins, and machine learning can be combined with closed-loop monitoring and control systems.

2. It is evident from the previous studies that different researchers have used different compositions of other materials powders in Ti powder to fabricate Ti-6Al-4V parts using the SLM process. However, there is no comprehensive research on the effect of other materials alongside Al and V. It is, therefore, imperative to investigate in depth the role of Al and V, as well as other chemical powders, when it comes to achieving optimal powder behavior during the SLM process.
3. A strategy needs to be developed for how different grades of powders can be reused, recycled, and handled without affecting the build processing and performance.
4. The effects of scanning strategy, physically induced force and chemical compositions should be properly researched, which may provide desirable microstructures along with expected mechanical and fatigue properties for commercial requirements.
5. Some researchers have reported that post-treatment (i.e., heat treatment, HIP treatment, etcetera) increases the fatigue life of SLMed Ti-6Al-4V parts, whereas opposite statements can easily be found. But the interesting thing is that while discussing the effect of post-process heat treatment and HIP treatment, the effect of load ratio and geometrical configurations of the specimen has not been considered. Thus, further research is needed

regarding the role of post-process heat treatments and HIP treatments, considering the geometrical configurations and load ratio.

6. In order to further improve the fatigue properties of the material by using various post-treatments over the AB condition, it would be of interest to investigate the underlying mechanisms involved in each post-treatment.
7. Cryogenic treatment has been successfully applied to several alloys, including titanium alloys, to improve the engineering performance of these alloys. The effect of cryogenic treatment on the fatigue behavior of the SLMed Ti-6Al-4V parts would also be a worthy area of investigation in the future.
8. There have been several studies that have shown that HIPtreatment can reduce the porosity level in SLM-Ti-6Al-4V parts as a means to increase the fatigue life of the parts. It is necessary to conduct further research with regard to the choice of temperature and pressure for HIP treatment. Hence, the study will help determine the effect of temperature and pressure in the HIP process on the metallurgical behavior and pore-collapsing phenomena.
9. A limited number of studies have been conducted on identifying hot tears and fish scales in SLMed Ti-6Al-4 V parts. Further research is needed to understand why hot tears and fish scales are formed. This will enable researchers to minimize detrimental impacts associated with hot tears and fish scales.

In terms of the issues outlined above, it is important to note that they are related not only to SLM/L-PBF Ti-6Al-4V alloy but also to other additively manufactured metals given the inherent trans-scale, hierarchical and heterogeneous characteristics of AM-induced microstructures. Hence, it can be expected that the knowledge gained from the paper can be potentially applied to the development of emerging SLM/AM alloys, particularly Ti alloys.

Chapter 3

Very high cycle fatigue characterization of additive manufactured Ti-6Al-4V alloy: Effect of Stress relieved (SR) heat treatment, microstructure, and defect characteristics

Md Mehide Hasan Tusher[1], Ayhan Ince[1, *]

[1]Mechanical, Industrial & Aerospace Engineering, Concordia University, 1455, boulevard de Maisonneuve Ouest
Montreal, Quebec, H3G 1M8

* Corresponding author: E-mail: ayhan.ince@concordia.ca

Article under review in << Fatigue & Fracture of Engineering Materials & Structures >>

3.1 Abstract

Laser Powder Bed Fusion (L-PBF) technique produces intricate structures in various industries. The durability of L-PBF components should be evaluated when subjected to different types of stresses in order to extend their applicability to other fields. There is no doubt that cyclic loading plays an important role in many applications, although most previous studies have focused on static loads. This investigation explored how stress-relieved (SR) heat treatment affects the very high cycle fatigue (VHCF) performance of L-PBF-Ti-6Al-4V alloy. The SR heat treatment increased the VHCF response of the alloy by lowering defect levels and their size along with

changing the microstructure, thus demonstrating their increased versatility for wider industrial applications.

Keywords: additive manufacturing; laser powder bed fusion; Ti-6Al-4V alloy; stress relieve; very high cycle fatigue

3.2 Introduction

A large number of alloys, especially Ti-6Al-4V, have been processed using L-PBF technology in recent years due to its strength, low density, and corrosion resistance [4]. Thus, Ti-6Al-4V plays a significant role in designing and developing many structural components with complex geometries in aerospace, automotive, defense, transportation, and biomechanical industries [2-4,11,13-16] . However, the low thermal conductivity and chemical reactivity of titanium alloys make traditional manufacturing difficult and expensive, which significantly reduces their service life.[98]. Recently, Additive manufacturing (AM) technology allows the realization of lightweight structures with geometric flexibility, which has not been, otherwise, possible by the conventional manufacturing process [2-4]. There are currently a large number of companies manufacturing Titanium alloy components using additive manufacturing techniques to minimize expensive and time-consuming manual processes. However, there are still concerns about the structural integrity of the components manufactured using these techniques. In order to understand the failure mechanisms of AM titanium alloys and ensure the safety of the design, it is necessary to carry out experimental assessments of their mechanical properties. Many studies have been conducted on the quasi-static mechanical properties of titanium alloys [138,231,232] and the response of AM titanium alloys to high-cycle fatigue (HCF) over time [41,136,202,210,211], especially when it comes to the Ti-6Al-4V alloy, which is one of the most commonly used alloys in the industry today. However, a few studies have also been conducted on the behavior of very high-cycle fatigue (VHCF)

[4,40,72,119,128,144,146,165]. The effects of a stress relief heat treatment and a hot-isostatic pressing process (HIP) have been investigated in [40,165]; in [119] crack initiation mechanisms under different stress ratio was investigated; On the other hand, in [146], fatigue tests were performed up to 10^9 cycles on specimens with large loaded volumes in order to explore the effects of size on fatigue performance. So, still there is very limited research on the effect of stress relieved heat treatment on VHCF performance of L-PBF-Ti-6Al-4V alloy. Therefore, the aim of this study is to explore how combining controlled platform temperatures with stress relieved heat treatment can affect the very high cycle fatigue (VHCF) response of L-PBF-Ti-6Al-4V alloy. To achieve this, specimens of Ti-6Al-4V alloy made on a substrate with a temperature of 80^0C were tested using an Ultrasonic fatigue testing machine with a stress ratio of -1. This study aimed to determine how stress-relieved heat treatment affects VHCF response and identify critical factors that affect VHCF response. In order to analyze the fracture surfaces of the samples, scanning electron microscopy (SEM) was used, and features such as nature, size, and position of crack-initiating features were analyzed using μ-CT investigation.

3.3 Materials and Methods

The pre-alloyed gas atomized Ti-6Al-4V powder managed by FusiA impression 3D Métal Inc. was used to manufacture test samples. Table 7 gives the chemical composition of the powder analyzed by Luvak Inc. in accordance with ASTM F2924 [114] and provided by the manufacturer (FusiA impression 3D Métal Inc.).

Table 7. chemical composition of Ti-6Al-4V powder used for manufacturing the cylindrical samples (weight %).

Material	Al	V	Fe	O	C	N	H	Y	Others (each)	Others (total)	Ti
Measured	6.38	4.09	0.21	0.18	0.02	0.01	0.002	<0.001	<0.10	<0.40	Bal.
Required	5.50-6.75	3.50-4.50	≤0.30	≤0.20	≤0.08	≤0.05	≤0.015	≤0.005	≤0.10	≤0.40	Bal.

The particle size distribution of Ti-6Al-4V powder was determined using a laser diffraction analyzer (Coulter® LS Particle Size Analyzer) in accordance with ASTM B822[233]. This method allowed for a quick and easy determination of the particle sizes. The Ti-6Al-4V powder exhibited a range particle sizes with a D10 of 21.0 µm, D50 of 35.0 µm, and D90 of 47.0 µm. It was also found that only 3% (by volume) of metallic powders were less than 15.0 µm. According to ASTM B214[234] 95.3 % (by mass) of powder possesses a size less than or equal to 45.0 µm and the rest of the powder possesses a size greater than 45.0 µm. However, there was no metallic powder possessing a size greater than 63.0 µm. The metallic powder exhibited an apparent density of 2.55 2.55 g/cm^3 based on ASTM B212[235] and the flow rate of the powder was 31 sec/50g based on ASTM B213[236]. L-PBF parts were manufactured using an EOS M290. The substrate was heated to 80^{0}C. The last step of the fabrication process involved fabricating 11 mm cylindrical samples perpendicular to the print bed in the vertical direction as shown in **Fig. 90** by closely controlling the L-PBF process parameters as specified in ***Table 8***.

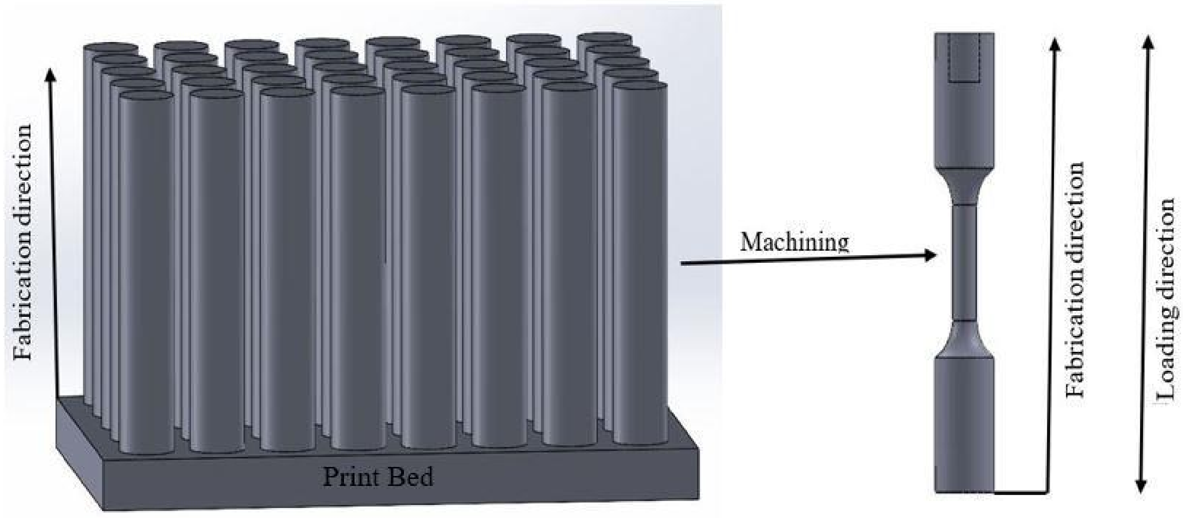

Fig. 90. *Schematic representation of fabrications and loading directions of the fatigue samples.*

Therefore, the building direction corresponded to the direction of fully reversed tension-compression stresses. A total of 40 samples were fabricated to conduct this study. The manufacturing process was carried out using argon gas throughout the entire manufacturing process in order to reduce the chance of imperfections caused by foreign materials. Half of the samples were heat-treated following a conventional stress relieved heat treatment procedure. Post-processing heat treatment on L-PBF samples consisted of exposure to 593^0 C for 2 h min in an attempt to reduce residual stress, porosity and yield a more consistent microstructure.

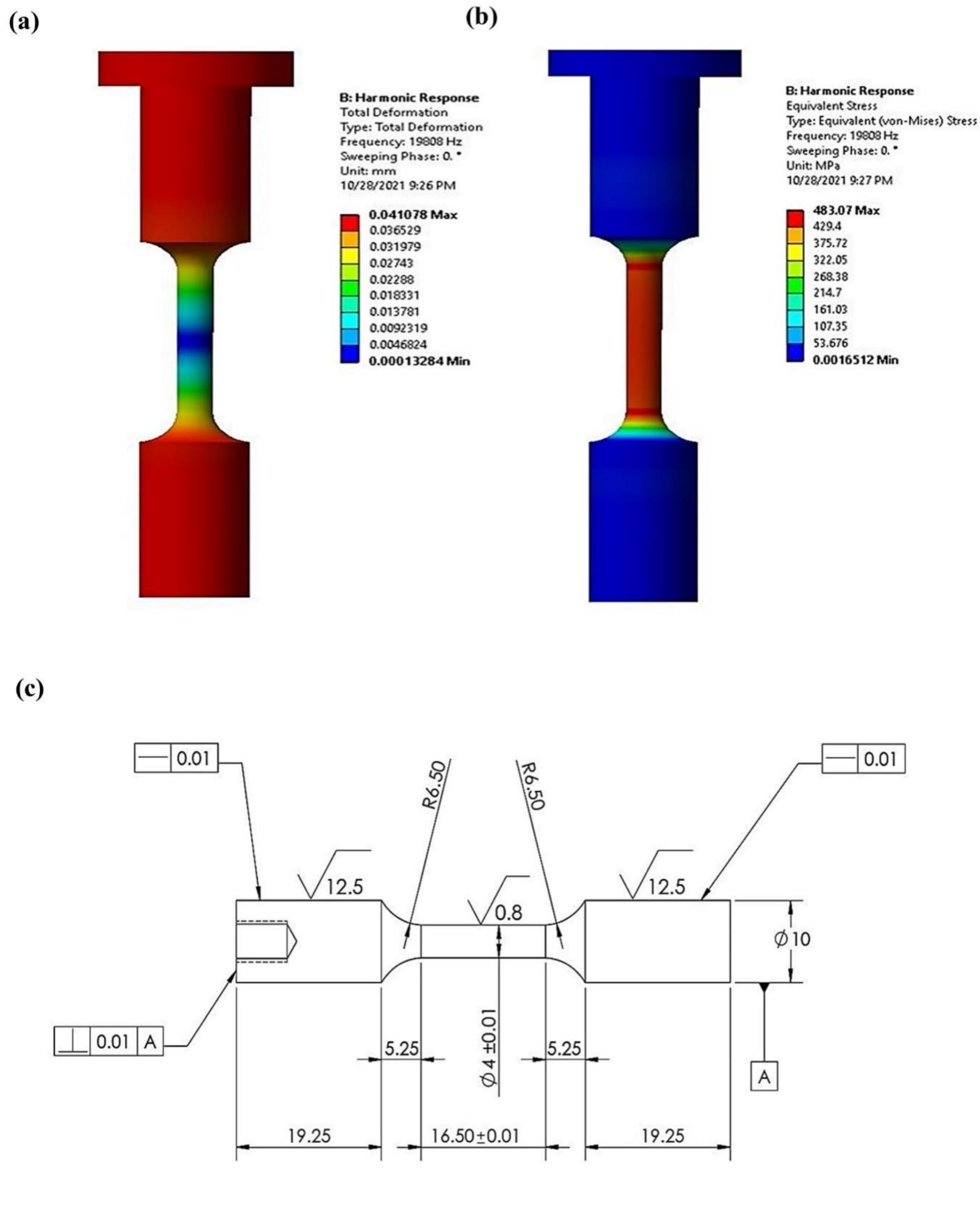

Fig. 91. *Design of the fatigue sample (a) deformation results from Finite element (FE) harmonic analysis of Ti-6Al-4V samples;(b) stress results from Finite element (FE) harmonic analysis of Ti-6Al-4V samples; (c) dimensions of dog bone shaped Ti-6Al-4V fatigue samples*

Table 8. Parameter sets employed for the manufacture of L-PBF-Ti-6Al-4V cylindrical samples.

Laser Power	340W
Laser focus diameter	0.100 mm
Scan speed	1250 mm/s
Layer thickness	60 μm
Substrate temperature	80^0C
Inert gas flow rate	3L/min

In order to analyze fatigue performance in the Ultrasonic Fatigue Testing Machine (UFTM) [237], a dog bone-shaped fatigue sample with a risk volume of 207.3456 mm^3 was designed and fabricated for use with a resonance frequency of 20 kHz ± 400 Hz. In order to map out natural frequencies, deformations, and stresses of test samples under resonance conditions, the use of finite element (FE) modal and harmonic analyses was performed on the specimens. **Fig. 91** displays the dimensions of the fatigue specimens along with the FE results. This document uses the term "AB" samples to refer to the samples that were machined from as-built cylindrical samples, while "SR" samples refer to the samples that were machined from cylindrical samples that underwent stress relief heat treatment.

To identify the porosity that results from manufacturing processing, printed samples were inspected using an XT H225 X-ray μ-CT system (Nikon, MI, USA) to perform computed tomography (CT) observations on the gage sections of the samples. The CT scans provided a detailed 3D analysis of the porosity, allowing for a comprehensive evaluation of its effects on the fatigue performance of the samples. A transmission scan source was used for the scanning of the samples, which used a beryllium target configured with a scan voltage of 130 kV and a beam current of 90 μA for scanning. A voxel size of about 1.00145 μm^3 was obtained from scan data by adjusting the specimen position in the machine. This setup allowed for the acquisition of detailed data from the sample, as the voxel size was small enough to allow for the acquisition of small features, and the beam current and voltage were high enough to ensure the desired accuracy and resolution of the scan. It was necessary to reconstruct the obtained images using CT PRO 3D software from Nikon Metrology. Then, the images were processed using Dragonfly image processing software (Object Research Systems, QC, Canada) to detect process-induced defects and to determine their geometric properties, such as volume, area, aspect ratio, and position. In order to eliminate image noise from the scanned specimens, a detection threshold of 9 contiguous voxels was considered.

The presence of imperfections on the surface of L-PBF-Ti-6Al-4V samples can be reduced by machining. In spite of this, it still has the undesirable side effect of exposing the subsurface pores that are present in the material when it is produced by the L-PBF process. In a similar manner to inner pores, surface roughness is considered a potential cause of fatigue life degradation. In addition to having an impact on the HCF testing results, the specimen surface roughness has an effect on the VHCF testing results as well [238]. As a result, for the design of L-PBF-Ti-6Al-4V parts, it is imperative to consider the effects of the surface finish on the fatigue behavior of the built part. If the roughness is too large, the fatigue strength will be dominated by surface roughness[238]. It is considered a smooth surface if the surface finish of the sample is lower than the critical value[238]. Therefore, in order to determine the surface finish of samples, the Mitutoyo SJ-410 surface roughness measuring apparatus was used to ensure the surface finish did not exceed the threshold value.

An Ultrasonic Fatigue Testing machine (UFTM) developed at Concordia University [237] was used to characterize fatigue performance of additively manufactured Ti-6Al-4V alloy in very high cycle fatigue (VHCF) regime. It was determined that all of the specimens were run to failure in each test conducted, and there was no run out condition established for any of the tests performed. A total of 16 AB and 14 SR heat-treated samples were tested to obtain the S-N curve. Testing was carried out with a stress ratio of R = -1(fully reversed constant amplitude load Cycles) applied in a sinusoidal waveform with a frequency of 20 kHz ± 400 Hz. Cool air was used to maintain the temperature of the fatigue samples at room temperature during the tests of the specimens at a frequency of 20 kHz ± 400 Hz. To carry out the fatigue test, the loading direction was parallel to the building direction of the samples. UFT tests were initially performed on AB samples. Unusual UFT failures occurred both in AB and SR heat-treated samples. This appears to be due to the fact that UFT technology uses resonance to test specimens, which results in the testing sample not totally failing when the samples are tested. When the fatigue crack grows in size, there is a decrease in the stiffness of the sample and the resonance frequency as well. As soon as the crack in the sample reaches a certain size, the resonance frequency of the sample decreases. The frequency of the ultrasonic set is reduced to a level that is outside the operating range of the transducer, which causes the testing to stop. Afterward, the sample was completely fractured. The test set up and a sample test result is shown in **Fig. 92**.The reduction in the frequency of the sample might not have had a significant impact on the reduction of the ultrasonic sample-horn-booster set, as these specimens are lighter than other materials that are commonly tested. As a first step, a high-stress amplitude was applied, and then the stress amplitude was adjusted as a function of the previous stress-life results obtained from the sample in order to reach failure within the VHCF regime. There is no correlation between the number of samples in the graph and the order in which they were tested.

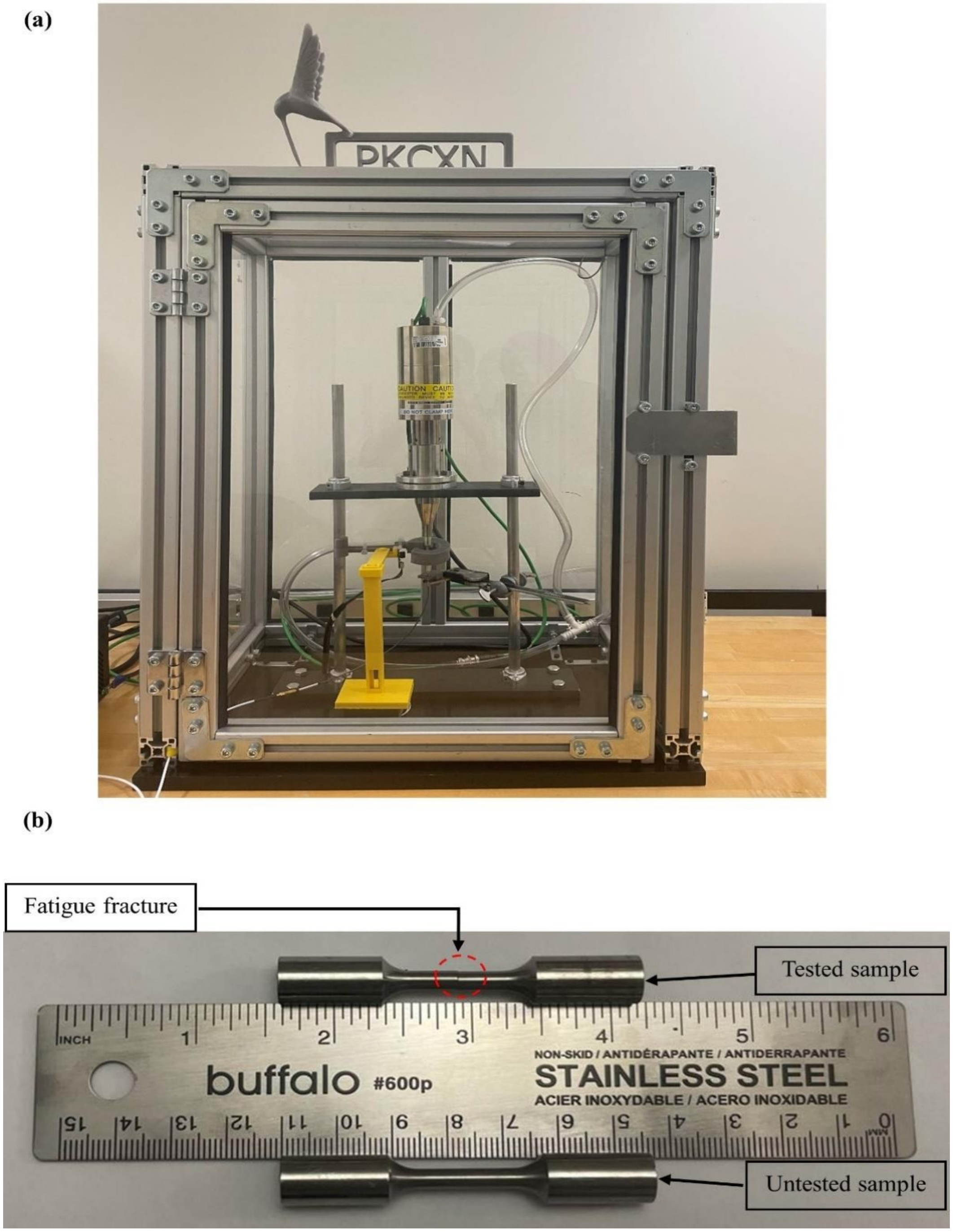

Fig. 92*. (a) Test set up (b)Fatigue fracture sample with dimension of the sample.*

A Scanning Electron Microscope (SEM) was used to observe and analyze the morphology of fatigue fractures after the VHCF test. Fractographic analyses were carried out on two samples for each condition. In the case of the AB condition, two samples tested under stresses of 76.05 MPa and 97.50 MPa to give 1.44E+09 and 7.2433E+07 cycles were used in the fractography process. In the case of the SR heat-treated condition, two samples tested under stresses of 88.01 MPa and 109.06 MPa to give 1.1964E+09 and 6.10E+07 cycles were used in the fractography process. A Hitachi Regulus 8230 SEM in secondary electron mode at 15 kV was used to examine the fracture surfaces and identify the fatigue crack initiation sites. Additionally, Energy-dispersive X-ray spectroscopy (EDS) was done to detect the chemical composition of the material on the fracture surface.

3.4 Results and discussion

3.4.1 S-N curve of the tested specimens

The S-N curve of the fatigue samples in **Fig. 93** shows the averaged results for the applied fully reversed fatigue strength and the number of cycles to failure from ultrasonic fatigue testing. It has been found that from the data of the S-N curves, there will be an increase in fatigue life with decreasing stress amplitude, without an increase in traditional fatigue life. From **Fig. 93**, it is clearly seen that heat treated samples exhibited improved VHCF performance compared to the AB samples. At the stress of 75.08 MPa, SR heat treated sample survived for an average of 8.81×10^9 cycles at 76.1 MPa whereas AB sample showed 3.13×10^9 cycles at 76.1 MPa.

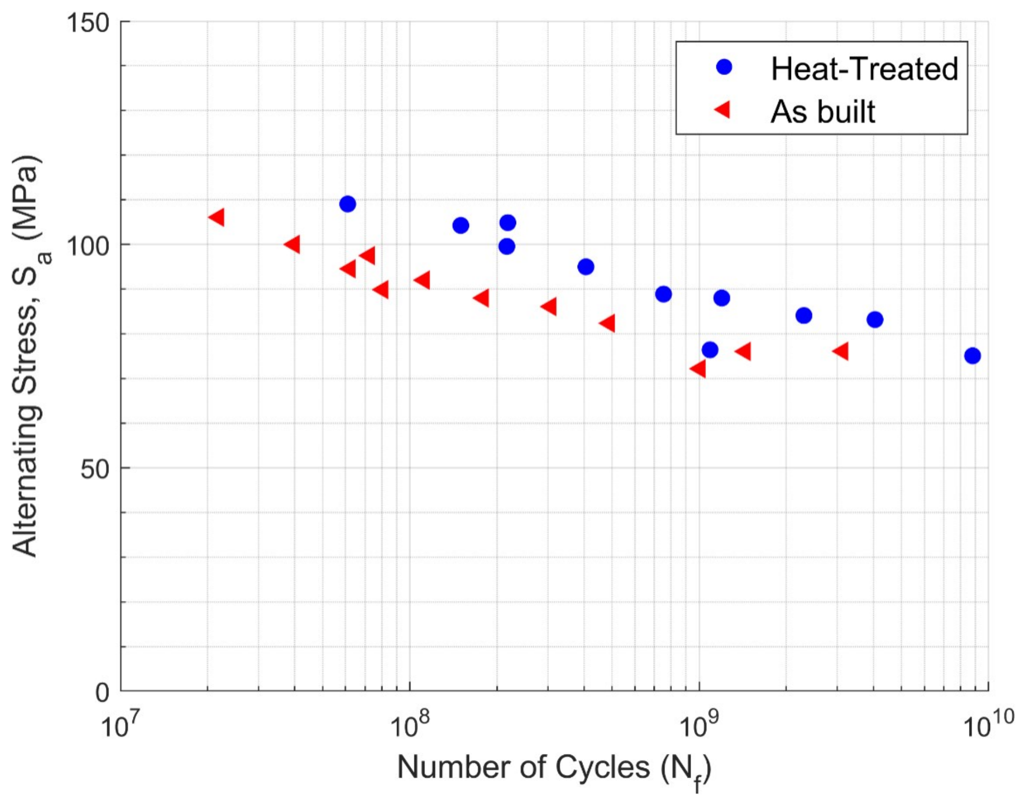

Fig. 93. *S-N curves superimposed for all the investigated conditions, namely (a) AB and (b) SR heat treated.*

As can be seen in the **Fig. 94**, the fatigue data was further fit with a Basquin fit in order to get a quantitative understanding of the observed results. When the fatigue data, applied fully reversed fatigue strength (S_{Nf}) and number of cycles to failure (N_f), is fitted with a Basquin fit [239], it can then be presented in the form of $S_{Nf} = a(N_f)^b$. It is possible to determine **'a'** by plotting the observed data on a log-log scale that is then fitted with linear regression, where **'a'** will be the intercept of the linear fit, and **'b'** will be its gradient. These parameters were extracted from the plots shown in **Fig. 94** and presented in **Table *9***.

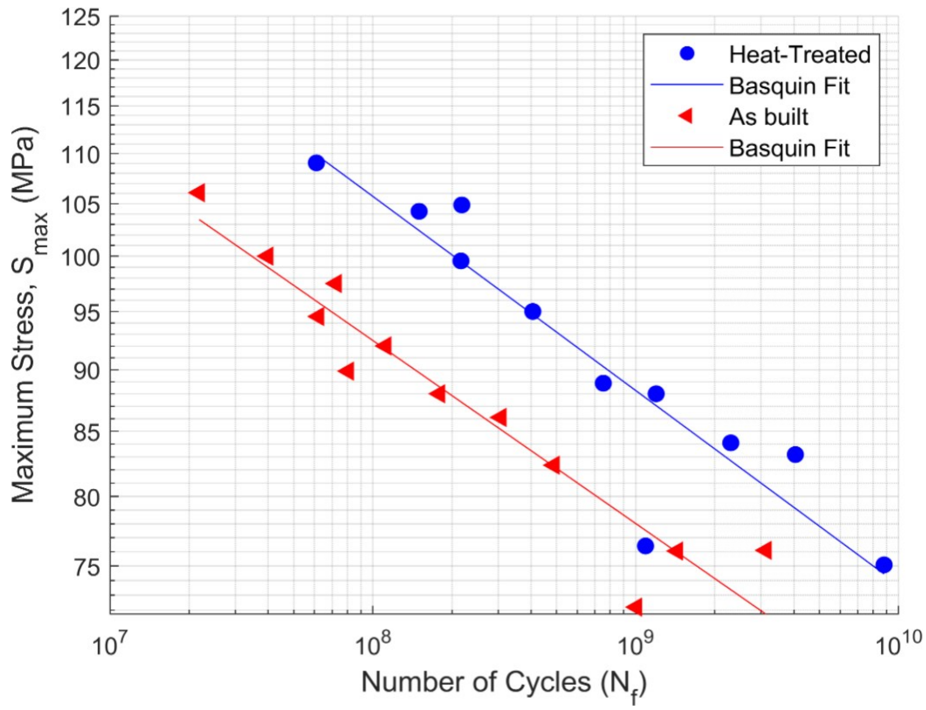

***Fig. 94**. Basquin S-N curves superimposed for all the investigated conditions, namely (a) AB and (b) SR heat treated.*

Table 9 Basquin fit parameters for the fatigue data of samples with different conditions.

Condition	Fatigue strength co-efficient, a	Fatigue strength exponent, b
AB	360.2961	-0.0738
Heat treated	447.3619	-0.0783

The curves in **Fig. 94** show that the SR heat treatment has significantly increased the fatigue performance of the samples at all tested stress levels. The fatigue strength exponent of the Basquin fit was increased from (360.30) to (447.36) after SR heat treatment, indicating a significantly increased performance alongside the overall shift to a higher cycles range at the lower stress levels.

The results from **Fig. 94** and **Table *9*** confirm a positive effect of SR heat treatments on the fatigue resistance of L-PBF-Ti-6Al-4V samples.

3.4.2 Effect of Surface roughness on fatigue performances

There is a strong correlation between the roughness of the surface and the fatigue life of the samples [39]. The surface roughness of Ti-6Al-4V specimens in both the AB and SR heat-treated conditions is illustrated in **Fig. 95**.

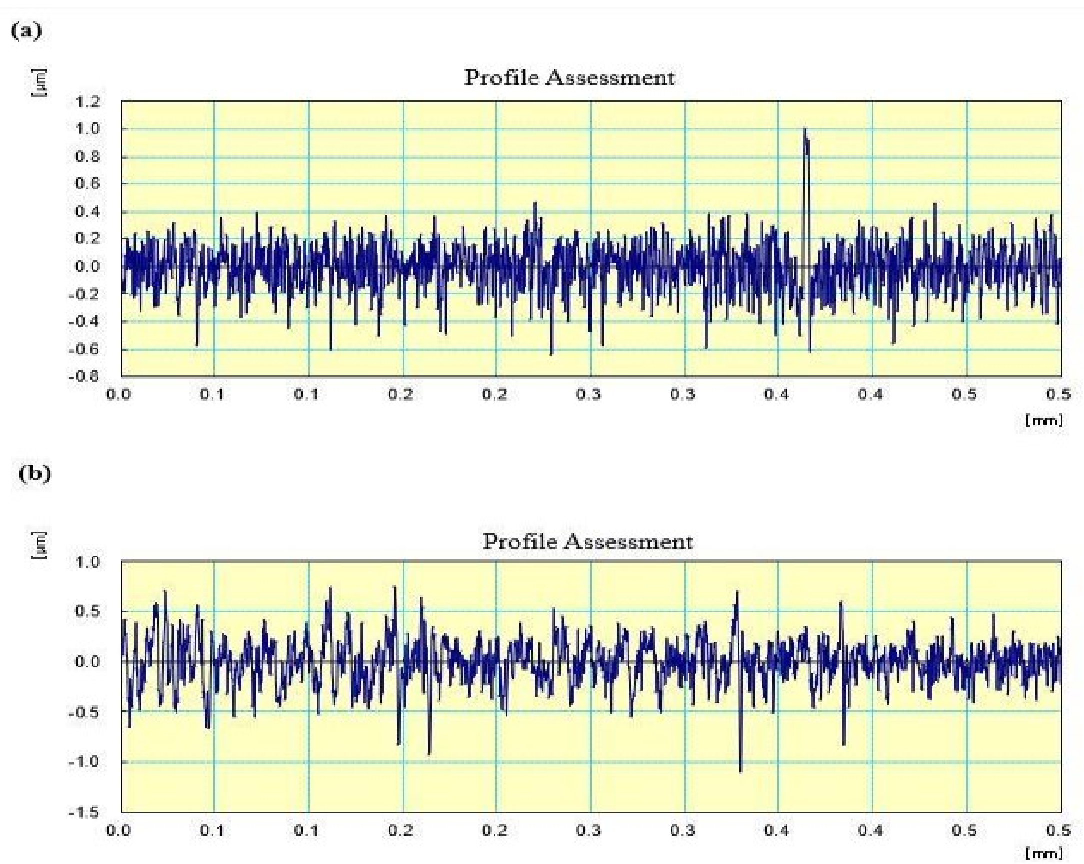

Fig. 95. *(a) Surface roughness profile of AB samples; (b) surface roughness profile of SR heat-treated samples.*

Surface roughness measurements were conducted with a cut length of 0.25 mm and an evaluation length of 16.50 mm. A fatigue fracture is most likely to occur at the gage length, the smallest portion of the dog bone-shaped specimen. Therefore, the surface roughness of the gage length 16.50 mm area of the test specimen represents the whole sample. The measurement software automatically recorded Twenty-four surface roughness indexes, including Ra, Rp, Rv, Rz, etc. The surface roughness parameters (Ra- Arithmetic mean roughness, Rp-Maximum height of the profile, Rz-Point height of irregularities, Rv- Maximum depth of the valley, RSm-Mean width of the profile elements, Rmr-Average support ratio of a unit) of specimens with two kinds of surface conditions are listed in **Table *10*** measured by the Mitutoyo SJ-410 surface roughness measuring apparatus.

Table 10 Surface roughness measurement of the tested samples

Type of specimen	Ra (μm)	Rz(μm)	Rp (μm)	Rv (μm)	Rsm (μm)	Rmr (%)
AB	0.125	0.855	0.375	0.479	29	0.230
Heat-treated	0.168	1.052	0.485	0.567	46.6	0.240

As a way of evaluating the surface profile of the material, this paper employs three of the most famous models of the stress concentration factor. These models are the Peterson model [240], the Neuber model [240], and the Arola-Ramulu model [241,242].

$$K_t1 = 1 + 2\sqrt{\frac{t}{r}}\ ;\ \text{(Peterson Model)} \qquad \text{Eq. 34}$$

$$K_t2 = 1 + 2\left(\frac{R_p}{z}\right)\left(\frac{R_a}{r}\right)\ ;\ \text{(Neuber model)} \qquad \text{Eq. 35}$$

$$K_t3 = 1 + 2 \times \frac{R_z}{r}\sqrt{\frac{b}{t}}\ ;\ (\text{Arola} - \text{Ramulu Model}) \qquad \text{Eq. 36}$$

Where,

$Kt1$=single-notch elastic stress concentration factor,

$Kt2$=continuous notch stress concentration factor, and

$Kt3$=stress concentration factor proposed by Arola-Ramulu.

t=notch depth.

r=radius of the notch valley,

b= average distance between surface gaps

The surface gaps b is equal to the average unit width Rsm [243] and the notch depth t is approximately equal to the maximum valley depth Rv [243].

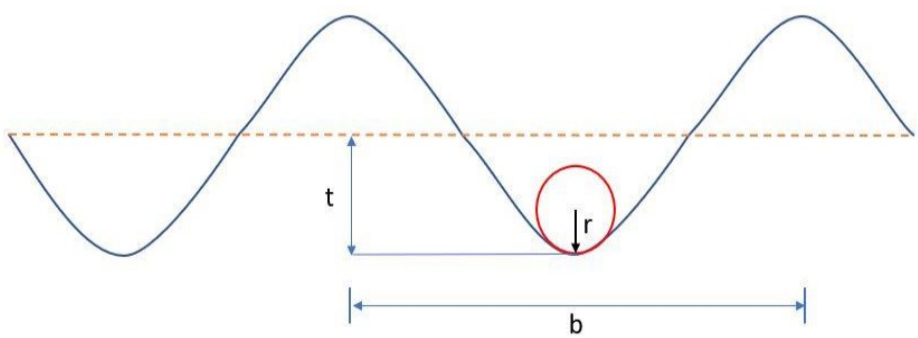

Fig. 96. *The calculation principle of equivalent notch root radius, depth of notch and average distance between surface gaps*

From equation **Eq. *34*** - **Eq. *36***, it is clearly seen that to calculate stress concentration factor from the surface roughness value, notch root radius r should be evaluated. Fang et al.[243] proposed a method to calculate notch root radius, r analytically. The authors proposed two equations: one for deep notch and another one for shallow notch.

For shallow notch ($t \leq \frac{w}{2}$),

$$r = \frac{t}{2} + \frac{w^2}{8t} \qquad \text{Eq. 37}$$

For deep notch ($t > \frac{w}{2}$),

$$r = \frac{w}{2} \qquad \text{Eq. 38}$$

Where, t is the notch depth and w is the notch width which is equal to Rsm(1-Rmr) [243]. After calculating the value of r, from equation **Eq. *37***- **Eq. *38*** stress intensity factor K_t was calculated which are listed in **Table 11**.

Table 11 The stress concentration factors obtained by different methods.

Sample	Notch root radius, r (μm)	K_t1 (Peterson model)	K_t2 (Arola-Ramulu model)	K_t3 (Neuber model)
AB	130.3619	1.1212	1.0008	1.0065
SR	276.8031	1.0905	1.0006	1.0044

From **Table 11**, it is clearly seen that the stress concentration factor K_t on the gage surface of the sample in SR heat-treated condition is little bit lower than the samples in AB condition. This is true for all the models. The reason is the notch root radius r which is higher in SR heat-treated samples. It is also seen that the value of stress concentration factor can be considered as equal to 1 for all the samples both in AB and SR heat-treated condition that means the surface finish of the samples were very smooth. So, it can be said that there was no impact or negligible impact of surface roughness on the VHCF performances of Ti-6Al-4V alloy.

3.4.3 Impact of defects on fatigue performances

It is shown in **Fig. 97** that X-ray μ-CT (computed tomography) results have been obtained as an indication of defect distribution in the tested samples of this alloy. The alloy was discovered to contain defects of different shapes and sizes. However, these defects made up only 0.0001% of the gage volume of the sample in AB condition whereas SR heat treatment drastically decreases the defect number which is 0.00001% of the gage volume indicating that in heat treated samples there were 10 times lower defects compared to the AB samples. The defects size was compared using √area parameter which is considered as a parameter for the size of the defects. For push-pull loads, it is mentioned that the critical defect size is in the range 30 μm- 46 μm [31]. It is seen that the range of √area parameter (effective defect size) for the samples in AB condition is between 20.01μm to 83.71μm (median defect-50.23 μm) whereas this range is between 14.15 μm to 34.66 μm (Median defect-35.24 μm) for the SR heat-treated samples which is almost 30% (in terms of median defect) lower than the AB samples.

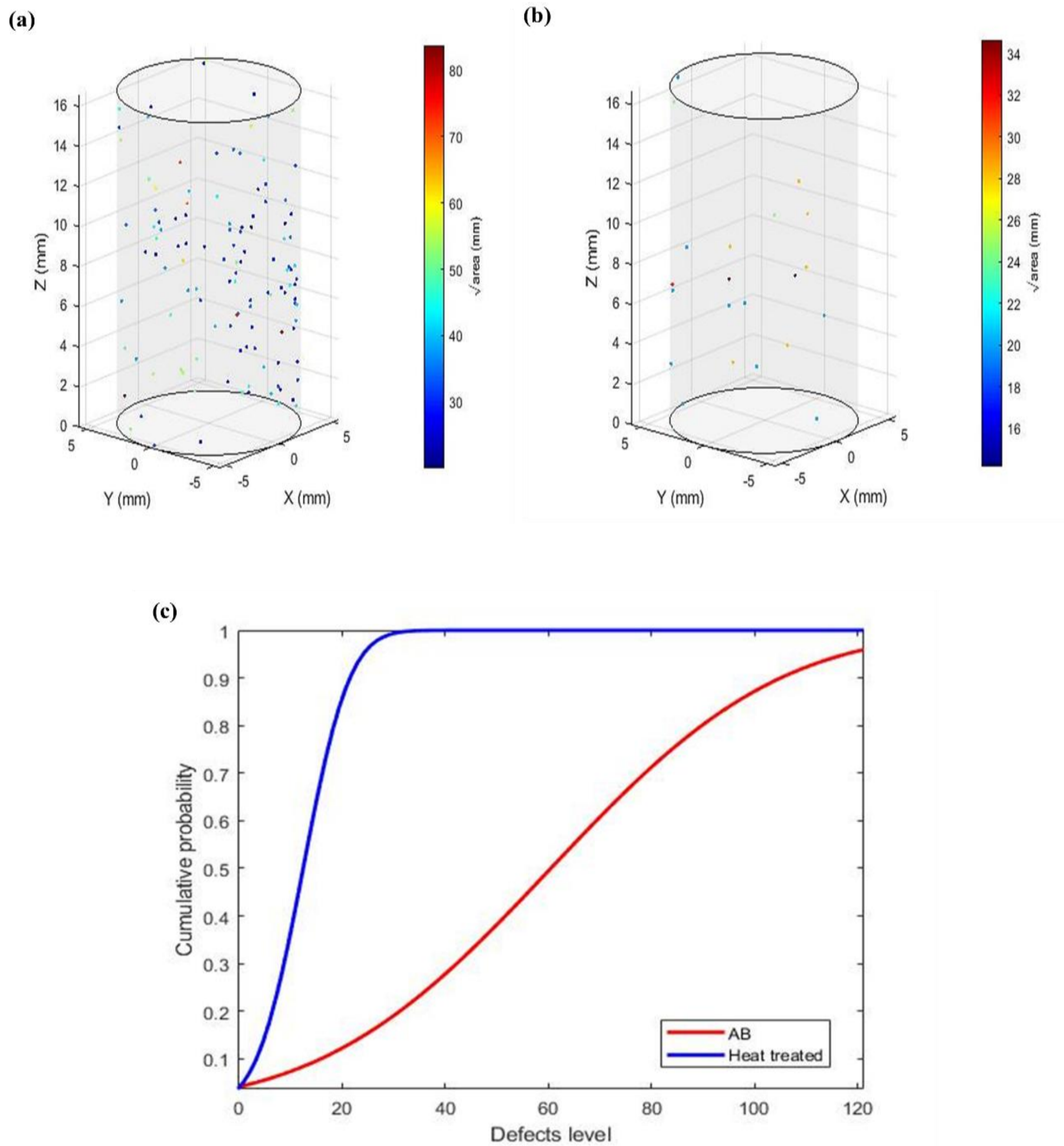

Fig. 97. *Defects distribution derived from μ-CT (a) AB condition; (b) SR heat-treated condition; (c) Cumulative probability of the defect distribution for each condition.*

Further, to detect the defect position, a new location parameter L is proposed.

$$L = \frac{r}{R}; 0 \leq L \leq 1 \quad \text{Eq. 39}$$

Where,

r = Radial position of the defect in polar coordinate system from the center; and

R = radius of the fatigue fracture surface

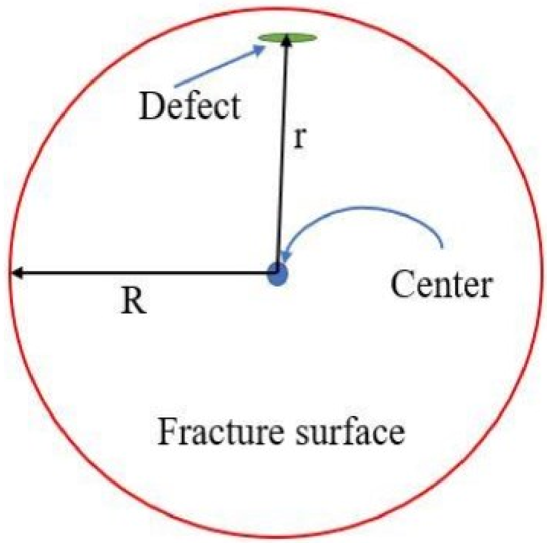

Fig. 98. *Schematic diagram of the fracture surface with defect feature.*

Larger values of the parameter L indicate a higher probability of cracks initiating at surface defects. A defect that has an L value ranging between 0.9 and 1 is classified as a surface defect; a defect that has an L value between 0.8 and 0.9 is classified as a subsurface defect; and a defect that has an L value between 0 and 0.8 is classified as an internal defect. A MATLAB script was written to detect the position of the defects using location parameter displayed in

Fig. *99* and **Fig. 100**. In AB samples there are 97 surface defects (80.83% of total pores), 10 sub-surface defects (8.33% of total pores), 13 internal defects (10.83% of total pores) whereas in heat treated samples there are 16 surface defects (66.67% of total pores), 6 sub-surface defects (25% of total pores), 2 internal defects (8.33% of total pores). In addition, there are 5 defects (4.17% of total defects) that have a stress intensity factor exceeding 1.5 MPa.m$^{-1/2}$ in AB samples whereas in

SR heat-treated samples there was no defect that has a stress intensity factor exceeding 1.5 $MPa.m^{-1/2}$.

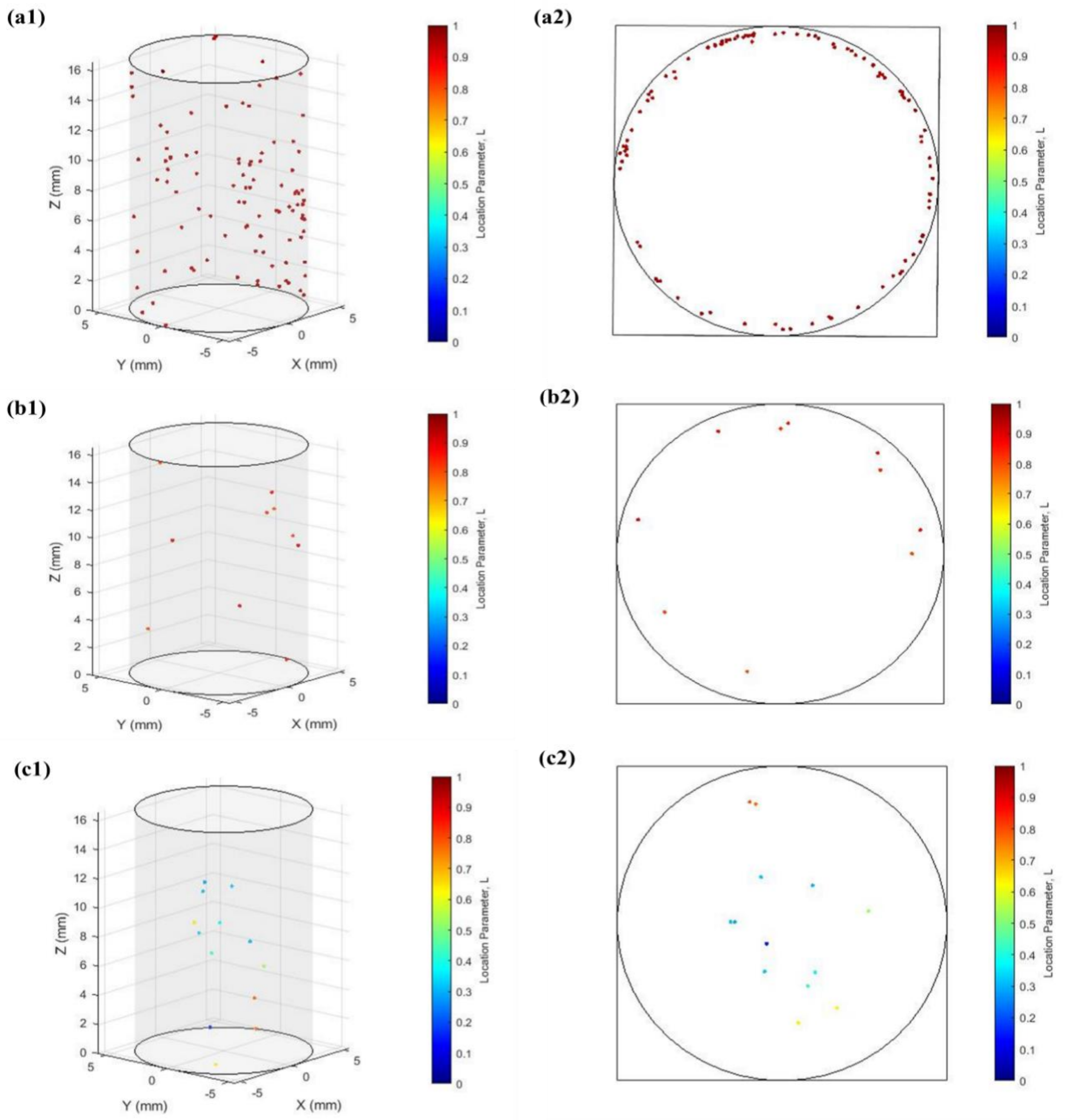

Fig. 99. *Defect location in AB samples derived from µ-CT (a) surface defects (b) subsurface defects (c) Internal defects.*

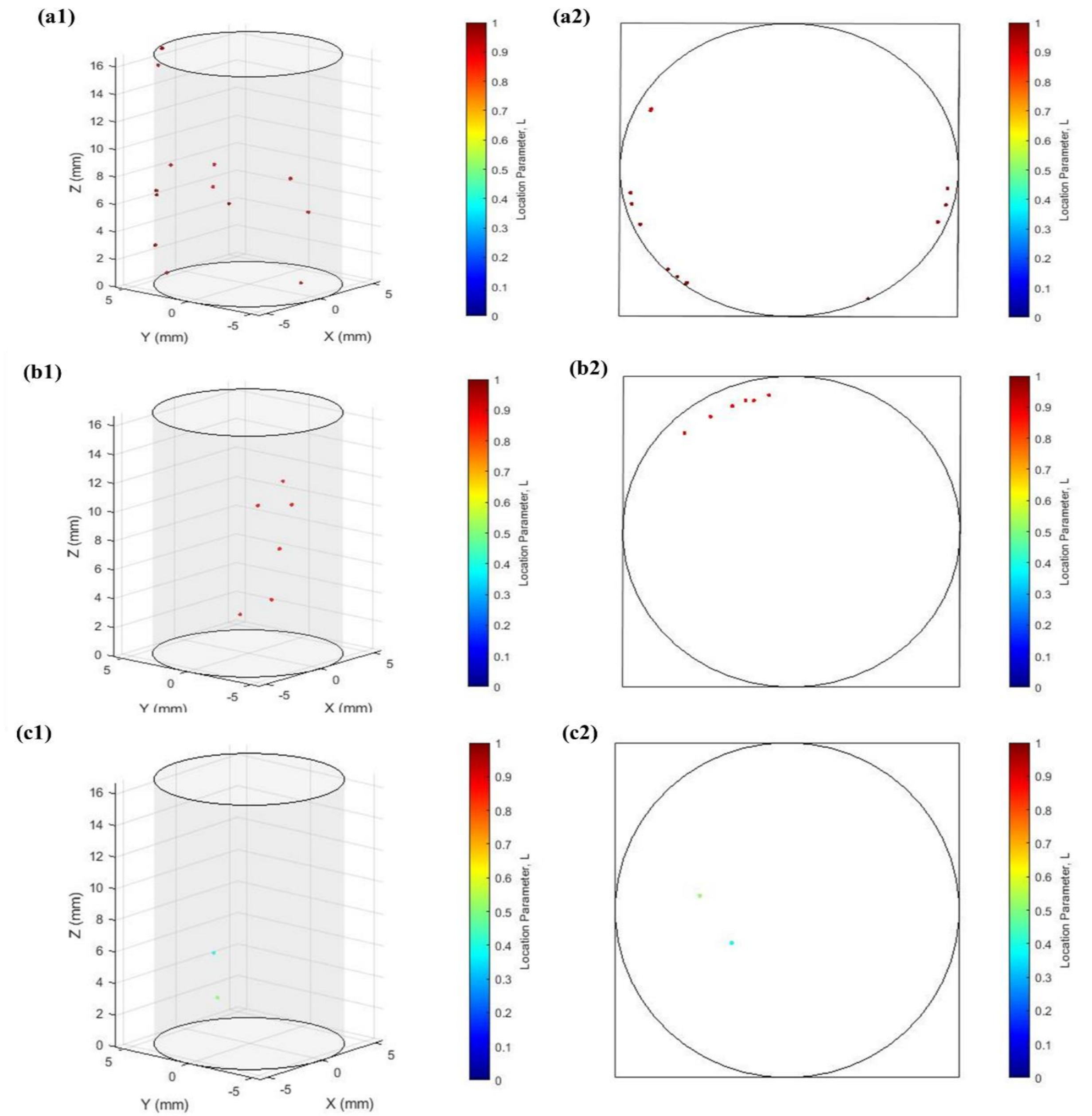

Fig. 100. *Defect location in SR heat treated samples derived from μ-CT (a) surface defects (b) subsurface defect (c) Internal defects.*

Fig. 101 displays the number of defect statistics for each condition. It is clearly seen that SR heat-treatment decreases the defects level irrespective of the position of the defects. Additionally, it is clearly visible that after SR heat-treatment both internal and sub surface defects critical for very high cycle fatigue [128] decreases.

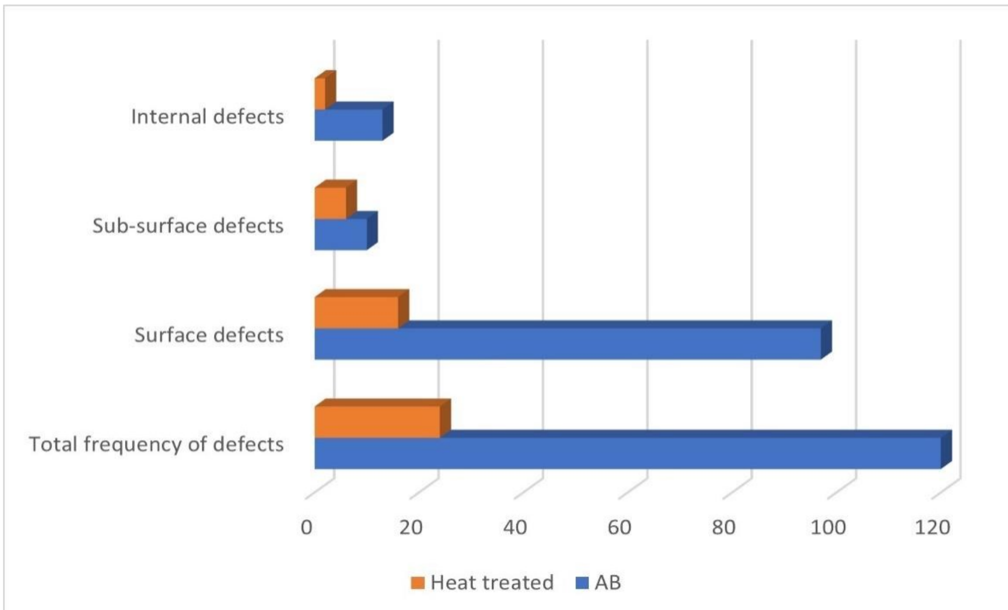

Fig. 101. *Defects statistics for the tested samples in each condition.*

It is almost established that the higher the defects level, the lower the fatigue performance [31]. So, higher defects level in AB samples might be one of the reasons of degrading fatigue life compared to SR heat-treated samples.

Analyzing the µ-CT scan results also enable us to determine the equivalent diameter and Feret diameter of the defects for further investigation. A volume-equivalent sphere has a diameter equal to the same volume as an equivalent spherical diameter, and its diameter has been calculated using the following equation [244].

$$D_v = (\frac{6}{\pi} V_d)^{\frac{1}{3}} \qquad \text{Eq. 40}$$

where D_v is the diameter of the volume-equivalent sphere and V_d is the volume of the defect.

Feret diameter is a measurement of the size of an object or particle in two dimensions. It is defined as the distance between two parallel lines that are tangential to the object on opposite sides and perpendicular to a specified direction, typically the longest axis of the object.

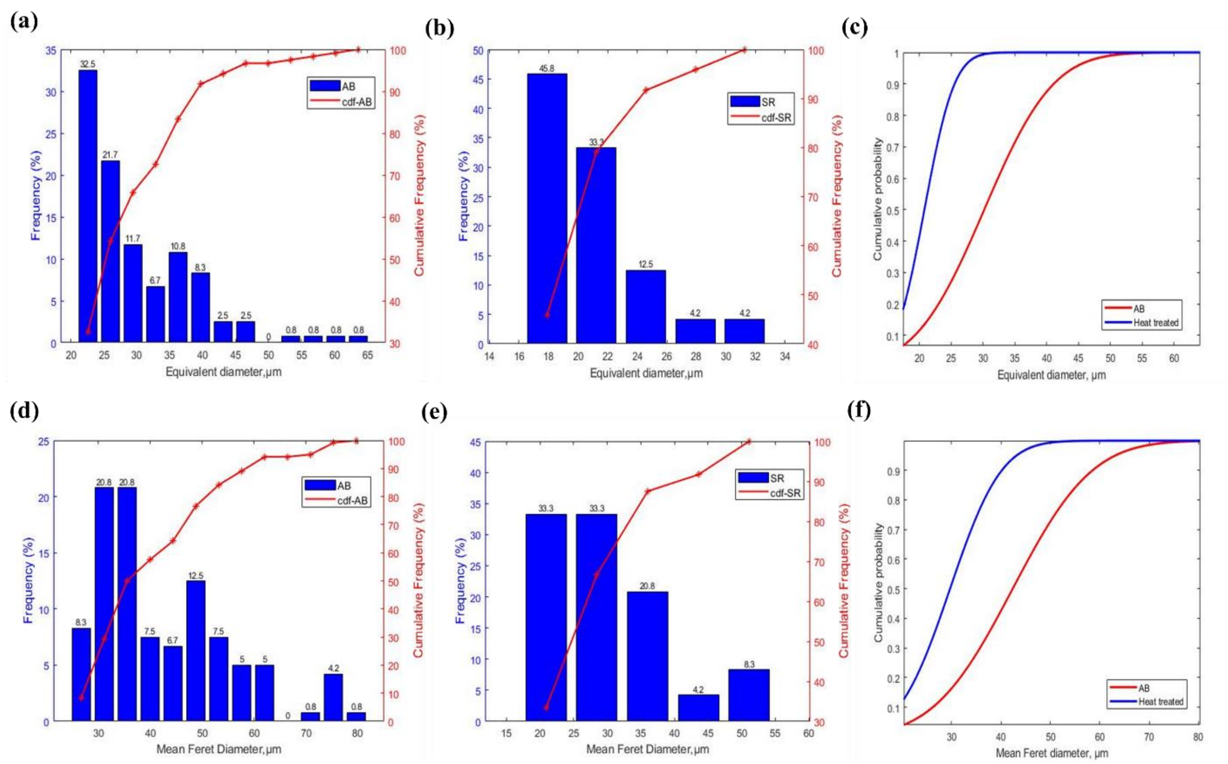

Fig. 102. *(a) equivalent diameter of AB samples (b) equivalent diameter of SR heat-treated samples (c) Cumulative probability of the equivalent diameter for each condition (d) Mean Feret diameter of AB samples (b) Mean Feret diameter of SR heat-treated samples (c) Cumulative probability of the mean Feret diameter for each condition.*

In other words, the Feret diameter is the maximum distance between any two points along a straight line that can be drawn across an object, while staying within the object's boundaries. It is commonly used in image analysis to quantify the size and shape of particles. **Fig. 102** (a) displays the spread of equivalent diameters of the defects in AB condition. Most of the defects have equivalent diameters between 22.56 to 63.68 μm, with the highest number of defects falling in the range of 22.56 to 24 μm, accounting for 32.5% of the total. **Fig. 102** (b) displays the spread of equivalent diameters of the defects in SR heat-treated condition. Most of the defects have equivalent diameters between 17.9026 to 31.2787 μm, with the highest number of defects falling in the range of 17.9026 to 19.26 μm, accounting for 45.8% of the total. From **Fig. 102** (c), it is seen that cumulative frequency of defects with equivalent diameters for AB samples between 17.9026 and 27.94 μm is around 96% whereas cumulative frequency of defects with equivalent diameters for SR heat-treated samples between 22.56 and 46.54 μm is around 97%. So, it is seen that the maximum equivalent spherical diameter of the defects of SR heat-treated samples is lower (~51 %) than the AB samples. According to the basics of mechanics, higher spherical diameter will give higher stress ultimately early crack initiation. When defects appear freely inside the specimen, their size in terms of Feret diameter needs to be taken into account. **Fig. 102** (d) demonstrates that the mean Feret diameter of AB samples is primarily distributed between 26.69 to 79.77 μm, with a peak frequency of 20.8% of the total from 28.67 to 35.24 μm. In addition, it was observed that there are defects of a size of 60 to 79.77 μm in the sample, yet their frequency is very low. In SR heat-treated condition, **Fig. 102** (e) demonstrates that the mean Feret diameter is primarily distributed between 20.91 to 51.312 μm, with a peak frequency of 20.91 to 31.49 μm, making up 33.3% of the total. From **Fig. 102** (f), it is seen that cumulative frequency of defects with mean Feret diameters for AB samples between 26.69 and 62.01 μm is around 95% whereas cumulative frequency of defects with equivalent diameters for SR heat-treated samples between 20.91 and 51.1312 μm is 100 %. So, it is seen that the maximum Feret diameter of the defects of heat-treated samples is lower (~36 %) than the AB samples which might be another reason of getting improved fatigue performance for SR heat-treated samples. **Fig. 103** (a) displays the spread of volume of the defects in AB samples. Most of the defects have volume between 6.0086E+03 to 1.3519E+05 μm^3, with the highest number of defects falling in the range of 6.0086E+03 to 1.040E+04 μm^3, accounting for 54.2% of the total. **Fig. 103** (b) displays the spread of volume of the defects in SR heat-treated samples. Most of the defects have volume between 3.0043E+03 to 1.6023E+04 μm^3, with the highest number of defects falling in the range of 3.0043E+03 to 4.078E+03 μm^3, accounting for 58.3% of the total. **Fig. 103** (c) displays that the cumulative frequency of defects in AB condition with volume between 6.0086E+04 and 9.21325E+04 μm^3 is around 98.33% whereas the cumulative frequency of defects for SR heat-treated samples with volume between 3.0043E+03 and 1.08E+04 μm^3 is around 96%. So, it is seen that the maximum volume of the defects of SR heat-treated samples is lower (~ 99 %) than the AB samples. **Fig. 103** (d) displays the spread of actual surface area of the defects in AB samples. Most of the defects have surface area between 1.6027E+03 to 1.3687E+04 μm^2, with the highest number of defects falling in the range of 1.6027E+03 to 2.059E+03 μm^2, accounting for 35.8% of the total. **Fig. 103** (e) displays the spread of actual surface area of the defects in SR heat-treated samples. Most of the defects have surface area between 1.0154E+03 to 3.2353E+03 μm^2, with the highest number of defects falling in the range of 1.0154E+03 to 1.194E+03 μm^2, accounting for 50% of the total. The cumulative frequency of defects with actual surface area between 1.6027E+03 and 1.07E+04 μm^2 is around 98% in AB condition whereas he cumulative frequency of defects with actual surface area between 1.0154E+03 and 2.791E+03 μm^2 is around 96% in SR heat-treated samples as shown in **Fig. 103** (f). So, it is seen that the surface area of the defects of SR heat-treated samples is lower (~ 77 %) than the AB samples.

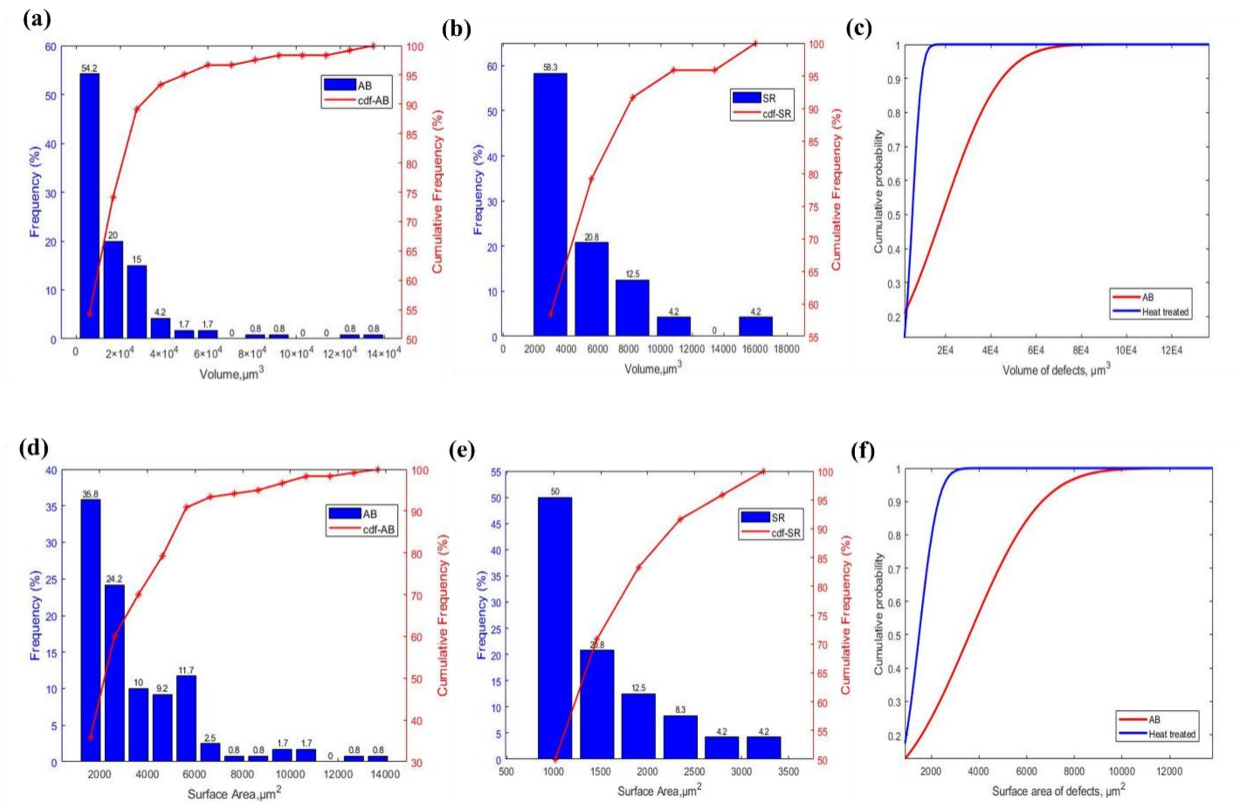

Fig. 103. *(a) defects volume of AB samples (b) defects volume of SR heat-treated samples (c) Cumulative probability of the defects volume for each condition (d) surface area of defects of AB samples (b) surface area of defects of SR heat-treated samples (c) Cumulative probability of the surface area of defects for each condition.*

The shape of the defects can also impact VHCF performances. To analyze shape of the defects, three parameters: shape factor, aspect ratio and sphericity are calculated from the data of μ-CT. In order to determine the shape factor S for a defect, the area of a sphere with the same volume as the defect must be compared to its actual area [128], that is,

$$S = \frac{{A_d}^3}{36 \times \pi \times {V_d}^2} \quad \text{Eq. 41}$$

where the V_d means the volume of the defect and A_d defines the actual area of the defect.

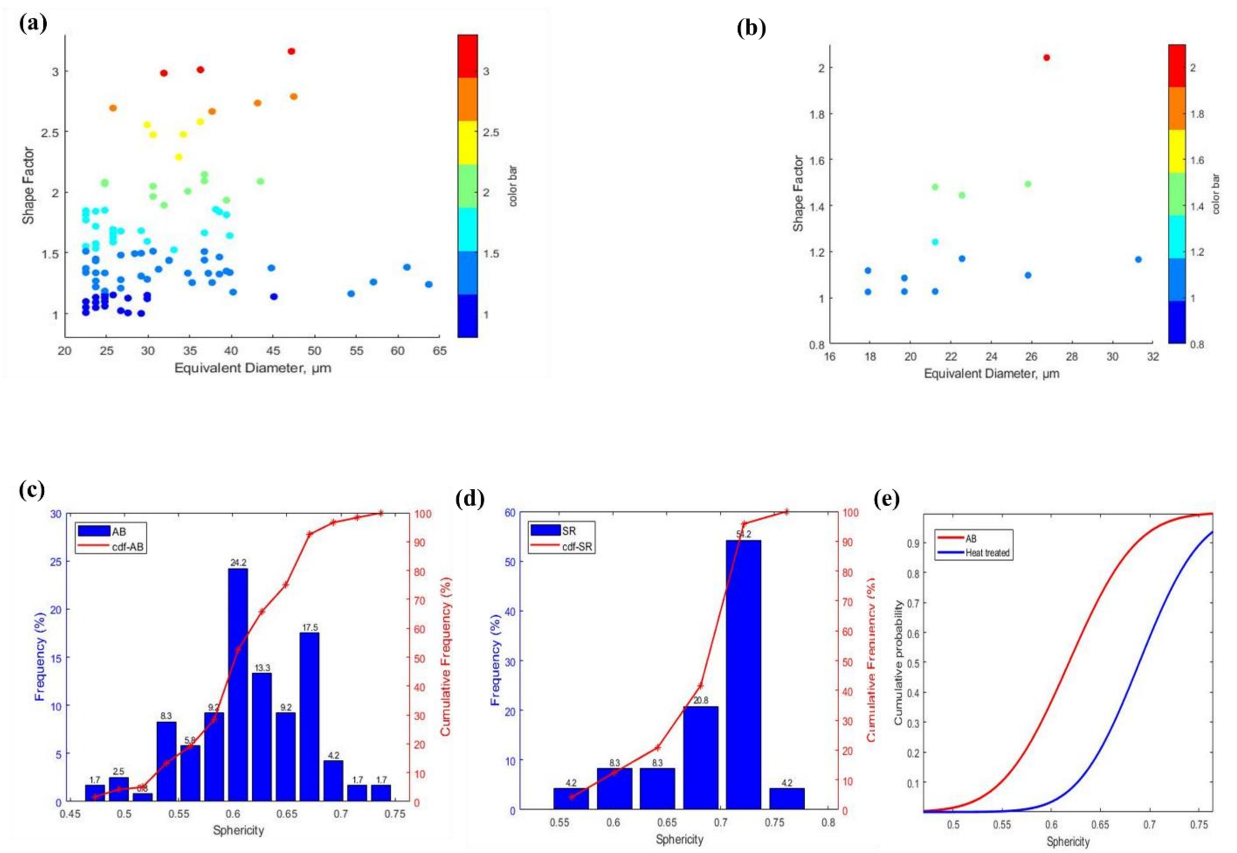

Fig. 104. *(a) shape factor of the defects in AB condition (b) shape factor of the defects in SR heat-treated condition (c) sphericity of the defects in AB condition (d) sphericity of the defects in SR heat-treated condition (e) Cumulative probability of the sphericity of defects for each condition.*

On the other hand, the sphericity of a defect refers to how much it deviates from a perfectly spherical shape, indicating its size and shape's similarity to a sphere [245]. The sphericity of the defects can be calculated using the given equation [244,245],

$$Sphericity = \left(\frac{Surface\ area\ of\ sphere\ of\ same\ volume}{Actual\ surface\ area\ of\ defect}\right) \qquad \text{Eq. 42}$$

Fig. 104 (a) demonstrates that the shape factors (S) of the defects in AB condition are mainly distributed between 0.9605 and 3.1606. It can be seen that at least 19 defects have shape factors of more than 2. **Fig. 104** (b) demonstrates that the shape factors (S) of the defects in SR heat-treated condition are mainly distributed between 1.0140 and 2.0423. It is clearly seen that only 1 defect has shape factor more than 2 and most of the shape factors are below 1.2. The higher the shape factor the higher the stress intensity factor ultimately the higher risk of crack initiation from those defects [128]. So, the possibilities of premature failure that will give lower fatigue performance from the defects are higher in AB samples than SR heat-treated samples. **Fig. 104** (c) displays the spread of sphericity of the defects. Most of the defects have sphericity between 0.4726 to 0.7373, with the highest number of defects falling in the range of 0.60 to 0.614, accounting for 24.2% of the total. **Fig. 104** (d) displays the spread of sphericity of the defects. Most of the defects have sphericity between 0.5612 to 0.7616, with the highest number of defects falling in the range of 0.71 to 0.74, accounting for 54.2% of the total. **Fig. 104** (e) shows that the cumulative frequency of defects with sphericity between 0.4375 and 0.772 is around 99% in AB condition whereas the cumulative frequency of defects with sphericity between 0.5612 and 0.715 is around 96% in SR heat-treated condition. Generally, defects with higher sphericity are more stable and less likely to cause issues than those with lower sphericity [246].

Fig. 105 compares the pdf, $fStress_{3.12\times10^9}$, of the VHCF strength at $N_f = 3.12 \times 10^9$ cycles for the median defect size, for each tested condition (median defect size =50.29 μm for AB, and 35.24 μm for SR). **Fig. 105** validates that the SR heat -treatment has a positive impact on the VHCF response of L-PBF-Ti-6Al-4V alloy. The reduction in VHCF response is approximately 6.37 % for 3.12 × 10^9 cycles when considering the median value. As a result, it is confirmed that the investigated SR heat treatment can be utilized for VHCF applications of LPBF-Ti-6Al-4V components.

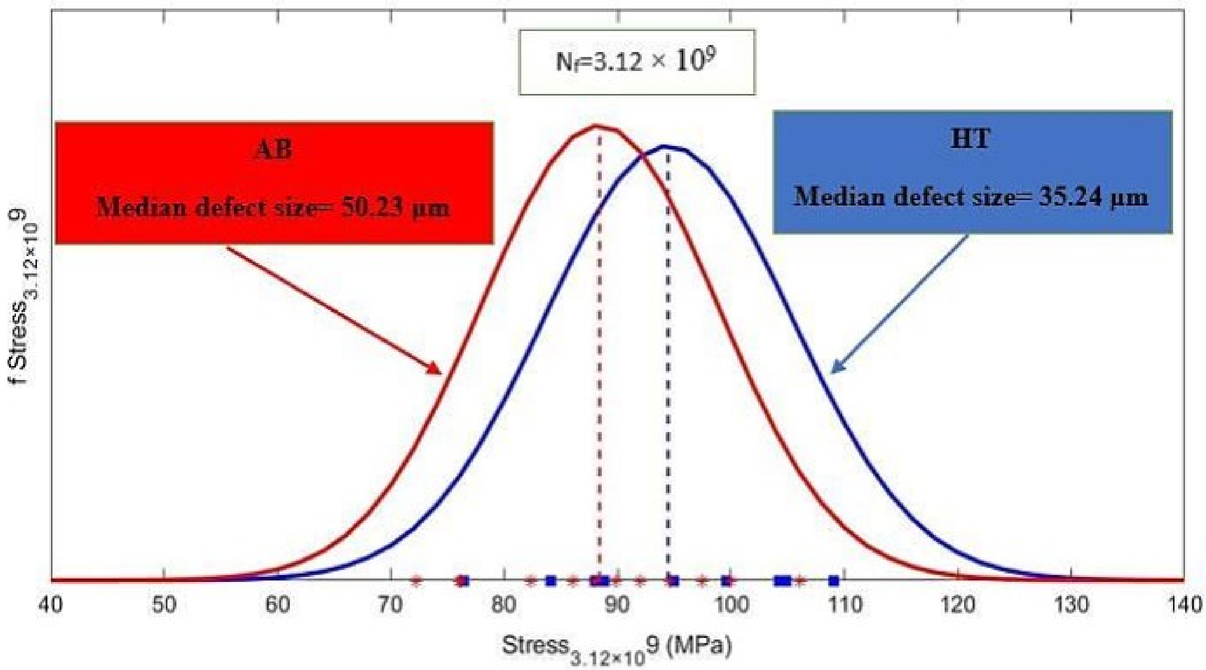

Fig. 105. *Probability density function of tested stresses at 3.12 × 10^9 cycles.*

3.4.4 Impact of microstructure on fatigue performances

There is a strong correlation between microstructure and fatigue behavior of L-PBF-Ti-6Al-4V samples [31]. The appropriate conditioning, reduction, or removal of pores may not improve fatigue performance if the microstructure necessary to satisfy the optimal combination of strength and ductility is sacrificed simultaneously [31].The microstructure of Ti–6Al–4V in its as-built configuration exhibits an acicular martensitic structure. There are fine needles of α′ martensite (supersaturated α slid solution [247]) visible in the figure **Fig. 106** (a). These α′ martensitic microstructure is brittle in nature [248]. It was also observed that Prior columnar β grains occurred in the direction of the building. A typical Martensitic microstructure in AB condition results from the rapid cooling rates during L-PBF processes [34].

(a)

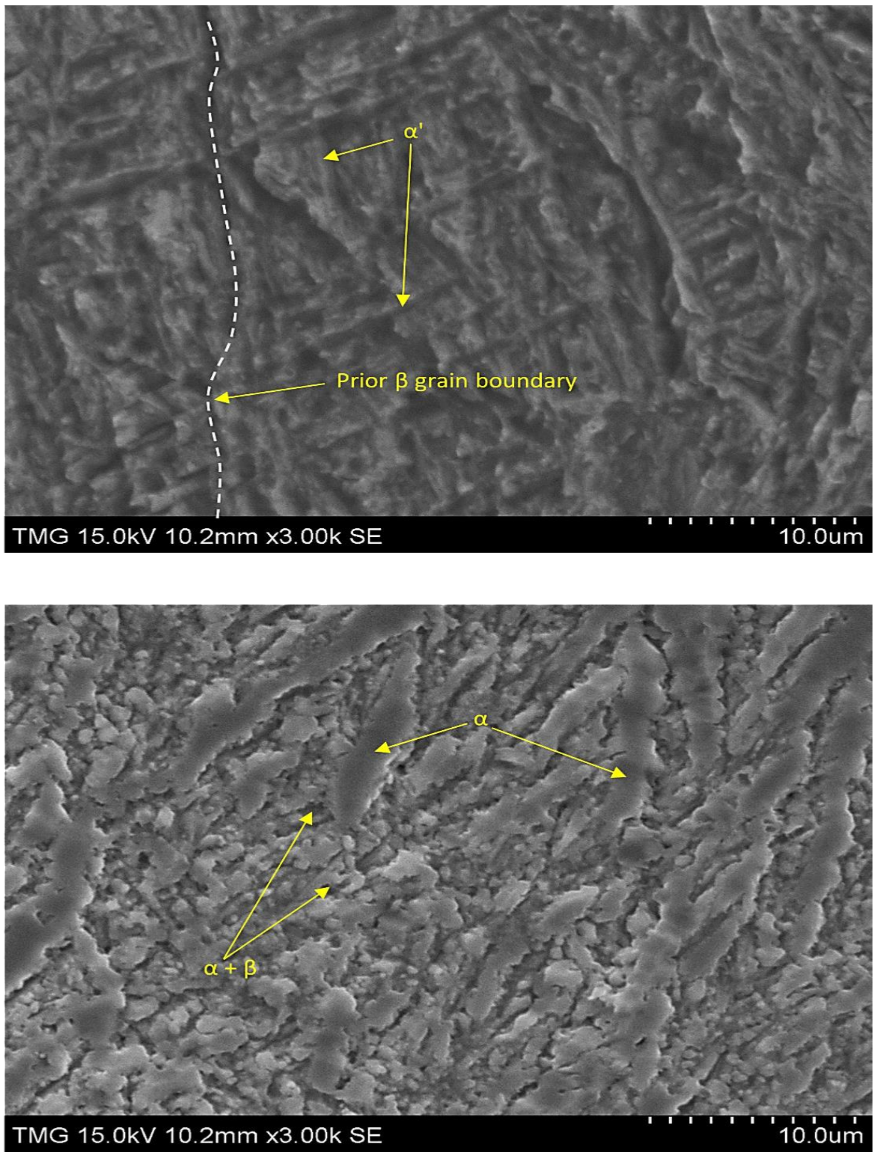

(b)

Fig. 106. *SEM micrographs of the microstructures of (a) AB (b) SR*

Fig. 106 (b), shows that a mixture of α+β/ α′ microstructure with increased α lathe thickness is achieved in the Ti-6Al-4V alloy after the SR heat treatment due to the incomplete decomposition of α′ martensite. This new microstructure is beneficial to the improved fatigue performance of Ti-

6Al-4V alloy [77]. The decomposition of the α’ martensite to α+ β is the reason for this lamellar microstructure. So, it can be said that stress relieved heat treatment increases the lamellar α phase which supports the outcome of Yu et al.[157]. Moreover, another aspect contributing to the improvement can be pointed out as the refinement of the α martensitic microstructure into a more finely lamellar α + β microstructure. It has also been demonstrated that the transformation from a α martensitic microstructure to a α + β lamellar microstructure increased the ductility of the material, which is advantageous in preventing crack propagation [77]. Therefore, it can be concluded that a lamellar α + β/ α′ microstructure with increased α lath thickness, freed from residual stresses by SR heat-treatment, can result in superior fatigue performance. Therefore, an optimum balance between strength and ductility can be found after SR heat treatment due to the lamellar structure (**Fig. 106** (b)). In addition to this rationale, the chosen SR heat-treatment appears to be beneficial for fatigue performance because it reduces lamellar crack initiation and propagation.

3.5 Fractographic morphologies

Fig. 107 shows the fracture surface morphologies of AB fatigue samples. There are three main zones on the fatigue fracture surface: (I) the cracked region, where cracks initiate and grow slowly, (II) the steady propagation region, where cracks propagate continuously, and (III) the final overload/fracture region, where fast crack propagation will be found giving ultimate fracture. Zone (I) is where a crack is first nucleated, and it occupies a larger area fraction of the fracture surface compared to the further stages of failure irrespective of the stress applied. At a stress amplitude of 97.50 MPa, the radius of zone (I) was 2.5 ± 0.2 mm, whereas this radius decreased to 2.40 ± 0.05 mm at nominal stress amplitude of 76.50 MPa which is virtually the same. **Fig. 107** also shows that after-crack initiation, crack propagated across the sample along a horizontal plane until zone

(III) when the fracture surface shifted to a plane that is inclined to the flat surface. The samples that were tested failed due to subsurface and internal defects, which were found to be almost similar. **Fig. 107** (a) shows the fracture surface of the sample failed after 7.24 × 10^7 cycles, where it can be observed that the crack started from a sub-surface defect and spread to the rest of the sample.

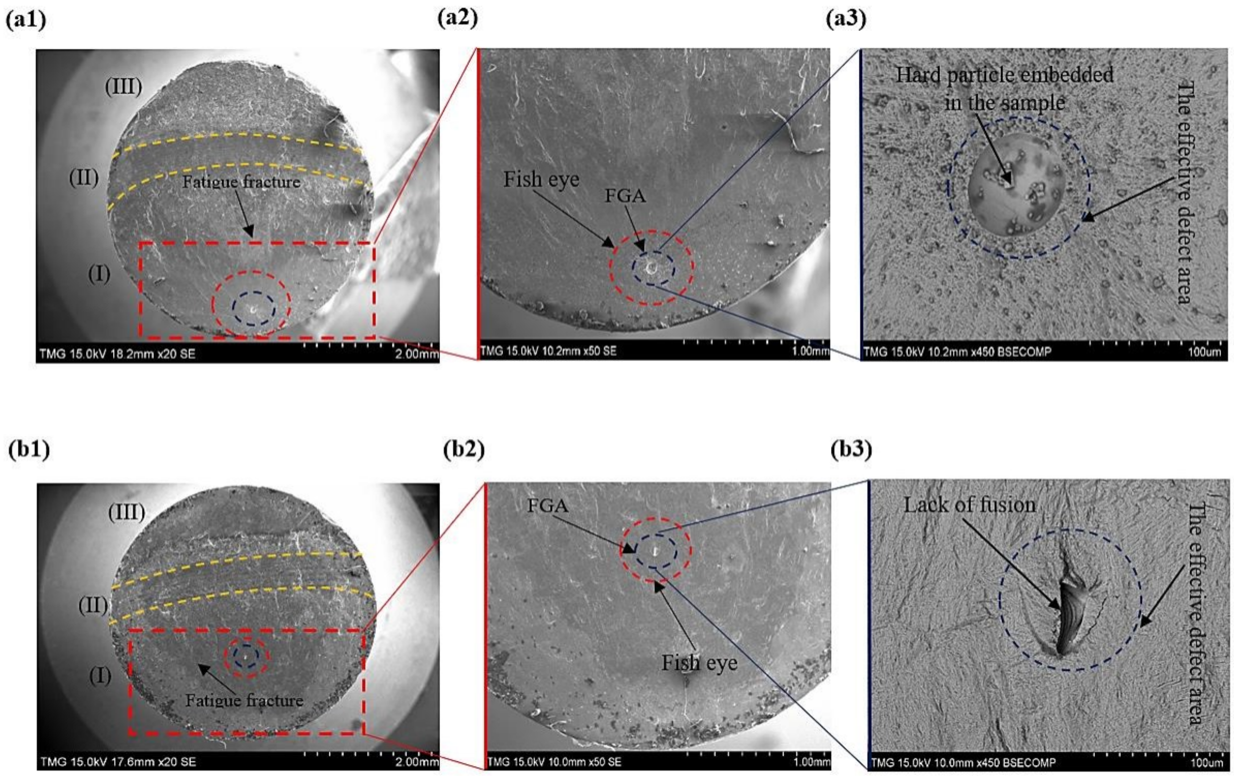

Fig. 107*. Micrographs of fatigue fracture of the L-PBF-Ti-6Al-4V samples in AB condition: (a) sub surface defect from lack of fusion (σ_a = 97.50 MPa, N_f = 7.24 × 10^7); (b) internal defect from lack of fusion (σ_a = 76.50 MPa, N_f = 1.44 × 10^9).*

In addition, the sample tested had a fisheye (FiE) structure around the crack initiation defect (lack of fusion) with fine granular area (FGA) in the center of the FiE which consumes most of fatigue lives. The samples subjected to cyclic loading suffer from stress concentration around defects (such as inclusions or voids). It is usually from these stress concentration areas that fatigue cracks begin to form. It may grow slowly, and the formation of an FGA may occur as a result of cyclic pressing (NCP), which then leads to a FiE pattern [249,250]. Therefore, an essential factor in determining the fatigue performance of Ti-6Al-4V is the size of the defects generated during the process of SLM. **Fig. 107** (b) depicts the fracture of the samples that failed at 1.44 x 10^9 cycles, where the crack originated from an internal defect and propagated along the sample surface. Similarly, to the previous sample, this one also had a FiE structure around the crack initiation defect, with a radial decorative pattern of transgranular fracture around the FiE zone. Here, also lack of fusion is visible in the fracture surface. It can be said that FiE structure with FGA at the center is the characteristics region for AB L-PBF-Ti-6Al-4V samples in VHCF regime. Regardless of whether a microcrack propagates internally or subsurfacely, due to the vacuum environment, microcrack propagation was slowed down, and fatigue life was prolonged, while surface defects experienced faster growth of microcracks because of exposure to the air [218]. Additionally, some foreign particles with spherical shape were observed on the fracture surfaces, as shown in **Fig. 108**. At point 1 (spectrum 1) in **Fig. 108** , the relative chemical composition calculated from EDS analysis was 7.61wt%Al, 4.63wt% V, and 87.86wt% Ti, whereas at point 2 (spectrum 2), the relative chemical composition was 6.09wt% Al, 3.92wt% V, and 92.37wt% Ti. It is possible that this particle is laser spatter based on its composition and spherical morphology. **Fig. 109** shows the fracture surface morphologies of the SR heat-treated fatigue samples. Here again, three main zones like AB samples (the cracked region, the steady propagation region, and the final overload/fracture region) were visible. The samples that were tested failed due to surface and internal defects, which were found. **Fig. 109** (a) shows the fracture surface of the sample failed after 6.10 × 10^7 cycles, where it can be observed that the crack started from a sub-surface defect like AB samples and spread to the rest of the sample. All these crack initiation sites are associated with lack of fusion defects with the main crack initiation site leading to the final fracture. Similar to AB samples the SR heat-treated samples tested had a FiE structure around the crack initiation defect (lack of fusion) with fine granular area (FGA) in the center of the FiE.

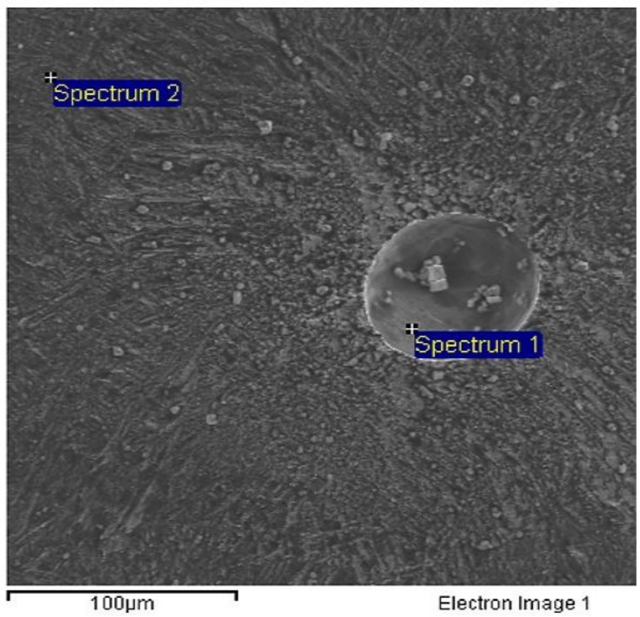

Fig. 108. *Embedded hard particle on the fracture surface of AB sample showing the particle rich in Al, V*

Fig. 109 (b) depicts the fracture of the specimens that failed at 1.20 x 10^9 cycles, where the crack originated from a sub-surface defect (lack of fusion) like the previous one and propagated along the specimen surface. In the crack initiation sites, multiple crack initiation sites were found along with secondary crack.

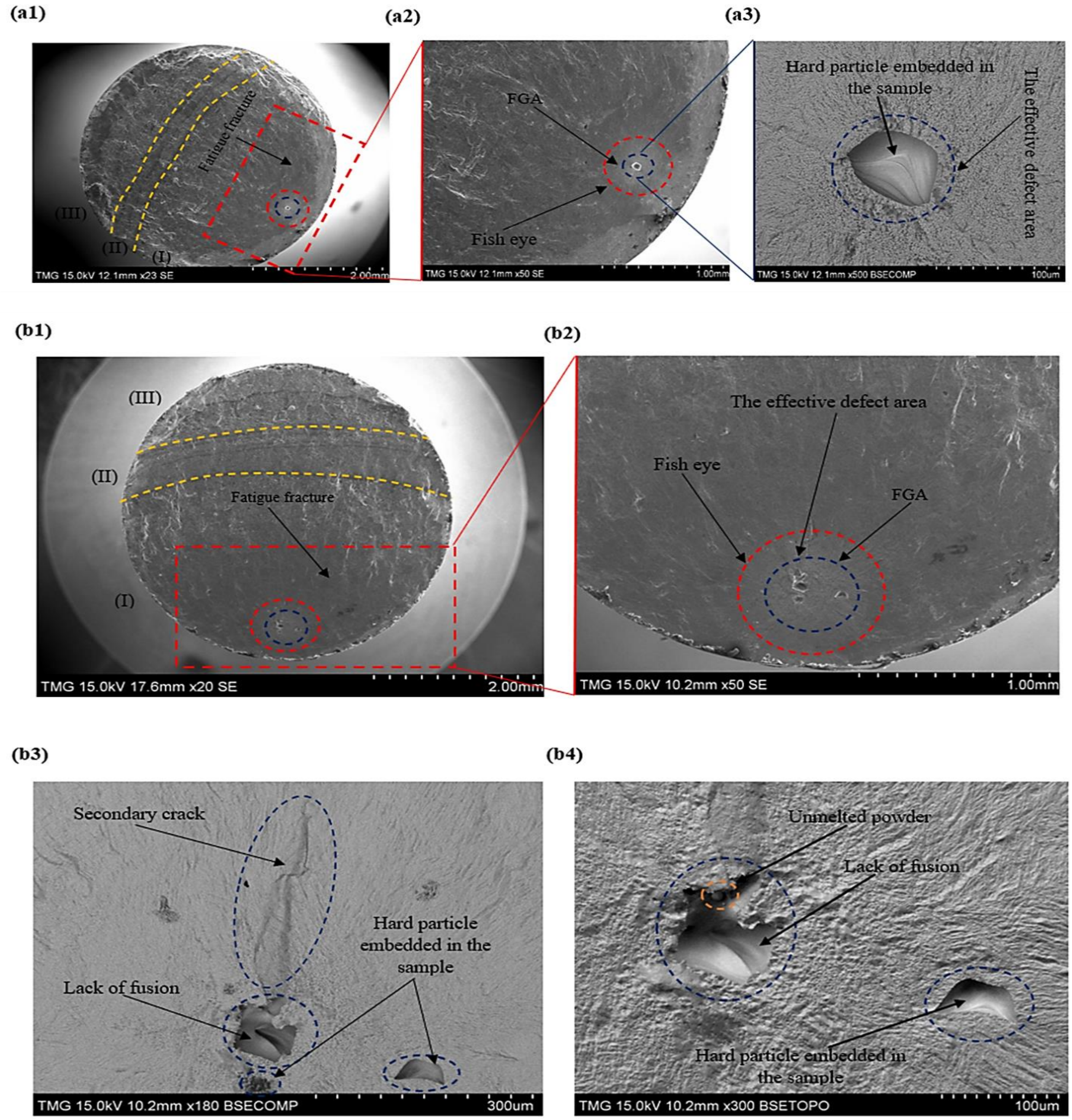

Fig. 109. *Micrographs of fatigue fracture of the L-PBF-Ti-6Al-4V specimens in SR heat-treated condition: (a) sub surface defect from lack of fusion (σ_a = 109.06 MPa, $N_f = 7.24 \times 10^7$); (b) sub surface defect from lack of fusion (σ_a = 88.01 MPa, $N_f = 1.44 \times 10^9$).*

Additionally, unmelted powder was also found on the fracture surface which is also critical for crack initiation. Like previous SR heat-treated samples here also FiE structure with FGA around the crack initiation defect was clearly visible. Furthermore, some foreign particles with irregular shape were observed on the fracture surfaces, as shown in **Fig. 110**. At point 1 (spectrum 1) in **Fig. 110** (a), the relative chemical composition calculated from EDS analysis was 0.42wt%Al, 10.38wt% V, and 89.20wt% Ti, whereas at point 2 (spectrum 2), the relative chemical composition was 5.41wt% Al, 2.85wt% V, and 87.01wt% Ti. Similarly, at point 2 (spectrum 2) in **Fig. 110** (b), the relative chemical composition calculated from EDS analysis was 0.46wt%Al, 8.88wt% V, and 90.67wt% Ti, whereas at point 3 (spectrum 3), the relative chemical composition was 3.09wt% Al, 4.14wt% V, and 82.19wt% Ti.

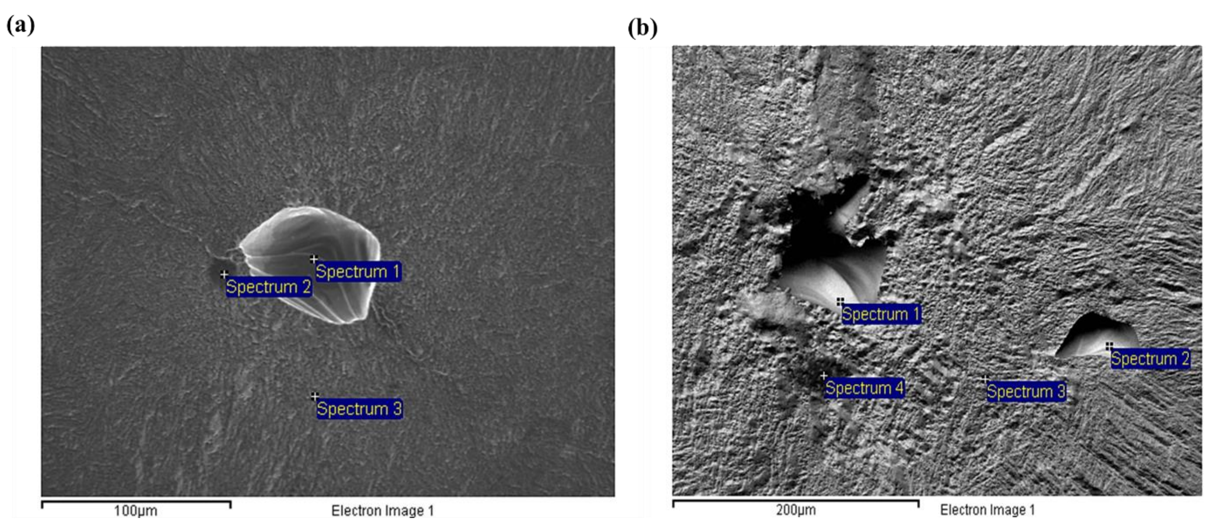

Fig. 110*. Embedded hard particle on the fracture surface of SR heat-treated samples showing the particle rich in V but low in Al.*

It is possible that this particle is laser spatter based on its composition. However, in SR heat-treated condition, laser spatter is in irregular shape whereas in AB condition it was in spherical shape.

Additionally, it is clearly seen that the laser spatter in SR heat-treated condition is rich in V but low in Al whereas in AB condition this particle is rich in both Al and V. So, it can be said that FiE structure with FGA at the center is the characteristics region for L-PBF-Ti-6Al-4V samples at VHCF regime irrespective of the post heat treatment. Lack of fusion defects are one of the critical reasons for initiating fatigue fracture. It is mentioned that lack of fusion defects has the most detrimental effect on fatigue performance as fatigue cracks initiate from LOF defects irrespective of the build direction [31]. It should be pointed out that some foreign particles most probably, laser spatter containing high amounts of Al and V in AB samples and high amounts of V with low Al in SR heat-treated samples are found on the effective area of the fracture surfaces as well.

3.6 Conclusion

The ultrasonic fatigue tests of the AB and SR heat-treated selective laser melted Ti-6Al-4V alloy were conducted. In order to obtain information regarding defects in the model sample, μ-computed tomography was used to characterize them in 3D. The experimental results have led to the following conclusion based on the results of the experiment:

1. The SR heat-treatment in this study showed improved fatigue performance under cyclic loading compared to AB samples. The fatigue strength decreases with the increase of the number of cycles, and the fatigue limit of AB specimens is about 72 MPa, which is much lower than the fatigue limit of the heat-treated Ti-6Al-4V specimens (88MPa) at 10^9 cycles. However, after that the difference becomes small.

2. The fatigue properties of the L-PBF-Ti-6Al-4V are greatly affected by defects inside the specimen. SR heat-treatment drastically decreases the defect number 10 times lower defects compared to the SR heat-treated samples. In AB samples there were surface defects

of about 80.83% of total pores, sub-surface defects of about 8.33% of total pores, internal defects of about 10.83% of total pores whereas in SR heat-treated samples there were surface defects of about 66.67% of total pores, sub-surface defects of about 25% of total pores, internal defects of about 8.33% of total pores. The equivalent diameter of defects is mainly distributed in 22.56 to 63.68 μm in AB samples whereas in SR heat-treated samples equivalent diameters was between 17.9026 to 31.2787 μm. For Feret diameter, the size is mainly distributed in 26.69 to 79.77 μm in AB samples whereas in SR heat-treated samples most of the defects have Feret diameters between 20.91 to 51.312 μm. These statistics support the tested results of decreased fatigue performance for AB samples as higher number of defects with larger diameter is detrimental to fatigue performance. Moreover, the shape factor of defect is dominated to a certain extent by the diameter of the defect.

3. SR heat-treatment has a great impact on the sphericity of L-PBF-Ti-6Al-4V alloy. SR heat-treatment has increased the sphericity of L-PBF-Ti-6Al-4V alloy. The higher sphericity might be one of other reasons of getting improved VHCF performance for SR heat-treated samples.

4. SR heat-treatment helps to decompose brittle α’ martensite to a finer α+ β/ α′ lamellar mixture microstructure with increased α lathe thickness which is beneficial to the improved fatigue performance for Ti-6Al-4V alloy. An optimum balance between strength and ductility can be found after SR heat-treatment due to the lamellar structure which helps to improve very high cycle fatigue performance.

5. The relief of residual stresses generated during the production process after SR heat-treatment can be considered to be one of another significant factors contributing to fatigue performance enhancement.

6. The fatigue cracks mainly originate from internal and subsurface defects both in the AB and SR heat-treated samples. Lack of fusion defects are one of the critical reasons for initiating fatigue fracture. Some foreign particles, most probably, laser spatter containing high amounts of Al and V in AB samples and high amount of V with low Al in SR heat-treated samples are found on the effective area of the fracture surfaces as well. Moreover, fisheye characteristic region with FGA will be found in VHCF regime irrespective of the post treatment.

Declaration of Competing Interest

The authors of this article do not have any known financial interests or personal relationships that could have influenced the research presented in the paper in any way.

Acknowledgments

As a token of appreciation, the authors wish to express their deep gratitude for the support provided by the Natural Sciences and Engineering Research Council of Canada (NSERC) (DGECR-2018-00232). The authors acknowledge the support of FusiA impression 3D Métal Inc. (180 Boulevard Industriel, Saint Eustache, Québec, J7R 5C2) for providing fabricated and treated cylindrical samples. The authors acknowledge the support of McGill laboratories for the machining of the fatigue samples. Th authors acknowledge Ecole de Technologie Superieure for providing μ-CT technical support.

Chapter 4

Conclusions and Future Recommendations

4.1 Concluding Remark

A comprehensive overview of the state of the art on the fatigue behavior of Ti-6Al-4V alloy manufactured by L-PBF has been presented in **Chapter 2**. HCF and VHCF performance of L-PBF-Ti-6Al-4V alloy is positively impacted by increased α lathe thickness, reduced defects level, reduced residual stress, post-heat treatment, and specimens with increased gauge diameter, as described in **Chapter 2**. Additionally, building orientation, surface roughness, load ratio, process parameters, and mechanical strength also impact HCF and VHCF performance of L-PBF-Ti-6Al-4V alloy. It is also described that some traditional approaches like Murakami approach can be used to predict fatigue performance.

In **Chapter 3**, An ultrasonic fatigue test was conducted on the AB and the SR heat-treated L-PBF-Ti-6Al-4V alloy to determine their fatigue properties. As part of the process of characterizing the defects in the model sample in a 3D manner, computed tomography was used to obtain information regarding defects in the sample. In this study, SR heat treatment showed improved fatigue performance under cyclic loading compared to AB samples. The main reason for getting improved fatigue performance for the SR heat treated samples are decreased defects level along with their size and the transformation of the microstructure with increased α lathe thickness.

The degree of sphericity of L-PBF-Ti-6Al-4V alloy has been found to be greatly increased by SR heat treatment resulting in better VHCF performance. Another important factor contributing to the enhancement of fatigue performance can be considered to be the relief of residual stresses after SR heat treatment generated during the production process.

According to the analysis of SEM images that were taken on both the AB and SR heat-treated samples, it can be observed that fatigue cracks are primarily brought about by internal and subsurface imperfections, among which lack of fusion defects and laser spatter can be considered to be the most critical causes of fatigue cracks initiations. Additionally, fisheye with FGA at the center can be considered as the characteristics region for VHCF regardless of the post heat treatment.

4.2 Limitations

a. In this study, the impact of SR heat treatment on the VHCF performance was studied. It is established that SR heat treatment reduces the residual stresses. However, in this study it is not analyzed how much residual stress is reduced by SR heat treatment. As a result, it was not possible to detect whether residual stresses are critical for VHCF performances or not.

4.3 Future Recommendations

It may be worthwhile to conduct future research in several areas that can contribute to further advancements of the VHCF performance of L-PBF-Ti-6Al-4V alloy. In order to advance the understanding of how the process and microstructure of AM -Ti-6Al-4V alloy relate to each other, and in order to explore the great potential of L-PBF-Ti-6Al-4V alloy to their full success, future studies will need to examine the following aspects:

a. Residual stresses should be measured after the SR heat treatment and then further analysis should be done to check whether the residual stresses are a critical factor or not. It should also be checked how much detrimental the residual stresses combining with defects statistics and microstructure transformation.

Bibliography

[1] Kakiuchi T, Kawaguchi R, Nakajima M, Hojo M, Fujimoto K, Uematsu Y. Prediction of fatigue limit in additively manufactured Ti-6Al-4V alloy at elevated temperature. International Journal of Fatigue. 2019;126:55-61.

[2] Liu W, Chen C, Shuai S, Zhao R, Liu L, Wang X, et al. Study of pore defect and mechanical properties in selective laser melted Ti6Al4V alloy based on X-ray computed tomography. Materials Science and Engineering: A. 2020;797:139981.

[3] Chang K, Liang E, Huang W, Zhang X, Chen Y, Dong J, et al. Microstructural feature and mechanical property in different building directions of additive manufactured Ti6Al4V alloy. Materials Letters. 2020;267:127516.

[4] da Costa PR, Sardinha M, Reis L, Freitas M, Fonte M. Ultrasonic fatigue testing in as-built and polished Ti6Al4V alloy manufactured by SLM. Forces in Mechanics. 2021;4:100024.

[5] Marques BM, Andrade CM, Neto DM, Oliveira MC, Alves JL, Menezes LF. Numerical analysis of residual stresses in parts produced by selective laser melting process. Procedia Manufacturing. 2020;47:1170-7.

[6] Pauzon C, Mishurova T, Evsevleev S, Dubiez-Le Goff S, Murugesan S, Bruno G, et al. Residual stresses and porosity in Ti-6Al-4V produced by laser powder bed fusion as a function of process atmosphere and component design. Additive Manufacturing. 2021;47:102340.

[7] Wegner N, Kotzem D, Wessarges Y, Emminghaus N, Hoff C, Tenkamp J, et al. Corrosion and corrosion fatigue properties of additively manufactured magnesium alloy WE43 in comparison to titanium alloy Ti-6Al-4V in physiological environment. Materials. 2019;12(18):2892.

[8] Chan KS, Koike M, Mason RL, Okabe T. Fatigue life of titanium alloys fabricated by additive layer manufacturing techniques for dental implants. Metallurgical and Materials Transactions A. 2013;44(2):1010-22.

[9] Hrabe N, Quinn T. Effects of processing on microstructure and mechanical properties of a titanium alloy (Ti–6Al–4V) fabricated using electron beam melting (EBM), part 1: Distance from build plate and part size. Materials Science and Engineering: A. 2013;573:264-70.

[10] Spierings AB, Starr TL, Wegener K. Fatigue performance of additive manufactured metallic parts. Rapid prototyping journal. 2013;19(2):88-94.

[11] Murr LEQ, S. A. Gaytan, S. M. Lopez, M. I. Rodela, A. Martinez, E. Y. Hernandez, D. H. Martinez, E. Medina, F. Wicker, R. B. Microstructure and mechanical behavior of Ti-6Al-4V produced by rapid layer manufacturing, for biomedical applications. J Mech Behav Biomed Mater. 2009;2(1):20-32.

[12] Mercelis P, Kruth JP. Residual stresses in selective laser sintering and selective laser melting. Rapid prototyping journal. 2006;12(5):254-65.

[13] Peters M, Kumpfert J, Ward CH, Leyens C. Titanium alloys for aerospace applications. Advanced engineering materials. 2003;5(6):419-27.

[14] Jiao Z, Wu X, Yu H, Xu R, Wu L. High cycle fatigue behavior of a selective laser melted Ti6Al4V alloy: anisotropy, defects effect and life prediction. International Journal of Fatigue. 2023;167:107252.

[15] DebRoy T, Wei H, Zuback J, Mukherjee T, Elmer J, Milewski J, et al. Additive manufacturing of metallic components–process, structure and properties. Progress in Materials Science. 2018;92:112-224.

[16] Frazier WE. Metal additive manufacturing: a review. Journal of Materials Engineering and performance. 2014;23(6):1917-28.

[17] Li X, Wang C, Zhang W, Li Y. Fabrication and characterization of porous Ti6Al4V parts for biomedical applications using electron beam melting process. Materials Letters. 2009;63(3-4):403-5.

[18] Nalla R, Ritchie R, Boyce B, Campbell J, Peters J. Influence of microstructure on high-cycle fatigue of Ti-6Al-4V: Bimodal vs. lamellar structures. Metallurgical and Materials Transactions A. 2002;33(3):899-918.

[19] Shanyavskiy A. Very-High-Cycle-Fatigue of in-service air-engine blades, compressor and turbine. Science China Physics, Mechanics and Astronomy. 2014;57(1):19-29.

[20] Kasperovich G, Hausmann J, editors. Thermomechanical treatment of TiAl6V4 alloy fabricated by selective laser melting: optimization of microstructure and fatigue properties. Proceeding,"Materials Science & Technology" 2013 Conference, Oct 27-31, Montreal, Quebec, Canada; 2013: Association For Iron & Steel Technology, Warrendale, PA.

[21] Aguado-Montero S, Navarro C, Vázquez J, Domínguez J. Experimental and numerical analysis of fatigue cracks emanating from internal defects in Ti6Al4V SLM. Procedia Structural Integrity. 2021;34:121-8.

[22] Sanaei N, Fatemi A, Phan N. Defect characteristics and analysis of their variability in metal L-PBF additive manufacturing. Materials & Design. 2019;182:108091.

[23] Kantzos C, Cunningham R, Tari V, Rollett A. Characterization of metal additive manufacturing surfaces using synchrotron X-ray CT and micromechanical modeling. Computational Mechanics. 2018;61(5):575-80.

[24] Molaei R, Fatemi A, Phan N. Significance of hot isostatic pressing (HIP) on multiaxial deformation and fatigue behaviors of additive manufactured Ti-6Al-4V including build orientation and surface roughness effects. International Journal of Fatigue. 2018;117:352-70.

[25] Ngo TD, Kashani A, Imbalzano G, Nguyen KT, Hui D. Additive manufacturing (3D printing): A review of materials, methods, applications and challenges. Composites Part B: Engineering. 2018;143:172-96.

[26] Gorelik M. Additive manufacturing in the context of structural integrity. International Journal of Fatigue. 2017;94:168-77.

[27] Seifi M, Gorelik M, Waller J, Hrabe N, Shamsaei N, Daniewicz S, et al. Progress towards metal additive manufacturing standardization to support qualification and certification. The journal of the Minerals, Metals & Materials Society. 2017;69(3):439-55.

[28] Seifi M, Salem A, Satko D, Shaffer J, Lewandowski JJ. Defect distribution and microstructure heterogeneity effects on fracture resistance and fatigue behavior of EBM Ti–6Al–4V. International Journal of Fatigue. 2017;94:263-87.

[29] Do DK, Li P. The effect of laser energy input on the microstructure, physical and mechanical properties of Ti-6Al-4V alloys by selective laser melting. Virtual and Physical Prototyping. 2016;11(1):41-7.

[30] Seifi M, Salem A, Beuth J, Harrysson O, Lewandowski JJ. Overview of materials qualification needs for metal additive manufacturing. Jom. 2016;68(3):747-64.

[31] Tusher MMH, Ince A. High Cycle Fatigue and Very High Cycle Fatigue Performance of Selective Laser Melting Ti-6Al-4V Titanium Alloy-A Review. Materials Performance and Characterization. 2022.

[32] Kasperovich G, Hausmann J. Improvement of fatigue resistance and ductility of TiAl6V4 processed by selective laser melting. Journal of Materials Processing Technology. 2015;220:202-14.

[33] Levy GN, Schindel R, Kruth J-P. Rapid manufacturing and rapid tooling with layer manufacturing (LM) technologies, state of the art and future perspectives. CIRP annals. 2003;52(2):589-609.

[34] Thijs L, Verhaeghe F, Craeghs T, Van Humbeeck J, Kruth J-P. A study of the microstructural evolution during selective laser melting of Ti–6Al–4V. Acta materialia. 2010;58(9):3303-12.

[35] Fatemi A, Molaei R, Sharifimehr S, Phan N, Shamsaei N. Multiaxial fatigue behavior of wrought and additive manufactured Ti-6Al-4V including surface finish effect. International Journal of Fatigue. 2017;100:347-66.

[36] Janeček M, Nový F, Harcuba P, Stráský J, Trško L, Mhaede M, et al. The Very High Cycle Fatigue Behaviour of Ti-6Al-4V Alloy. Acta Physica Polonica, A. 2015;128(4).

[37] Suresh S. Fatigue of materials. 2nd ed: Cambridge university press; 2012.

[38] Nový F, Bokůvka O, Palček P, Chalupová M. Effect of inclusions on very high cycle behaviour in a ferritic corrosion resisting steel. Procedia Engineering. 2011;10:1408-13.

[39] Chastand V, Tezenas A, Cadoret Y, Quaegebeur P, Maia W, Charkaluk E. Fatigue characterization of Titanium Ti-6Al-4V samples produced by Additive Manufacturing. Procedia Structural Integrity. 2016;2:3168-76.

[40] Günther J, Krewerth D, Lippmann T, Leuders S, Tröster T, Weidner A, et al. Fatigue life of additively manufactured Ti–6Al–4V in the very high cycle fatigue regime. International Journal of Fatigue. 2017;94:236-45.

[41] Wycisk E, Emmelmann C, Siddique S, Walther F. High Cycle Fatigue (HCF) Performance of Ti-6Al-4V Alloy Processed by Selective Laser Melting. Advanced Materials Research. 2013;816-817:134-9.

[42] Yap CY, Chua CK, Dong ZL, Liu ZH, Zhang DQ, Loh LE, et al. Review of selective laser melting: Materials and applications. Applied physics reviews. 2015;2(4):041101.

[43] Heinl P, Müller L, Körner C, Singer RF, Müller FA. Cellular Ti–6Al–4V structures with interconnected macro porosity for bone implants fabricated by selective electron beam melting. Acta biomaterialia. 2008;4(5):1536-44.

[44] Sames WJ, List F, Pannala S, Dehoff RR, Babu SS. The metallurgy and processing science of metal additive manufacturing. International materials reviews. 2016;61(5):315-60.

[45] Biamino S, Penna A, Ackelid U, Sabbadini S, Tassa O, Fino P, et al. Electron beam melting of Ti–48Al–2Cr–2Nb alloy: Microstructure and mechanical properties investigation. Intermetallics. 2011;19(6):776-81.

[46] Ferrar B, Mullen L, Jones E, Stamp R, Sutcliffe C. Gas flow effects on selective laser melting (SLM) manufacturing performance. Journal of Materials Processing Technology. 2012;212(2):355-64.

[47] Zhao X, Li S, Zhang M, Liu Y, Sercombe TB, Wang S, et al. Comparison of the microstructures and mechanical properties of Ti–6Al–4V fabricated by selective laser melting and electron beam melting. Materials & Design. 2016;95:21-31.

[48] Wang X, Chou K, editors. Residual stress in metal parts produced by powder-bed additive manufacturing processes. 26th International Solid Freeform Fabrication Symposium; 2015: University of Texas at Austin.

[49] Kok Y, Tan XP, Wang P, Nai M, Loh NH, Liu E, et al. Anisotropy and heterogeneity of microstructure and mechanical properties in metal additive manufacturing: A critical review. Materials & Design. 2018;139:565-86.

[50] Tan X, Wang P, Kok Y, Toh W, Sun Z, Nai S, et al. Carbide precipitation characteristics in additive manufacturing of Co-Cr-Mo alloy via selective electron beam melting. Scripta Materialia. 2018;143:117-21.

[51] Wang P, Nai MLS, Lu S, Bai J, Zhang B, Wei J. Study of direct fabrication of a Ti-6Al-4V impeller on a wrought Ti-6Al-4V plate by electron beam melting. The journal of the Minerals, Metals & Materials Society. 2017;69(12):2738-44.

[52] Wang P, Nai MLS, Tan X, Sin WJ, Tor SB, Wei J, editors. Anisotropic mechanical properties in a big-sized Ti-6Al-4V plate fabricated by electron beam melting. TMS 2016 145th Annual Meeting & Exhibition; 2016: Springer.

[53] Wang P, Tan X, Nai MLS, Tor SB, Wei J. Spatial and geometrical-based characterization of microstructure and microhardness for an electron beam melted Ti–6Al–4V component. Materials & Design. 2016;95:287-95.

[54] Carroll BE, Palmer TA, Beese AM. Anisotropic tensile behavior of Ti–6Al–4V components fabricated with directed energy deposition additive manufacturing. Acta Materialia. 2015;87:309-20.

[55] Tan X, Kok Y, Tan YJ, Descoins M, Mangelinck D, Tor SB, et al. Graded microstructure and mechanical properties of additive manufactured Ti–6Al–4V via electron beam melting. Acta Materialia. 2015;97:1-16.

[56] Al-Bermani S, Blackmore M, Zhang W, Todd I. The origin of microstructural diversity, texture, and mechanical properties in electron beam melted Ti-6Al-4V. Metallurgical and materials transactions a. 2010;41(13):3422-34.

[57] Qian L, Mei J, Liang J, Wu X. Influence of position and laser power on thermal history and microstructure of direct laser fabricated Ti–6Al–4V samples. Materials science and technology. 2005;21(5):597-605.

[58] Wu M-W, Chen J-K, Lin B-H, Chiang P-H. Improved fatigue endurance ratio of additive manufactured Ti-6Al-4V lattice by hot isostatic pressing. Materials & Design. 2017;134:163-70.

[59] Ladani L, Razmi J, Farhan Choudhury S. Mechanical anisotropy and strain rate dependency behavior of Ti-6Al-4V produced using E-beam additive fabrication. Journal of Engineering Materials and Technology. 2014;136(3):031006.

[60] Lewandowski JJ, Seifi M. Metal additive manufacturing: A review of mechanical properties. 2016;46:151-86.

[61] Everton SK, Hirsch M, Stravroulakis P, Leach RK, Clare AT. Review of in-situ process monitoring and in-situ metrology for metal additive manufacturing. Materials & Design. 2016;95:431-45.

[62] Wu M-W, Lai P-H, Chen J-K. Anisotropy in the impact toughness of selective laser melted Ti–6Al–4V alloy. Materials Science and Engineering: A. 2016;650:295-9.

[63] Judt PO, Ricoeur A, Linek G. Crack paths at multiple-crack systems in anisotropic structures: simulation and experiment. Procedia materials science. 2014;3:2122-7.

[64] Sridharan N, Gussev M, Seibert R, Parish C, Norfolk M, Terrani K, et al. Rationalization of anisotropic mechanical properties of Al-6061 fabricated using ultrasonic additive manufacturing. Acta Materialia. 2016;117:228-37.

[65] Raghavan S, Nai MLS, Wang P, Sin WJ, Li T, Wei J. Heat treatment of electron beam melted (EBM) Ti-6Al-4V: microstructure to mechanical property correlations. Rapid Prototyping Journal. 2018;24(4):774-83.

[66] Alcisto J, Enriquez A, Garcia H, Hinkson S, Steelman T, Silverman E, et al. Tensile properties and microstructures of laser-formed Ti-6Al-4V. Journal of materials engineering and performance. 2011;20(2):203-12.

[67] Vilaro T, Colin C, Bartout J-D. As-fabricated and heat-treated microstructures of the Ti-6Al-4V alloy processed by selective laser melting. Metallurgical and materials transactions A. 2011;42(10):3190-9.

[68] Yang J, Yu H, Yin J, Gao M, Wang Z, Zeng X. Formation and control of martensite in Ti-6Al-4V alloy produced by selective laser melting. Materials & Design. 2016;108:308-18.

[69] Cain V, Thijs L, Van Humbeeck J, Van Hooreweder B, Knutsen R. Crack propagation and fracture toughness of Ti-6Al-4V alloy produced by selective laser melting. Additive Manufacturing. 2015;5:68-76.

[70] Xu Z, Liu A, Wang X. Fatigue performance differences between rolled and selective laser melted Ti6Al4V alloys. Materials Characterization. 2022;189:111963.

[71] Xu Z, Liu A, Wang X, Liu B, Guo M. Fatigue limit prediction model and fatigue crack growth mechanism for selective laser melting Ti6Al4V samples with inherent defects. International Journal of Fatigue. 2021;143:106008.

[72] Qian G, Li Y, Paolino DS, Tridello A, Berto F, Hong Y. Very-high-cycle fatigue behavior of Ti-6Al-4V manufactured by selective laser melting: Effect of build orientation. International Journal of Fatigue. 2020;136:105628.

[73] Edwards P, Ramulu M. Effect of build direction on the fracture toughness and fatigue crack growth in selective laser melted Ti-6Al-4 V. Fatigue & Fracture of Engineering Materials & Structures. 2015;38(10):1228-36.

[74] Simonelli M, Tse YY, Tuck C. Effect of the build orientation on the mechanical properties and fracture modes of SLM Ti–6Al–4V. Materials Science and Engineering: A. 2014;616:1-11.

[75] Frkan M, Konecna R, Nicoletto G, Kunz L. Microstructure and fatigue performance of SLM-fabricated Ti6Al4V alloy after different stress-relief heat treatments. Transportation Research Procedia. 2019;40:24-9.

[76] Bhandari L, Gaur V. On study of process induced defects-based fatigue performance of additively manufactured Ti6Al4V alloys. Additive Manufacturing. 2022;60:103227.

[77] Cutolo A, Elangeswaran C, de Formanoir C, Muralidharan GK, Van Hooreweder B. Effect of Heat Treatments on Fatigue Properties of Ti–6Al–4V and 316L Produced by Laser Powder Bed Fusion in As-Built Surface Condition. TMS 2019 148th Annual Meeting & Exhibition Supplemental Proceedings. The Minerals, Metals & Materials Series. Pittsburgh, PA, USA: Springer; 2019. p. 395-405.

[78] Yu H, Li F, Wang Z, Zeng X. Fatigue performances of selective laser melted Ti-6Al-4V alloy: Influence of surface finishing, hot isostatic pressing and heat treatments. International Journal of Fatigue. 2019;120:175-83.

[79] Qian G, Jian Z, Pan X, Berto F. In-situ investigation on fatigue behaviors of Ti-6Al-4V manufactured by selective laser melting. International Journal of Fatigue. 2020;133:105424.

[80] Pegues JW, Shamsaei N, Roach MD, Williamson RS. Fatigue life estimation of additive manufactured parts in the as-built surface condition. Material Design & Processing Communications. 2019;1(3):e36.

[81] Nakatani M, Masuo H, Tanaka Y, Murakami Y. Effect of surface roughness on fatigue strength of Ti-6Al-4V alloy manufactured by additive manufacturing. Procedia Structural Integrity. 2019;19:294-301.

[82] Yan X, Yin S, Chen C, Jenkins R, Lupoi R, Bolot R, et al. Fatigue strength improvement of selective laser melted Ti6Al4V using ultrasonic surface mechanical attrition. Materials Research Letters. 2019;7(8):327-33.

[83] Song B, Zhao X, Li S, Han C, Wei Q, Wen S, et al. Differences in microstructure and properties between selective laser melting and traditional manufacturing for fabrication of metal parts: A review. Frontiers of Mechanical Engineering. 2015;10(2):111-25.

[84] Olakanmi EO, Cochrane R, Dalgarno K. A review on selective laser sintering/melting (SLS/SLM) of aluminium alloy powders: Processing, microstructure, and properties. Progress in Materials Science. 2015;74:401-77.

[85] Buchbinder D, Meiners W, Wissenbach K, Poprawe R. Selective laser melting of aluminum die-cast alloy—Correlations between process parameters, solidification conditions, and resulting mechanical properties. Journal of Laser Applications. 2015;27(S2):S29205.

[86] Gu D, Hagedorn Y-C, Meiners W, Meng G, Batista RJS, Wissenbach K, et al. Densification behavior, microstructure evolution, and wear performance of selective laser melting processed commercially pure titanium. Acta materialia. 2012;60(9):3849-60.

[87] Attar H, Bönisch M, Calin M, Zhang L-C, Scudino S, Eckert J. Selective laser melting of in situ titanium–titanium boride composites: processing, microstructure and mechanical properties. Acta Materialia. 2014;76:13-22.

[88] Khorasani AM, Gibson I, Goldberg M, Littlefair G. A survey on mechanisms and critical parameters on solidification of selective laser melting during fabrication of Ti-6Al-4V prosthetic acetabular cup. Materials & Design. 2016;103:348-55.

[89] Korkmaz ME, Gupta MK, Waqar S, Kuntoğlu M, Krolczyk GM, Maruda RW, et al. A short review on thermal treatments of Titanium & Nickel based alloys processed by selective laser melting. Journal of Materials Research and Technology. 2022;16:1090-101.

[90] Gibson I, Rosen D, Stucker B. Additive manufacturing technologies. Second ed: Springer; 2015.

[91] Loeber L, Biamino S, Ackelid U, Sabbadini S, Epicoco P, Fino P. Comparison of selective laser and electron beam melted titanium aluminides. International Solid freeform fabrication Symposium; University of Texas at Austin2011.

[92] Kempen K, Vrancken B, Thijs L, Buls S, Van Humbeeck J, Kruth J-P, editors. Lowering thermal gradients in selective laser melting by pre-heating the baseplate. Solid Freeform Fabrication Symposium Proceedings; 2013.

[93] Buchbinder D, Meiners W, Pirch N, Wissenbach K, Schrage J. Investigation on reducing distortion by preheating during manufacture of aluminum components using selective laser melting. Journal of laser applications. 2014;26(1):012004.

[94] Buchbinder D, Schleifenbaum H, Heidrich S, Meiners W, Bültmann J. High power selective laser melting (HP SLM) of aluminum parts. Physics Procedia. 2011;12:271-8.

[95] Schleifenbaum H, Meiners W, Wissenbach K, Hinke C. Individualized production by means of high power Selective Laser Melting. CIRP Journal of manufacturing science and technology. 2010;2(3):161-9.

[96] Liu S, Shin YC. Additive manufacturing of Ti6Al4V alloy: A review. Materials & Design. 2019;164:107552.

[97] Banerjee D, Williams J. Perspectives on titanium science and technology. Acta Materialia. 2013;61(3):844-79.

[98] Leyens C, Peters M. Titanium and titanium alloys: fundamentals and applications: John Wiley & Sons; 2003.

[99] Lütjering G, Williams JC. Titanium matrix composites: Springer; 2007.

[100] Cui C, Hu B, Zhao L, Liu S. Titanium alloy production technology, market prospects and industry development. Materials & Design. 2011;32(3):1684-91.

[101] Donachie MJ. Titanium: a technical guide: ASM international; 2000.

[102] Al-Rubaie KS, Melotti S, Rabelo A, Paiva JM, Elbestawi MA, Veldhuis SC. Machinability of SLM-produced Ti6Al4V titanium alloy parts. Journal of Manufacturing Processes. 2020;57:768-86.

[103] Campbell Jr FC. Manufacturing technology for aerospace structural materials: Elsevier; 2011.

[104] Davim JP. Machining of complex sculptured surfaces: Springer; 2012.

[105] Ezugwu E. Key improvements in the machining of difficult-to-cut aerospace superalloys. International Journal of Machine Tools and Manufacture. 2005;45(12-13):1353-67.

[106] Ezugwu E, Wang Z. Titanium alloys and their machinability—a review. Journal of materials processing technology. 1997;68(3):262-74.

[107] Veiga C, Davim JP, Loureiro A. Review on machinability of titanium alloys: the process perspective. Rev Adv Mater Sci. 2013;34(2):148-64.

[108] Taminger KM, Hafley RA, editors. Electron beam freeform fabrication for cost effective near-net shape manufacturing. NATO/RTO AVT-139 Specialists"Meeting on Cost Effective Manufacture via Net Shape Processing; 2006.

[109] Syed AK, Ahmad B, Guo H, Machry T, Eatock D, Meyer J, et al. An experimental study of residual stress and direction-dependence of fatigue crack growth behaviour in as-built and stress-relieved selective-laser-melted Ti6Al4V. Materials Science and Engineering: A. 2019;755:246-57.

[110] Liang Z, Sun Z, Zhang W, Wu S, Chang H. The effect of heat treatment on microstructure evolution and tensile properties of selective laser melted Ti6Al4V alloy. Journal of Alloys and Compounds. 2019;782:1041-8.

[111] Pal S, Lojen G, Kokol V, Drstvensek I. Evolution of metallurgical properties of Ti-6Al-4V alloy fabricated in different energy densities in the Selective Laser Melting technique. Journal of Manufacturing Processes. 2018;35:538-46.

[112] Vrancken B, Thijs L, Kruth J-P, Van Humbeeck J. Heat treatment of Ti6Al4V produced by Selective Laser Melting: Microstructure and mechanical properties. Journal of Alloys and Compounds. 2012;541:177-85.

[113] Yan X, Yin S, Chen C, Huang C, Bolot R, Lupoi R, et al. Effect of heat treatment on the phase transformation and mechanical properties of Ti6Al4V fabricated by selective laser melting. Journal of Alloys and Compounds. 2018;764:1056-71.

[114] Standard Specification for Additive Manufacturing Titanium-6 Aluminum-4 Vanadium with Powder Bed Fusion. ASTM F2924-14. (West Conshohocken, PA: ASTM International, approved February 1, 2014).

[115] Standard Specification for Additive Manufacturing Titanium-6 Aluminum-4 Vanadium ELI (Extra Low Interstitial) with Powder Bed Fusion. ASTM F3001-14. (West Conshohocken, PA: ASTM International, approved February 1, 2014).

[116] Alegre J, Díaz A, García R, Peral L, Cuesta I. Effect of HIP post-processing at 850° C/200 MPa in the fatigue behavior of Ti-6Al-4V alloy fabricated by Selective Laser Melting. International Journal of Fatigue. 2022;163:107097.

[117] Avateffazeli M, Haghshenas M. Ultrasonic Fatigue of Laser Beam Powder Bed Fused Metals: A State-of-the-art Review. Engineering Failure Analysis. 2022;134:106015.

[118] Carrion PE, Soltani-Tehrani A, Phan N, Shamsaei N. Powder recycling effects on the tensile and fatigue behavior of additively manufactured Ti-6Al-4V parts. Jom. 2019;71(3):963-73.

[119] Du L, Pan X, Qian G, Zheng L, Hong Y. Crack initiation mechanisms under two stress ratios up to very-high-cycle fatigue regime for a selective laser melted Ti-6Al-4V. International Journal of Fatigue. 2021;149:106294.

[120] Du L, Qian G, Zheng L, Hong Y. Influence of processing parameters of selective laser melting on high-cycle and very-high-cycle fatigue behaviour of Ti-6Al-4V. Fatigue & Fracture of Engineering Materials & Structures. 2021;44(1):240-56.

[121] Fatemi A, Molaei R, Simsiriwong J, Sanaei N, Pegues J, Torries B, et al. Fatigue behaviour of additive manufactured materials: An overview of some recent experimental studies on Ti-6Al-4V considering various processing and loading direction effects. Fatigue & Fracture of Engineering Materials & Structures. 2019;42(5):991-1009.

[122] Fu R, Zheng L, Ling C, Zhong Z, Hong Y. An experimental investigation of fatigue performance and crack initiation characteristics for an SLMed Ti-6Al-4V under different stress ratios up to very-high-cycle regime. International Journal of Fatigue. 2022;164:107119.

[123] Jiang Q, Li S, Zhou C, Zhang B, Zhang Y. Effects of laser shock peening on the ultra-high cycle fatigue performance of additively manufactured Ti6Al4V alloy. Optics & Laser Technology. 2021;144:107391.

[124] Jin P, Tang Q, Li K, Feng Q, Ren Z, Song J, et al. The relationship between the macro-and microstructure and the mechanical properties of selective-laser-melted Ti6Al4V samples under low energy inputs: Simulation and experiment. Optics & Laser Technology. 2022;148:107713.

[125] Kotadia H, Gibbons G, Das A, Howes P. A review of Laser Powder Bed Fusion Additive Manufacturing of aluminium alloys: Microstructure and properties. Additive Manufacturing. 2021;46:102155.

[126] Li H, Jia D, Yang Z, Liao X, Jin H, Cai D, et al. Effect of heat treatment on microstructure evolution and mechanical properties of selective laser melted Ti–6Al–4V and TiB/Ti–6Al–4V composite: A comparative study. Materials Science and Engineering: A. 2021;801:140415.

[127] Li P, Warner D, Pegues J, Roach M, Shamsaei N, Phan N. Towards predicting differences in fatigue performance of laser powder bed fused Ti-6Al-4V coupons from the same build. International Journal of Fatigue. 2019;126:284-96.

[128] Liu F, He C, Chen Y, Zhang H, Wang Q, Liu Y. Effects of defects on tensile and fatigue behaviors of selective laser melted titanium alloy in very high cycle regime. International Journal of Fatigue. 2020;140:105795.

[129] Liu J, Sun Q, Wang X, Li H, Guo K, Sun J. Achieving Ti6Al4V alloys with both high strength and ductility via selective laser melting. Materials Science and Engineering: A. 2019;766:138319.

[130] Milton S, Rigo O, LeCorre S, Morandeau A, Siriki R, Bocher P, et al. Microstructure effects on the machinability behaviour of Ti6Al4V produced by Selective Laser Melting and Electron Beam Melting process. Materials Science and Engineering: A. 2021;823:141773.

[131] Molaei R, Fatemi A, Sanaei N, Pegues J, Shamsaei N, Shao S, et al. Fatigue of additive manufactured Ti-6Al-4V, Part II: The relationship between microstructure, material cyclic properties, and component performance. International Journal of Fatigue. 2020;132:105363.

[132] Mukalay TA, Trimble JA, Mpofu K, Muvunzi R. A systematic review of process uncertainty in Ti6Al4V-selective laser melting. CIRP Journal of Manufacturing Science and Technology. 2022;36:185-212.

[133] Nguyen HD, Pramanik A, Basak A, Dong Y, Prakash C, Debnath S, et al. A critical review on additive manufacturing of Ti-6Al-4V alloy: microstructure and mechanical properties. journal of materials research and technology. 2022;18:4641-61.

[134] Palmeri D, Buffa G, Pollara G, Fratini L. Sample building orientation effect on porosity and mechanical properties in Selective Laser Melting of Ti6Al4V titanium alloy. Materials Science and Engineering A. 2022;830:142306.

[135] Pan X, Hong Y. High-cycle and very-high-cycle fatigue behaviour of a titanium alloy with equiaxed microstructure under different mean stresses. Fatigue & Fracture of Engineering Materials & Structures. 2019;42(9):1950-64.

[136] Pegues J, Shao S, Shamsaei N, Sanaei N, Fatemi A, Warner D, et al. Fatigue of additive manufactured Ti-6Al-4V, Part I: The effects of powder feedstock, manufacturing, and post-process conditions on the resulting microstructure and defects. International Journal of Fatigue. 2020;132:105358.

[137] Razavi S, Askes H, Berto F, Susmel L. Length scale parameters to estimate fatigue lifetime of 3D-printed titanium alloy Ti6Al4V containing notches in the as-manufactured condition. International Journal of Fatigue. 2023;167:107348.

[138] Ren S, Chen Y, Liu T, Qu X. Effect of build orientation on mechanical properties and microstructure of Ti-6Al-4V manufactured by selective laser melting. Metallurgical and Materials Transactions A. 2019;50(9):4388-409.

[139] Renzo DA, Maletta C, Sgambitterra E, Furgiuele F, Berto F. Surface roughness effect on multiaxial fatigue behavior of additively manufactured Ti6Al4V alloy. International Journal of Fatigue. 2022;163:107022.

[140] Sanaei N, Fatemi A. Defects in additive manufactured metals and their effect on fatigue performance: a state-of-the-art review. Progress in Materials Science. 2021;117:100724.

[141] Segurajauregi U, Álvarez-Vázquez A, Muñiz-Calvente M, Urresti Í, Naveiras H. Fatigue Assessment of Selective Laser Melted Ti-6Al-4V: Influence of Speed Manufacturing and Porosity. Metals. 2021;11(7):1022.

[142] Singh N, Hameed P, Ummethala R, Manivasagam G, Prashanth K, Eckert J. Selective laser manufacturing of Ti-based alloys and composites: Impact of process parameters, application trends, and future prospects. Materials Today Advances. 2020;8:100097.

[143] Singla AK, Banerjee M, Sharma A, Singh J, Bansal A, Gupta MK, et al. Selective laser melting of Ti6Al4V alloy: Process parameters, defects and post-treatments. Journal of Manufacturing Processes. 2021;64:161-87.

[144] Sun C, Chi W, Wang W, Duan Y. Characteristic and mechanism of crack initiation and early growth of an additively manufactured Ti-6Al-4V in very high cycle fatigue regime. International Journal of Mechanical Sciences. 2021;205:106591.

[145] Sun S, Zhang D, Palanisamy S, Liu Q, Dargusch MS. Mechanical properties and deformation mechanisms of martensitic Ti6Al4V alloy processed by laser powder bed fusion and water quenching. Materials Science and Engineering A. 2022;839:142817.

[146] Tridello A, Fiocchi J, Biffi C, Chiandussi G, Rossetto M, Tuissi A, et al. VHCF response of heat-treated SLM Ti6Al4V Gaussian specimens with large loaded volume. Procedia Structural Integrity. 2019;18:314-21.

[147] Wickmann C, Benz C, Heyer H, Witte-Bodnar K, Schäfer J, Sander M. Internal Crack Initiation and Growth Starting from Artificially Generated Defects in Additively Manufactured Ti6Al4V Specimen in the VHCF Regime. Materials. 2021;14(18):5315.

[148] Xiao Z, Chen C, Hu Z, Zhu H, Zeng X. Effect of rescanning cycles on the characteristics of selective laser melting of Ti6Al4V. Optics & Laser Technology. 2020;122:105890.

[149] Xiao Z, Chen C, Zhu H, Hu Z, Nagarajan B, Guo L, et al. Study of residual stress in selective laser melting of Ti6Al4V. Materials & Design. 2020;193:108846.

[150] Stephens RI, Fatemi A, Stephens RR, Fuchs HO. Metal fatigue in engineering: John Wiley & Sons; 2000.

[151] Zhang B, Meng WJ, Shao S, Phan N, Shamsaei N. Effect of heat treatments on pore morphology and microstructure of laser additive manufactured parts. Material Design & Processing Communications. 2019;1(1):e29.

[152] Cutolo A, Elangeswaran C, Formanoir Cd, Muralidharan GK, Hooreweder BV, editors. Effect of heat treatments on fatigue properties of Ti–6Al–4V and 316L produced by laser powder bed fusion in as-built surface condition. TMS 2019 148th Annual Meeting & Exhibition Supplemental Proceedings; 2019: Springer.

[153] Gong H, Rafi K, Gu H, Janaki Ram GD, Starr T, Stucker B. Influence of defects on mechanical properties of Ti–6Al–4V components produced by selective laser melting and electron beam melting. Materials & Design. 2015;86:545-54.

[154] Xu W, Brandt M, Sun S, Elambasseril J, Liu Q, Latham K, et al. Additive manufacturing of strong and ductile Ti–6Al–4V by selective laser melting via in situ martensite decomposition. Acta Materialia. 2015;85:74-84.

[155] Hasib MT, Ostergaard HE, Li X, Kruzic JJ. Fatigue crack growth behavior of laser powder bed fusion additive manufactured Ti-6Al-4V: Roles of post heat treatment and build orientation. International Journal of Fatigue. 2021;142:105955.

[156] Li P, Warner D, Pegues J, Roach M, Shamsaei N, Phan N. Investigation of the mechanisms by which hot isostatic pressing improves the fatigue performance of powder bed fused Ti-6Al-4V. International journal of fatigue. 2019;120:342-52.

[157] Yu G, Li Z, Hua Y, Liu H, Zhao X, Li W, et al. The effects of post heat treatment on the microstructural and mechanical properties of an additive-manufactured porous titanium alloy. Materials. 2020;13(3):593.

[158] Zhang M, Yang Y, Wang D, Xiao Z, Song C, Weng C. Effect of heat treatment on the microstructure and mechanical properties of Ti6Al4V gradient structures manufactured by selective laser melting. Materials Science and Engineering: A. 2018;736:288-97.

[159] Leuders S, Thöne M, Riemer A, Niendorf T, Tröster T, Richard Ha, et al. On the mechanical behaviour of titanium alloy TiAl6V4 manufactured by selective laser melting: Fatigue resistance and crack growth performance. International Journal of Fatigue. 2013;48:300-7.

[160] Rafi H, Karthik N, Gong H, Starr TL, Stucker BE. Microstructures and mechanical properties of Ti6Al4V parts fabricated by selective laser melting and electron beam melting. Journal of materials engineering and performance. 2013;22(12):3872-83.

[161] Leuders S, Meiners S, Wu L, Taube A, Tröster T, Niendorf T. Structural components manufactured by selective laser melting and investment casting—impact of the process route on the damage mechanism under cyclic loading. Journal of Materials Processing Technology. 2017;248:130-42.

[162] Ivanova SG, Biederman RR, Sisson RD. Investigation of fatigue crack initiation in Ti-6Al-4V during tensile-tensile fatigue. Journal of materials engineering and performance. 2002;11(2):226-31.

[163] Gong H, Rafi K, Starr T, Stucker B, editors. Effect of Defects on Fatigue Tests of As-Build Ti-6Al-4V Parts Fabricated by Selective Laser Melting. 2012 International Solid Freeform Fabrication Symposium; 2012: University of Texas at Austin.

[164] Hu Y, Wu S, Withers P, Zhang J, Bao H, Fu Y, et al. The effect of manufacturing defects on the fatigue life of selective laser melted Ti-6Al-4V structures. Materials & Design. 2020;192:108708.

[165] Wycisk E, Siddique S, Herzog D, Walther F, Emmelmann C. Fatigue performance of laser additive manufactured Ti–6Al–4V in very high cycle fatigue regime up to 109 cycles. Frontiers in Materials. 2015;2:72.

[166] Gong H, Rafi K, Gu H, Starr T, Stucker B. Analysis of defect generation in Ti–6Al–4V parts made using powder bed fusion additive manufacturing processes. Additive Manufacturing. 2014;1:87-98.

[167] Cao F, Zhang T, Ryder MA, Lados DA. A review of the fatigue properties of additively manufactured Ti-6Al-4V. Jom. 2018;70(3):349-57.

[168] Choi YR, Sun SD, Liu Q, Brandt M, Qian M. Influence of deposition strategy on the microstructure and fatigue properties of laser metal deposited Ti-6Al-4V powder on Ti-6Al-4V substrate. International Journal of Fatigue. 2020;130:105236.

[169] Liu QC, Elambasseril J, Sun SJ, Leary M, Brandt M, Sharp PK, editors. The effect of manufacturing defects on the fatigue behaviour of Ti-6Al-4V specimens fabricated using selective laser melting. Advanced Materials Research; 2014: Trans Tech Publ.

[170] Pessard E, Lavialle M, Laheurte P, Didier P, Brochu M. High-cycle fatigue behavior of a laser powder bed fusion additive manufactured Ti-6Al-4V titanium: Effect of pores and tested volume size. International Journal of Fatigue. 2021;149:106206.

[171] Zhang C, Zhu H, Liao H, Cheng Y, Hu Z, Zeng X. Effect of heat treatments on fatigue property of selective laser melting AlSi10Mg. International Journal of Fatigue. 2018;116:513-22.

[172] Shipley H, McDonnell D, Culleton M, Coull R, Lupoi R, O'Donnell G, et al. Optimisation of process parameters to address fundamental challenges during selective laser melting of Ti-6Al-4V: A review. International Journal of Machine Tools and Manufacture. 2018;128:1-20.

[173] Qiu C, Adkins NJ, Attallah MM. Microstructure and tensile properties of selectively laser-melted and of HIPed laser-melted Ti–6Al–4V. Materials Science and Engineering: A. 2013;578:230-9.

[174] Elsayed M, Ghazy M, Youssef Y, Essa K. Optimization of SLM process parameters for Ti6Al4V medical implants. Rapid Prototyping Journal. 2018;25(3):433-47.

[175] Song B, Dong S, Zhang B, Liao H, Coddet C. Effects of processing parameters on microstructure and mechanical property of selective laser melted Ti6Al4V. Materials & Design. 2012;35:120-5.

[176] Meng L, Yang H, Ben D, Ji H, Lian D, Ren D, et al. Effects of defects and microstructures on tensile properties of selective laser melted Ti6Al4V alloys fabricated in the optimal process zone. Materials Science and Engineering: A. 2022;830:142294.

[177] Karimi J, Suryanarayana C, Okulov I, Prashanth K. Selective laser melting of Ti6Al4V: Effect of laser re-melting. Materials Science and Engineering: A. 2021;805:140558.

[178] Miao X, Wu M, Han J, Li H, Ye X. Effect of laser rescanning on the characteristics and residual stress of selective laser melted titanium Ti6Al4V alloy. Materials. 2020;13(18):3940.

[179] Bartlett JL, Li X. An overview of residual stresses in metal powder bed fusion. Additive Manufacturing. 2019;27:131-49.

[180] Luo Y-w, Wang M-y, Tu J-g, Jiang Y, Jiao S-q. Reduction of residual stress in porous Ti6Al4V by in situ double scanning during laser additive manufacturing. International Journal of Minerals, Metallurgy and Materials. 2021;28(11):1844-53.

[181] Ali H, Ma L, Ghadbeigi H, Mumtaz K. In-situ residual stress reduction, martensitic decomposition and mechanical properties enhancement through high temperature powder bed pre-heating of Selective Laser Melted Ti6Al4V. Materials Science and Engineering: A. 2017;695:211-20.

[182] Edwards P, Ramulu M. Fatigue performance evaluation of selective laser melted Ti–6Al–4V. Materials Science and Engineering: A. 2014;598:327-37.

[183] Cain V, Thijs L, Van Humbeeck J, Van Hooreweder B, Knutsen R. Crack propagation and fracture toughness of Ti6Al4V alloy produced by selective laser melting. Additive Manufacturing. 2015;5:68-76.

[184] Shamsaei N, Simsiriwong J. Fatigue behaviour of additively-manufactured metallic parts. Procedia Structural Integrity. 2017;7:3-10.

[185] Chen S-g, Gao H-j, Wu Q, Gao Z-h, Zhou X. Review on residual stresses in metal additive manufacturing: formation mechanisms, parameter dependencies, prediction and control approaches. Journal of Materials Research and Technology. 2022;17:2950-74.

[186] Leuders S, Lieneke T, Lammers S, Tröster T, Niendorf T. On the fatigue properties of metals manufactured by selective laser melting–The role of ductility. Journal of Materials Research. 2014;29(17):1911-9.

[187] Acevedo R, Sedlak P, Kolman R, Fredel M. Residual stress analysis of additive manufacturing of metallic parts using ultrasonic waves: State of the art review. Journal of Materials Research and Technology. 2020;9(4):9457-77.

[188] Thöne M, Leuders S, Riemer A, Tröster T, Richard H, editors. Influence of Heat-Treatment of Selective Laser Melting Products-eg Ti6Al4V. 2012 International Solid Freeform Fabrication Symposium; 2012: University of Texas at Austin.

[189] Karami K, Blok A, Weber L, Ahmadi S, Petrov R, Nikolic K, et al. Continuous and pulsed selective laser melting of Ti6Al4V lattice structures: Effect of post-processing on microstructural anisotropy and fatigue behaviour. Additive Manufacturing. 2020;36:101433.

[190] Benedetti M, Fontanari V, Bandini M, Zanini F, Carmignato S. Low-and high-cycle fatigue resistance of Ti-6Al-4V ELI additively manufactured via selective laser melting: Mean stress and defect sensitivity. International journal of fatigue. 2018;107:96-109.

[191] Mertova K, Dzugan J, Roudnicka M, editors. Fatigue properties of SLM-produced Ti6Al4V with various post-processing processes. IOP Conference Series: Materials Science and Engineering; 2018: IOP Publishing.

[192] du Plessis A, Rossouw P. Investigation of Porosity Changes in Cast Ti6Al4V Rods After Hot Isostatic Pressing. Journal of Materials Engineering and Performance. 2015;24(8):3137-41.

[193] Dallago M, Fontanari V, Torresani E, Leoni M, Pederzolli C, Potrich C, et al. Fatigue and biological properties of Ti-6Al-4V ELI cellular structures with variously arranged cubic cells made by selective laser melting. Journal of the mechanical behavior of biomedical materials. 2018;78:381-94.

[194] Dallago M, Fontanari V, Winiarski B, Zanini F, Carmignato S, Benedetti M. Fatigue properties of Ti6Al4V cellular specimens fabricated via SLM: CAD vs real geometry. Procedia Structural Integrity. 2017;7:116-23.

[195] Gockel J, Sheridan L, Koerper B, Whip B. The influence of additive manufacturing processing parameters on surface roughness and fatigue life. International Journal of Fatigue. 2019;124:380-8.

[196] Kahlin M, Ansell H, Basu D, Kerwin A, Newton L, Smith B, et al. Improved fatigue strength of additively manufactured Ti6Al4V by surface post processing. International Journal of Fatigue. 2020;134:105497.

[197] Vayssette B, Saintier N, Brugger C, El May M, Pessard E. Numerical modelling of surface roughness effect on the fatigue behavior of Ti-6Al-4V obtained by additive manufacturing. International Journal of Fatigue. 2019;123:180-95.

[198] Benedetti M, Torresani E, Leoni M, Fontanari V, Bandini M, Pederzolli C, et al. The effect of post-sintering treatments on the fatigue and biological behavior of Ti-6Al-4V ELI parts made

by selective laser melting. Journal of the mechanical behavior of biomedical materials. 2017;71:295-306.

[199] Wagner L, Luetjering G, editors. Influence of shot peening on the fatigue behavior of titanium alloys. International Conference on Shot Peening; 1981.

[200] Zhang H, Chiang R, Qin H, Ren Z, Hou X, Lin D, et al. The effects of ultrasonic nanocrystal surface modification on the fatigue performance of 3D-printed Ti64. International Journal of Fatigue. 2017;103:136-46.

[201] Wycisk E, Emmelmann C, Siddique S, Walther F, editors. High cycle fatigue (HCF) performance of Ti-6Al-4V alloy processed by selective laser melting. Advanced materials research; 2013: Trans Tech Publ.

[202] Pegues J, Roach M, Scott Williamson R, Shamsaei N. Surface roughness effects on the fatigue strength of additively manufactured Ti-6Al-4V. International Journal of Fatigue. 2018;116:543-52.

[203] Masuo H, Tanaka Y, Morokoshi S, Yagura H, Uchida T, Yamamoto Y, et al. Influence of defects, surface roughness and HIP on the fatigue strength of Ti-6Al-4V manufactured by additive manufacturing. International Journal of Fatigue. 2018;117:163-79.

[204] Greitemeier D, Palm F, Syassen F, Melz T. Fatigue performance of additive manufactured TiAl6V4 using electron and laser beam melting. International Journal of Fatigue. 2017;94:211-7.

[205] Kahlin M, Ansell H, Moverare J. Fatigue behaviour of additive manufactured Ti6Al4V, with as-built surfaces, exposed to variable amplitude loading. International Journal of Fatigue. 2017;103:353-62.

[206] Kahlin M, Ansell HM, J.J. Fatigue behaviour of notched additive manufactured Ti6Al4V with as-built surfaces. International Journal of Fatigue. 2017;101:51-60.

[207] Sun W, Ai X, Li J. Effects of the building direction on fatigue crack growth behavior of Ti-6Al-4V manufactured by selective laser melting. Procedia Structural Integrity. 2018;13:1020-5.

[208] Farhangdoost K, Provan JW. A stochastic systems approach to fatigue reliability—an application to Ti-6Al-4V. Engineering fracture mechanics. 1996;53(5):687-706.

[209] Jiao Z, Xu R, Yu H, Wu X. Evaluation on tensile and fatigue crack growth performances of Ti6Al4V alloy produced by selective laser melting. Procedia Structural Integrity. 2017;7:124-32.

[210] Pegues J, Roach M, Williamson RS, Shamsaei N, editors. Effect of specimen surface area size on fatigue strength of additively manufactured Ti-6Al-4V parts. 2017 International Solid Freeform Fabrication Symposium; 2017: University of Texas at Austin.

[211] Pegues JR, Michael Williamson, R Scott Shamsaei, Nima, editor Volume effects on the fatigue behavior of additively manufactured Ti-6Al-4V Parts. 2018 International Solid Freeform Fabrication Symposium; 2018: University of Texas at Austin.

[212] Agius D, Kourousis KI, Wallbrink C. A review of the as-built SLM Ti-6Al-4V mechanical properties towards achieving fatigue resistant designs. Metals. 2018;8(1):75.

[213] Leuders S, Vollmer M, Brenne F, Tröster T, Niendorf T. Fatigue strength prediction for titanium alloy TiAl6V4 manufactured by selective laser melting. Metallurgical and materials transactions A. 2015;46(9):3816-23.

[214] Rafi HK, Karthik NV, Gong H, Starr TL, Stucker BE. Microstructures and Mechanical Properties of Ti6Al4V Parts Fabricated by Selective Laser Melting and Electron Beam Melting. Journal of Materials Engineering and Performance. 2013;22(12):3872-83.

[215] Wycisk E, Solbach A, Siddique S, Herzog D, Walther F, Emmelmann C. Effects of defects in laser additive manufactured Ti-6Al-4V on fatigue properties. Physics Procedia. 2014;56:371-8.

[216] Zhu M-L, Jin L, Xuan F-Z. Fatigue life and mechanistic modeling of interior micro-defect induced cracking in high cycle and very high cycle regimes. Acta Materialia. 2018;157:259-75.

[217] Wu W, Zhu ML, Liu X, Xuan FZ. Effect of temperature on high-cycle fatigue and very high cycle fatigue behaviours of a low-strength Cr–Ni–Mo–V steel welded joint. Fatigue & Fracture of Engineering Materials & Structures. 2017;40(1):45-54.

[218] Zhu M-L, Xuan F-Z, Chen J. Influence of microstructure and microdefects on long-term fatigue behavior of a Cr–Mo–V steel. Materials Science and Engineering: A. 2012;546:90-6.

[219] Zhu M-L, Xuan F-Z, Du Y-N, Tu S-T. Very high cycle fatigue behavior of a low strength welded joint at moderate temperature. International journal of fatigue. 2012;40:74-83.

[220] Murakami Y. Metal Fatigue: Effects of Small Defects and Nonmetallic Inclusions. First ed. Elsevier2002. 325-44 p.

[221] Liu Y, Li Y, Li S, Yang Z, Chen S, Hui W, et al. Prediction of the S–N curves of high-strength steels in the very high cycle fatigue regime. International journal of fatigue. 2010;32(8):1351-7.

[222] Wang Q, Bathias C, Kawagoishi N, Chen Q. Effect of inclusion on subsurface crack initiation and gigacycle fatigue strength. International Journal of Fatigue. 2002;24(12):1269-74.

[223] Yang K, Huang Q, Wang Q, Chen Q. Competing crack initiation behaviors of a laser additively manufactured nickel-based superalloy in high and very high cycle fatigue regimes. International Journal of Fatigue. 2020;136:105580.

[224] Fan Y, Gui X, Liu M, Wang X, Feng C, Gao G. High-Cycle Fatigue Life and Strength Prediction for Medium-Carbon Bainitic Steels. Metals. 2022;12(5):856.

[225] Tanaka K, Akiniwa Y. Fatigue crack propagation behaviour derived from S–N data in very high cycle regime. Fatigue & Fracture of Engineering Materials & Structures. 2002;25(8-9):775-84.

[226] Chapetti M, Tagawa T, Miyata T. Ultra-long cycle fatigue of high-strength carbon steels part II: estimation of fatigue limit for failure from internal inclusions. Materials Science and Engineering: A. 2003;356(1-2):236-44.

[227] Mayer H, Haydn W, Schuller R, Issler S, Furtner B, Bacher-Höchst M. Very high cycle fatigue properties of bainitic high carbon–chromium steel. International Journal of Fatigue. 2009;31(2):242-9.

[228] Pugno N, Ciavarella M, Cornetti P, Carpinteri A. A generalized Paris' law for fatigue crack growth. Journal of the Mechanics and Physics of Solids. 2006;54(7):1333-49.

[229] Paolino D, Chiandussi G, Rossetto M. A unified statistical model for S-N fatigue curves: probabilistic definition. Fatigue & Fracture of Engineering Materials & Structures. 2013;36(3):187-201.

[230] Paolino DS, Tridello A, Chiandussi G, Rossetto M, editors. Statistical estimation of duplex SN curves. Key Engineering Materials; 2016: Trans Tech Publ.

[231] Kasperovich G, Haubrich J, Gussone J, Requena G. Correlation between porosity and processing parameters in TiAl6V4 produced by selective laser melting. Materials & Design. 2016;105:160-70.

[232] Leuders S, Thöne M, Riemer A, Niendorf T, Tröster T, Richard HA, et al. On the mechanical behaviour of titanium alloy TiAl6V4 manufactured by selective laser melting: Fatigue resistance and crack growth performance. International Journal of Fatigue. 2013;48:300-7.

[233] Standard test method for particle size distribution of metal powders and related compounds by light scattering. ASTM B822-17. (West Conshohocken, PA: ASTM International, approved April 1, 2017).

[234] Standard Test Method for Sieve Analysis of Metal Powders. ASTM B214-16. (West Conshohocken, PA: ASTM International, approved April 1, 2016).

[235] Standard Test Method for Apparent Density of Free-Flowing Metal Powders Using the Hall Flowmeter Funnel. ASTM B212-17. (West Conshohocken, PA: ASTM International, approved April 1, 2017).

[236] Standard test methods for flow rate of metal powders using the hall flowmeter funnel. ASTM B213-17. (West Conshohocken, PA: ASTM International, approved April 1, 2017).

[237] Ilie P, Lesperance X, Ince A. Development of an ultrasonic fatigue testing system for gigacycle fatigue. Material Design & Processing Communications. 2020;2(6):e120.

[238] Wen-jie P, Huan X, editors. The influential factors on very high cycle fatigue testing results. MATEC Web of Conferences; 2018: EDP Sciences.

[239] Basquin O, editor The exponential law of endurance tests. Proc Am Soc Test Mater; 1910.

[240] Pilkey WD, Pilkey DF, Bi Z. Peterson's stress concentration factors: John Wiley & Sons; 2020.

[241] Arola D, Ramulu M. An examination of the effects from surface texture on the strength of fiber reinforced plastics. Journal of Composite materials. 1999;33(2):102-23.

[242] Arola D, Williams C. Estimating the fatigue stress concentration factor of machined surfaces. International Journal of fatigue. 2002;24(9):923-30.

[243] Quan F, Chen Z, Ye H, Cui C, Cui Y. Study of the effect of surface roughness on fatigue strength of GH4169 based on indirect evaluation of the notch root radius. International Journal of Fatigue. 2021;152:106440.

[244] Pabst W, Gregorova E. Characterization of particles and particle systems. ICT Prague. 2007;122:122.

[245] Grace JR, Ebneyamini A. Connecting particle sphericity and circularity. Particuology. 2021;54:1-4.

[246] Liu Y, Gao R, Chen J. Exploring the influence of sphericity on the mechanical behaviors of ballast particles subjected to direct shear. Granular Matter. 2019;21:1-17.

[247] Motyka M, Kubiak K, Sieniawski J, Ziaja W. Phase transformations and characterization of α+ β titanium alloys. Comprehensive materials processing. 2014;2:7-36.

[248] Xu W, Sun S, Elambasseril J, Liu Q, Brandt M, Qian M. Ti-6Al-4V additively manufactured by selective laser melting with superior mechanical properties. Jom. 2015;67(3):668-73.

[249] Hong Y, Liu X, Lei Z, Sun C. The formation mechanism of characteristic region at crack initiation for very-high-cycle fatigue of high-strength steels. International Journal of Fatigue. 2016;89:108-18.

[250] Hong Y, Sun C. The nature and the mechanism of crack initiation and early growth for very-high-cycle fatigue of metallic materials–An overview. Theoretical and Applied Fracture Mechanics. 2017;92:331-50.